

Exploration of the parameter space for the excitation and saturation of Edge Harmonic Oscillations

Présentée le 5 mai 2023

Faculté des sciences de base
SPC - Théorie
Programme doctoral en physique

pour l'obtention du grade de Docteur ès Sciences

par

Guillermo BUSTOS RAMIREZ

Acceptée sur proposition du jury

Prof. F. Mila, président du jury
Prof. J. Graves, directeur de thèse
Dr S. Y. Medvedev, rapporteur
Dr C. J. Ham, rapporteur
Dr J. Schober, rapporteuse

Abstract

This thesis presents advancements in the understanding of the plasma conditions leading to the excitation and saturation of the Edge Harmonic Oscillations (EHOs) observed during QH-mode operation in tokamak plasmas. Such operations represent a safer alternative with respect to H-mode due to the absence of Edge Localised Modes (ELMs) while retaining high energy confinement and pedestal height. In this work, EHOs have been assumed to be the nonlinear evolution of linearly unstable external infernal (*exfernal*) modes. It is consistently found that exfernal modes can be excited and nonlinearly saturated in wide regions of the parameter space. Such regions have been identified through the use of various analytical and numerical tools developed within the ideal MHD model, including linear analytical modelling, linear stability software, and nonlinear equilibrium and initial value simulations. An expanded set of large aspect ratio equations describing the linear stability of exfernal modes is derived analytically, including higher order terms in the expansion of the safety factor around the rational surface, which allows for the effects of finite edge magnetic shear. Numerical solution of the equations provides the linearly unstable exfernal mode parameter space with respect to pedestal pressure gradient, pedestal width, edge safety factor and edge magnetic shear. Nonlinearly saturated exfernal modes calculated with the 3D VMEC free boundary code are found in regions of the parameter space where the exfernal modes are linearly unstable to the 2D VMEC neighbour state. The obtained critical value of the edge magnetic shear in the VMEC simulations is also recovered by the linear stability analysis. The parameter space is found to be reduced by the presence of a plasma separatrix due to a partial stabilisation of the external kink current-driven branch of the exfernal mode. An analytical estimation of the critical magnetic shear for the excitation of exfernal modes in diverted plasmas is also presented. Finally, it is shown that the parameter space for the saturation of external modes can be expanded through the application of non-axisymmetric Magnetic Perturbations (MPs). This is done analytically using a linear time-invariant perturbation of the 2D equilibrium assuming an external helical magnetic perturbation, and also in the VMEC code by the inclusion of non-axisymmetric coils in the calculation of the vacuum field. The approaches were applied to saturated external kink and exfernal modes. For the external kink case, quantitative agreement is found in the saturated amplitude obtained with the linear model and with the VMEC code for cases where the external kink is stable in the absence of MPs. For the case of saturated exfernal modes, only

Abstract

qualitative agreement is found, possibly due to the approximations taken in the calculation of the analytical model. Nevertheless, a significant expansion of the parameter space of saturated external modes is obtained via the introduction of symmetry breaking coils, resulting in an appealing route for future reactor operations.

Key words: external, internal, Edge Harmonic Oscillations, QH-mode, MHD, 3D, stability, equilibrium, nonlinear, magnetic perturbations.

Résumé

Cette thèse présente les avancées dans la compréhension des conditions du plasma menant à l'excitation et à la saturation des Oscillations Harmoniques de Bord (EHOs) observées pendant le fonctionnement en QH-mode dans les plasmas de tokamak. Ces opérations représentent une alternative plus sûre par rapport au H-mode en raison de l'absence de Modes Localisés de Bord tout en conservant un confinement d'énergie et une hauteur de piédestal élevé. Dans ce travail, les EHO ont été supposés être l'évolution non linéaire des modes 'infernal' externes linéairement instables (exfernal). On constate systématiquement que les modes exfernal peuvent être excités et saturés de manière non linéaire dans de larges régions de l'espace des paramètres. Ces régions ont été identifiées par l'utilisation de divers outils analytiques et numériques développés dans le cadre du modèle MHD idéal, y compris la modélisation analytique linéaire, de logiciel de stabilité linéaire et les simulations non linéaires d'équilibre et de valeur initiale. Un ensemble élargi d'équations décrivant la stabilité linéaire des modes exfernal est dérivé analytiquement, y compris les termes d'ordre supérieur dans l'expansion du facteur de sécurité (q) autour de la surface rationnelle, qui permet les effets du cisaillement magnétique de bord fini. La solution numérique des équations fournit l'espace des paramètres des modes exfernal linéairement instables en ce qui concerne le gradient de pression du piédestal, la largeur du piédestal, le facteur de sécurité du bord et le cisaillement magnétique du bord. Des modes exfernal saturés de façon non linéaire, calculée avec le code 3D VMEC avec des conditions aux bord libres, sont trouvés dans les régions de l'espace des paramètres où les modes exfernal sont linéairement instables par rapport à l'état voisin 2D VMEC. La valeur critique obtenue du cisaillement magnétique de bord dans les simulations VMEC est également retrouvée par l'analyse de stabilité linéaire. On constate que l'espace des paramètres est réduit par la présence d'une séparatrice du plasma en raison d'une stabilisation partielle de la branche du kink externe du mode exfernal. Une estimation analytique du cisaillement magnétique critique pour l'excitation des modes exfernal dans les plasmas avec une séparatrice du plasma est également présentée. Enfin, il est montré que l'espace des paramètres pour la saturation des modes externes peut être étendu par l'application de perturbations magnétiques (MPs) non-axisymétriques. Ceci est réalisé analytiquement en utilisant une perturbation linéaire invariante dans le temps de l'équilibre 2D en supposant une perturbation magnétique hélicoïdale externe, et également dans le code VMEC par l'inclusion de bobines

Abstract

non-axisymétriques dans le calcul du champ de vide. Ces approches ont été appliquées à des modes saturés de type kink externe et exernal. Pour le cas du kink externe, un accord quantitatif est trouvé dans l'amplitude saturée obtenue avec le modèle linéaire et avec le code VMEC pour les cas où le kink externe est stable en l'absence de MPs. Pour le cas des modes exernal saturés, seul un accord qualitatif est trouvé, peut-être en raison des approximations prises dans le calcul du modèle analytique. Néanmoins, une expansion significative de l'espace des paramètres des modes exernal saturés est obtenue via l'introduction de bobines de rupture de symétrie, ce qui constitue une voie intéressante pour l'exploitation future des réacteurs.

Mots **clefs** : exernal, infernal, Oscillations Harmoniques de Bord (EHOs), QH-mode, MHD, 3D, stabilité, équilibre, non linéaire, perturbations magnétiques.

To my parents, for giving me everything I would ever need.

To Karen, for brightening my days.

To Oliver, our little sunshine, for filling my life with hope.

Contents

Abstract (English/Français)	i
1 Introduction	1
1.1 Magnetic confinement fusion as an energy source	1
1.2 Tokamak modes of operation, safety limits and other concerns	6
1.3 Thesis contribution and outline	8
2 The ideal MHD model	13
2.1 Description and validity of the ideal MHD model	13
2.2 Flux coordinate systems and representation of the magnetic field	16
2.3 MHD equilibria in toroidal devices	20
2.3.1 The Grad-Shafranov equation with toroidal rotation	22
2.3.2 The tokamak ordering	25
2.4 Linear MHD fluctuations and stability	27
2.4.1 Paths into solution	28
2.4.2 Field Line Bending and the magnetic operator	30
2.4.3 Vacuum physics and external modes	31
2.4.4 Ideal instabilities at the plasma edge	32
2.5 Nonlinear stability and 3D saturated modes	35
2.5.1 Nonlinear approaches to equilibrium	36
3 Exfernal modes as a model for EHOs	41
3.1 Experimental observation of EHOs	41
3.1.1 The nature of EHOs	41
3.1.2 Access to QH-mode and key drivers	43
3.2 Linear theory of exfernal modes	46

Contents

3.3	Nonlinear saturated EHOs	50
3.3.1	Equilibrium approach to EHO numerical modelling: application to DEMO	51
3.3.2	Comparison of the external saturated states in VMEC and JOREK	59
3.4	Prospects for the EHOs parameter space	64
4	Effect of edge magnetic shear on the excitation mechanism of external modes	67
4.1	Introduction	68
4.2	Analytical expansion of the equilibrium equations	70
4.3	Derivation of the stability equations	72
4.3.1	High Shear region	73
4.3.2	Low Shear region	73
4.3.3	Boundary conditions	78
4.4	Numerical solutions	80
4.4.1	A comparative test: zero shear cases	82
4.4.2	The role of magnetic shear	84
4.4.3	Stability diagrams	85
4.5	Comparison with linear (KINX) and nonlinear (VMEC) codes	88
4.6	Model of the plasma separatrix	91
4.6.1	Modification of the parameter space with a separatrix	96
4.6.2	Analytical estimation of edge critical shear with a separatrix	97
4.7	Conclusions	101
5	The effect of non-Axisymmetric Magnetic Perturbations on non-resonant external modes	105
5.1	Models for the non-axisymmetric magnetic perturbations	107
5.1.1	The antenna time-invariant linear model	107
5.1.2	The VMEC nonlinear model	109
5.2	MP-induced saturated external kink modes	115
5.2.1	Linear equilibrium equation for the analytic treatment of external kink modes with MP	115
5.2.2	Comparison with 3D states calculated with the VMEC code	118
5.3	MP-induced saturated external modes	121
5.3.1	Linear equilibrium equation for external modes with MP	122
5.3.2	Comparison with 3D states calculated with the VMEC code	126

5.3.3 Beyond linear modelling: The extended parameter space of saturated external modes	127
5.4 Summary and conclusions	129
6 General conclusions and outlook	131
A Numerical tools	135
A.1 The VMEC code	135
A.1.1 Stellarator symmetry	137
A.2 The FreeGS code	138
A.3 The KINX stability code	139
B Mathematical derivations	141
B.1 Equilibrium torodial flow	141
B.2 Corrected sideband equations with shear	143
B.2.1 Calculation of the constants of integration	145
B.3 Reference model in Chapter 4	146
C VENUS-MHDpy code	151
C.1 Motivation and numerical method	151
C.2 Numerical implementation: A finite element implementation for vector languages	154
C.3 Normalisation in VENUS-MHDpy	155
C.4 Benchmark and convergence test	156
C.5 Future prospects	157
D Acronyms	159
Acknowledgements	161
Bibliography	182
Curriculum Vitae	183

1 Introduction

1.1 Magnetic confinement fusion as an energy source

The technological advancements in the production of clean energy should be able to keep pace with the increased global energy demands if we want to maintain the living standards of modern society without producing enormous amounts of greenhouse gases. The current model in most countries produces most of its electricity ‘on demand’ due to the lack of energy storage capacity¹, meaning that large-scale, continuous source of electricity is always needed. Right now, that spot is occupied by a combination of fossil fuel and nuclear *fission* power. The use of fossil fuels needs to be reduced to the minimum possible for environmental and public health reasons, as discussed at length in reference [Man22]. The positive use of nuclear fission power is, on the other hand, debated in some countries. As of today, fission power is the single available option that could replace the use of fossil fuel for on demand electricity production, but it still has some caveats. Firstly, the fuel used is not renewable nor available for every country, is highly radioactive and can in principle be used to increase the proliferation of nuclear weapons, meaning that strict regulations need to take place in order to guarantee a safe use of the resource. Secondly, while the risk of an accident is very low in novel fission reactors, the consequences can be catastrophic².

¹The most popular ways to store energy are in hydroelectric dams, batteries and hydrogen cells. Though all of them promising, they still have issues. The first one depends on geographical conditions and is not available everywhere, the second one is very expensive to do in large scale and has potential environmental issues, and the technology of the third one is not mature enough to be economically viable.

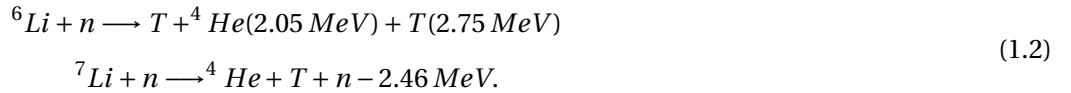
²Contrary to popular belief, nuclear fission is one of the safest ways to generate electricity, even accounting for all nuclear accidents [Mana]. Moreover, as of 2011 it was estimated that nuclear power saved 1.84 million of lives and avoided 64 Gigatonnes of CO_2 emission [KH13].

Introduction

A promising alternative for a large-scale continuous energy source is nuclear *fusion* power. Fusion is the reaction that powers the stars, where light nuclei fuse together to create a heavier elements. During the process, some of the mass of the reactants is transformed into energy through Einstein's equation $\Delta E = (m_r - m_p)c^2$, where m_r and m_p are the mass of the reactants and of the products respectively, and c is the speed of light. The most promising fusion fuel for energy production (at least for the first generation of reactors) is the Deuterium-Tritium (DT) mix, that fuse through the following reaction



Note that the difference in energy goes to the reaction products as kinetic energy, where the energy carried by the neutron is what is ultimately transformed into electricity through heat exchange³. No radioactive products are produced from the fusion reaction, but the highly energetic neutrons activate the reactor walls, making them radioactive. Low-activation materials such as steel and concrete are currently under development, with the goal of fully disposing or recycling the components of a fusion power plant within 100 years [Gor15]. Taking this into account, hundreds of tons of medium time-scale radioactive waste are expected when closing a fusion power plant. Nevertheless, the level of radioactivity would be several orders of magnitude smaller than in fission power plants, where both the fuel and the products are highly radioactive, with a half-life of thousands of years. Deuterium occurs vastly on Earth, as it can be found in sea water in a concentration of 1 Deuterium per 6700 protons [Fri53]. Tritium however is extremely rare on Earth, but it can be bred from Lithium⁴ "on site" using the neutrons produced by DT burn through one of the following reactions



³Other ideas to produce electricity from fusion are considered, including the use of hydrogen cells.

⁴Note that a starting amount of Tritium is required in a power plant, which might not be available following current Tritium production trends [Cle22]. This however can be solved by breeding the Tritium for the first fusion power plants in fission power plants.

According to reference [US 22], it is estimated that the total land reserves of Lithium that can potentially be mined in the near term are $\sim 8.8 \times 10^7$ t. Assuming 10% of recirculating energy, 40% of fusion-to-electricity power conversion efficiency and a conversion of 1% of the Lithium atoms into Tritium, the DT reaction could power the Earth for roughly ~ 500 years taking into account everyone in the current population consuming $\sim 7 \text{ MWh/year}$ (European energy consumption level). Lithium is also diluted in sea water ($\sim 2.24 \times 10^{11}$ t [För81]), and methods to extract it are expected to be exploited in the coming years due to the increased Lithium global demand [Liu+20]. It is therefore clear that fusion fuel is widely available and may potentially last for thousands of years⁵.

While fusion reactions can be produced with relatively simple methods (for example: [Glu20]), the only way to get fusion energy gain is through thermonuclear reactions due to the relatively small fusion cross section. In a thermonuclear process, the fuel must be heated to very high temperatures ($\sim 10 - 50$ KeV for DT reactions in fusion reactors) and confined so that fusion reactions can happen randomly over a period of time. At such high temperatures the atoms in the fuel are in a ionised state, known as *plasma* state⁶. A sustained fusion reaction occurs when the plasma is confined for long enough so that the energy produced by nuclear fusion (carried by the ^4He particle as the neutron cannot continue to heat the fuel) overcomes the losses from all the other mechanisms, where the confinement time τ_E is given by the Lawson criteria [Law57] for DT fuel

$$nT\tau_E > 3 \times 10^{21} \text{ m}^{-3} \text{ keVs}, \quad (1.3)$$

where n and T are respectively the density and temperature of the plasma. In contrast with a nuclear fission reactor, where a chain reaction needs to be controlled to maintain a manageable amount of output power, in a nuclear fusion reactor the fuel needs to be confined so that the reactions can take place. If confinement is lost, the fuel gets cold and the reactions stop, so no major accidents (beyond damaging the reactor) can occur. A few methods exist to confine

⁵This figure is only related to the availability of D and T. Other materials related to fusion energy production such as neutron multipliers to increase Tritium breeding impose a more severe restriction on the availability of fusion power.

⁶A plasma is characterised by globally quasi-neutrality and by exhibiting collective particle behaviour, particularly in response to electric and magnetic fields.

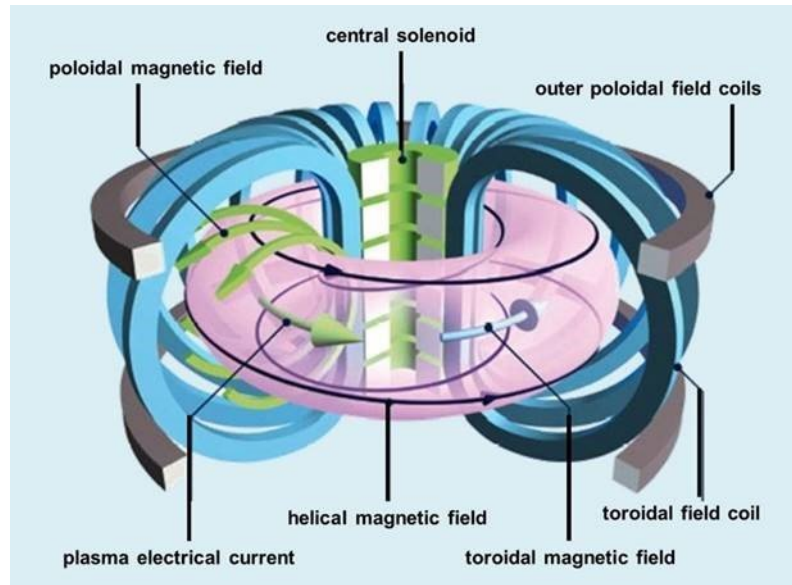


Figure 1.1: Schematic diagram of a tokamak. The toroidal coils (blue) produce the magnetic field in the toroidal direction (blue arrows), while the a time-varying current in the central solenoid (green) induce a toroidal current (single green arrow) in the plasma producing a magnetic field in the poloidal direction (green arrows). The superposition of the two magnetic fields creates magnetic flux surfaces with helical field lines (black). Also in the figure are shown the outer poloidal field coils, which are used for plasma shaping and control. Obtained from EUROfusion.

fusion plasmas. This thesis is focused on the *magnetic confinement* approach, where the main idea is to magnetically levitate the super-hot plasma inside of a vacuum chamber to avoid both cooling the fuel and damaging the walls of the container. The most successful magnetic confinement configuration up to date is the tokamak, presented schematically in figure 1.1. A tokamak is a toroidal device where the particles in the plasma are confined by two superimposed sources of magnetic field. The first one is produced by toroidal coils, which provide a magnetic field in the symmetry axis of the torus, herein referred to as the *toroidal* direction. The second one is a magnetic field in the *poloidal* direction, created by driving a toroidal electrical current in the plasma itself. Such current can be driven by injecting energy into the plasma in one preferential direction (by either microwave power heating or injection of highly energetic neutral particles), with the aid of a central solenoid acting as an inductive transformer, or through a kinetic mechanism known as bootstrap current generation [Pee00]. The resulting magnetic field lines revolve helically around the plasma with a certain pitch angle. As will be discussed later in Chapter 2, the pitch angle defines the strength at which

magnetic field lines bend in response to a plasma perturbation. The macroscopic interplay between the plasma pressure, current and external magnetic field can be described by the Magneto-hydrodynamics (MHD) model, where the plasma is assumed to be an electrically conductive fluid. In this thesis, the MHD model is used to assess equilibrium and stability of tokamak plasmas in advanced operational scenarios with optimised confinement properties.

As we have seen, fusion power is in many ways the ideal energy source. Energy production is carbon-neutral, the fuel is abundant and widely available to most countries, it produces a much lower amount of radioactive waste compared to fission, and is intrinsically safe. The caveat with fusion power is that it is extremely difficult to achieve. After more than 60 years of experiments, as of 2022 the world record on fusion energy produced is held by the Joint European Torus (JET) tokamak, which in 2021 produced 59 Mega Joules over 5 seconds during its second DT experimental campaign [Gib22]. The ratio of the output power with respect to the input power (denominated as the Q factor) on the aforementioned discharge was of $Q = 0.33$. For electricity production, it is projected that a power plant should have at least $Q = 10$, which is the goal of the International Thermonuclear Experimental Reactor (ITER), expected to start DT operations around 2035. Even if ITER is successful in achieving $Q = 10$, it is still an experiment and will not produce electricity. The European road map considers that the DEMO reactor, which is the next step after ITER, will be the first-of-a-kind power plant, but operation is expected to start around the year 2050. Countries as the United Kingdom [Manb], China and South Korea [LNL19] also plan to have their own first-of-a-kind fusion power plants in operation between 2040 and 2050. It is therefore clear that the current road map for including fusion power into the electrical grid does not match the goals for lowering carbon emissions ⁷. The main reason for such long timelines is that the most conservative scaling laws provided by empirical data on present-day tokamaks suggest that the plasma volume in a power plant should be between $\sim 1000 - 3500 \text{ m}^3$. Building such a large reactor requires a huge monetary investment and strong international collaboration. ITER for example, which is $\sim 800 \text{ m}^3$, is being built by the European Union, United States, India, Japan, Russia, North Korea and China, with an estimated cost of \$ 22 billion US dollars [Gib22]. While the cost of future power plants is expected to drop as the industrial processes related to the construction of fusion reactors are optimised [LLK16], it is not yet clear when (if ever) fusion power will be commercially competitive with other sources of electricity due to the current uncertainties on its feasibility

⁷Many private companies have now entered the race for fusion energy, promising to deliver electricity around the year 2030. It is however unclear if they will be able to achieve it.

as an energy source.

Such uncertainties are related to the management of power exhaust from the plasma, Tritium breeding technology, wall and magnet damage due to neutron irradiation, steady state operation and plasma disruption avoidance. These issues are experimental targets of the ITER project, and most of the fusion-related research done in the world is dedicated to the solution of these problems. The focus of the present thesis is related to the plasma disruption avoidance, particularly on the study of disruption-free tokamak operational modes. The importance of this topic relies on the fact that disruptions can release large portions of the confined energy and particles into the **Plasma-Facing Components (PFC)** and seriously damage some of the components (e.g. superconducting coils) due to the large electromagnetic forces associated with the disruption. Regular maintenance of the PFC and other components due to disruption damage will limit the operational time of the reactor, having a direct impact on the cost of electricity of a power plant.

In summary, fusion power offers a clean source of continuous electricity, but the complexity of the technology and cost of electricity might make it out of reach to be deployed in large-scale, especially in developing countries. Research and development is therefore needed to solve these problems and make fusion energy a reality in the near future.

1.2 Tokamak modes of operation, safety limits and other concerns

In tokamak devices, the combination of the toroidal and poloidal magnetic fields creates toroidally axisymmetric nested magnetic surfaces (a detailed description is given in Chapter 2). The movement of plasma particles along the magnetic field lines remains well confined to the surfaces thanks to the toroidal symmetry of the device⁸. Particle transport across magnetic surfaces occurs due to different types of particle collisions, but is ultimately dominated by turbulence. Depending on how well the particles are confined in their magnetic surfaces, two basic families of tokamak operation can be defined: the low-confinement mode (L-mode) and the high-confinement mode (H-mode) families. In the L-mode family, the density and temperature are normally higher at the plasma core and monotonically decrease towards the edge without sharp gradients. Energy, particle and impurity transport are relatively high, and

⁸In magnetic confinement configurations without toroidal symmetry (such as stellarators), confinement along the magnetic field direction is not guaranteed.

heat exhaust across the last closed magnetic surface is continuous and manageable.

The H-mode family of tokamak operation is characterised by the presence of edge **Transport Barriers** (TB), which are regions of steep density and temperature gradient that are associated with reduced turbulent transport across magnetic surfaces. It is believed that the TB is created due to an increased deepness in the radial electric field (E_r) well at the plasma edge formed by a self-reorganisation in the plasma when a threshold on injected external power is crossed [FFH92; Wag07]. The core plasma density and temperature profiles sit on top of the TB (commonly denominated as the ‘pedestal’), reaching higher values with respect to L-mode confinement, as shown schematically in figure 1.2. Energy, particle and impurity confinement is improved by a factor of ~ 2 [Wag07] with respect to L-mode, but the large gradients associated with the TB make the plasma equilibrium prone to MHD instabilities such as **Edge Localised Modes** (ELMs). ELMs are short-lived, periodic, violent bursts of plasma that release a fraction of the confined heat and particles from the plasma locally. Because the fusion power yield scales favourably with plasma pressure, H-mode has become the operational baseline for nearly all tokamaks today and for future reactors like ITER and DEMO. Nevertheless, the periodic confinement degradation and the heat load deposited on the PFC caused by ELMs might significantly shorten the lifetime of reactor-size tokamaks. In addition to this problem, H-mode might confine impurities coming from the wall ‘too well’, which in JET, ITER and future reactors must be made of high-Z metals to avoid Tritium retention inside the walls. Accumulation of high-Z impurities inside the plasma decreases the temperature and can lead to radiative termination of the discharge due to Bremsstrahlung radiation [Püt+13; Las+21].

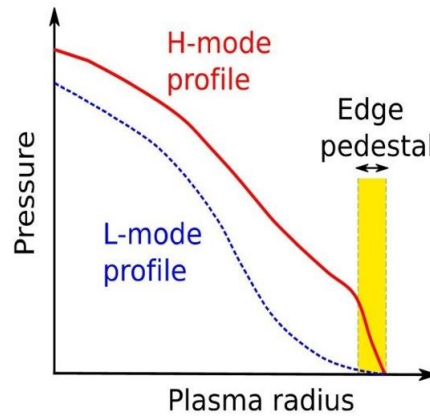


Figure 1.2: Diagram of the radial pressure profiles observed in L-mode and H-mode. Note that $P \sim nT$, where P , n and T are the plasma pressure, density and temperature respectively.

Because of this, an increased effort has been devoted to develop ELM-free operational modes that could be scaled up to power plant scale. Two modes of operation stand out within the L-mode family, the so-called I-mode [Why+10] and negative triangularity [Por+] operation. In I-mode, a TB is formed in the temperature profile but not in the density profile, thus providing continuous transport of particle exhaust and impurities while maintaining high energy confinement and avoiding ELMs. Negative triangularity plasmas do not exhibit a TB, but the energy confinement is improved due to the shape-related partial stabilisation of trapped electron modes, which is the dominant drive for turbulence transport in such plasmas [Mar+09]. Within the H-mode family, ELM control (and avoidance) can be achieved by applying **R**esonant **M**agnetic **P**erturbations (RMPs) from a set of non-axisymmetric external coils [Eva+04]. It is thought that the local destabilisation of MHD modes at the plasma edge together with the stochatisation of the magnetic field lines induced by the RMPs enhance the particle transport, thus avoiding crossing the threshold of ELMs onset [Ora+17]. A good review of the H-mode operational regimes with no ELMs is given in reference [Vie18].

An additional intrinsically ELM-free operational mode exists within the H-mode family: the Quiescent H-mode (QH-mode). Temperature and density TBs are formed during QH-mode operation, but ELMs are avoided by operating on an ‘ELM-stable’ region of the parameter space, accessed in plasmas with low edge collisionality and in the presence of sheared poloidal plasma flows. The precise access conditions to QH-mode are discussed in Chapter 3. Under such conditions, ELMs are replaced by long-wavelength MHD instabilities called Edge Harmonic Oscillations (EHOs) that saturates at the plasma edge and enhances the particle transport across the last closed magnetic surface. While QH-mode has been obtained in some tokamaks today [Bur+01; Sol+10; Sut+04; Oya+06], robust QH-mode operation in present-day machines with metallic walls has not been very successful so far, which is crucial to prepare operations for ITER and DEMO. Therefore, a careful revision of the parameter space of excitation and saturation of EHOs is required. The exploration of such parameter space using numerical modelling and analytical methods is the main focus of this thesis.

1.3 Thesis contribution and outline

The study of QH-mode plasmas and the conditions leading to the excitation and saturation of Edge Harmonic Oscillations is undertaken in this thesis within the frame of the ideal MHD model. Because of this, Chapter 2 is dedicated to the description of the model, the fundamental

equations and their validity to describe the dynamics of fusion plasmas. The mathematical formalism used to describe the magnetic field in toroidal devices is presented along with the straight field line coordinate system, which is used throughout the thesis to perform calculations and analysis. The ideal MHD equilibrium equation and the perturbed MHD momentum equation are the two pillars on which this thesis rests. A description of these equations and methods to solve them analytically and numerically are discussed for different configurations of interest.

In Chapter 3 a detailed review of the physics related to the access of QH-mode and the excitation conditions of EHOs is presented. The linear theory of external modes, proposed as the mechanism for the excitation of EHOs in [ZHS12; ZKV13a], and fully developed in [Bru+18b; Bru+19b] is also introduced. External modes can be excited by the combined effect of large pressure gradient in the pedestal region and low magnetic field line bending stabilisation. The latter effect occurs due to an increased drive on the edge bootstrap current, which can potentially make the edge magnetic shear⁹ weak over an extended region of the plasma. The parameter space with respect to these two effects is calculated using the linear theory, reproducing the results of previous analytical and numerical work [ZKV13a; Bru+18b]. The nonlinear saturation of external modes is associated to the observed EHOs. Therefore, an example on the calculation of nonlinearly saturated external modes in DEMO is presented. Due to the complexity of the problem, such a calculation is performed numerically with the aid of a suit of MHD equilibrium and stability codes, which are presented in appendix A. Since EHOs are saturated instabilities that perturb the plasma boundary, free boundary simulations were needed to recover the measured edge corrugations. An integrated tool composed of different MHD codes was developed during the thesis in order to calculate the necessary vacuum field to produce the desired free boundary QH-mode equilibrium. This work was part of a EUROfusion work package to assess the effect of EHOs on fast particle transport in DEMO. The full report is given in reference [BSG20]. Finally, in this chapter we present a comparison of the saturated states calculated numerically in JET-like plasmas using two different nonlinear approaches, provided by the VMEC [HW83] and JOREK [Hoe+21] codes. The work was done during this thesis in collaboration with R. Ramasamy and M. Hoelzl, from the Max Plank Institute for Plasma Physics. The obtained results led to the publication: *Modeling of saturated external MHD instabilities in tokamaks: A comparison of 3D free boundary equilibria*

⁹The magnetic shear is proportional to the gradient of the ‘safety factor’, which is defined as the inverse magnetic field line pitch angle. A detailed description is given in Chapter 2.

and nonlinear stability calculations by R. Ramasamy, G. Bustos-Ramirez, et. al. in *Physics of Plasmas* [Ram+22]. The author's contributions to this paper included the calculation of the VMEC 2D and 3D equilibria, help in the related VMEC numerical diagnostics, help on the design of the input parameters of the JOEREK simulations, and help on the interpretation and comparison of the JOEREK results with VMEC.

Chapter 4 further explores the parameter space for the excitation of external modes, considering that the magnetic shear does not completely vanish at the plasma edge. To include such effects in the linear theory of external modes, new stability equations that include higher order corrections on the field line bending stabilisation contribution were derived. While such equations are applied to the case of external modes, they are general and can be used also for internal modes by applying the appropriate boundary conditions. A generalisation of the equations including plasma resistivity effects is given by J. P. Graves et. al. in reference [GCW22]. The equations were solved numerically for simplified profiles that qualitatively reproduce the key aspects observed during QH-mode operation, which led to the calculation of the parameter space of external modes with respect to edge magnetic shear. A comparison of the obtained linear results with well established MHD codes is also presented in this chapter. Finally, the modification of the parameter space due to the presence of a plasma separatrix (defined in Chapter 2) is explored, and numerical and analytical solutions are presented. The findings in this chapter were published in *Edge harmonic oscillations in plasmas with a separatrix and the effect of edge magnetic shear* by G. Bustos-Ramirez, J. P. Graves and D. Brunetti in the *Plasma Physics and Controlled Fusion Journal* [BGB21].

In Chapter 5 we present an analytical linear model to describe the saturated states of external modes in the presence of 3D vacuum magnetic perturbations. The model is applied first to the case of saturated external kink modes (defined in Chapter 2). It is found that such magnetic perturbations can induce saturated external kink modes in stable regions of the parameter space. The saturated states obtained analytically are compared with the ones obtained numerically using the fully nonlinear VMEC free boundary equilibrium code. To make a proper comparison between the two approaches, the geometry of the 3D vacuum perturbations in VMEC is fully characterised. It is found that saturated states in VMEC agree well with the analytical model for cases where the external kink mode is stable in the absence of the externally applied 3D perturbations. Next, the analytical model was applied to saturated external modes and was again compared to the saturated states obtained numerically with

the VMEC code. In this case the agreement is limited due to the approximations taken in the derivation of the analytical model, but induced saturated external modes were found in both approaches for cases where the external mode is stable in the absence of the magnetic perturbations. Finally, the amplification of the parameter space for the saturation of external modes in the presence of 3D vacuum magnetic perturbations is explored. The results presented in this chapter are under preparation for publication in the Plasma Physics and Controlled Fusion journal: ‘*The effects of non-axisymmetric magnetic perturbations on non-resonant external modes*’, by G. Bustos-Ramirez, J. P. Graves and D. Brunetti.

A final contribution of this thesis is the development of the VENUS-MHDpy code, presented in appendix C. VENUS-MHDpy is suite of Python modules designed to discretise and solve general eigenvalue problems in toroidal geometry, and is based on a previous Fortran version written by S. Lanthaler [Lan20]. The code uses a mixed discretisation scheme, with Fourier discretisation in the toroidal and poloidal directions, and finite element discretisation with arbitrary order B-spline elements in the radial direction. For the Python code to be efficient, a novel numerical approach was designed to take advantage of vector operations. Several MHD linear stability models were implemented and benchmarked against the KINX linear stability code [Deg+97]. One of these models considers the inclusion of strong plasma flows in the MHD equilibrium equations, which are calculated using the upgraded flow version of the VMEC code [Coo+14]. Up to now, the models cannot handle vacuum boundary conditions. The code is currently being upgraded to handle such conditions in order to asses the stability of external modes in the presence of strong toroidal flows.

Finally, Chapter 6 offers some general conclusions of the thesis and provides an outlook for future work.

2 The ideal MHD model

The goal of this chapter is to introduce the ideal **M**agneto**H**ydro**D**ynamics (MHD) model along with the analytical and numerical tools that will be used throughout the rest of the thesis. This is done first by providing a description of the ideal MHD equations and their region of validity, particularly concerning their use on describing fusion plasmas. Later, the representation of the magnetic field in generalised flux coordinates is discussed in detail, as well as the quantities describing the magnetic field that are used in analytical and numerical calculations throughout the thesis. Next, the concept of MHD equilibria in tokamaks is presented, which is used in the calculation of 2D and 3D saturated plasma states in Chapters 3, 4 and 5. Unstable 2D equilibria might evolve into 3D saturated states, so the concept of linear MHD stability along with the mathematical formalism leading to the perturbed MHD equations is also introduced in this chapter. Finally, the relation between linear MHD unstable plasmas and nonlinear 3D saturated states is addressed.

2.1 Description and validity of the ideal MHD model

The trajectories of the plasma particles in phase space can be described by the distribution function of each of the particle species. The dynamics of the distribution function depends on the interaction between the particles and electromagnetic fields (through Maxwell's equations) and between the particles themselves (through particle collision operators). The electric and magnetic fields change according to the particle dynamics, and need to be calculated self-consistently along with the evolution of the distribution function. While this procedure

The ideal MHD model

should in principle provide an accurate description of the plasma dynamics, it is extremely complicated to perform. Because of this, several simplifications exist whose purpose is to resolve only a fraction of the physics, one of them being the ideal MHD model.

Ideal MHD aims to describe low-frequency, long-wavelength phenomena in a plasma, which is itself modelled as a single superconducting fluid. Such phenomena includes the equilibrium states of multidimensional configurations found in fusion plasmas, as well as some of the most important instabilities observed experimentally. The MHD regime of interest is characterised by the macroscopic motion of the plasma, which occurs over the time the thermal ions move across the whole plasma volume: $\tau_{MHD} = a/V_{Ti}$ (where a is the characteristic plasma length and $V_{Ti} = \sqrt{2T_i/m_i}$ is the ion thermal velocity, with T_i and m_i the ion temperature and mass respectively). In fusion relevant scenarios this corresponds to a few microseconds.

Several approximations are made in the ideal MHD model to target the length and time scales of interest. The first one neglects the displacement current in Ampere's law ($\partial \mathbf{E}/\partial t \sim 0$), which implies that the phase velocity of the electromagnetic waves and the thermal velocity of the particles are non-relativistic (i.e. $\omega/k, V_{Ti}, V_{Te} \ll c$). The second one neglects the net charge density ($\rho = \epsilon_0 \nabla \cdot \mathbf{E} \sim 0$) and electron inertia ($m_e \rightarrow 0$), implying that the electrons move on a time scale much faster than the MHD time ($\tau_{pe} \ll \tau_{MHD}$) to cancel any charge imbalance that appears as a result of a macroscopic charge separation. This leads to *global* quasi-neutrality ($n_e = n_i = n$, where n_e, n_i are the electron and ion number density respectively). As a result, ideal MHD describes phenomena on a length scale much larger than the Debye length ($\lambda_D \ll a$, where $\lambda_D = V_{Te}/\omega_{pe}$) and that occurs with a frequency much smaller than the electron plasma frequency ($\omega_{MHD} \ll \omega_{pe}$, where $\omega_{pe} = \tau_{pe}^{-1} = \sqrt{ne^2/m_e\epsilon_0}$, with e the electron charge). These initial assumptions are well satisfied for most processes in fusion plasmas, and allow to introduce the following fluid quantities:

$$\begin{aligned}
 \rho &= m_i n \\
 \mathbf{u} &= \mathbf{v}_i \\
 \mathbf{J} &= en(\mathbf{v}_i - \mathbf{v}_e) \\
 P &= P_i + P_e = 2nT \\
 T &= (T_i + T_e)/2,
 \end{aligned} \tag{2.1}$$

2.1 Description and validity of the ideal MHD model

where ρ is the mass density, \mathbf{u} is the fluid bulk velocity, \mathbf{v}_i and \mathbf{v}_e are the ion and electron velocities, \mathbf{J} is the current density, P the total plasma pressure and T the total plasma temperature. The ideal MHD model relates these quantities through the following equations [GP04; Fre14]:

$$\frac{\partial \rho}{\partial t} + \nabla \cdot (\rho \mathbf{u}) = 0, \quad (2.2)$$

$$\rho \frac{d\mathbf{u}}{dt} - \mathbf{J} \times \mathbf{B} + \nabla P = 0, \quad (2.3)$$

$$\frac{d}{dt} \left(\frac{P}{\rho \Gamma} \right) = 0, \quad (2.4)$$

$$\mathbf{E} + \mathbf{u} \times \mathbf{B} = 0, \quad (2.5)$$

$$\nabla \times \mathbf{E} + \frac{\partial \mathbf{B}}{\partial t} = 0, \quad (2.6)$$

$$\nabla \times \mathbf{B} - \mu_0 \mathbf{J} = 0, \quad (2.7)$$

$$\nabla \cdot \mathbf{B} = 0, \quad (2.8)$$

where $\frac{d}{dt} \equiv \frac{\partial}{\partial t} + \mathbf{u} \cdot \nabla$ is the convective derivative, \mathbf{B} and \mathbf{E} are the magnetic and electric fields respectively and Γ is the ratio of specific heats.

Important to the derivation of the momentum equation (2.3) is the assumption that the plasma is collision-dominated, meaning that the particle collision time ($\sim \tau_{ii}$) is much smaller than the characteristic MHD time. Then, the particle distribution function can be considered as Maxwellian and the pressure isotropic. Moreover, the adiabatic equation of state (2.4), which provides closure to the system of equations, requires the energy equalisation time ($\tau_{eq} \sim (m_i/m_e)^{1/2} \tau_{ii}$) being much smaller than MHD time so that $T_e \sim T_i \sim T$. Unfortunately, plasmas of interest for fusion are nearly collisionless and therefore neither of these conditions are satisfied. Nevertheless, near marginal stability and for many MHD instabilities the plasma motion is incompressible and the dynamics parallel to the magnetic field becomes unimportant. On the other hand, the dynamics perpendicular to the magnetic field can be considered "pseudo-collisional" because particles are confined in the vicinity of the field lines while executing their gyromotion orbit motion. Under this condition, equations 2.3 and 2.4 provide an accurate description of phenomena in fusion plasmas in the perpendicular direction to the magnetic field, which is enough to describe long time-scale MHD equilibrium

conditions and some of the most important plasma instabilities near marginal stability. It is worth pointing out that instabilities that are significantly modified by plasma compression or pressure anisotropy are also frequent in fusion experiments, and the physics needed to describe these phenomena needs an accurate model of the parallel dynamics. Such dynamics is more accurately modelled by kinetic theory, which is beyond the scope of this thesis.

The rest of the ideal MHD equations are the conservation of mass (equation 2.2), ideal Ohm's law (equation 2.5) and the pre-Maxwellian electrodynamics laws (equations 2.6-2.8). These equations are well satisfied for fusion plasmas, but leave out the effect of magnetic diffusion. This is important for closed field lines ($\mathbf{B} \cdot \nabla \sim 0$) where resistivity is of the same order as the other terms in the equations, so that in practice magnetic islands are allowed develop through tearing and reconnection. Plasma resistivity (η) can be introduced into the equations via Ohm's law by substituting the right-hand-side of equation 2.5 with $\eta \mathbf{J}$, giving rise to the *resistive* MHD model. Nevertheless, time scales for resistive instabilities are much longer than the characteristic MHD times, so it has little effect on ideal MHD times.

In summary, ideal MHD can accurately model slow ($\tau_{pe} \ll \tau_{MHD}$), macroscopic ($\lambda_D \ll a$) highly collisional ($(m_i/m_e)^{1/2} \tau_{ii} \ll \tau_{MHD}$) ideal ($\eta \sim 0$) plasma phenomena. For collisionless plasmas, ideal MHD still provides a good description of equilibrium and stability perpendicular to the magnetic field and long time-scale non-linear behaviour.

2.2 Flux coordinate systems and representation of the magnetic field

The most efficient way to confine a plasma is if it lies on closed magnetic surfaces. This minimises the losses due to parallel particle and energy transport. Topologically speaking, a torus allows the existence of closed magnetic surfaces because it can be fully covered by a non-vanishing vector field. To represent the magnetic field in a torus it is useful to introduce the concepts of stream functions and flux functions. A *stream function* is defined as a scalar field $f(\mathbf{r})$ such that $\mathbf{B} \cdot \nabla f(\mathbf{r}) = 0$. If the stream function is constant not only along the field line but also defines closed magnetic surfaces, then it is known as a *flux function*. The name of the later derives from the fact that the magnetic flux in both poloidal and toroidal directions define nested toroidal magnetic surfaces. The magnetic field in a torus can be written in Clebsch form [Dha+91]

$$\mathbf{B} = \nabla s \times \nabla G, \quad (2.9)$$

where s and G are stream functions and equation 2.8 is automatically satisfied. ∇s is chosen to be perpendicular to the magnetic surfaces and ∇G lies on magnetic surfaces but is perpendicular to the magnetic field (see figure 2.1a). Note that any function that depends solely on the variable ' s ' is automatically a flux function, while in general stream functions can have the form of $f(s)g(G)$. It is very convenient to define the coordinate system (s, θ, ϕ) which follows the alignment of field lines. Here, s is any function that labels flux surfaces (for example the poloidal or toroidal magnetic flux), θ is a measure of the poloidal angle and ϕ is the geometrical toroidal angle. The most general form to write the stream function G in this set of coordinates is [Dha+91]:

$$G = a(s)\theta + b(s)\phi + \tilde{\lambda}(s, \theta, \phi), \quad (2.10)$$

where $\tilde{\lambda}(s, \theta, \phi)$ is periodic in both angles. It follows that the contravariant components of the magnetic field are $B^\theta = \mathbf{B} \cdot \nabla \theta = (a + \partial_\theta \tilde{\lambda}) / \sqrt{g}$ and $B^\phi = \mathbf{B} \cdot \nabla \phi = (b + \partial_\phi \tilde{\lambda}) / \sqrt{g}$, where \sqrt{g} is the Jacobian of the coordinate system. The functions $a(s)$ and $b(s)$ are obtained by calculating the magnetic flux passing through the toroidal and poloidal surfaces in the torus. To start the calculation, consider the integral

$$\int dV \mathbf{B} \cdot \nabla \phi = \int dV \nabla(\phi \mathbf{B}) = \int \phi \mathbf{B} \cdot d\mathbf{S}$$

where dV is the differential volume integral and the first equality follows from equation 2.8. Considering the flux passing through an open torus cut at a poloidal plane in the angle $\phi = 2\pi$, then its possible to write $d\mathbf{S} = \hat{\mathbf{n}} dS_{surf} + d\mathbf{S}_p(\phi = 0) + d\mathbf{S}_p(\phi = 2\pi)$. Since $\mathbf{B} \perp \hat{\mathbf{n}}$ by definition and ϕ is evaluated at 0 and 2π , the integral reduces to

$$\int dV \mathbf{B} \cdot \nabla \phi = 2\pi \int_{S_p} \mathbf{B} \cdot d\mathbf{S}_p = 2\pi \Psi_t(s), \quad (2.11)$$

where the toroidal flux $\Psi_t(s)$ is a flux function that only depends on the coordinate 's'. Using similar arguments, the poloidal flux $\Psi_p(s)$ is calculated as

$$\int dV \mathbf{B} \cdot \nabla \theta = 2\pi \int_{S_t} \mathbf{B} \cdot d\mathbf{S}_t = 2\pi \Psi_p(s). \quad (2.12)$$

where dS_t is the differential element of a toroidal cut of the torus. Taking the derivative of equations 2.11 and 2.12 with respect to 's' and substituting the contravariant components of the magnetic field give

$$\begin{aligned} \frac{d\Psi_t}{ds} &= \frac{1}{2\pi} \frac{d}{ds} \int \frac{dV}{\sqrt{g}} (a + \partial_\theta \tilde{\lambda}) = \frac{1}{2\pi} \int_0^{2\pi} \int_0^{2\pi} d\theta d\phi (a + \partial_\theta \tilde{\lambda}) = 2\pi a(s) \\ \frac{d\Psi_p}{ds} &= -\frac{1}{2\pi} \frac{d}{ds} \int \frac{dV}{\sqrt{g}} (b + \partial_\phi \tilde{\lambda}) = -\frac{1}{2\pi} \int_0^{2\pi} \int_0^{2\pi} d\theta d\phi (b + \partial_\phi \tilde{\lambda}) = -2\pi b(s), \end{aligned} \quad (2.13)$$

where we have used $\nabla s \times \nabla \theta \cdot \nabla \phi = 1/\sqrt{g}$ and the fact that $\tilde{\lambda}$ is periodic so that $\int_0^{2\pi} \int_0^{2\pi} \partial_i \tilde{\lambda} d\theta d\phi = 0$. The magnetic field can therefore be written as

$$\mathbf{B} = \psi'_t [1 + \partial_\theta \lambda] \nabla s \times \nabla \theta - \psi'_p [1 - q(s) \partial_\phi \lambda] \nabla s \times \nabla \phi, \quad (2.14)$$

where $\Psi_t = 2\pi \psi_t$, $\Psi_p = 2\pi \psi_p$ and $f' \rightarrow df/ds$. Note the normalisation of the function $\lambda = \tilde{\lambda}/\psi'_t$. The representation of the magnetic field given in equation 2.14 will be used later in the thesis as it is adapted in the VMEC code [HW83]. The toroidal winding number $q(s) = \psi'_t/\psi'_p$ (also known as the 'safety factor') has been substituted in equation 2.14. It represents the average change in the toroidal angle with respect to the poloidal angle when moving along the field line. It can also be interpreted as the number of times a magnetic field line performs a toroidal

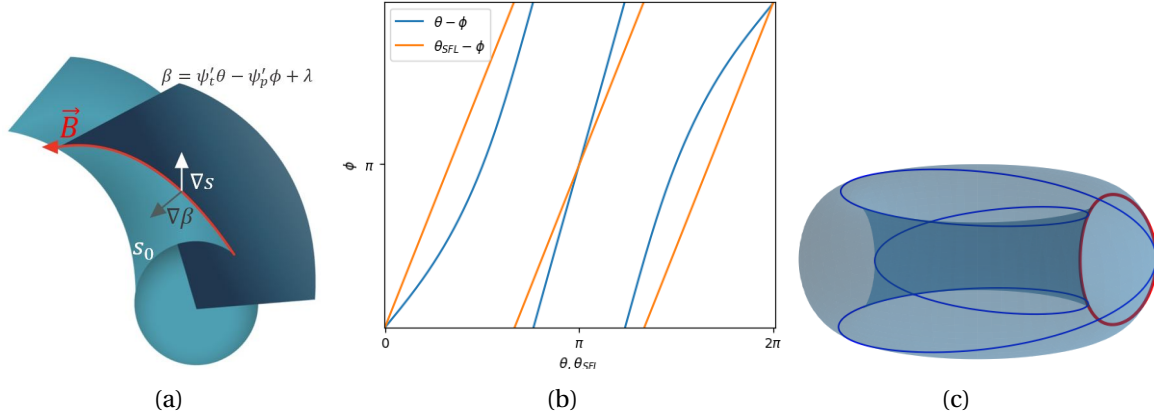


Figure 2.1: Representation of the magnetic field and magnetic field lines. (a) Surfaces defined by Clebsch stream functions, (b) magnetic field lines in the $\theta - \phi$ plane (also in SFL coordinates) and (c) 3D representation of the field lines. Note that in figure (b) the field line gives 3 turns in the toroidal direction for one poloidal turn, which can be seen in figure (c) by the 3 intersections in the poloidal cut. Therefore, the safety factor of this particular magnetic surface is $q(s_0) = 3$.

loop for each poloidal loop. A simple calculation of the *local* winding number can be directly obtained from the equation of the magnetic field lines $\mathbf{B} \times d\mathbf{r} = 0$, where $d\mathbf{r}$ is the differential line element parallel to the field. The 's' component of the equation can be arranged to give

$$q_{loc}(s, \theta, \phi) = \frac{d\phi}{d\theta} = \frac{\mathbf{B} \cdot \nabla \phi}{\mathbf{B} \cdot \nabla \theta} = q(s) \frac{1 + \partial_\theta \lambda}{1 - q(s) \partial_\phi \lambda}. \quad (2.15)$$

Under the change of variables $\theta_{SFL} = \theta + \lambda$ the expression above reduces to

$$q(s) = \frac{1}{2\pi} \int_0^{2\pi} q_{loc}(s, \theta_{SFL}, \phi) d\theta_{SFL} = \frac{\mathbf{B} \cdot \nabla \phi}{\mathbf{B} \cdot \nabla \theta_{SFL}}. \quad (2.16)$$

In the set of coordinates (s, θ_{SFL}, ϕ) it is easy to see from equation 2.15 that $\phi = q(s)\theta_{SFL} + \theta_0$, meaning that the magnetic field lines are straight lines in the $\phi - \theta_{SFL}$ plane with a pitch angle equal to $q(s)$ (see figure 2.1b). The set of coordinates (s, θ_{SFL}, ϕ) is therefore known as **Straight Field Line (SFL)** coordinate system. Note that the VMEC code does not in general use SFL coordinates. The magnetic field is written in the more conventional Clebsch form

$$\mathbf{B} = \nabla \psi_P(s) \times \nabla (q(s)\theta_{SFL} - \phi). \quad (2.17)$$

This reflects an important property of the magnetic field in a torus: field lines lie on surfaces defined by the stream functions $\psi_P(s)$ and $q(s)\theta_{SFL} - \phi$. When taking a constant $s = s_0$, the function $\psi_P(s_0)$ defines a toroidal magnetic surface. Therefore, hereon the $\nabla \psi_P \propto \nabla s$ direction is referred to as the ‘radial direction’. On the other hand $q(s)\theta_{SFL} - \phi$ defines a surface that revolves helically around the torus. The intersection, given by $q(s_0)\theta_{SFL} - \phi$, defines the magnetic field lines that lie on surface s_0 (see figure 2.1a).

A final remark is that the flux coordinate representation of the magnetic field is particularly useful for closed flux surfaces, but not so much for open surfaces. In magnetic confinement fusion devices one normally can have 2 configurations: limited and diverted. In the limited one, the flux surfaces are closed from the core to the edge, where the last flux surface is intercepted by a piece of material called a limiter that separates the plasma from the vacuum chamber. In diverted configurations, the magnetic surfaces are closed from the core to almost the edge, and they are separated from the vacuum by an open flux surface called the separatrix. The magnetic field lines of the separatrix cross at one or more locations forming x-points, then continue their trajectory towards a specific part of the machine called divertor, which has been engineered to stand high heat flux. A property of diverted configurations is that the poloidal magnetic field vanishes at the x-points, in which case field align coordinates are singular (note that $q \rightarrow \infty$), and pose a problem for numerical computations. Normally, codes that are able to calculate MHD equilibrium with separatrix use approximations to represent the singularity or switch to a coordinate system that is not singular at the x-points, like Cartesian coordinates.

2.3 MHD equilibria in toroidal devices

Macroscopic equilibria in plasmas is described by equations 2.2-2.8 with $\frac{\partial}{\partial t} \rightarrow 0$. In particular, the equilibrium momentum equation reads

$$\rho(\mathbf{u} \cdot \nabla)\mathbf{u} - \mathbf{J} \times \mathbf{B} + \nabla P = 0, \quad (2.18)$$

which describes how the magnetic force $\left(\frac{1}{\mu_0}(\nabla \times \mathbf{B}) \times \mathbf{B}\right)$ balances the fluid forces $(\rho(\mathbf{u} \cdot \nabla)\mathbf{u} + \nabla P)$. The order of the pressure gradient relative to the magnetic force is

$$\frac{\nabla p}{\mathbf{J} \times \mathbf{B}} \sim \frac{2\mu_0 P}{B^2} \equiv \beta, \quad (2.19)$$

where the plasma parameter β has been defined as the ratio between the fluid pressure over the magnetic pressure. It can be interpreted as the ‘amount’ of magnetic field needed to confine a certain plasma pressure in equilibrium. Since the pressure is monotonically related to fusion power, and increased magnetic field strength normally scales up the cost of the fusion reactor, ideally it is aimed for β to be as large as possible. In reality, MHD instabilities set an upper limit to the attainable value of β , which is of a few percent depending on the type of magnetic configuration.

The order of the inertia term with respect to the pressure gradient is

$$\frac{\rho(\mathbf{u} \cdot \nabla)\mathbf{u}}{\nabla p} \sim \frac{\Omega^2 R^2}{2T/m_i} \equiv M_i^2, \quad (2.20)$$

where Ω is the plasma rotation frequency and M_i is the ion Mach number, defined as the ratio between the plasma flow velocity ($\sim \Omega R$) over the ion thermal velocity V_{Ti} . The equilibrium equations can be solved in the rotating frame of reference taking into account the force exerted on the plasma due to the non-inertial reference frame. As it turns out, in most fusion experiments without external momentum input, the plasma flow is strongly subsonic ($M_i^2 \ll 1$). This means that for those experiments inertial forces are negligible compared to the pressure gradient force. Then, the momentum equation is reduced to

$$\mathbf{J} \times \mathbf{B} = \nabla P. \quad (2.21)$$

Equation 2.21 is known as the *static* ideal MHD equilibrium equation. An important property of MHD equilibria can be immediately derived from the projection of equation 2.21 on \mathbf{B} and \mathbf{J}

to give

$$\begin{aligned}\mathbf{B} \cdot \nabla P &= 0 \\ \mathbf{J} \cdot \nabla P &= 0.\end{aligned}\tag{2.22}$$

In equilibrium, the magnetic and current density fields lie on nested surfaces of constant pressure. It is pointed out here that it is common in experiments to have $M_i \sim 1$, for instance when external momentum is added to the plasma by neutral beam injection in spherical tokamaks¹. Moreover, certain instabilities are particularly sensitive to the plasma rotation even when $M_i \ll 1$ [Bru+14a; GHH00; WCG09], in which case equation 2.22 is not valid and the pressure does not longer define magnetic surfaces (see appendix B.1 for details). Such cases are not considered in the scope of this thesis.

2.3.1 The Grad-Shafranov equation with toroidal rotation

A great simplification in the analysis of plasma equilibria is to consider axisymmetry, meaning that the physical quantities are independent from the variable representing a symmetry axis, in this case, the toroidal angle: $\partial/\partial\phi \rightarrow 0$. It follows naturally to define a coordinate system where one basis vector points in the direction of the symmetry (\hat{e}_ϕ), while the other two basis vectors lie on the poloidal plane. This is the case for the set of coordinates defined in section § 2.2. Another common choice of coordinates is the cylindrical set (R, Z, ϕ) , where ϕ moves in clockwise direction to preserve a right-hand system. The magnetic field in equation 2.14 can be simplified by using the property of the coordinate basis $\hat{e}_\phi = R^2 \nabla \phi = \sqrt{g} \nabla s \times \nabla \theta$ to write

$$\mathbf{B} = \psi'_p \nabla \phi \times \nabla s + F \nabla \phi,\tag{2.23}$$

where $F = B_\phi = \psi'_t [1 + \partial_\theta \lambda] \frac{R^2}{\sqrt{g}}$. Taking now the toroidal contravariant component of the momentum equation

¹Currently there are no fusion reactors designed for putting energy on the electrical grid that use neutral beam injection, which is the main heating scheme introducing angular plasma momentum.

$$\begin{aligned}
 \rho \nabla \phi \cdot (\mathbf{u} \cdot \nabla) \mathbf{u} &= \mathbf{B} \cdot (\nabla \phi \times \mathbf{J}) - \nabla P \cdot \nabla \phi \\
 -\rho R \Omega^2 \nabla R \cdot \nabla \phi &= \frac{1}{\mu_0 R^2} B^i (\partial_\phi B_i - \partial_i B_\phi) \\
 0 &= -\frac{\mathbf{B} \cdot \nabla F}{\mu_0 R^2},
 \end{aligned} \tag{2.24}$$

where it has been assumed that the plasma velocity only flows in the toroidal direction, so $(\mathbf{u} \cdot \nabla) \mathbf{u} = -\frac{1}{2} \Omega^2(s) \nabla R^2$, with Ω the toroidal frequency rotation (see appendix B.1). Since in axisymmetry any stream function is a flux function ($(\mathbf{B} \cdot \nabla) f = B^\theta \partial_\theta f + B^\phi \partial_\phi f = B^\theta \partial_\theta f = 0$), equation 2.24 shows that $F = F(s)$ is a flux function. An immediate consequence is that the radial contravariant component of the current density is zero

$$J^s = \mathbf{J} \cdot \nabla s = \frac{1}{\mu_0} (\partial_\theta B_\phi - \partial_\phi B_\theta) = 0, \tag{2.25}$$

where the first term vanishes because $B_\phi = F(s)$ and the second due to axisymmetry. This means that the current density still flows along well defined magnetic flux surfaces even in plasmas with equilibrium toroidal flow.

Equilibrium perpendicular to the flux surfaces is given by the *Grad-Shafranov* equation [GR58; Sha58]. It is derived by simply projecting equation 2.18 on the radial covariant vector \hat{e}_s

$$\begin{aligned}
 -p U \hat{e}_s \cdot \nabla R^2 &= \hat{e}_s \cdot (\mathbf{J} \times \mathbf{B}) - \hat{e}_s \cdot \nabla P \\
 -p U \partial_s R^2 &= \hat{e}_s \cdot [\mathbf{J} \times (\nabla \phi \times \nabla \psi_p + F \nabla \phi)] - \partial_s P \\
 -p U \partial_s R^2 &= \hat{e}_s \cdot [-\nabla \psi_p J^\phi + F \mathbf{J} \times \nabla \phi] - [\hat{P}' + \hat{P}(R^2 - R_0^2) \partial_s U + \hat{P} U \partial_s R^2] e^{U(R^2 - R_0^2)} \\
 \psi_p' J^\phi &= -\frac{F F'}{\mu_0 R^2} - [\hat{P}' + \hat{P}(R^2 - R_0^2) U'] e^{U(R^2 - R_0^2)},
 \end{aligned} \tag{2.26}$$

where the pressure has been substituted using equation B.5. The calculation of J^ϕ in general coordinates follows from Ampere's law (2.7)

$$\begin{aligned}
\mu_0 J^\phi &= (\nabla \times \mathbf{B})^\phi = [\nabla \times (\nabla \phi \times \nabla \psi_p + F \nabla \phi)] \cdot \nabla \phi \\
&= [\nabla \phi (\nabla \cdot \nabla \psi_p) + (\nabla \psi_p \cdot \nabla) \nabla \phi - (\nabla \phi \cdot \nabla) \nabla \psi_p] \cdot \nabla \phi \\
&= \frac{1}{R^2} \nabla \cdot \nabla \psi_p + \nabla \psi_p \cdot \nabla \left(\frac{1}{R^2} \right) \\
&= \nabla \cdot \left(\frac{\nabla \psi_p}{R^2} \right).
\end{aligned} \tag{2.27}$$

Defining the operator $\Delta^* \psi_p \equiv R^2 \nabla \cdot \left(\frac{\nabla \psi_p}{R^2} \right)$ and setting the coordinate $s = \psi_p$ gives the classical form of the Grad-Shafranov equation with toroidal flow [MP80]

$$\Delta^* \psi_p = -F \frac{dF}{d\psi_p} - \mu_0 R^2 \left[\frac{d\hat{P}}{d\psi_p} + \hat{P}(R^2 - R_0^2) \frac{dU}{d\psi_p} \right] e^{UR^2}. \tag{2.28}$$

Equation 2.28 is an elliptical second order non-linear differential equation for ψ_p . The solution requires the free functions $p(s)$, $F(s)$ and $U(s)$ (or equivalent functions) to be provided externally along appropriate boundary conditions, which are normally extracted from experimental data or physical intuition. Particularly, one can show that the functions $F(s)$ and $q(s)$ are related using equation 2.15:

$$q(s) = \frac{1}{2\pi} \int_0^{2\pi} \frac{\mathbf{B} \cdot \nabla \phi}{\mathbf{B} \cdot \nabla \theta} d\theta = \frac{F(s)}{2\pi \psi_p'} \int_0^{2\pi} \frac{\mathcal{J}(s, \theta)}{R^2} d\theta, \tag{2.29}$$

where \mathcal{J} is the Jacobian and the prime again denotes derivative with respect to 's'. Note that comparing the equation above with equation 2.16, it follows that the magnetic field will trace straight field lines in the $\phi - \theta$ plane if the Jacobian is proportional to R^2 , in which case

$$q(s) = \frac{F \mathcal{J}(s, \theta_{SFL})}{R^2 \psi_p'}. \tag{2.30}$$

Due to its nonlinear nature, equation 2.28 is normally solved numerically (see for example the CHEASE code [LBS96] or FreeGS code [Dud]). Analytical solutions exist for particular functions of $P(\psi_p)$ and $F(\psi_p)$ whose dependency on ψ_p is simple enough. Most notable, Solov'ev proposed a set of linear profiles for the pressure and current density with zero rotation, for which an exact analytical solution is found [Sol68]. While the solution gives incredibly useful physical insight and is used routinely for code benchmark, it is not realistic for certain magnetic configurations. Generalisations to include rotation [MP80] or other high- β configurations in the presence of a separatrix [CF10] have been also obtained throughout the years.

2.3.2 The tokamak ordering

Solving equation 2.28 analytically in toroidal geometry is not a trivial task, but it can be simplified considering different limits. A particularly useful one is the *tokamak ordering* [WH66; GJW71], where the plasma is treated as a large aspect ratio torus: $\epsilon \equiv a/R_0 \ll 1$, where ϵ^{-1} is the tokamak aspect ratio and a and R_0 are the minor and major radius respectively. Other quantities describing the equilibrium are ordered with respect to ϵ as

$$\beta \sim \frac{2\mu_0 P}{B_0^2} \sim \epsilon^2, \quad \frac{B_p}{B_t} = \frac{\psi'_p |\nabla \phi \times \nabla s|}{|F \nabla \phi|} \sim \epsilon, \quad q(s) \sim 1. \quad (2.31)$$

These conditions describe (at least qualitatively) the physical phenomena required for MHD equilibrium and stability in most experimental scenarios and have been used extensively (the present thesis included) to gain physical insight on MHD phenomena. The equilibrium solution is normally found by expanding the cylindrical map on flux coordinates as [GJW71]

$$\begin{aligned} R(r, \theta) &= R_0 \left(1 + \epsilon \frac{r}{R_0} \cos \theta - \frac{\epsilon^2}{R_0} \left[\Delta(r) + \sum_{m=2}^{\infty} S_m(r) \cos(m-1)\theta \right] + \mathcal{O}(\epsilon^3) \right) \\ Z(r, \theta) &= R_0 \left(\epsilon \frac{r}{R_0} - \frac{\epsilon^2}{R_0} \sum_{m=2}^{\infty} S_m(r) \sin(m-1)\theta + \mathcal{O}(\epsilon^3) \right), \end{aligned} \quad (2.32)$$

where the coefficients $S_m(r)$ describe the plasma shape, $\Delta(s)$ is the Shafranov Shift² and the

²The inner magnetic surfaces are shifted along the \hat{e}_R axis due to a combination of the hoop force and tyre tube

The ideal MHD model

artificial tag ϵ labels the ordering of the terms. In this mapping, r has been chosen as the radial coordinate with units of length, where the transformation is given by

$$r^2 = 2R_0 \int_0^s \frac{\psi'_p q}{F} ds. \quad (2.33)$$

Substituting the mapping in the Grad-Shafranov equation (2.28) in the flux coordinate system (r, θ, ϕ) gives to leading order

$$\frac{1}{2r^2} (r^2 \psi_p^2)' + R_0^2 \mu_0 \hat{P}' + FF' = 0, \quad (2.34)$$

which describes the force balance between the plasma pressure gradient $\sim P'$ and the toroidal ($\sim FF'$) and poloidal ($\sim \psi_p$) magnetic pressures in the \hat{e}_r direction. At the next order the following independent equations are found for each harmonic

$$\begin{aligned} \Delta'' + \left(2 \frac{\psi_p''}{\psi_p'} + \frac{1}{r} \right) \Delta' - \frac{1}{R_0} + 2 \frac{r R_0}{(\psi_p')^2} [\hat{P}(1 + R_0^2 U)]' &= 0, \\ S_m'' + \left(2 \frac{\psi_p''}{\psi_p'} + \frac{1}{r} \right) S_m' + \frac{1 - m^2}{r^2} S_m &= 0, \end{aligned} \quad (2.35)$$

where FF' has been substituted using equation 2.34. The first equation solves for the Shafranov shift, and describes the force balance in the \hat{e}_R direction considering the plasma pressure gradient, poloidal magnetic field and the centrifugal force due to toroidal rotation. The second equation describes the penetration of shaping from the edge to the core. Note that equation 2.35 is homogeneous, while equation 2.34 can be solved in terms of the given functions F , P and U along with appropriate boundary conditions.

force. The hoop force appears as a consequence of the toroidal current, similar to how a loop of wire expands when carrying current. The tyre tube force arises due to the difference in the surface area between the inner and outer parts of the torus on a magnetic surface with constant pressure.

2.4 Linear MHD fluctuations and stability

If an axisymmetric MHD equilibria has been achieved in a plasma, it may not stay in the same state for a long time. In experiments, the axisymmetric equilibrium might be perturbed by external changes on the plasma, such as fuelling, heating, operation errors, etc. Moreover, ideal MHD equilibria only assures that the sum of the slow macroscopic forces acting on the plasma is zero, but fast and microscopic forces which are not present in the fluid description can very well disturb the MHD equilibrium. The stability of the plasma is determined by how the ideal MHD forces evolve in response to a perturbation. If the forces push the plasma towards its initial equilibrium state, then the equilibrium is *stable*. Conversely, if the forces evolve in such a way that the perturbation is amplified, the equilibrium is *unstable*. To elaborate a mathematical formalism for the MHD stability theory, physical quantities describing the plasma are written as

$$f(\mathbf{r}, t) = f_0(\mathbf{r}) + \delta f(\mathbf{r}, t), \quad (2.36)$$

where f_0 is the equilibrium quantity and δf the perturbation. The evolution of the perturbation is described by equations 2.2-2.8, where all quantities are expressed in the same form as equation 2.36. The focus of this section is to study *linear* stability, i.e. study the evolution of a perturbation that is small compared to the equilibrium quantity ($\delta f / f_0 \ll 1$) so that the equations can be linearised. As discussed in section §2.3, it is a good approximation to neglect equilibrium plasma flows if the ion Mach number is small: $M_i^2 \ll 1$, which is the case for many experimental situations of interest. In the analytical work performed on this thesis the equilibrium flow is neglected, and is only considered in the numerical formulation of the MHD problem implemented in the VENUS-MHDpy code. The perturbed quantities are expressed in terms of the Lagrangian³ plasma displacement

$$\partial_t \xi = \delta \mathbf{u}. \quad (2.37)$$

³In a Lagrangian description of fluid dynamics, physical quantities are attributed to a unit of fluid volume, which is followed in time. In contrast, in a Eulerian description physical quantities are described as functions fixed in the coordinate space.

so that the perturbed momentum equation can be written as

$$\rho \partial_t^2 \xi = \delta \mathbf{F}(\xi) \quad (2.38)$$

$$\delta \mathbf{F}(\xi) = -\nabla \delta P + \frac{1}{\mu_0} (\nabla \times \mathbf{B}) \times \delta \mathbf{B} + \frac{1}{\mu_0} (\nabla \times \delta \mathbf{B}) \times \mathbf{B}. \quad (2.39)$$

where the sub index '0' has been removed from equilibrium quantities for convenience and

$$\begin{aligned} \delta P &= -\xi \cdot \nabla P - \Gamma P \nabla \cdot \xi \\ \delta \mathbf{B} &= \nabla \times (\xi \times \mathbf{B}), \end{aligned} \quad (2.40)$$

are obtained after perturbing and integrating in time equations 2.4 and 2.5. Note that the equations are only valid if the perturbation is small, and exact in the limit of infinitesimal perturbations. A generalisation of the stability equation including the effect of equilibrium plasma flows is given by Frieman and Rotenberg [FR60].

2.4.1 Paths into solution

Equation 2.38 can be solved as an initial value problem using the initial conditions $\xi(\mathbf{r}, t=0) = 0$ and $\partial_t \xi(\mathbf{r}, t=0) \ll 1 \neq 0$. Alternatively, assuming that the perturbed quantities have a normal mode time dependency as $\delta f(\mathbf{r}, t) = \hat{\delta} f(\mathbf{r}) e^{\lambda t}$, equation 2.38 takes the form of an eigenvalue problem

$$\lambda^2 \rho \xi = \delta \mathbf{F}(\xi), \quad (2.41)$$

which can be solved with spectral methods for the eigenvalue λ^2 and the eigenvectors $\hat{\xi}$. An important property of the operator $\delta \mathbf{F}$ is self-adjointness⁴ [Fre14; Ber+58], which consequently

⁴An operator \mathbf{F} is self-adjoint if two vector fields $\boldsymbol{\eta}$ and $\boldsymbol{\xi}$ which belong to a particular vector space V with inner product $\langle \cdot, \cdot \rangle$ fulfil $\langle \mathbf{F}\boldsymbol{\eta} | \boldsymbol{\xi} \rangle = \langle \boldsymbol{\eta} | \mathbf{F}\boldsymbol{\xi} \rangle$. In the case of Ideal MHD, the inner product is given by the integral relation $\langle \mathbf{F}\boldsymbol{\eta} | \boldsymbol{\xi} \rangle = \int \mathbf{F}(\boldsymbol{\eta})^* \cdot \boldsymbol{\xi} dV = \int \boldsymbol{\eta}^* \cdot \mathbf{F}(\boldsymbol{\xi}) dV = \langle \boldsymbol{\eta} | \mathbf{F}\boldsymbol{\xi} \rangle$.

means that the eigenvalue λ^2 is purely real. Therefore, if $\lambda^2 < 0$, then $\lambda = \pm i|\lambda|$ and the perturbed quantities have oscillatory solutions. If $\lambda^2 > 0$, then $\lambda = \pm|\lambda|$ and the perturbed solution grows exponentially. If $\lambda^2 = 0$ then the plasma state is located at the stability boundary, and it is said to be *marginally stable*.

The eigenvalue problem can be posed in integral form by taking the inner product $\langle . | . \rangle$ of equation 2.41 with ξ^* and multiplying by a factor of 1/2 [Ber+58]

$$\lambda^2 \frac{1}{2} \int \rho |\xi|^2 dV - \frac{1}{2} \int \xi^* \mathbf{F}(\xi) dV = \lambda^2 K(\xi) + \delta W(\xi) = 0 \quad (2.42)$$

$$\Rightarrow \lambda^2 = - \frac{\delta W(\xi)}{K(\xi)} \quad (2.43)$$

where δW and $\lambda^2 K$ are interpreted as the change in potential and kinetic energy respectively due to the perturbation. It is immediately seen from equation 2.43 that since $K \geq 0$, the plasma will only be stable if $\delta W(\xi) > 0$, giving rise to the *energy principle*, which roughly states [Ber+58]

"A plasma is unstable if, and only if, there exist some displacement ξ which makes the change in potential energy δW negative".

It is possible to show (see for example [Ber+58; Fre14]) that equation 2.42 constitutes a variational principle, and so all allowable functions ξ that produce an extrema in the eigenvalue will correspond to actual solutions of equation 2.41. To find the function ξ that produces an extrema one can formally apply the Euler-Lagrange equations on the variational integral with respect to each of the variables (ξ_1, ξ_2, ξ_3) , giving 3 partial differential equations. Then, the solution can be substituted back into $\delta W(\xi)$ and check if the sign is positive or negative, according to the energy principle. This procedure is equivalent to taking projections of the perturbed momentum equation 2.41 to obtain the differential equations describing (ξ_1, ξ_2, ξ_3) , which is what is done in the analytical work presented in Chapter 4.

Due to the geometry of the system, it is natural to Fourier decompose the perturbed variables along the poloidal and toroidal directions

$$\hat{\delta}f(s, \theta, \phi) = \sum_n \sum_m \hat{\delta}f_{mn}(s) e^{i(m\theta - n\phi)}. \quad (2.44)$$

Note that due to the symmetry in the toroidal direction in axisymmetric devices, linear toroidal modes ‘ n ’ will be decoupled. This can be seen by expressing $\xi \sim \sum_n e^{in\phi}$ and $\xi^* \sim \sum_{\bar{n}} e^{-i\bar{n}\phi}$ and noticing that the only non-vanishing integrals in equation 2.42 occur when $n = \bar{n}$. In a cylindrical plasma there is symmetry in the poloidal direction as well, and consequently poloidal modes ‘ m ’ are also decoupled.

2.4.2 Field Line Bending and the magnetic operator

A strong stabilising mechanism in the plasma is the magnetic Field Line Bending (FLB), which is related to the perpendicular perturbation of the magnetic field $\delta\mathbf{B}_\perp$. In the coordinate system (r, G, b) where r labels flux surfaces, $G = q\theta - \phi$ as in equation 2.10 and $\hat{e}_b = \mathbf{B}/B$, one can write the perturbed perpendicular field in contravariant form as

$$\delta\mathbf{B}_\perp = \delta B^r \frac{\nabla G \times \mathbf{B}}{B^2} + \delta B^G \frac{\mathbf{B} \times \nabla r}{B^2} \quad (2.45)$$

where $\delta B^l = \mathbf{B} \cdot \nabla(\xi_\perp \cdot \nabla l)$ with $l = r, G$. Using the SFL coordinate system (r, θ, ϕ) to express the magnetic operator $(\mathbf{B} \cdot \nabla)$ and the component $\xi_\perp^G = q'\theta\xi_\perp^r + q\xi_\perp^\theta - \xi_\perp^\phi$ gives

$$\begin{aligned} \delta B^r &= \sum_n \sum_m \frac{imF}{R^2} \left(\frac{1}{q} - \frac{n}{m} \right) \xi_\perp^r \\ \delta B^G &= \sum_n \sum_m \left[\frac{imF}{R^2} \left(\frac{1}{q} - \frac{n}{m} \right) \xi_\perp^G + \frac{Fs}{rR^2} \xi_\perp^r \right], \end{aligned} \quad (2.46)$$

where $s = \frac{r}{q} \frac{dq}{dr}$ is the *magnetic shear*. While this representation is not often used due to the linear dependency of ξ_\perp^G on θ , equations 2.45 and 2.46 reveal an important aspect of MHD stability: the FLB stabilisation mechanism ($\sim \delta\mathbf{B}_\perp^2$) of a perturbation related with the mode number (m, n) almost entirely vanishes at $q(r_r) = m/n$, where $r = r_r$ is known as a *rational*

surface. This means that the regions in the plasma at more risk of becoming unstable are located at (or close to) rational surfaces, and the reason why $q(r)$ is known as the ‘safety factor’ has become clear. The present thesis is mostly focused on advanced tokamak scenarios where an extended region of the plasma has low magnetic shear and is located near a rational surface, such that $\delta\mathbf{B}_\perp \ll 1$. This constraint will be relaxed in Chapter 3 for the case of external modes.

2.4.3 Vacuum physics and external modes

This thesis is focused on the analysis of instabilities that occur at the edge of the plasma. To properly model the interaction of the perturbation at the plasma-vacuum interface (located at $r = a$), it is necessary to apply the following jump conditions [Gla60; Fre14]:

$$[\delta P + \mathbf{B} \cdot \delta \mathbf{B}]_a = 0 \quad (2.47)$$

$$[\hat{n} \cdot \delta \mathbf{B}]_a = 0. \quad (2.48)$$

The current density in the vacuum region must be zero ($\nabla \times \delta \mathbf{B}_V = 0$), which allows us to write $\delta \mathbf{B}_V = \nabla \Phi$ and $\nabla^2 \Phi = 0$. The solution for Φ in general torodial geometry is not a trivial task and must be performed numerically. For example, the KINX [Deg+97] code solves the stability problem in free boundary calculating the function Φ using the Green function technique. An approximate analytical boundary condition at the plasma-vacuum interface can be obtained following the tokamak ordering (§ 2.31). Assuming $\Phi(r, \theta, \phi) = \hat{\Phi}(r) e^{-i(m\theta - n\phi)}$, the leading order equation for $\hat{\Phi}(r)$ is described by

$$\frac{d}{dr} \left[r \frac{d\hat{\Phi}}{dr} \right] - m^2 \hat{\Phi} = 0. \quad (2.49)$$

The solution is

$$\hat{\Phi}(r) = A \left[(r/b)^m + (r/b)^{-m} \right], \quad (2.50)$$

The ideal MHD model

where the boundary condition at the ideal wall $\hat{n} \cdot \delta \mathbf{B}_V = 0|_b$ located in $r = b$ has been applied. Assuming no equilibrium skin currents, the equilibrium vacuum magnetic field equals the plasma magnetic field at the interface, $\mathbf{B}_V(a) = \mathbf{B}(a)$. To leading order in the vacuum side of the interface ($r = a + \delta$):

$$\mathbf{B}(a) \cdot \delta \mathbf{B}_V(a) = -A \frac{iB_0}{R_0 q_a} (m - nq_a) [(a/b)^m + (a/b)^{-m}] \quad (2.51)$$

$$\hat{n} \cdot \delta \mathbf{B}_V(a) = A \frac{m}{a} [(a/b)^m - (a/b)^{-m}], \quad (2.52)$$

and in the plasma side of the interface ($r = a - \delta$):

$$\delta P(a) + \mathbf{B}(a) \cdot \delta \mathbf{B}(a) = -\frac{aB_0}{m^2 q_a R_0^3} (m - nq_a) \left[(m - nq_a) a \frac{d\xi_{(m)}^r}{dr}(a) - (m + nq_a) \xi_{(m)}^r(a) \right] \quad (2.53)$$

$$\hat{n} \cdot \delta \mathbf{B}(a) = -\frac{i}{R_0^2 q_a} (m - nq_a) \xi_{(m)}^r(a). \quad (2.54)$$

Taking $\frac{\delta P(a) + \mathbf{B}(a) \cdot \delta \mathbf{B}(a)}{\hat{n} \cdot \delta \mathbf{B}(a)} = \frac{\mathbf{B}(a) \cdot \delta \mathbf{B}_V(a)}{\hat{n} \cdot \delta \mathbf{B}_V(a)}$ eliminates the constant A and ultimately gives [Wes78; Fre14; Bru+18b]

$$\frac{r}{\xi_{(m)}^r} \frac{d\xi_{(m)}^r}{dr} \bigg|_{a-\delta} = \frac{2m}{m - nq_a} - \frac{m + 1 + (m - 1)(a/b)^{2m}}{1 - (a/b)^{2m}}. \quad (2.55)$$

2.4.4 Ideal instabilities at the plasma edge

The question of plasma stability is an important one in the context of the present thesis. The dynamics that follows the onset of an instability can either disrupt the plasma or lead to the formation of a new equilibrium. Therefore, the plasma conditions leading to the avoidance (or triggering) of certain instabilities define the parameter space of safe operation against ideal MHD plasma motion, or the route to enter an optimised confinement regime. The

present thesis focuses on the study of instabilities that are observed at the plasma edge during the Quiescent-High confinement (QH-mode) regime, and the plasma parameters which are related to the onset Edge Harmonic Oscillations (EHOs) and the avoidance of Edge Localised Modes (ELMs). A comprehensive review of the plasma conditions observed during QH-mode operation and the physics of EHOs is given in chapter 3. The relevant ideal instabilities leading to EHOs and ELMs that are treated in the following chapters are the external kink, peeling, infernal and ballooning modes, which can be understood with respect to the physical mechanism driving the stabilisation (or destabilisation) of the plasma. Magnetic FLB, magnetic field compression and plasma compression lead to stable plasma motion in the form of shear Alfvén waves, compressional Alfvén waves and sound waves respectively. Fluid pressure gradient, current gradients and total parallel plasma current can drive instabilities. In the following, a short description of the physics driving each of these modes is provided.

External kink modes

External kink modes are long-wavelength (low- n) current-driven plasma instabilities. The perturbed vacuum energy provides an unstable drive for the Fourier mode component (m, n) if the rational surface lies in the vacuum region, meaning that external kink modes are unstable when $q_a < m/n$. The mode can be stabilised by the averaged FLB stabilisation mechanism of the whole plasma region. The typical radial structure of the plasma displacement of an external kink mode vanishes at the magnetic axis and peaks at the plasma edge. External kink modes are described to the lowest order (in ϵ , following the tokamak ordering) by a single Fourier component of the radial plasma displacement (ξ_m^r) , which is a solution of Newcomb's equation [New60]

$$\frac{d}{dr} \left\{ r^3 \left[\left(\frac{1}{q} - \frac{n}{m} \right)^2 + I \right] \frac{d}{dr} \xi_{(m)}^r \right\} + \left\{ (1 - m^2) \left[\left(\frac{1}{q} - \frac{n}{m} \right)^2 + I \right] + r \frac{d}{dr} I \right\} r \xi_{(m)}^r = 0, \quad (2.56)$$

where $I = \frac{\lambda^2}{\omega_A^2} \frac{1+2q^2}{m^2}$ is the plasma inertia, λ is the growth rate and ω_A is the Alfvén frequency. The equation above follows from the minimisation of the perturbed plasma energy $(\lambda^2 K(\xi) + \delta W(\xi))$ by applying Euler-Lagrange equations with respect to the normal plasma displacement ξ_m^r with mode number (m, n) . Finally, casting equation 2.55 as a Robin boundary condition for

Newcomb's equation 2.56 completes the formulation of the external kink problem.

At this order, only cylindrical and current-driven effects appear, with toroidal and pressure effects appearing at higher orders of ϵ . If the magnetic shear is small, or if there is an extended region of the plasma where $q - m/n \ll 1$, then equation 2.56 is of higher order in ϵ and other physics of similar order need to be considered to assess stability. This situation will be considered in section 3.2.

Peeling modes

Peeling modes are instabilities mainly driven by the parallel current flowing at the very edge of the plasma, near the plasma-vacuum interface. Contrary to external kink modes, pure (high- n) peeling modes are very localised at the plasma edge and are not very sensitive to the core conditions. Indeed, it is possible to formulate the stability condition against peeling modes only from the perturbed energy of the vacuum region and the perturbed surface energy [Wil+99; WG09]. Stabilisation of peeling modes is achieved by increasing the magnetic well at the plasma edge, which can be done by increasing the edge pressure gradient or by strong plasma shaping. The stability criteria of pure peeling modes in a large aspect ratio tokamak is given by equation 4.21 in chapter 4.

Ballooning modes

Ballooning modes are short-wavelength (high- n) pressure-driven instabilities excited due to the alternation of the magnetic field lines between regions of 'good' and 'bad' magnetic curvature within a single flux surface⁵, corresponding to the high-field side and the low-field side of the torus respectively. The resulting structure of the mode localises the instability in the bad curvature region, making the plasma mode to 'balloon' outwards in the low-field side. Equation 4.20 describes infinite- n ballooning modes, which are stabilised by magnetic shear and destabilised by plasma pressure gradient. Nevertheless, at high values of pressure gradient, the *local* magnetic shear in the bad curvature region can become negative and large (while the *average* magnetic shear is maintained low). Since the stabilisation mechanism is proportional to the square of the local magnetic shear, a second region of stability opens up in

⁵When the magnetic curvature vector is parallel (anti-parallel) to the plasma pressure gradient, the change in the perturbed energy provides an unstable (stable) contribution.

the parameter space for high-pressure gradient and low average magnetic shear. As will be shown in chapter 4, ideal external modes are unstable in this region of the parameter space.

Infernal modes

As introduced in section 2.4.2, a region of low magnetic shear has weak FLB stabilisation in response to a perturbation with Fourier mode number (m, n) , which occurs when the safety factor is close (though an exact resonance is not required) to a rational surface ($q \sim m/n$) for an extended region of the plasma. Under such conditions, long-wavelength (low- n) pressure-driven infernal instabilities can develop providing that the pressure gradient is large enough in the low-shear region. The typical mode structure of the (m, n) Fourier component expands over the low-shear region of the plasma, though strong toroidicity-induced poloidal coupling with neighbouring sidebands (where the number of relevant sidebands ' l ' depends on the geometry of the plasma) can excite the $(m \pm l, n)$ Fourier components of the mode. If the low-shear, high-pressure gradient region is located near the plasma boundary, the upper sidebands $(m + l, n)$ connection to the vacuum region provide a drive to excite external kink modes, giving rise to a new kind of instability called *exfernal* mode [Bru+18b; Bru+19a]. As will be presented in detail on Chapter 3, the conditions for the appearance of an external instability can be fulfilled during QH-mode tokamak operation. The equations describing the stability of infernal (and external) modes are presented in section 3.2

2.5 Nonlinear stability and 3D saturated modes

According to the analysis on the previous section, an unstable mode will grow exponentially at a certain speed given by the linear growth rate. However, once the instability becomes large enough, the assumptions made by the linear analysis break down, and nonlinear physics is required to describe the dynamics that follows. Two main scenarios are possible, either the nonlinear forces reinforce the unstable mode and it continues to steadily grow until the plasma disrupts, or the nonlinear forces damp the growth rate and push the plasma towards a new saturated equilibria in 3D. In the latter scenario, it is possible that the discharge continues without disrupting the plasma, particularly if the instability saturates at low amplitude. This is often desired since the new equilibria might offer better confinement properties. For example, the instability can help to expel impurities from the core [Ödb+98] or regulate the plasma

density at the pedestal and thus avoid to cross a hard stability limit [Bur+01; Gar+15; Che+16]. On the other hand, it has been recently shown that a 3D saturated internal kink in combination with strong flows can lead to impurity accumulation at the magnetic axis, followed by radiative termination of the discharge [JN22]. Because of this, it is important to explore the plasma conditions that allow the existence of favourable saturated instabilities with optimal plasma performance.

2.5.1 Nonlinear approaches to equilibrium

Dynamic approach

The path from a linearly unstable 2D state to a non-linearly saturated 3D state can be obtained via initial value nonlinear MHD codes, like XTOR [LL10] and JOREK [Hoe+21]. Such simulations require the introduction of diffusive parameters (such as fluid viscosity) to achieve numerical convergence, which are hard to prescribe accurately and might lead the simulation to evolve to different physical states. Moreover, full nonlinear dynamic simulations are very demanding numerically due to the need to evolve several physical effects at different time scales. Nevertheless, when used carefully such codes can in principle provide the complete nonlinear evolution of the MHD plasma parameters and guarantee that the final saturated state is physically accessible. This methodology has been used extensively to calculate the plasma response to Resonant Magnetic Perturbations (RMPs) [Ora+17; Tur12; Tur+13].

Equilibrium approach

The final saturated state in the ideal limit must satisfy the nonlinear MHD force balance equation $\mathbf{J} \times \mathbf{B} - \nabla p = 0$, whose solution can be found by equilibrium codes. The ‘equilibrium approach’ bypasses the nonlinear evolution of the system and directly calculates the final equilibrium state in 3D by other means, for example by minimising the plasma energy as done by the VMEC [HW83] and SPEC [Hud+12] codes. The main advantages of this approach is that the computational demands are strongly relaxed, and no dissipative effects are required to find the solution. The disadvantage however, is that while the calculated equilibrium is physical, there is no guarantee that the initial 2D unstable state will evolve to the solution found by the equilibrium code, or that the equilibria is physically accessible. To relate the 2D and 3D equilibrium states, a good approach is to find a physical or topological constraint

(i.e. a conserved quantity) that is fulfilled throughout the minimisation process from the 2D axisymmetric equilibrium to the 3D final saturated state. As it turns out, it can be shown that by maintaining the rotational transform fixed, global magnetic helicity is conserved throughout the energy minimisation process in VMEC simulations [Ram+22]. Other constraints fulfilled by VMEC include conservation of mass and conservation of nested flux surfaces. But even then, the solution can be stuck at a local minima which doesn't correspond to a 3D saturated state nor possibly to the lowest energy state. Modelling of 3D saturated instabilities using the VMEC code for the case of a saturated helical core [Coo+10; Coo+11] show that the accessible equilibrium solutions exist in a bifurcated state, where the equilibrium can either result in a standard axisymmetric state or in a 3D state, with a very low energy difference between the two. This means that both equilibrium configurations in the bifurcation are neighbour states, and suggest that the 3D equilibria corresponds to the nonlinear evolution of his neighbouring 2D axisymmetric unstable state. To verify this, one can follow the nonlinear evolution of the unstable state using an initial value nonlinear MHD code. In reference [Bru+14b] a saturated internal kink calculated in VMEC was recovered by XTOR when approaching the ideal MHD limit (no resistivity, diamagnetism or neoclassical effects). More recently, saturated external kink modes calculated in VMEC [Kle+19] were also recovered by JOREK for current driven cases where the edge resistivity does not play an important role [Ram+22].

The two methods are therefore complementary, and serve different purposes. Since nonlinear dynamic codes can in principle recover the ideal equilibrium solution, one can proceed with confidence to add non-ideal effects to analyse more complex scenarios in the dynamic approach. The fact that VMEC can produce physically accessible 3D saturated states gives confidence to perform extensive parameter scans given the relaxed computational demands, as was done for the internal kink case [Coo+10], external kink [Kle+18], JET snakes [Coo+15b; Coo+11], kink/peeling modes [Coo+16; Coo+15a] and external modes [Kle+19].

Since comparing the 3D VMEC equilibrium solution with an equivalent saturated state in XTOR or JOREK for each parameter scan is computationally expensive, a different diagnostic is proposed to link the axisymmetric unstable equilibrium with the 3D saturated state. The methodology was first introduced in reference [Kle+18], but repeated here for convenience as since it is heavily used in this thesis. Linearly unstable axisymmetric equilibria can be characterised by a set of eigenfunctions which describe the plasma displacement. Here, an equivalent nonlinear plasma displacement is calculated, which corresponds to the normal

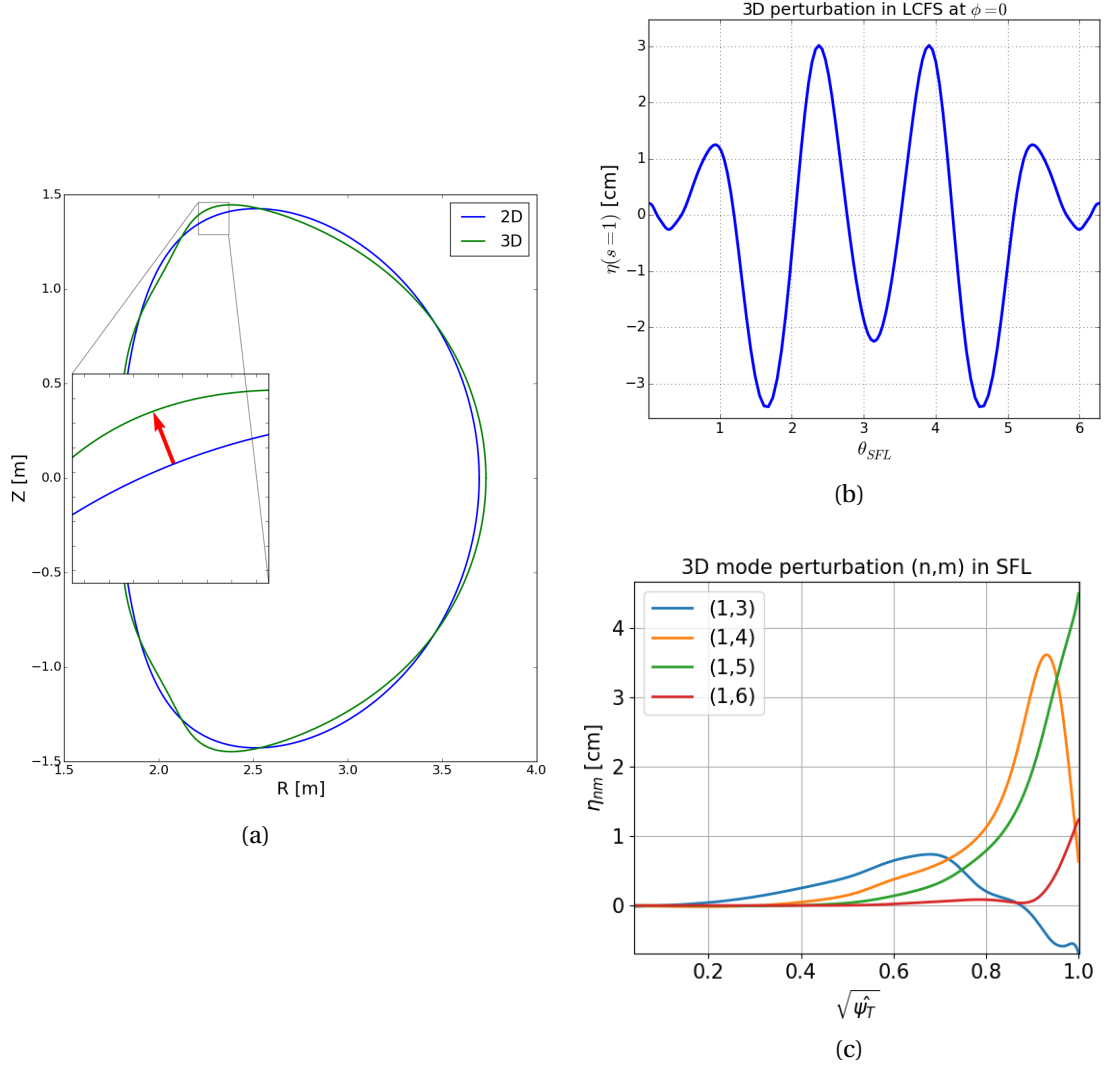


Figure 2.2: Calculation of the radial nonlinear saturated amplitude of a 3D configuration. (a) First, the distance between the 3D and the 2D surface is measured in the normal direction of the 2D surface at each poloidal angle. (b) Transformation to SFL is applied through the VMEC stream function $\lambda(s, \theta, \phi)$ (eq. A.3). (c) Reconstruction of the radial profiles for each Fourier mode (only $n = 1$ modes are plotted in the figure).

distance from the 3D surface with respect its 2D neighbour surface

$$\eta(s, \theta, \phi) \mathbf{N}(s, \theta, \phi) = \mathbf{S}_{3D}(s, \theta_{3D}, \phi) - \mathbf{S}_{2D}(s, \theta_{2D}, \phi) \quad (2.57)$$

where \mathbf{N} is the normal vector unitary vector of the 2D surface. Note that since the coordinates are aligned with the magnetic surfaces, the poloidal angle is different in both equilibria i.e. $\theta_{2D} \neq \theta_{3D}$. The VMEC poloidal angle is optimised to ensure fast and accurate convergence of the steepest descent numerical scheme, but is not optimal for analysis and can lead to misleading interpretations [Kle+18]. Therefore, transformation to a SFL poloidal angle of the 2D equilibria is performed using equation A.3. Repeating this calculation at all flux surfaces and finally Fourier decomposing into poloidal and toroidal components, the radial profile of each mode can be reconstructed. The method is graphically outlined in figure 2.2. The resulting nonlinear ‘eigenfunction’ can be qualitatively compared with the linear eigenfunction of the mode obtained analytically or numerically e.g. using the KINX code.

3 External modes as a model for EHOs

The goal of this chapter is to clarify the connection between the experimentally observed Edge Harmonic Oscillations and the linearly unstable external modes. First, a review of the experimental results of the QH-mode is presented and the key observed parameters are analysed, where different theories on the origin of EHOs are discussed. Next, a description of the linear theory of external modes is presented in preparation for the next chapters. The plasma profiles related to the excitation of external modes are used to obtain an equilibrium configuration in the DEMO QH-mode baseline. Linear stability analysis performed with the KINX code and nonlinear saturated states calculated with the VMEC code are presented and discussed for this particular case. Later, a comparison between the dynamic (using the JOREK code) and equilibrium (using the VMEC code) approaches to compute saturated states is presented for the case of external kink and external modes. It is found that the agreement between the two approaches varies due to the different physics included both codes. Finally, the prospects for the investigation of the parameter space to excite and saturate EHOs will be presented.

3.1 Experimental observation of EHOs

3.1.1 The nature of EHOs

Within the family of intrinsically ELM-free operational regimes, the Quiescent H-mode (QH-mode) is one of the most promising possibilities. As observed in DIII-D [Bur+01], JET [Sol+10], ASDEX-U [Sut+04] and JT-60U [Oya+06], QH-mode discharges avoid ELMs and exhibit instead

Edge Harmonic Oscillations (EHOs), which provide enough particle transport to avoid crossing a hard stability limit while sustaining high pedestal pressure. Contrary to ELMs, EHOs do not deposit very large heat loads on the divertor. EHOs are continuous long-wavelength MHD modes which saturate at finite amplitude, typically dominated by a $n = 1, 2$ though the subsequent harmonics (from $n = 1$ up to $n \sim 8$) are also observed. The harmonic spectrum corresponds to a rigidly rotating mode, since the signal in the magnetic diagnostics show the same wave form at different toroidal locations [Sut+05]. The magnetic fluctuation from EHOs is accompanied by electron density fluctuations, as measured experimentally by the electron cyclotron emission (ECE) diagnostic. Indeed, the rotation frequency observed in the Mirnov coils closely matches the oscillation frequency in the ECE channels whose line-of-sight is aligned with the pedestal region [Sut+04; Che+16; Bru+22], meaning that EHOs are highly localised in the pedestal.

The poloidal structure of EHOs is difficult to measure experimentally and therefore not usually reported. In the DIII-D tokamak, EHOs are robustly accessed in a wide range of q_{95} ¹ values [Bur+05], meaning that resonant conditions at the edge don't seem to be required and therefore no particular poloidal structure is favoured. This is however not what is observed in the other machines. EHO saturation in JT-60U do favour values of q_{95} near the $q = 4$ surface [Oya+06]. In JET, an analysis on the H-mode and QH-mode discharge database shows that ELMy and EHO discharges have different values of q_{95} when other pedestal parameters (electron pressure, collisionality and triangularity) are similar [Bru+22]. In ASDEX-U, EHOs are seen strongest at the ECE channels near the $q = 4$ or 5 surfaces [Sut+04]. Note that these surfaces correspond to the steep-gradient region of the pedestal, and not to the q_{95} surfaces. Therefore, the poloidal structure of EHOs and its relation to the rational surface location is not clear and requires further attention.

Figure 3.1a shows the time evolution of a typical QH-mode discharge in DIII-D. EHOs are captured in the magnetic diagnostic by the Mirnov coils with a frequency $f \sim n\Omega_{ped}$, where Ω_{ped} is the toroidal plasma rotation at the pedestal top. The integrated plasma density and the density at the pedestal are maintained at a constant value due to the enhanced transport driven by the EHOs, which is seen by D_α light at the lower divertor. Note that at around 1500 ms a single ELM is observed following a short period without EHOs and an associated increase on pedestal electron density. The distance between the LCFS and the wall is reported in the

¹ q_{95} is defined as the value of the safety factor at 95 % of the magnetic surfaces.

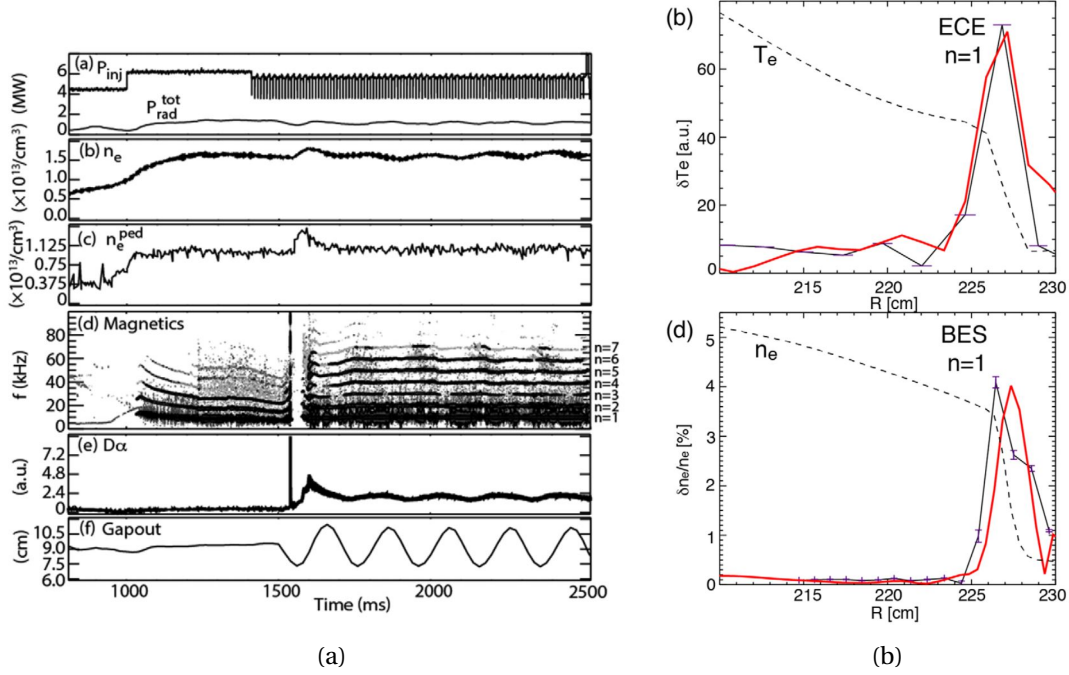


Figure 3.1: DIII-D discharge 157102, obtained from [Che+16]. (a) Time evolution of different plasma parameters. From top to bottom, injected and radiated power, electron density, pedestal electron density, Mirnov coil signal spectrogram, D_α emission line measured in the divertor and plasma distance from the wall to the last closed flux surface in the high-field side. (b) Electron temperature and density fluctuation as measured by the Electron Cyclotron Emission (ECE) and Beam Emission Spectroscopy (BES) diagnostics respectively (black). The red curve corresponds to the modelling using the M3D-C1 code. For more information, refer to reference [Che+16].

last plot, showing a variation in this gap of about ± 2 cm, or $\sim 3\%$ of the minor radius. Figure 3.1b shows the radial localisation of the electron density and temperature perturbation of the main harmonic as observed by the ECE and Beam Emission Spectrometer (BES) diagnostics.

3.1.2 Access to QH-mode and key drivers

QH-mode is accessed in the low collisionality regime, normally obtained in low density and high temperature discharges. Nevertheless, the pedestal pressure is of similar height as in a standard H-mode discharge, giving rise to a large bootstrap current in the pedestal and pushing the equilibrium towards the peeling stability boundary. Indeed, QH-mode discharges are always observed near (but below) the peeling boundary limit of the peeling-ballooning

stability diagram [Sny+07]. The large bootstrap current at the plasma edge also weakens the magnetic shear over the pedestal region, which combined with the destabilising effect of the large pressure gradient can excite instabilities of infernal nature [ZKV13a].

QH-mode is more easily accessed in discharges with strong flows, though the interaction between EHOs and plasma rotation is not yet well understood. One interpretation is that the toroidal flow sets the frequency at which low- n modes are observed and its influence on the stability is weak, though normally a certain threshold needs to be reached in order to avoid the mode locking to the wall [Gar+15]. Sheared flow of $\mathbf{E} \times \mathbf{B}$ origin ($\omega_E \propto E_r$) has been identified as the key mechanism to access QH-mode and therefore to the observation of EHOs [Gar+11], where its main effect on the ideal MHD modes is to stabilise high- n perturbations, as predicted by analytical [Bru+19a] and numerical modelling [Che+16; Ram+22]. $\mathbf{E} \times \mathbf{B}$ shear flow also destabilises low- n kink/peeling modes [Che+17a], but due to the complex mechanism played by the well deepness of the radial electric field (E_r) in creating the edge transport barrier in standard H-mode discharges, it is difficult to conclude that the role of $\mathbf{E} \times \mathbf{B}$ shear flow on EHOs is to merely destabilise an ‘otherwise stable’ kink/peeling mode. Moreover, numerical simulations suggest that the nonlinear interaction of the growing EHOs with the plasma flows pushes the equilibrium to a more stable domain by either damping or accelerating the flow [Don+19]. In more recent numerical modelling, plasma rotation is found to have a stabilising effect also for low- n modes if the ion diamagnetic drift effects are included in the calculations [Aib+21]. Therefore, the role of $\mathbf{E} \times \mathbf{B}$ flow and its shear remains an open question, though it appears, at least from the experimental results in the DIII-D tokamak, that a critical amount of it is necessary both to access QH-mode and to sustain it [Che+16].

We can imagine the trajectory of QH-mode equilibria in a similar way as the ELM cycle in standard H-mode discharges, as depicted in figure 3.2. Once the edge transport barrier is formed at high pedestal pressure, the equilibrium goes from the ballooning-side to the peeling-side (located in the second region of ballooning stability) as the collisionality decreases by cryopumping from the divertor. Note that in figure 3.2 the pedestal pressure gradient is proportional to the parameter $\alpha \sim P^{-1}$. Just before reaching the peeling boundary, low- n MHD modes become unstable and start to grow. If a certain threshold in the $\mathbf{E} \times \mathbf{B}$ shear rotation is not reached, the plasma will cross the stability boundary resulting on ELM onset. In fact, some experimental findings in JET have observed MHD activity similar to EHOs as precursors to ELMs [Bru+22]. If the rotation threshold is reached however, medium- n peeling-ballooning

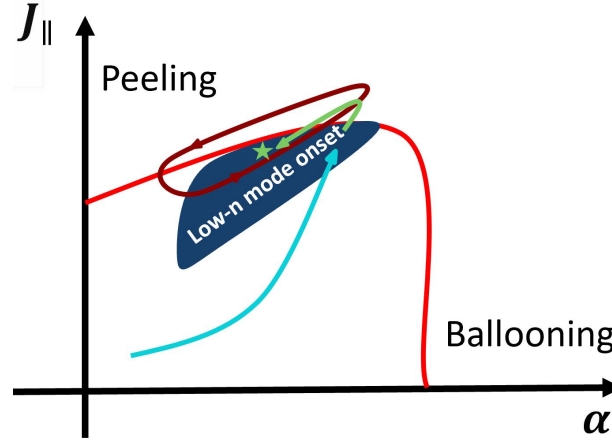


Figure 3.2: Cartoon of QH-mode access, inspired by the ELM cycle given in [Wil+06]. The plasma follows the blue arrow towards the peeling boundary as bootstrap current rises due to decrease in collisionality. Once in the ‘low-n mode onset’ region, the plasma will follow the dark red arrow and be trapped in an ELM cycle if the threshold in $\omega_{E \times B}$ is not reached. If it is, then the plasma will follow the green arrow, allowing low-n modes to saturate to a new 3D equilibrium state without destabilising medium-to-high-n peeling-ballooning modes.

modes are stabilised and the low-n modes will be allowed to grow and saturate to form a new 3D equilibrium state near the peeling boundary. Note that in ELMy discharges, EHOs are not excited either because the discharge is not located on the low-n mode onset region of the parameter space (closer to ballooning boundary). The EHOs in the new state will provide enough transport to maintain the equilibrium at the same location in the stability diagram.

Such low-n MHD modes have been theorised to be either kink/peeling [Sny+07] or edge infernal modes [ZKV13a], depending on the plasma conditions at the pedestal (safety factor, current density, pressure, temperature, rotation, etc.). In this work we explore the conditions in which the low-n mode corresponds to an edge infernal (*exfernal*) mode, where the drive requires toroidicity induced coupling of the main harmonic with the neighbouring sidebands, vanishing field line bending stabilisation contribution due to weak magnetic shear and proximity to a rational surface, and a vacuum region between the plasma surface and a metallic wall.

Several experimental findings hint towards the possibility that EHOs correspond to the nonlinear saturated state of exfernal modes. First, the mode is highly localised in the pedestal region where the temperature and density gradients associated with the edge transport barrier are

strongest, suggesting that a pressure-driven component is necessary. Indeed, analysis on the parameter space of a set of QH-mode discharges in JET, the electron plasma β at the pedestal is always above a certain threshold [Bru+22]. Second, citing Zheng et. al. [ZKV13b], ‘[...] *Since multiple inertial layers are involved in determining the mode frequency in kink/peeling modes, and since the rotation frequency varies radially, the mode frequency may not follow the n -multiplying rule. However, this frequency n -multiplying rule can become ensured if one of the Fourier components becomes dominant, as occurs in the infernal mode case*’. Third, JET [Bru+22], ASDEX-U [Sut+04] and JT-60U [Oya+06] do observe a dependency on the value of q at the pedestal, meaning that a resonant (or quasi-resonant) component is needed to excite EHOs, consistent with the infernal drive. Moreover, the poloidal structure measured in ASDEX-U by a set of poloidally distributed Mirnov coils identifies a $m = 4, n = 1$ and a $m = 5, n = 1$ mode when the EHOs are seen near the $q = 4$ and $q = 5$ surfaces respectively [Sut+04]. Fourth, as shown by numerous studies [Huy05; WG09; Kle+19], current-driven modes are strongly stabilised by the presence of a separatrix, and particularly the peeling-branch of peeling-ballooning modes is completely stabilised [SKK11]. As will be shown in detail in chapter 4, exfernal modes are still unstable in the presence of a plasma separatrix, with the instability sustained by the infernal pressure-driven branch. Fifth, the linear analytical model of exfernal modes is able to recover many of the experimentally observed features of EHOs and QH-mode access [Bru+19a]. This model will be introduced in the next section.

Recent experimental campaigns in the DIII-D tokamak have found a bifurcation in QH-mode operation denominated as ‘wide pedestal QH-mode’ [Bur+16; Che+17b]. In wide pedestal discharges, EHOs are replaced by broadband edge turbulence, which assume the same role of enhancing particle transport across the transport barrier. Since the excitation and saturation of EHOs is the main focus of this work, the physical mechanism leading to wide pedestal QH-mode operation is not discussed in the present thesis.

3.2 Linear theory of exfernal modes

This section discusses the main characteristics of the linear stability of exfernal modes. For simplicity, the summary presented here only considers the effects within the static ideal MHD model [Bru+18a], since effects such as toroidal rotation [Bru+18b], sheared helical flow [Bru+19b], and diamagnetic and sheared parallel $\mathbf{E} \times \mathbf{B}$ flows [Bru+19a] have been considered in previous work. The stability analysis will be generalised in the next chapter to allow the

3.2 Linear theory of external modes

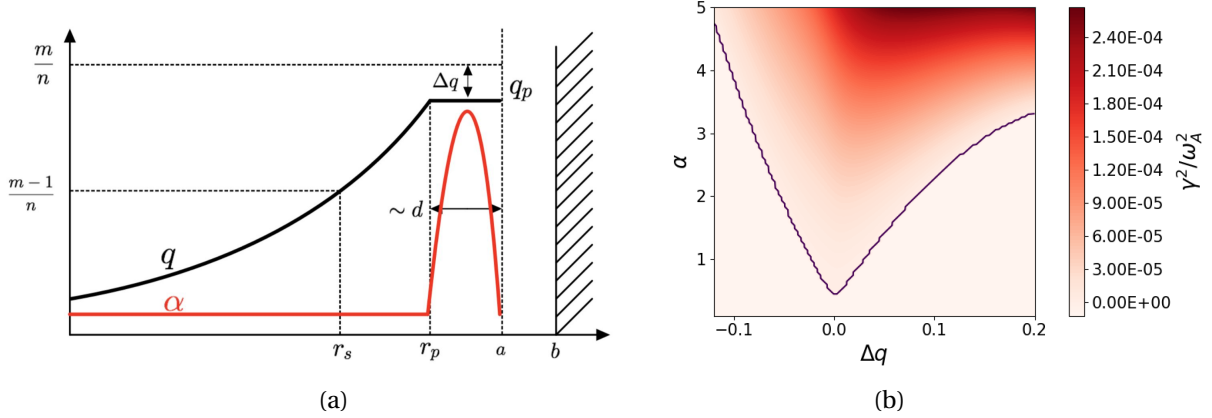


Figure 3.3: (a) Cartoon of the profiles considered in the equilibrium model. The parameter $\alpha \sim -P'$ is defined in the text. (b) $\alpha - \Delta q$ stability diagram, obtained from the numerical solution of equations 3.2 and 3.3 with extended vacuum boundary conditions (equation 2.55) on the sidebands.

inclusion of finite edge magnetic shear. Since the procedure and equations are similar, only the main assumptions and results of previous work will be discussed in this section.

The equilibrium under consideration models the key aspects observed during a QH-mode discharge, as seen in a simplified cartoon in figure 3.3a. The pressure profile sits on a pedestal located near the plasma edge, creating a region of high pressure gradient. The safety factor monotonically increases from the core up to the pedestal top, where it flattens as a consequence of the large bootstrap current generated in the low collisionality regime. The value of the safety factor plateau is located near a rational surface, i.e. $q = m/n + \Delta q$, where $|\Delta q| \ll 1$. It is pointed out that Δq can be positive or negative. The full magnetic equilibrium is given by the solution to the Grad Shafranov equation 2.28, which is solved order by order considering a large aspect ratio tokamak with circular cross sections and applying the tokamak ordering (§ 2.3.2).

The stability is investigated by separating the plasma in two regions: a high-shear and low-shear region. The high-shear region extends from the core to roughly the pedestal top, just before the magnetic shear starts to vanish. Mode coupling between poloidal Fourier harmonics in this region is weak in the large aspect ratio approximation for small pressure gradient, so the dynamics of each individual harmonic is given by Newcomb's equation (2.56) introduced in section § 2.4.2. The physical mechanism driving the external modes is located in the low shear region, which extends from the pedestal top to the plasma-vacuum interface. Due to the

closeness to the rational surface on an extended region of the plasma, the FLB stabilisation is now of the same order as the pressure gradient instability drive, resulting in coupling between neighbouring poloidal Fourier harmonics through toroidicity in the geometric components. The combination of large pressure gradients and weak FLB stabilisation provides an infernal stability drive [WH88; MPT87]. For a circular cross section large aspect ratio tokamak, only the upper and lower sidebands are necessary to determine stability [HH88; GHH96]. The plasma displacement is therefore written in this region as

$$\xi^r(r, \theta, \phi) = \sum_{l=m-1}^{m+1} \xi_{(l)}^r(r) e^{i(l\theta - n\phi)}, \quad (3.1)$$

where $\xi_{(m)}^r / \xi_{(m\pm 1)}^r \sim \epsilon$. As outlined in section 2.4.1, one possible way to obtain the stability of a mode is through the energy principle [Ber+58]. Substituting the equilibrium and geometric quantities to relevant order in ϵ into equation 2.42, the following equations describing the main mode (m, n) and sidebands $(m \pm 1, n)$ are obtained in the limit of $q \sim m/n$ [HH88; GHH96]

$$\begin{aligned} \frac{1}{r} \frac{d}{dr} \left\{ r^3 \left[\left(\frac{1}{q} - \frac{n}{m} \right)^2 + I \right] \frac{d}{dr} \xi_{(m)}^r \right\} - \left\{ (m^2 - 1) \left[\left(\frac{1}{q} - \frac{n}{m} \right)^2 + I \right] + r \frac{d}{dr} I \right\} \xi_{(m)}^r = \\ - \frac{\alpha}{q^2} \left[\frac{r}{R_0} \left(\frac{1}{q^2} - 1 \right) \right] \xi_{(m)}^r + \frac{\alpha^2}{2q^2} \xi_{(m)}^r - \frac{\alpha}{2q^2} \left[\frac{r^{-(1+m)}}{1+m} \frac{d}{dr} (r^{2+m} \xi_{(m+1)}^r) + \frac{r^{-(1-m)}}{1-m} \frac{d}{dr} (r^{2-m} \xi_{(m-1)}^r) \right] \end{aligned} \quad (3.2)$$

$$\frac{d}{dr} \left[r^{-(1\pm 2m)} \frac{d}{dr} (r^{2\pm m} \xi_{(m\pm 1)}^r) \right] = \frac{1 \pm m}{2} \frac{d}{dr} (r^{\mp m} \alpha \xi_{(m)}^r). \quad (3.3)$$

where $I = \frac{\lambda^2}{\omega_A^2} \frac{1+2q^2}{m^2}$ the plasma inertia and $\alpha = -\frac{2\mu_0 P' q^2}{B_0^2}$ is the ballooning α parameter. The left hand side in equation 3.2 corresponds to the cylindrical equation calculated by Newcomb [New60]. The first term in the right hand side is the Mercier term with a toroidal correction, and the last term couples the main modes with the neighbouring sidebands. Equations 3.2 and 3.3 are valid only on the low-shear region since they assume $\Delta q \ll 1$, particularly because

the cylindrical corrections to FLB due to magnetic shear in the sideband equations are not complete. First order FLB corrections to equation 3.3 are given in appendix B.2. Boundary conditions for each mode are required to solve this system of equations, which in the plasma side (at the interface with the high-shear region) are given by the solution of equation 2.56 for each individual mode in the high-shear region. At the plasma-vacuum interface, boundary conditions are applied as discussed in section § 2.4.3. More details on the application of boundary conditions will be given in chapter 4.

Figure 3.4a shows the numerical solution to equations 3.2, 3.3 (in the low-shear region) and equation 2.56 (in the high-shear region) for the plasma profiles described in figure 3.3a. Figure 3.4b shows the numerical eigenfunctions calculated with the KINX code, which considers full MHD physics and a much larger spectrum of poloidal Fourier Harmonics. As can be seen, the solution is very similar for both cases, meaning that the physics relevant in the ideal KINX simulations is most likely captured by the simplified equations presented above. The dominant mode (m, n) of the plasma displacement is a ‘bell-shaped’ pressure-driven perturbation localised in the pedestal that expands over the region where the safety factor is flat. Note that this shape is in agreement with the density perturbations observed in the pedestal during the onset of EHOs [Bur+04; Che+16] (see figure 3.1b). The infernal drive of the main mode couples with the external kink current-driven upper sideband $(m + 1, n)$, which perturbs the plasma edge in the absence of a separatrix. The lower sideband is a little further in the core, roughly constant from its rational surface (around $r \sim 0.8$) until the pedestal region, where it drops at the same place where the main mode peaks.

The numerically calculated growth rate is plotted in figure 3.3b. As expected by physical intuition, the mode is driven unstable by pressure gradient ($\sim \alpha$) and stabilised by bending of the magnetic field lines ($\sim \Delta q$). There is a slight asymmetry towards positive Δq due to the stronger coupling with the upper sideband external kink drive. The system of equations 3.2 and 3.3 can also be solved analytically for simplified profiles of the pressure and safety factor. Particularly, for step-like pressure and density profiles, with the step in the pedestal region ($r = r_p$), an analytical dispersion relation has been obtained by Brunetti et. al. [Bru+18b]

$$\frac{1}{2} \left(\frac{\gamma}{\omega_A(0)} \right)^2 = \frac{\Delta}{4a} \left[\frac{\hat{\beta}^2}{2\epsilon_p^2} \Lambda - \hat{\beta} \right] - \left(\frac{\Delta q}{q} \right)^2, \quad (3.4)$$

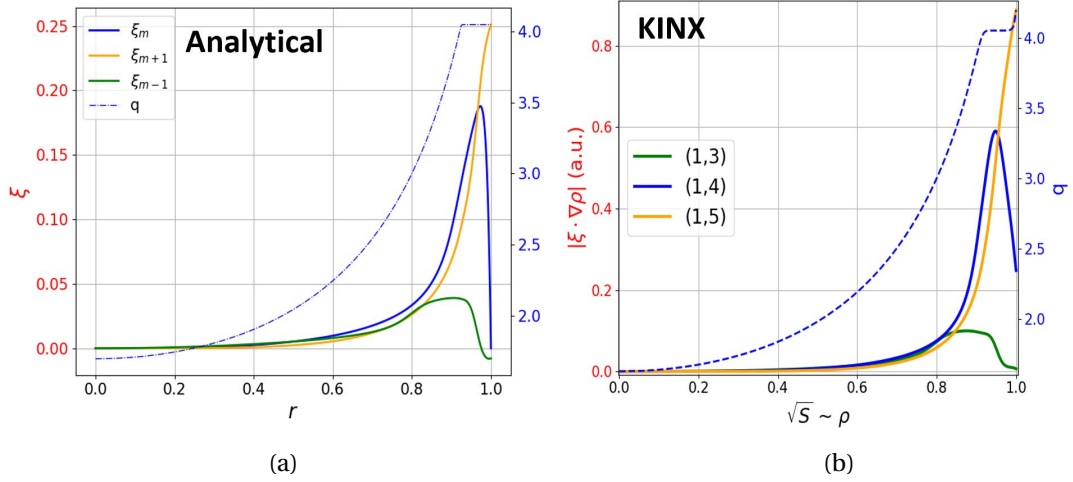


Figure 3.4: Eigenfunctions of the eigenvalue stability problem corresponding to the poloidal Fourier components of the normal displacement, calculated (a) numerically from equations 2.56, 3.2, 3.3 and (b) using the full MHD KINX code. The safety factor is plotted in dashed lines in both figures.

where $\hat{\beta} = 2\mu_0 P(r_p) q^2 / B_0^2$, $\epsilon_p = r_p / R_0$, $\Delta = 2(a - r_p)$, a and R_0 are the minor and major radius, and Λ is a factor containing the coupling and boundary conditions of the sidebands. The dispersion relation recovers the dependencies observed numerically on the parameters α and Δq (note $\alpha \propto \hat{\beta}$). Moreover, in the marginal stability limit ($\gamma \rightarrow 0$), the dispersion relation yields the marginal condition $\alpha \sim |\Delta q / q|$, which is also roughly reproduced by the numerically calculated stability limit.

3.3 Nonlinear saturated EHOs

Now that the linear mechanism for the excitation of external modes has been laid out, the nonlinear saturation mechanism will be discussed. As presented in section 2.5, two different but complementary methods can be used to explore 3D saturated states in tokamak plasmas. The first one starts with an axisymmetric equilibrium, and then evolves the plasma non-linearly in time until a saturated state is reached (labelled as ‘dynamic approach’), and the second one consists on directly calculating the final 3D saturated state which is a solution of the ideal MHD equilibrium equation (labelled as ‘equilibrium approach’). The nonlinear saturated states calculated in the present thesis mainly focus on the ‘equilibrium approach’ using the VMEC 3D free boundary code. An example of such calculation is given in section §

3.3.1, where saturated EHOs are obtained for the DEMO1 QH-mode baseline.

Both the ‘dynamic’ and ‘equilibrium’ approaches have been independently reported in the literature for certain types of saturated EHOs. For example, Liu et. al. [Liu+18] performed JOREK initial value simulations of DIII-D QH-mode plasmas and obtained saturated low-n MHD structures similar to those observed in experiments. Kleiner et. al. [Kle+19] calculated 3D saturated equilibrium states using the VMEC code for QH-mode plasma profiles in JET-like geometry. Two types of saturated structures were identified, one current-driven (external kink type) and one pressure-driven (external type). Both types of saturated instabilities will be explored in this thesis. In Dong et. al. [Don+19] quasi-linear initial value simulations using the MARS-Q code were performed to study the nonlinear interaction between external modes and different types of plasma flows. It was found that external modes can either damp or accelerate the plasma flows with both scenarios leading to mode saturation, meaning that the saturated state could be independent of the final flow profile. A direct comparison between the ‘equilibrium’ and ‘dynamic’ approaches for external kink and external modes is presented in section § 3.3.2.

3.3.1 Equilibrium approach to EHO numerical modelling: application to DEMO

EHOs have been robustly obtained in TCV, JET and DEMO geometries using the VMEC free boundary code. The resulting equilibria has the advantage that the Fourier decomposition of the magnetic field and geometric components can be calculated with very high accuracy, often up to machine precision. These quantities can be used for advanced analysis of fast particle and impurity transport using guiding-centre codes such as VENUS-LEVIS [Pfe+14]. Poor fast particle confinement can occur during QH-mode operation. While EHOs provide the necessary particle transport to sustain high pedestal pressure without incurring into ELMs [Bur+01; Gar+15; Che+16], their 3D magnetic structure might deteriorate the confinement of highly energetic NBI particles or fusion-born alpha particles. Because of this, an assessment of fast ion confinement on the QH-mode DEMO baseline was performed under a EUROfusion Enabling Research work package, which is reported in reference [BSG20].

The DEMO tokamak should be the first-of-a-kind European demonstration power plant to produce electricity from fusion reactions, breed tritium and recirculate energy to operate the machine. It is envisaged to be operational around the middle of the century, but with many of

the current problems in fusion technology not yet solved, the design of DEMO is not yet agreed upon. The calculations presented here are based on the 2019 QH-mode baseline described in a EUROfusion report by Roberto Ambrosino [Amb19], where an equilibria was calculated using the CREATE-NL code [AAM15] on the DEMO1 design. The final goal of this section is to recreate a similar equilibrium in the free-boundary VMEC code, which has the advantage of being able to calculate 3D magnetic equilibria, a characteristic that will be essential to obtain non-linearly saturated instabilities. The procedure on how to obtain and classify saturated external modes will be outlined in detail, from the computation of the fixed and free boundary equilibrium, to the linear and nonlinear stability properties. The calculation also helps to exemplify the concepts of equilibrium developed in chapter 2 and the suite of codes that are used in the next chapters of this thesis. The methodology described here is depicted in figure 3.5. First, a fixed boundary axisymmetric VMEC equilibria is calculated with the desired 2D edge geometry and plasma profiles. The resulting equilibria together with the coil geometry is given to the FreeGS code [Dud] to calculate the necessary coil currents that would produce an equivalent axisymmetric free boundary VMEC equilibria. In order to obtain edge corrugations, the free boundary VMEC code is run using the current in the coils calculated by FreeGS and allowing higher toroidal harmonics in the VMEC Fourier expansion (equation A.2).

Free boundary axisymmetric magnetic equilibrium

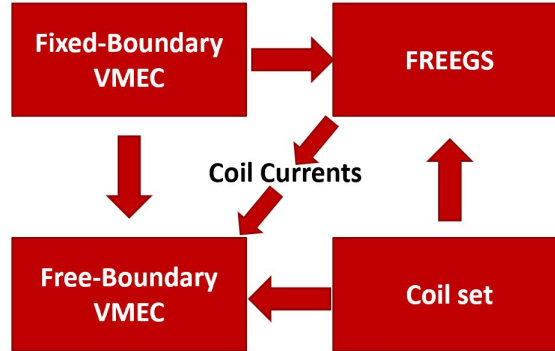


Figure 3.5: Diagram of the codes used to obtain a VMEC free-boundary equilibria. First, a fixed-boundary VMEC equilibria is calculated. The resulting profiles are used as an input to free-boundary VMEC and FreeGS. The later code uses the coil set to calculate the necessary currents for free boundary equilibria, which are then used as an input to VMEC.

First, a VMEC axisymmetric equilibria in fixed-boundary conditions needs to be calculated.

Due to the better convergence properties of VMEC when imposing stellarator symmetry², the equilibrium is constrained to be up-down symmetric. The description of the plasma boundary is given by

$$\begin{aligned} R(\theta) &= R_0 + r_0 \cos(\theta) - E \cos(\theta) + T \cos(2\theta) \\ Z(\theta) &= r_0 \sin(\theta) + E \sin(\theta) - T \sin(2\theta), \end{aligned} \quad (3.5)$$

where $R_0 = 9.338m$ is the major radius, $r_0 = 4.0m$ is the minor radius, $E = 1.0m$ and $T = 0.33m$ are the elongation and triangularity coefficients respectively. This representation is compatible with the VMEC Fourier expansion assuming stellarator symmetry (equation A.4). The plasma boundary is plotted in figure 3.6a together with the boundary from the CREATE-NL baseline for comparison.

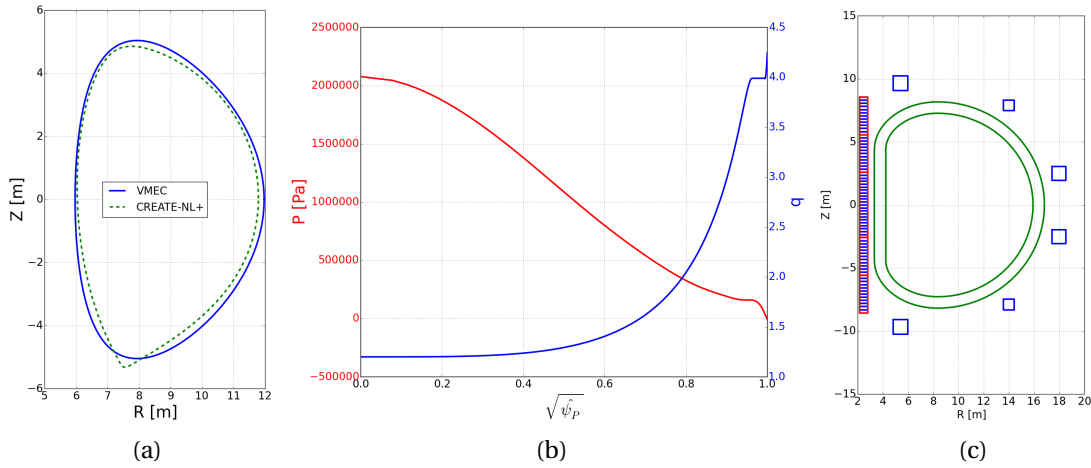


Figure 3.6: Input parameters for VMEC and FreeGS simulations: (a) Comparison between LCFS in VMEC (solid line) and extracted from CREATE-NL simulation reported in [Amb19] (dashed line), (b) pressure and safety factor profiles and (c) DEMO coils modified to fulfil stellarator symmetry.

The pressure and safety factor profiles are chosen as the free functions to calculate the equilibrium. The pressure monotonically decreases from the core until the edge, where a pedestal is added to the plasma so to emulate H-mode-like operation. The safety factor increases monotonically up to the pedestal, where a flat region is added between $0.95 < s < 0.99$. Finally,

²A discussion on the constraints imposed by stellarator symmetry is given in appendix A.1

the total enclosed toroidal magnetic flux can be calculated by solving the differential equation for the safety factor $q(s) = d\psi_t / d\psi_p$

$$\begin{aligned} \psi_t(s) - \psi_t(0) &= [\psi_p(1) - \psi_p(0)] \int_0^s q(s') ds' \\ \psi_t(1) - \psi_t(0) &= 261.29 [Wb], \end{aligned} \tag{3.6}$$

where $\psi_p(0)$ and $\psi_p(1)$ are extracted from Ambrosino's report [Amb19]. The VMEC code is first used to obtain an axisymmetric equilibrium solution with fixed-boundary conditions. This is achieved by restricting the VMEC Fourier expansion to have only $n = 0$ toroidal modes. The simulation was calculated with a radial discretisation of 500 flux surfaces and a spectrum of $0 \leq m \leq 16$ poloidal Fourier modes.

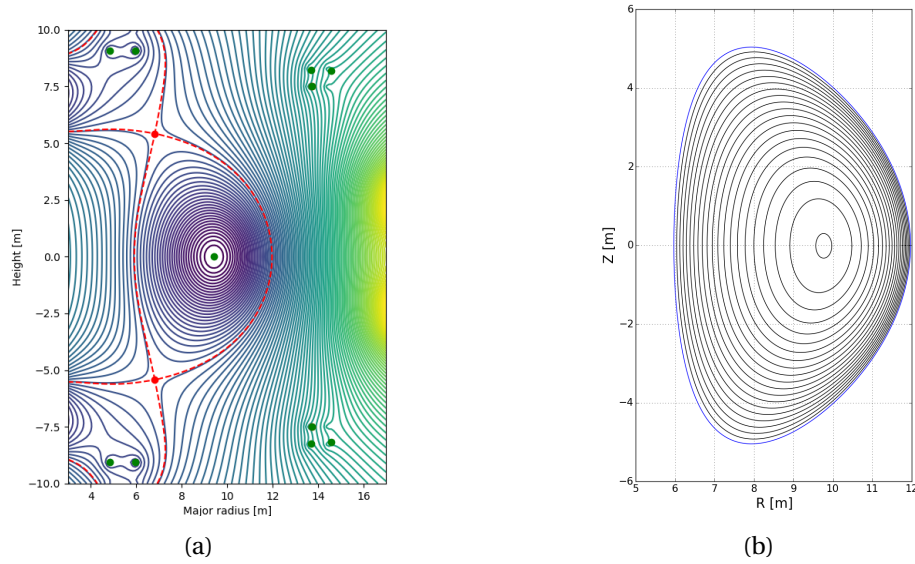


Figure 3.7: Resulting flux surfaces in FreeGS (a) and VMEC (b) simulations

The computation of free-boundary equilibria requires the description of the vacuum magnetic field, which in VMEC is calculated through the Biot-Savart law by a set of one dimensional filaments carrying current. As pointed out in appendix A.1, the magnetic field will only be stellarator symmetric if the coil system is as well. A rough description of the coil system in DEMO baseline 2019 is reported in reference [Amb19], which is slightly modified so that the coils are stellarator symmetric. The final set is plotted in figure 3.6c, consisting on 16 toroidal

coils, 6 poloidal coils and a central solenoid, where the later is divided on 5 sections and each coil is formed by 4 filaments carrying $1/4$ of the coil current. The current in the coils that would produce the required magnetic field to obtain an equivalent free-boundary equilibria are calculated using the `FreeGS` code [Dud] (see appendix A.2 for more details on the code). The input parameters required by `FreeGS` are extracted from the fixed-boundary VMEC solution so that the equilibrium calculated in the two free boundary codes is as close as possible. The calculation in VMEC is repeated but now in free-boundary conditions. To that end, the vacuum magnetic field is calculated using the `MAKEGRID` code and the current in the coils calculated by `FreeGS`. Note that 16 toroidal planes in the VMEC numerical grid are used to avoid aliasing the frequency of the toroidal ripple³. The resulting flux surfaces in both codes are plotted in figure 3.7. Up to this point, 3D effects were not allowed in the calculation for either fixed or free boundary VMEC calculations.

Linear departure from axisymmetric equilibrium

The stability of the DEMO QH-mode baseline equilibria is studied using the `KINX` code [Deg+97]. The safety factor shown in figure 3.6b is flat in two regions of the plasma, the core and the edge, hinting that the equilibrium might be unstable to both internal and external infernal modes. Moreover, the value of the safety factor is close to a rational surface in both cases ($m/n = 1$ in the core and $m/n = 4$ in the edge). The safety factor profile exhibits a spike at the plasma edge that takes the value of q_a just above the rational surface, which stabilises the external kink contribution of the ($m/n = 4$) mode and at the same time serves as a model of the transition between the plasma edge and the vacuum region in a diverted configuration. A detailed investigation on the effect of the spike on the stability of external modes is given in chapter 4.

A `KINX` calculation considering 128×128 grid points in the radial and poloidal direction was performed in free boundary conditions, with an ideal wall located at a distance $b = 10a$, where a is the minor radius. The normal plasma displacement for a toroidal mode number $n = 1$ is plotted in figure 3.8a, where the normalised growth rate calculated by the code is $\hat{\gamma}^2 = (\gamma/\omega_A)^2 = 4.25 \times 10^{-3}$. As can be seen, the displacement is strongest at the core and at the edge. A clearer picture of the instability is given by the Fourier spectrum of the eigenfunction

³Such effect happens when the frequency of a measured signal is higher than two times the sampling rate, violating the Nyquist criterion. Aliasing is the shift in the frequency of the signal to an observable signal within the sampling rate. Details on this effect applied to the toroidal ripple are given in detail Chapter 5

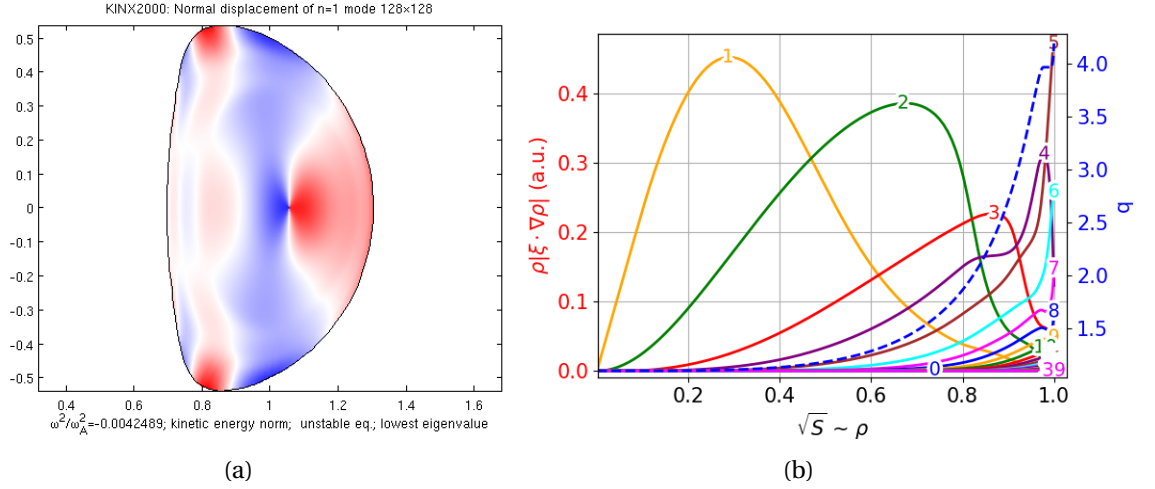


Figure 3.8: $n = 1$ Normal plasma displacement for DEMO QH-mode baseline. (a) Plasma displacement in toroidal cross section and (b) Fourier decomposition in SFL poloidal angle. In figure (b) the numbers in the solid lines correspond to the poloidal mode number. The safety factor is also plotted in dashed lines.

in SFL coordinates, plotted in figure 3.8b. The dominant mode is a core infernal ($m = 1, n = 1$) mode, which expands roughly over the region of low shear, along with its upper sideband ($m = 2, n = 1$) which is of similar amplitude. Also visible is the external ($m = 4, n = 1$) mode, localised on the pedestal region where the safety factor is flat. The upper sideband ($m = 5, n = 1$) is associated with the external kink drive, which couples with the infernal drive and perturbs the plasma edge. Both core and edge infernal modes are excited independently, but coupling between the two is observed on the small shoulder of the ($m = 4, n = 1$) mode at around $\rho \sim 0.8$. While this calculation in DEMO geometry considers ad-hoc profiles with the qualitative components of QH-mode operation, a very similar case has been reported in the literature where a core and an edge infernal mode are excited independently in a DIII-D QH-mode discharge (reference [Gar+15], figure 8).

Figure 3.9a shows the normalised growth rate for toroidal mode numbers $n \in [1, 10]$, where it can be seen that larger toroidal harmonics are more unstable. Low- n instabilities have infernal-like features, as can be seen in figure 3.10, where the eigenfunctions with toroidal mode numbers $n = 2$ and $n = 3$ show that the infernal $m/n = 4$ modes and their respective sidebands dominate the spectrum. In both cases, the core infernal mode $m/n = 1$ is no longer dominant, but still present.

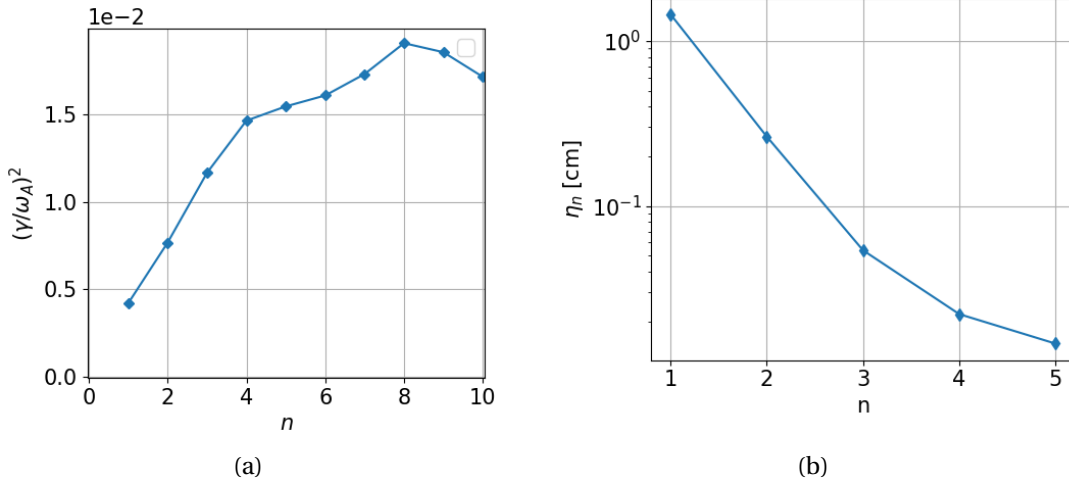


Figure 3.9: (a) Growth rates and (b) nonlinear saturated amplitude for toroidal Fourier modes in DEMO QH-mode baseline equilibria.

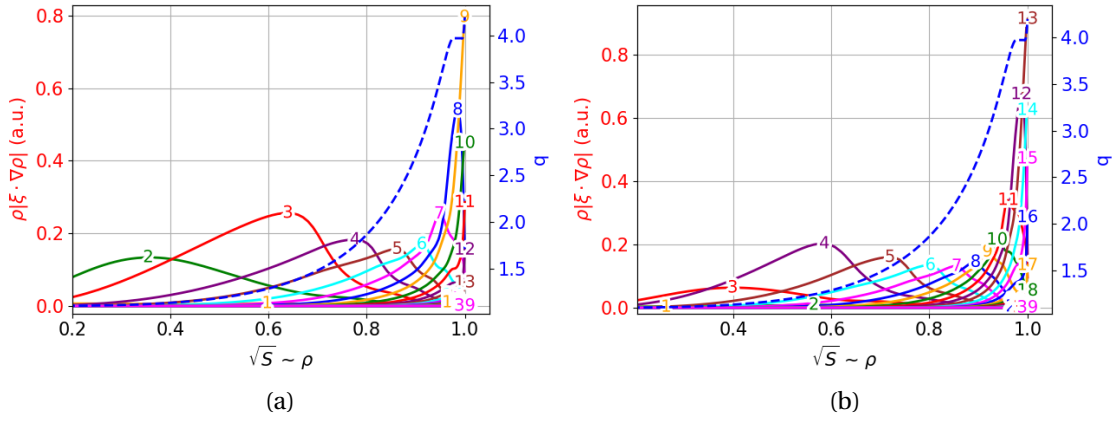


Figure 3.10: Poloidal Fourier components of the radial plasma displacement for the toroidal mode number (a) $n = 2$ and (b) $n = 3$. The safety factor is plotted with dashed lines.

Nonlinearly saturated EHOs

The effort of calculating a free-boundary DEMO equilibria pays off in this section, as now the restriction of using only $n = 0$ modes in the VMEC Fourier expansion is relaxed, allowing for the saturation of 3D external modes. The VMEC 3D free boundary simulation is performed with 500 flux surfaces and a spectrum of $-6 \leq n \leq$ and $0 \leq m \leq 16$ toroidal and poloidal Fourier modes.

A 3D saturated state is found, with the normal plasma displacement amplitude calculated through equation 2.57 peaking at the core and edge, as shown in figure 3.11a. The structure of the mode is quite similar to the $n = 1$ linear plasma displacement in figure 3.8a, even though the nonlinear plasma displacement contains all the toroidal components. This is because the nonlinear plasma displacement in VMEC is dominated by the $n = 1$ component, as shown by the toroidal Fourier decomposition of the displacement shown in figure 3.9b. Recalling that high- n modes dominate the linear phase (figure 3.9a), these modes are non-linearly damped in VMEC. Nonlinear damping of high- n modes has been previously observed numerically in nonlinear simulations [Liu+15; Kle+19; Ram+22; Pan+20] and experimentally in the TCV tokamak [Wen+13]. Finally, Fourier decomposition of the plasma displacement in toroidal and poloidal modes gives the radial spectra of the nonlinear plasma displacement (figure 3.11b shows the $n = 1$ component of the displacement), showing the very same qualitative trails as the linear eigenfunction spectra for $n = 1$. This is a strong indication that the 3D state calculated by VMEC is the non-linear extension of the linear perturbation of the 2D neighbouring equilibrium state described earlier.

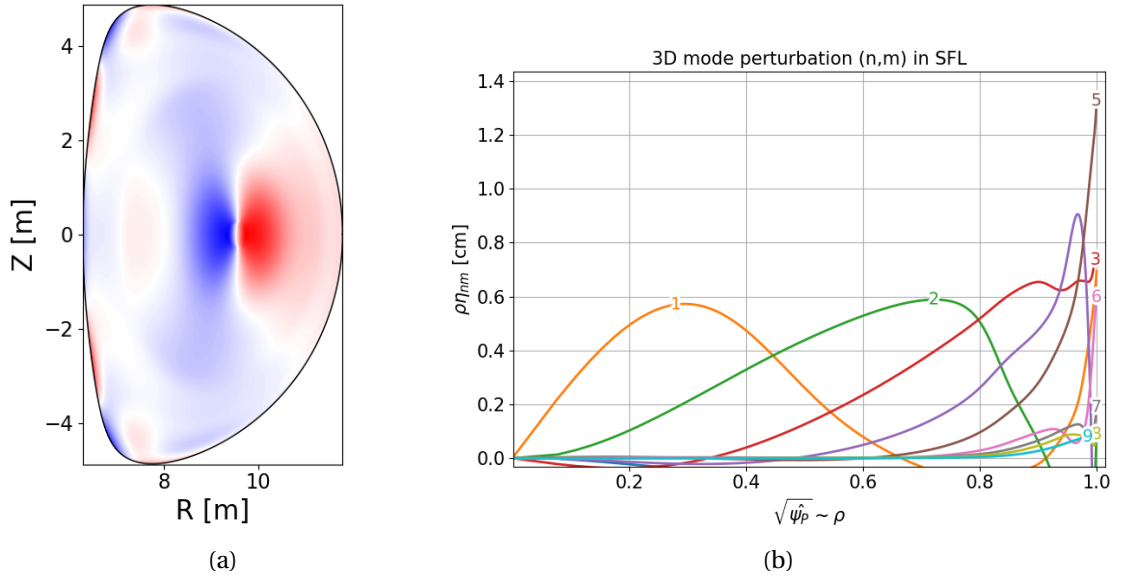


Figure 3.11: Nonlinear plasma displacement for DEMO QH-mode baseline. (a) Plasma displacement in toroidal cross section and (b) Fourier decomposition in SFL poloidal angle. In figure (b) only the toroidal mode number $n = 1$ is plotted, with the numbers in the solid lines corresponding to the poloidal mode number.

The 3D magnetic structure presented in this section was used by the VENUS-LEVIS code

[Pfe+14] to simulate the losses of fast particles due to edge corrugations, then later compared with the losses of its neighbouring axisymmetric state. While this investigation was only a first approximation and more research is needed to assess the full problem, it was observed that the presence of EHOs increases the fast ion first orbit losses by a factor smaller than 0.1 % of the total ion population. In addition, EHOs modify the pattern of the fast particle deposition which might translate in a local increase of the thermal loads on the plasma facing components. For a detailed description of the results, refer to reference [BSG20].

3.3.2 Comparison of the external saturated states in VMEC and JOEREK

The nonlinear 3D equilibrium state calculated by the VMEC code and the saturated state obtained in a JOEREK nonlinear initial value simulation were compared for two types of saturated external instabilities: current-driven external kink and pressure-driven external modes. This section provides a brief summary of the important aspects of the work and the significance of the results. For a detailed description of the results, refer to reference [Ram+22].

Code assumptions and initial conditions

VMEC and JOEREK have a few fundamental differences that can make the comparison of saturated states challenging, even when JOEREK is executed close to the ‘ideal’ limit (vanishing resistivity). As this limit is approached, JOEREK nonlinear simulations require higher numerical resolution and computational power, so it is common practice to set the resistivity such that the Lundquist number is 10-100 times smaller than the experimental values. These differences are more noticeable particularly when analysing external perturbations that corrugate the plasma boundary. The LCFS in VMEC defines the computational domain, which is free to move and calculated self-consistently with the vacuum magnetic field. The boundary conditions at the plasma-vacuum interface are given by the ideal jump conditions of the magnetic field, therefore defining a sharp division between the plasma and the vacuum region. In contrast, the computational boundary in JOEREK is fixed by the imposed Dirichlet boundary conditions on the velocity field, while the magnetic field has the correct jump conditions at the computational boundary⁴. To obtain edge corrugations in JOEREK, an artificially high resistivity is enforced in the region of the computational domain outside of what is defined as the plasma region, where the pressure profile vanishes. The thin layer of sharp increase in the resistivity

⁴For these boundary conditions to be applied, the JOEREK code is coupled to the STARWALL code [Höl+12]

emulates, by damping currents, the vacuum transition that is assumed in the VMEC code. In the simulations presented in [Ram+22], the ratio between core and edge resistivity is $\sim 10^5$. While the fluid boundary conditions in the two codes are remarkably different, in some cases they yield similar interface conditions, as it is shown when comparing the saturated external kink mode case. Note that in the nonlinear phase of JOREK simulations, the relaxation of the profiles and thermal losses modify the resistivity at the interface, which can produce stochatisation of the magnetic field lines at the plasma edge, where the dynamics in which we are interested is most important. It is worth noting that this effect cannot be reproduced in VMEC due to the enforced existence of nested flux surfaces. Nevertheless, the resistive dynamics is expected to occur over a longer time scale than ideal dynamical time scales, making the separation between resistive and ideal effects possible and thus permitting a the comparison between the ideal behaviour of two codes.

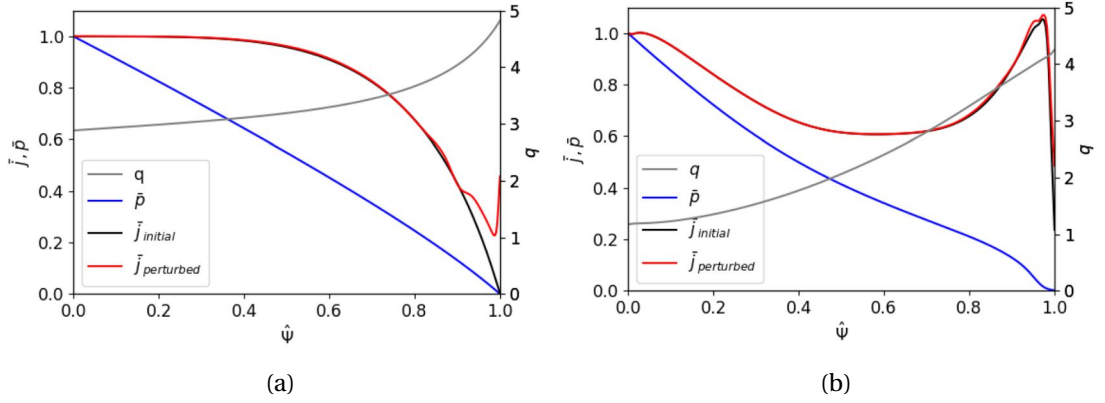


Figure 3.12: Equilibrium profiles used in VMEC free boundary calculation for the (a) external kink and (b) external cases. Obtained from [Ram+22]

In the VMEC equilibrium approach, the input profiles are consistent with the saturated equilibrium state. In a more consistent comparison, the plasma profiles of the final saturated JOREK state would be used as input in the VMEC equilibrium calculation, but the absence of well defined magnetic surfaces due to the ergodisation of the magnetic field lines in the saturated state (especially at the edge) makes it difficult to define the radial plasma profiles. Instead, a neighbouring VMEC axisymmetric equilibrium is used as the initial state in the JOREK simulation, and it is assumed that the nonlinear evolution of the JOREK profiles is weak and will not significantly change the final saturated state. The profiles used in the VMEC and JOREK simulations are plotted in figure 3.12 for the external kink and external cases. For the external

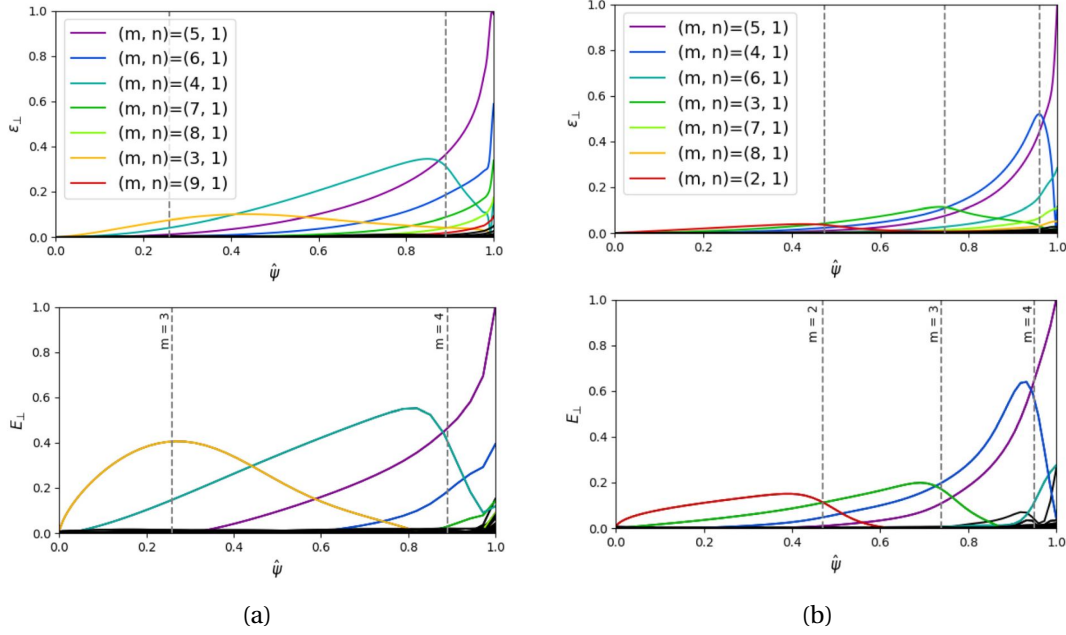


Figure 3.13: Poloidal Fourier spectrum of the $n = 1$ radial linear eigenfunction calculated in the linear phase in JOREK (top) and of the nonlinear normal plasma displacement calculated in VMEC (bottom) for the (a) external kink case and for the (b) external case. Obtained from [Ram+22]

kink case the pressure gradient is constant and the safety factor monotonically increases from the core to the edge, with $q_a \lesssim 5$. For the external case, the profiles contain the qualitative characteristics of a QH-mode discharge discussed earlier in this chapter. As will be shown in chapter 4, either a complete or a partial flattening of the safety factor can lead to the excitation of external modes. A completely flat safety factor is thus avoided to keep the JOREK simulation more empirically realistic. Still, the magnetic shear in the pedestal region for the external case is kept low ($s \sim 1$). The pressure and safety factor are conserved throughout the VMEC energy minimisation process, while the toroidal current is calculated self-consistently for the corresponding equilibrium. The external case exhibits an increased edge current density with respect to typical H-mode discharges due to the large bootstrap current associated with the steep pedestal pressure gradient in the low collisionality regime. This contribution is absent in the external kink case. Two toroidal current profiles calculated in free boundary VMEC are shown in figure 3.12, one corresponding to an axisymmetric calculation (labelled as $\bar{j}_{initial}$) and one where 3D effects were allowed (labelled as $\bar{j}_{perturbed}$). It can be seen that both profiles match closely except at the edge, where the perturbed current density has a peak in external

kink case, but is only weakly modified in the external case. It is pointed out that VMEC does not evolve the plasma state and therefore an ‘initial’ equilibrium has no meaning, so the labelling corresponds to the initial profiles used in the equivalent JOREK initial value simulation.

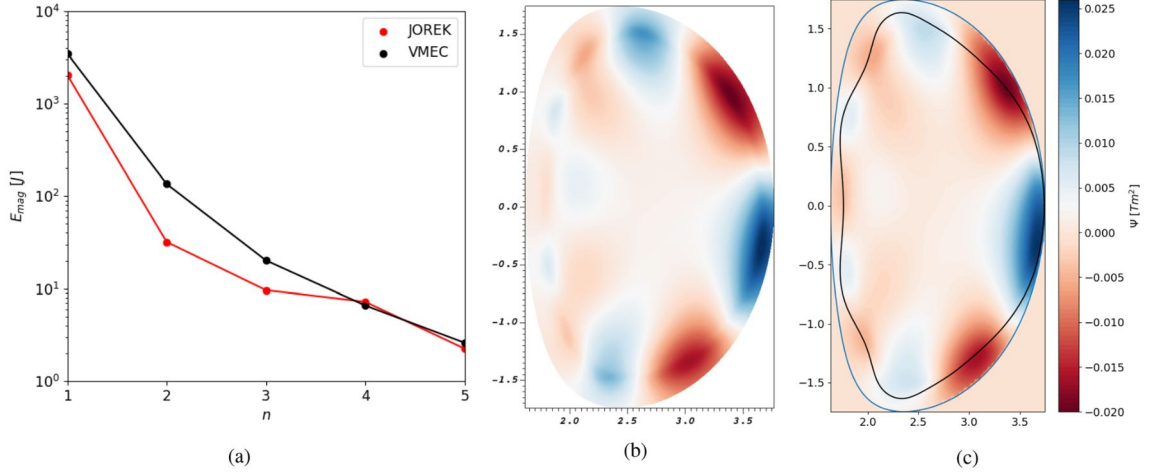


Figure 3.14: (a) Toroidal spectrum of the perturbed magnetic energy in VMEC and JOREK. (b) Perturbed poloidal flux in JOREK at the beginning of the saturated phase. (c) Perturbed poloidal flux in VMEC saturated state. Obtained from [Ram+22].

External kink case

Very good agreement between the saturated states calculated in both codes was found for the external kink case. The nonlinear normal plasma displacement in the VMEC simulation calculated through equation 2.57 exhibits a clear ($m = 5, n = 1$) dominant external kink mode, as shown in figure 3.13a. The qualitative characteristics of the nonlinear poloidal spectrum agree with the JOREK radial eigenfunctions in the linear phase, reproducing the previous results obtained by Kleiner et. al. [Kle+18]. In the nonlinear phase, the JOREK $n = 1$ mode quickly becomes the only dominant component and saturates within ideal time scales, with very weak stochatisation of the magnetic field lines. A comparison of the perturbed poloidal flux and of the toroidal spectrum of the perturbed magnetic field energy (figure 3.14) shows quantitative agreement between the saturated states calculated in both codes. This result indicates that the final saturated state obtained in VMEC does correspond to an equilibrium state that is accessible by the physical nonlinear evolution of the unstable axisymmetric equivalent equilibria, at least for this simple case. Another way to interpret this result is that the JOREK simulation does converge to a physical equilibrium state despite the fact that the

dissipative parameters in the simulation might not correspond to real experimental values. Note that the energy in JOREK is expected to be slightly lower than in VMEC due to the inclusion of resistivity near the edge.

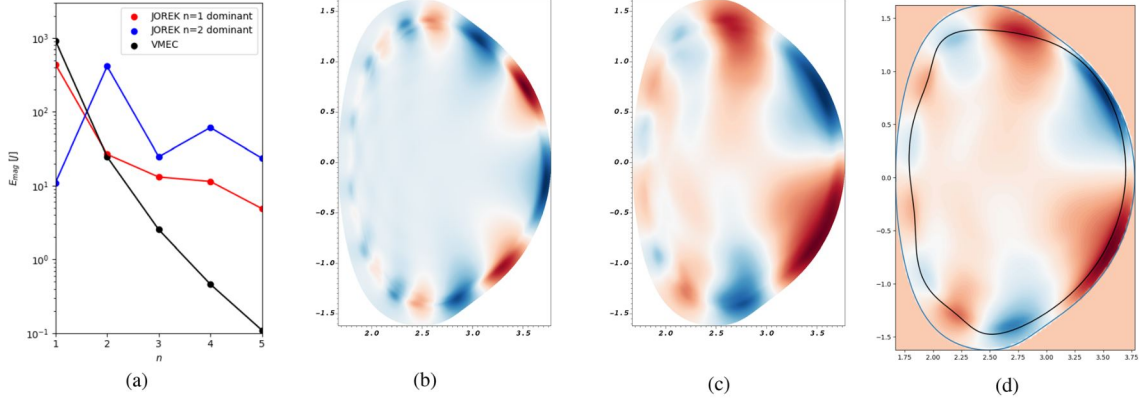


Figure 3.15: (a) Toroidal spectrum of the perturbed magnetic energy in VMEC and in JOREK at different times of the simulation, corresponding to dominant $n = 1$ and $n = 2$. Perturbed poloidal flux at the beginning of the saturated phase when (b) $n = 2$ and (c) $n = 1$ are the dominant modes in JOREK. (d) Perturbed poloidal flux in VMEC saturated state. Obtained from [Ram+22].

Exfernal case

For the saturated exfernal case the agreement between JOREK and VMEC is limited. Figure 3.13b shows that the saturated normal plasma displacement calculated in VMEC through equation 2.57 again agrees with the eigenmode structure of the $n = 1$ mode obtained during the linear phase in JOREK, reproducing the results obtained in reference [Kle+19]. Toroidal mode numbers $n = 2 - 5$ are also linearly unstable due to the exfernal drive, but which mode becomes dominant in the saturation phase is dictated by nonlinear dynamics. Note that in JOREK such dynamics is extremely sensitive to diffusion parameters, such as resistivity, while in VMEC the dynamics is bypassed. Indeed, in [Ram+22] it is shown for the external kink case that an increase of resistivity in the core (Spitzer like) and a softer transition to vacuum leads to an early stochasticisation of the edge magnetic field lines and a higher- n mode (ballooning-like) dominating the nonlinear plasma dynamics.

Early in the nonlinear phase of the JOREK simulation, a $n = 2$ mode saturates and dominates the dynamics, contrary to the dominant $n = 1$ saturated mode observed in the perturbed VMEC

equilibrium solution. Nevertheless, in both saturated equilibria the instability is of exfernal kind, with a (m, n) mode localised in the pedestal and a $(m + 1, n)$ mode perturbing the plasma edge, though considerable stochatisation of the magnetic field lines at the edge is observed even in the early nonlinear saturation phase. Stronger toroidal coupling is seen in the JOREK calculations, as shown by the toroidal spectrum of the perturbed magnetic energy in figure 3.15. It is speculated that the nonlinear energy transfer between the two modes through quadratic coupling stabilises the $n = 1$ mode [Kre+13], allowing the more unstable $n = 2$ to grow and saturate. The $n = 1$ mode grows on the resistive time scale, dominating over the $n = 2$ in its much later saturation phase. However, this state can not be directly compared with VMEC because the dynamics leading to its saturation were dictated by resistive effects, which are not included in VMEC. Still, there is a reasonably good qualitative agreement between the saturated magnetic field structure found in VMEC and the resistive $n = 1$ saturated mode found in JOREK, as shown by the perturbed magnetic flux in figure 3.15. Moreover, Poincaré analysis of the saturated modes in JOREK show that there is considerable stochatisation of the magnetic field lines in the plasma edge, with the stochastic structure roughly following a similar edge perturbation as the one observed in VMEC (figure 13 of [Ram+22]). These nonlinear resistive structures may not necessarily be remotely connected to the saturated exfernal mode observed in VMEC, regardless of the similarities. However, they could point towards the possibility that the ideal exfernal drive still influences the global magnetic structure on resistive time scales. These issues could be resolved by improvements on the initial value models (see limitations of JOREK mentioned above) and/or improved nonlinear analytic theory.

3.4 Prospects for the EHOs parameter space

The link between the linearly unstable exfernal modes and the nonlinearly saturated EHOs observed during QH-mode operation has been discussed in this chapter. One of the contributions of this thesis is the exploration of the parameter space where these type of instabilities can be excited. Up to now, it has been shown that the pressure gradient and the distance to the rational surface in equilibria with vanishing edge magnetic shear define a relatively narrow parameter space for the excitation of exfernal modes. The goal of the following chapter is to study this parameter space in more detail. Since exfernal modes are coupled current and pressure driven instabilities which are localised at the pedestal, it is convenient to define the parameter space with respect a few physical quantities evaluated in the pedestal region. Weak

FLB stabilisation is necessary to provide the infernal drive of external modes, but it does not necessarily require vanishing magnetic shear over the pedestal. Moreover, the critical shear at which external modes can be excited can provide an estimation of the critical current density needed to access QH-mode. Pedestal width is also expected to modify the parameter space since the infernal drive depends on the radial extension of the weak FLB region. Finally, in a realistic diverted plasma, the safety factor diverges as the flux surfaces approach the separatrix. Such divergence has an influence on external kink modes, and therefore on external modes. The parameter space for the excitation of external modes with respect to these three physical quantities (edge magnetic shear, pedestal width and value of q_a , including $q_a \rightarrow \infty$) is studied in Chapter 4.

Robust access to QH-mode in different plasma conditions might need expansion of the parameter space for the excitation and saturation of external modes. The application of non-axisymmetric magnetic perturbations is extensively used for ELM control and avoidance, where the physical mechanism involved is thought to be related to the amplification of the applied field through its interaction with external kink modes [Ora+17]. Therefore, non-axisymmetric magnetic perturbations might influence the parameter space of saturated external modes. This is shown to be the case in Chapter 5.

4 Effect of edge magnetic shear on the excitation mechanism of external modes

This chapter presents an extension of external mode theory, where the effects of edge magnetic shear and plasma separatrix are investigated and applied to Edge Harmonic Oscillations (EHOs). Linear analytical modelling is performed on a large aspect ratio tokamak with circular cross section, from which a set of three coupled differential equations describing the dispersion relation are derived. To correctly assess the effect of edge shear on external modes, higher order corrections need to be retained in the expansion of the safety factor around the rational surface. The equations are solved numerically for equilibrium pressure and safety factor profiles containing the key features for the excitation of external modes, including a model of a plasma separatrix. The current-driven branch of the instability is significantly reduced by the inclusion of the separatrix, but the mode remains unstable through coupling with the pressure-driven internal drive. The obtained parameter space for the instability without the effect of the separatrix is compared with the growth rates calculated using the KINX code, and with the nonlinear plasma displacement calculated using the VMEC free-boundary code. From the comparison it was found that the edge shear can be of order unity and still excite external modes, implying that EHOs can be excited even with weak flattening of the local safety factor at the edge, which is in line with some current experimental observations, but contrary to the previous simpler analytic theory presented in chapter 3. The work presented in this chapter was published in reference [BGB21].

4.1 Introduction

As introduced by the previous chapter, under QH-mode equilibrium conditions low- n external infernal (*exfernal*) modes can grow and saturate. These modes arise from the coupling of external kink and infernal drives, where the latter comes from the combination of low magnetic shear and high pressure gradient over the pedestal region. Linear analytic [Bru+18a; Bru+18b; Bru+19a] and numerical [ZKV13b; Kle+19; Don+17] modelling suggests that EHOs might correspond to the nonlinear saturated state of exfernal modes when a plateau in the safety factor is observed. However, other numerical studies and experimental observations [Gar+15; Cfe+20] have found MHD structures similar to EHOs in cases where the magnetic shear over the pedestal region is of order unity. This means that analytical exfernal mode theory requires the inclusion of finite edge magnetic shear in order to offer a robust explanation for the excitation of EHOs.

The present chapter investigates the effect of finite magnetic shear in the pedestal on the excitation mechanism of low- n exfernal modes. This is done using a semi-analytical approach which extends previous work on exfernal modes [Bru+18a] in a large aspect ratio tokamak, where now the assumption of having vanishing magnetic shear near the edge is relaxed. This is achieved by expressing the safety factor in the pedestal region as $q(r) = q_s(1 + \Delta q(r)/q_s)$, where $q_s = m/n$ with m and n integers and $\Delta q(r)/q_s \ll 1$. An expansion in $\Delta q(r)/q_s$ is performed including terms of order $\mathcal{O}(\Delta q^1/q_s)$ which account for finite magnetic shear contributions. Note that in previous work such terms are not present [Bru+19a; Bru+18b; Bru+18a; GHH96]. Numerical solution of the equations allows us to solve the exfernal problem for more realistic profiles, while using a simplified large aspect ratio model allows us to keep track of the relevant physics in the equations. Both approaches will be performed in this chapter.

Access to the QH-mode regime is often considered to be related to the presence of toroidal rotation and in particular $\mathbf{E} \times \mathbf{B}$ poloidal plasma sheared flow. Experimental evidence [Gar+11] shows that $\mathbf{E} \times \mathbf{B}$ flow shear rather than net toroidal flow is what determines the accessibility to QH-mode, which is somewhat recovered by analytical [Bru+19a] and numerical [Che+17a; Liu+15; Che+16; Xu+17] modelling. The direct impact of toroidal rotation on low- n modes is mainly an empirically measurable Doppler shift of the eigenfrequency, i.e. the introduction of a mode frequency which is proportional to the plasma bulk rotation Ω according to the rule $f \propto n\Omega$, provided Ω is high enough. In such conditions, locked modes that would otherwise

terminate the discharge are avoided [Gar+15]. In the nonlinear regime, saturated external modes calculated in VMEC show that the derivative of the perturbed poloidal magnetic field (which is what is measured in experiments) persist for various toroidal harmonics. When the correct Doppler shift is taken into account ($d\delta B^\theta/dt \propto n\Omega\delta B^\theta$) the associated VMEC spectrogram agrees well with experiments [Kle+19]. Hence, in our study we drop toroidal rotation in the equilibrium, bearing in mind that the eigenvalue should be Doppler shifted post-calculation if one wishes to treat the EHO dynamics in the laboratory frame. Continuum damping, plasma resistivity, the interaction with resistive external structures, and kinetic effects which all may affect the dynamics of a rotating mode are not treated in this work, and so are left for a more refined analysis. The combined effect of ion diamagnetic and $\mathbf{E} \times \mathbf{B}$ poloidal flow shear, which results in net-zero ion poloidal flow, influences the mode structure of the instability by damping high- n modes while allowing low- n modes to grow, with a modest effect on their growth rate. For simplicity, such effects are also neglected in the present work as they have been already treated analytically [Bru+19a] and numerically [Ram+22], so their effect is assumed to be independent from the effect of edge magnetic shear in the excitation mechanism of low- n modes.

Separatrix effects are also modelled in this work by assuming that each resonant surface lies within the plasma by taking $q \rightarrow \infty$ as $r \rightarrow a$. Such divergence in the safety factor in this simplified model of the separatrix has a strong stabilising influence on edge current driven modes (e.g. peeling modes) [WG09; Huy05; HC07]. However, for instabilities driven both by pressure and current (e.g. peeling-ballooning and external modes) the modes remain unstable in the presence of a separatrix [SKK11]: the current-driven branch disappears, while the pressure-driven branch can persist. This is indeed what is observed in the present study, though as $q \rightarrow \infty$ the external mode formally becomes an internal internal mode with no connection to the vacuum region within the approximations of our analytical model.

The chapter is organised as follows: Section § 4.2 describes the equilibrium configuration. Using a large aspect ratio expansion, stability equations for the equilibrium configuration are derived in section § 4.3 by taking projections of the vorticity operator applied to the linearised momentum equation. Three coupled differential equations that describe the linear evolution of a main mode (m, n) and its sidebands $(m \pm 1)$ are obtained. These equations are solved numerically in section § 4.4 and various cases of interest are analysed. Section § 4.5 compares the obtained analytical results with well established codes, first against full 3D nonlinear

simulations in JET-like geometry using the VMEC free boundary code, and later against the KINX linear stability code. In section § 4.6 we introduce and implement a simple model of the plasma separatrix, and the external equations are again solved numerically. Finally, section § 4.7 summarises the work and offers conclusive remarks.

4.2 Analytical expansion of the equilibrium equations

The plasma equilibrium is expanded analytically with respect to small inverse aspect ratio ($a/R_0 \sim \epsilon \ll 1$) assuming shifted circular cross sections, where a and R_0 are the minor and major radii respectively. The analysis is performed on a right-handed coordinate system (r, θ, ϕ) , where r is a flux coordinate with units of length, $\theta(\omega) = \frac{F(r)}{q(r)} \int^\omega \frac{\mathcal{J}_\omega}{R^2} d\omega$ is the straight field line poloidal angle and ϕ the toroidal angle. Here, ω and r define the transformation to cylindrical coordinates

$$\begin{aligned} R(r, \omega) &= R_0 + r \cos(\omega) - \Delta(r) - \mathcal{P}(r) \cos(\omega) \\ Z(r, \omega) &= r \sin(\omega) - \mathcal{P}(r) \sin(\omega), \end{aligned} \tag{4.1}$$

where R_0 is the major radius, $\Delta(r)$ is the Shafranov shift, $\mathcal{P}(r) = \frac{r^3}{8R_0^2} + \frac{r\Delta(r)}{2R_0}$, and \mathcal{J}_ω is the Jacobian in the (r, ω, ϕ) coordinate system. Standard tokamak ordering is assumed (§ 2.3.2): $B_P \sim \epsilon B_T$ and $\beta = 2\mu_0 P / B^2 \sim \epsilon^2$, with $\mathbf{B}_P = \nabla\phi \times \nabla\psi$ the poloidal field, $\mathbf{B}_T = F(\psi)\nabla\phi$ the toroidal field, P the plasma pressure, $F(\psi) = RB_\phi$ and $2\pi\psi$ the poloidal magnetic flux.

Equilibrium profiles are chosen so that they reproduce the key aspects of QH-mode operation [Bur+05] qualitatively. The pressure profile has an edge pedestal close to the vacuum region, where the pressure gradient associated with the pedestal drives a strong bootstrap current in the low collisionality regime. To separate the driving mechanism of pressure gradient and current density we model the safety factor and magnetic shear to monotonically increase from the core, then the magnetic shear gets weaker in the pedestal region as a consequence of the bootstrap current (Figure 4.1). Variations in the edge safety factor (or equivalently the edge current density) can be seen as variations in the edge collisionality at constant pressure gradient, thus avoiding the difficulty of accurately modelling a bootstrap current that is consistent with the pressure profile at constant collisionality. A convenient safety factor

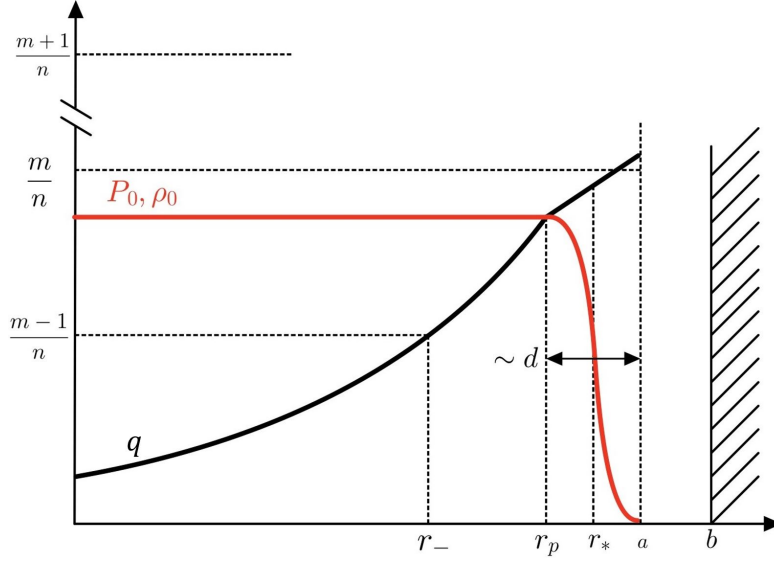


Figure 4.1: Model of the radial profiles of the safety factor, pressure and density. The weakening of the magnetic shear covers the pedestal region going from r_p to a . Note that the model and analysis do not require the resonance m/n to be at r_* .

profile with the required characteristics is:

$$q(r) = \begin{cases} \frac{m-1}{\kappa[1-(r/r_-)^\mu] + n} & \text{if } r \leq r_p \\ q_* [1 - s_*(1 - r/r_*)] & \text{if } r \geq r_p \end{cases} \quad (4.2)$$

where r_- is the radius of the lower sideband resonance, μ is a constant that defines how fast q grows in the core region, r_p roughly denotes the radius of the pedestal shoulder (which we choose to roughly coincide with the region where the shear starts to vanish), κ is a constant that guarantees continuity of the safety factor at r_p , s_* is the magnetic shear at r_* , $r_* = \frac{1}{2}(r_p + a)$ and $q_* = q(r_*)$.

It is worth to mention at this point that within our ordering the stability properties in the region $[0, r_p]$ are mostly determined by current effects rather than pressure or inertial effects. Therefore, for simplicity we are free to consider the pressure (and density) to be roughly constant in that region, then model a large gradient in the pedestal region. A suitable analytical expression is given by:

$$\frac{P(r)}{P_0} = \frac{\rho(r)}{\rho_0} = \frac{1}{2} \left[1 - \tanh \left(\frac{4(r - r_*)}{d} \right) \right] \quad (4.3)$$

with P_0 and ρ_0 the pressure and density at the magnetic axis and d a measure of the pedestal width.

With the pressure profile described above, we may have the ballooning parameter $\alpha = -Rq^2\beta' \sim 1$ in the pedestal region. Nevertheless, the total β can still be of order ϵ^2 if the pedestal region only covers a narrow region of width $\sim d \ll r$, so that $\beta' \sim \beta/d \sim \epsilon$. In such a scenario, the assumption of concentric flux surfaces still holds [Bru+18b; GC81; CHT78], and one can consistently use the low- β expansion of the equilibrium equations. We point out that the profiles described above are consistent with these approximations, and that the low- β equations used in this work yield good results when compared with numerical modelling using QH-mode-like equilibrium profiles [Bru+19a; Bru+18a; Kle+19; Ram+22]. In the limit of high- β or large pressure gradient over a wide section of the tokamak, the model does not hold anymore, and new equilibrium equations have to be derived. This has been done in Ref. [Bru+18b] for external modes, where no major differences in the solutions were found in cases where the pressure gradient is large only on a narrow region.

4.3 Derivation of the stability equations

For the stability analysis we separate the plasma domain into three intervals, delimited by the newly introduced parameters r_1 and r_2 , with $0 \leq r_1 < r_2 \leq a$. We regard the intervals $[0, r_1] \cup [r_2, a]$ as ‘high shear’ regions, where poloidal coupling is neglected due to the Field Line Bending (FLB) stabilisation dominating in the absence of strong pressure gradients. The interval $[r_1, r_2]$ (roughly, but not exactly equal to $[r_p, a]$ in figure 4.1) is regarded as a ‘low shear’ region, where poloidal coupling with neighbouring sidebands is induced through the effect of toroidicity in the geometrical coefficients. The parameters r_1 and r_2 are allowed to vary, but it is pointed out that their values don’t change the equilibrium in any way, and their role is to delimit the regions in which each set of stability equations is to be used. The definition of what can be considered as ‘low shear’ and ‘high shear’ is in general vague, more so because now finite edge magnetic shear is allowed. One way to set r_1 and r_2 is to identify values which

maximise the growth rate, as was done for example in reference [HH88] for infernal modes.

4.3.1 High Shear region

In the high shear region all modes are independent, and the equation describing the radial plasma displacement for any Fourier harmonic with mode numbers (m', n) is given by Newcomb's equation [Fre14; New60], introduced in section § 2.4.2, but repeated here for convenience

$$\frac{1}{r} \frac{d}{dr} \left[r^3 \left(\frac{1}{q} - \frac{n}{m'} \right)^2 \frac{d}{dr} \xi_{(m')}^r \right] - (m'^2 - 1) \left(\frac{1}{q} - \frac{n}{m'} \right)^2 \xi_{(m')}^r = 0. \quad (4.4)$$

This equation also corresponds to the leading order marginal stability equation in a straight cylinder away from the rational surface. The singularity at $q = m'/n$ can be removed by adding finite inertia [Mik17], as in equation 2.56. The present study neglects inertia effects in the high shear region, and the singularity is avoided by imposing the solution to be finite at its own rational surface. Residual inertia effects in the high-shear region were studied in reference [Bru+18b] which concluded that the effect on the growth rate is small close to marginal stability.

4.3.2 Low Shear region

The driving mechanism for external modes lies within this region, where there is combination of a large pressure gradient over an extended region of low magnetic shear close to the plasma edge, and the safety factor is close to a rational surface at $q \sim q_s = m/n$. A main helical mode (n, m) develops in this region, and couples with the corresponding upper and lower sidebands $(n, m \pm 1)$. The analytical treatment follows the standard tokamak ordering described in section § 2.31. Stability equations are derived from the linearised ideal MHD perturbed momentum equation:

$$L(\xi) = \delta F(\xi) + \rho \gamma^2 \xi = 0, \quad (4.5)$$

where $\boldsymbol{\xi}(t, r, \theta, \phi) = \boldsymbol{\xi}(r, \theta, \phi)e^{i\gamma t}$ is the Lagrangian fluid displacement and ρ is the mass fluid density. The force operator $\delta\mathbf{F}(\boldsymbol{\xi})$ is given in its covariant form by [Fre14]:

$$\delta\mathbf{F}_i = \delta B^k \partial_k B_i + B^k \partial_k \delta B_i - \Gamma_{ik}^j \left(\delta B^k B_j + B^k \delta B_j \right) - \partial_i \left(\delta B^k B_k \right) + \partial_i \left(\xi^k \partial_k P + \frac{\Gamma P}{\mathcal{J}} \partial_k (\mathcal{J} \xi^k) \right), \quad (4.6)$$

where Γ_{ik}^j are the Christoffel symbols of second kind. The first five terms correspond to the expansion of the terms $\mathbf{J} \times \delta\mathbf{B} + \delta\mathbf{J} \times \mathbf{B}$, with $\delta\mathbf{J} = \nabla \times \delta\mathbf{B}$ the perturbed current and $\delta\mathbf{B} = \nabla \times (\boldsymbol{\xi} \times \mathbf{B})$ is the perturbed magnetic field (we have normalised $\mu_0 = 1$). The last two terms correspond to the gradient of the perturbed pressure $\nabla \delta P$.

Following Bussac [Bus+75] we separate the fluid displacement as $\boldsymbol{\xi}(r, \theta, \phi) = \boldsymbol{\xi}_{\mathbf{B}} + \boldsymbol{\zeta}_{\mathbf{B}}$, where $\boldsymbol{\xi}_{\mathbf{B}} \cdot \nabla \phi = 0$, $\xi_{(r)} = F \boldsymbol{\xi}_{\mathbf{B}} \cdot \nabla r$ and $\xi_{(\theta)} = r F \boldsymbol{\xi}_{\mathbf{B}} \cdot \nabla \theta$. Different toroidal harmonics denoted by the toroidal mode number n are decoupled because of toroidal symmetry in the equilibrium, so we can write $\boldsymbol{\xi}(r, \theta, \phi) = \boldsymbol{\xi}(r, \theta) e^{in\phi}$. For simplicity we remove the ϕ dependency in our equations by substituting $\partial_\phi \rightarrow in$. We expand the Bussac variables in our large aspect ratio parameter ϵ and Fourier expand in the poloidal direction as

$$\xi_{(r)}(r, \theta) = \left[\xi_{r0}^{(m)}(r) + \epsilon \left(\xi_{r1}^{(m+1)}(r) e^{-i\theta} + \xi_{r1}^{(m-1)}(r) e^{i\theta} \right) \right] e^{-im\theta} \quad (4.7)$$

$$\xi_{(\theta)}(r, \theta) = \left[\xi_{\theta 0}^{(m)}(r) + \epsilon \left(\xi_{\theta 1}^{(m+1)}(r) e^{-i\theta} + \xi_{\theta 1}^{(m-1)}(r) e^{i\theta} \right) + \epsilon^2 \xi_{\theta 2}^{(m)}(r) \right] e^{-im\theta} \quad (4.8)$$

$$\zeta(r, \theta) = \zeta_0^{(m)}(r) + \left(\zeta^{(m+1)}(r) e^{-i\theta} + \zeta^{(m-1)}(r) e^{i\theta} \right) e^{-im\theta}. \quad (4.9)$$

The Fourier decomposition considers a dominant harmonic component with poloidal mode number m , and its two sidebands $m \pm 1$ which are formally one order smaller. The higher order $\mathcal{O}(\epsilon^2)$ helical component of the poloidal displacement contains corrections to the lower order $\mathcal{O}(\epsilon^0)$ radial displacement $\xi_{(r)}$. The parallel plasma displacement also considers a main harmonic perturbation and its two smaller sidebands, though the main harmonic vanishes to leading order. It can be shown that this expansion completely describes the perturbation to relevant order [GHH96]. For full expansion including order $\mathcal{O}(\epsilon^3)$ terms, see [GCW22].

4.3 Derivation of the stability equations

Expressions relating $\xi_{(\theta)}$ and $\xi_{(r)}$ are found by taking the appropriate Fourier components of equation 4.5 at each order, resulting in [Gra+19]

$$\begin{aligned}\mathcal{O}(\epsilon^0) &\rightarrow \xi_{\theta 0}^{(m)} = -\frac{i}{m} \frac{d}{dr} \left(r \xi_{r0}^{(m)} \right) \\ \mathcal{O}(\epsilon^1) &\rightarrow \xi_{\theta 1}^{(m \pm 1)} = -\frac{i}{m \pm 1} \frac{d}{dr} \left(r \xi_{r1}^{(m \pm 1)} \right) \\ \mathcal{O}(\epsilon^2) &\rightarrow \xi_{\theta 2}^{(m)} = \frac{i r^2}{m R_0^2} \left[\frac{n^2}{m^2} \frac{d}{dr} \left(r \xi_{r0}^{(m)} \right) + \frac{R_0 \alpha}{2r} \xi_{r0}^{(m)} + \frac{\xi_{r0}^{(m)}}{q} \left(\frac{n}{m} - \frac{2}{q} \right) + \frac{r}{q^2} \left(\xi_{r0}^{(m)} q' - q \frac{n}{m} \xi_{r0}^{(m)} \right) \right]\end{aligned}\tag{4.10}$$

where we have made use of the ballooning parameter $\alpha = -\frac{2q_s^2 R_0 P'}{B_0^2}$, with B_0 the magnetic field at the magnetic axis. The relation between ζ and $\xi_{(r)}$ is found by projecting the momentum equation in the equilibrium magnetic field ($\mathbf{L}(\boldsymbol{\xi}) \cdot \mathbf{B} = 0$), then taking Fourier components of the resulting equations order by order. We adopt the following ordering for the growth rate:

$$\frac{r^2}{R_0^2} \left(\frac{\gamma}{\omega_A} \right)^2 \sim \epsilon^4, \quad \left(\frac{\omega_s}{\omega_A} \right)^2 \sim \epsilon^2, \quad \frac{\gamma^2}{\omega_s^2} \ll 1,\tag{4.11}$$

where $\omega_A^2 = \frac{B_0^2}{\rho R_0^2}$ is the Alfvén frequency and $\omega_s = \frac{5P}{3\rho R_0^2}$ is the sound frequency. The leading order contribution to $\zeta(r, \theta)$ is (it is found that the lowest order $\zeta_0^{(m)} = 0$):

$$\zeta^{m \pm 1}(r) = \pm i \frac{q \omega_s^2 (m - nq \pm 1) \left((1 \mp m) \xi_{r0}^{(m)} + r (\xi_{r0}^{(m)})' \right)}{B_0^2 m R_0 (\omega_s^2 (m - nq \pm 1)^2 - \gamma^2 q^2)}.\tag{4.12}$$

Now that the poloidal and parallel components of the plasma displacement have been written as functions of the radial component, the eigenvalue equations for the radial components of the main mode and sidebands in the low shear region are derived by Fourier analysing the toroidal component of the vorticity equation $\mathcal{J} \nabla \times \frac{\mathbf{L}(\boldsymbol{\xi})}{B^\phi}$ [Bru+19a; Mik17], with \mathcal{J} the Jacobian in our straight field line coordinate system. This can be written in terms of the covariant components of the momentum equation as:

$$V^\phi(\xi, p) = \frac{1}{2\pi} \int_0^{2\pi} d\theta \left[\partial_r \left(\frac{L_\phi}{B^\phi} \right) + ip \frac{L_r}{B^\phi} \right] e^{ip\theta}. \quad (4.13)$$

Equations are found order by order for the main mode and sidebands via $V^\phi(r, m)$ and $V^\phi(r, m \pm 1)$ respectively. At order $\mathcal{O}(\epsilon^2)$ we recover the cylindrical equation 4.4, which describe the main mode of the plasma displacement to relevant order as long as $q - q_s \sim 1$.

The equations at $\mathcal{O}(\epsilon^4)$ include toroidal coupling and pressure. The full $\mathcal{O}(\epsilon^4)$ equations, derived from equation 4.13, are reported in Appendix B.3. Nevertheless, according to our ordering such effects are only relevant in the vicinity of a rational surface. To formally apply this condition, we write the safety factor as $q(r) = q_s + \Delta q(r)$, where $q_s = m/n$ and $\Delta q/q_s \ll 1$. This allows us to introduce a second ordering in $\Delta q/q_s$. We adopt the ordering notation $\mathcal{O}(\epsilon, \Delta q/q_s)$ to make the distinction between small terms due to the tokamak ordering in large aspect ratio (ϵ) and the small terms due to proximity to the rational surface ($\Delta q/q_s$). The resulting equation for the main mode to order $\mathcal{O}(\epsilon^4, \Delta q/q_s)$ is then: (see also the ideal limit of Ref. [GCW22])

$$\begin{aligned} V_4^\phi(\xi_B, m) = & \frac{1}{r} \frac{d}{dr} \left[r^3 \left(\frac{1}{q} - \frac{1}{q_s} \right)^2 \frac{d}{dr} \xi_{r0}^{(m)} \right] - (m^2 - 1) \left(\frac{1}{q} - \frac{1}{q_s} \right)^2 \xi_{r0}^{(m)} \\ & + \frac{\alpha}{q_s^2} \left[\frac{r}{R_0} \left(\frac{1}{q_s^2} - 1 \right) - \frac{\alpha}{2} \right] \xi_{r0}^{(m)} + \frac{\alpha}{2q_s^2} \left[\frac{r^{-(1+m)}}{1+m} \frac{d}{dr} (r^{2+m} \xi_{r1}^{(m+1)}) + \frac{r^{-(1-m)}}{1-m} \frac{d}{dr} (r^{2-m} \xi_{r1}^{(m-1)}) \right] \\ & - \frac{\Delta q}{q_s^3} \left\{ \Delta' r \frac{d}{dr} \left[\frac{r^{-(1+m)}}{1+m} \frac{d}{dr} (r^{2+m} \xi_{r1}^{(m+1)}) + \frac{r^{-(1-m)}}{1-m} \frac{d}{dr} (r^{2-m} \xi_{r1}^{(m-1)}) \right] \right. \\ & + \left[2(1+m) \frac{r}{R_0} + (1+m)\alpha - (4+3m)\Delta' \right] \frac{r^{-(1+m)}}{1+m} \frac{d}{dr} (r^{2+m} \xi_{r1}^{(m+1)}) - \left(\frac{r}{R_0} + \alpha - 4\Delta' \right) (2+m) \xi_{r1}^{(m+1)} \\ & + \left. \left[2(1-m) \frac{r}{R_0} + (1-m)\alpha - (4-3m)\Delta' \right] \frac{r^{-(1-m)}}{1-m} \frac{d}{dr} (r^{2-m} \xi_{r1}^{(m-1)}) - \left(\frac{r}{R_0} + \alpha - 4\Delta' \right) (2-m) \xi_{r1}^{(m-1)} \right\} \\ & + \left\{ \frac{\Delta q}{q_s^3} \left[\frac{4r^2}{R_0^2} \left(2 - \frac{1}{q_s^2} \right) + \frac{3r}{R_0} \alpha - \Delta' \left(\frac{6r}{R_0} + 7\alpha - r\alpha' \right) + 12(\Delta')^2 \right] - \frac{\Delta q'}{q_s^3} \alpha r \Delta' \right\} \xi_{r0}^{(m)}, \end{aligned} \quad (4.14)$$

where the safety factor dependency on the ballooning parameter has also being expanded,

4.3 Derivation of the stability equations

leading to the redefinition $\alpha \rightarrow -\frac{2q_s^2 R_0 P'}{B_0^2}$. The notation $V_4^\phi(\xi_B, m)$ specifies that we have taken into account only terms coming from the perpendicular plasma displacement. Inertia and compression terms, which are related to the parallel displacement ζ , are considered in the analysis below. Here we have included the order $\mathcal{O}(\epsilon^2)$ terms (first line), which enter this equation when $q - q_s \ll 1$ (equivalently, when $q - q_s \sim \epsilon$). Therefore, these cylindrical terms are expected to dominate the behaviour of the main mode when $q - q_s \sim 1$. The terms in the second line correspond to the Mercier contribution and the sideband coupling to order $\mathcal{O}(\epsilon^4, \Delta q^0/q_s)$. Order $\mathcal{O}(\epsilon^4, \Delta q/q_s)$ corrections to the main mode component of the plasma displacement appear in the last line of equation 4.14. The remaining terms couple the main mode with the sidebands at order $\mathcal{O}(\epsilon^4, \Delta q/q_s)$, and can be linked directly to toroidicity (through the r/R_0 parameter), to plasma pressure gradient (through the α parameter) and to magnetic pressure gradient (through the Shafranov shift Δ').

We proceed with the calculation of the sideband equations in the low-shear region (see also the ideal limit of Ref. [GCW22])

$$\begin{aligned}
 V_4^\phi(\xi_B, m \pm 1) = & \frac{d}{dr} \left[r^{-(1 \pm 2m)} \frac{d}{dr} \left(r^{2 \pm m} \xi_{r1}^{(m \pm 1)} \right) \right] \\
 & - 2(1 \pm m) \left\{ \frac{d}{dr} \left[\frac{\Delta q}{q_s} r^{-(1 \pm 2m)} \frac{d}{dr} \left(r^{2 \pm m} \xi_{r1}^{(m \pm 1)} \right) \right] - (2 \pm m) r^{\mp m} \xi_{r1}^{(m \pm 1)} \frac{\Delta q'}{q_s} \right\} \\
 & - \frac{1 \pm m}{2} \frac{d}{dr} (r^{\mp m} \alpha \xi_{r0}^{(m)}) + (1 \pm m)^2 (2 \pm m) r^{-(1 \pm m)} \left(\frac{r}{R_0} + \alpha - 4\Delta' \right) \frac{\Delta q}{q_s} \xi_{r0}^{(m)} \\
 & - (1 \pm m) \frac{d}{dr} \left\{ r^{\mp m} \Delta' r \frac{d}{dr} \left(\frac{\Delta q}{q_s} \xi_{r0}^{(m)} \right) - r^{\mp m} \left[(1 \pm 2m) \frac{r}{R_0} \pm m\alpha - 3(1 \pm m)\Delta' \right] \frac{\Delta q}{q_s} \xi_{r0}^{(m)} \right\}.
 \end{aligned} \tag{4.15}$$

We note that the terms proportional to $\xi_{r1}^{(m \pm 1)}$ and derivatives correspond to the expansion in the safety factor of the cylindrical equation 4.4, keeping corrections up to order $\mathcal{O}(\Delta q^1/q_s)$. As such, they contain the FLB stabilisation contribution of the sidebands. Contrary to the main mode equation, all of the terms are formally order $\mathcal{O}(\epsilon^4)$, meaning that the cylindrical contribution does not dominate the equation even when pushing Δq to larger values. Moreover, because of this the equation gradually loses its validity in the high shear region, or in other words, r_1 must remain relatively close to r_p .

To finalise the derivation of the equations we consider the inertial and compression terms at order $\mathcal{O}(\epsilon^4)$. Inertial effects are only important in the near vicinity of the rational surface, where $\Delta q \ll 1$. Therefore, higher order Δq corrections could in principle be neglected, but for the present work such corrections are included for completeness. Using the expansion of the safety factor and retaining terms up to order $\mathcal{O}(\epsilon^4, \Delta q/q_s)$ gives

$$V_4^\phi(\gamma^2(\zeta + \xi_B), m) = \frac{\gamma^2}{m^2} \left\{ (1 + 2q_s^2) \left[\frac{1}{r} \frac{d}{dr} \left(\frac{r^3}{\omega_A^2} \frac{d}{dr} \xi_{r0}^{(m)} \right) + \xi_{r0}^{(m)} \left(\frac{1 - m^2}{\omega_A^2} + r \frac{d}{dr} \frac{1}{\omega_A^2} \right) \right] \right. \\ \left. + 4q_s \left[\frac{1}{r} \frac{d}{dr} \left(\frac{\Delta q r^3}{\omega_A^2} \frac{d}{dr} \xi_{r0}^{(m)} \right) + \xi_{r0}^{(m)} (1 - m^2) \frac{d}{dr} \left(\frac{r \Delta q}{\omega_A^2} \right) \right] \right\}. \quad (4.16)$$

These terms should be added to the resulting vorticity equation in the low shear region (equation 4.14) giving an eigenvalue problem for γ^2 :

$$V_4^\phi(\xi_B, m) + V_4^\phi(\gamma^2(\zeta + \xi_B), m) = 0 \\ V_4^\phi(\xi_B, m \pm 1) = 0 \quad (4.17)$$

where we note that since these equations are to be used in a region close to the main mode rational surface, the inertia of the sidebands can be neglected. Equation 4.17 can be reduced to a single equation in terms of $\xi_{r0}^{(m)}$ by substituting the sideband equations into the main mode equation, as exemplified in appendix B.2. It is finally emphasised that by neglecting $\mathcal{O}(\epsilon^4, \Delta q/q_s)$ terms (which for the remaining of this chapter are referred to as ‘ Δq corrections’), the equations derived in previous papers [Bru+18a; GHH96] are recovered. The higher order terms associated with $\xi \sim \mathcal{O}(\epsilon^3)$ were formally found to exactly vanish [GCW22].

4.3.3 Boundary conditions

Equations 4.17 can be solved given appropriate boundary conditions. To obtain the eigenvalues (growth rates) and eigenfunctions in the low shear region it is sufficient to know the logarithmic derivative $\mathcal{B}(r) = r \frac{d}{dr} \ln \left[\xi_r^{(m')} \right]$ at the boundaries between the high shear and low shear regions ($r = r_1, r_2$), as well as at the plasma-vacuum interface ($r = a$). The logarithmic

derivatives are cast as Robin boundary conditions for equations 4.17

$$r \frac{d}{dr} \xi_r^{(m')}(r) - \mathcal{B}(r) \xi_r^{(m')}(r) = 0. \quad (4.18)$$

Sidebands

The logarithmic derivative of the upper sideband at the boundary between the high shear and low shear regions can be obtained by solving equation 4.4 with $m' = m + 1$ from $[0, r_1]$ assuming that the perturbation at the magnetic axis does not diverge. The rational surface of the lower sideband lies in the high shear region, meaning that equation 4.4 with $m' = m - 1$ is singular at the rational surface. To avoid the singularity, the equation for the lower sideband is solved in the open interval $(r_-, r_1]$, where we recall that r_- is the radius of the rational surface. For the profile defined in equation 4.2 analytical solutions exist and are given in terms of hypergeometric functions [Bru+18b; Mik17], from which the logarithmic derivative can be directly calculated. If $r_1 > r_p$ the logarithmic derivative needs to be calculated numerically by solving equation 4.4 with the Dirichlet boundary condition for the upper sideband $(\xi_{r1}^{(m+1)}(\delta) = \delta^m = \text{constant}, \text{ with } \delta \ll 1)$ and Neumann boundary condition for the lower sideband $\left(\frac{d}{dr} \xi_{r1}^{(m-1)} \Big|_{r_-} = 0 \right)$. This procedure leaves a degree of freedom in the solution, which is removed when taking the logarithmic derivative.

Main mode

We consider the main mode perturbation localised in the low shear region, which requires $\xi_{r0}^{(m)}(r_1) \approx 0$. This follows from multiplying equation 4.4 with $m' = m$ by $\xi_{r0}^{(m)}$ and integrating from 0 to r_1 [Bru+18a; Bru+18b; GHH96]. This boundary condition at r_1 forces the main mode to be localised to the low shear region. This is a valid approximation since shear is known to localise the mode, and as will be seen later in the results section, even when $q(r_1)$ is well below the rational surface the main mode remains localised in the pedestal region.

Vacuum boundary conditions

The plasma is separated from an ideal metal wall by a vacuum region. The logarithmic derivative at the plasma-vacuum interface is given by [Wes78; Fre14; Bru+18b] (see also section § 2.4.3)

$$\left. \frac{r}{\xi_r^{(m')}} \frac{d\xi_r^{(m')}}{dr} \right|_a = \frac{2m'}{m' - nq_a} - \frac{m' + 1 + (m' - 1)(a/b)^{2m'}}{1 - (a/b)^{2m'}}, \quad (4.19)$$

where a is the minor radius of the plasma and b the radius of the ideal wall (see figure 4.1). This equation can be cast as a Robin boundary condition for the sidebands $m' = m \pm 1$. While this equation applies as well to the main mode perturbation $m' = m$, we will usually have $q_a \sim m/n$, which can make the logarithmic derivative arbitrarily large, and so we can approximate $\xi_{r0}^{(m)}(a) = 0$. This boundary condition can equivalently be derived by extending the definition of the plasma perturbation into the vacuum region ($\delta \mathbf{B}_V = \nabla \times (\boldsymbol{\xi} \times \mathbf{B})$) and noticing that it can be written in a similar form as equation 4.4 [Bru+18a; Bru+18b]. One can then follow the same procedure as at the boundary between the high shear and low shear regions, namely multiplying by ξ_{r0}^m and integrating from a to b .

4.4 Numerical solutions

In this section equations 4.17 are solved numerically. The differential operators are written in weak form, then discretised using a linear finite element scheme. The resulting matrix equations correspond to a generalised eigenvalue problem, which is solved using the Implicitly Restarted Arnoldi method built in the ARPACK [Leh+97] software package.

To empirically determine the relevance of the corrections in the safety factor, we compare three models

- *Original Exfernal model*, developed in previous work [Bru+19a; Bru+18a; Bru+18b].
- *Corrected Exfernal model*, presented in this work (equations 4.14-4.17).
- *Reference model*.

The relation between the 3 models is as follows. The *Reference* model is derived in the large aspect ratio approximation, obtaining equations up to order $\mathcal{O}(\epsilon^4)$. Note that no assumption on the shape of the safety factor is made for the *Reference* model, and thus is valid in the whole plasma domain. The full equations for the *Reference* model are reported appendix B.3. This model is the most complete of all, and provides a benchmark of the safety factor expansion done for the other two models. The *Corrected Exfernal* model assumes relatively low shear close to the rational surface. It is obtained by expanding the *Reference* model equations in the small variable $\Delta q(r)/q_s$ up to order $\mathcal{O}(\epsilon^4, \Delta q(r)^1/q_s)$ (see section 4.3). Finally, the *Original Exfernal* model is obtained by neglecting order $\mathcal{O}(\epsilon^4, \Delta q(r)^1/q_s)$ terms in equations 4.14-4.17.

The equations in all the models are solved in the interval $[r_1, r_2]$, where r_1 and r_2 can be varied in order to maximise the growth rate [GHH96], and we remind the reader that r_1 and r_2 only define the region where the high- and low-shear equations are solved, and therefore do not modify the equilibrium. It is consistently found that the three models maximise the growth rate at $r_2 = a$ independently of the shear. Growth rates with respect to variations in r_1 are shown in figure 4.2. Two main things happen when moving r_1 towards zero: (1) the region where the effect of mode coupling is allowed increases (destabilising) and (2) the average magnetic shear in the region where such effects are allowed is also increased (stabilising). The stability of the mode upon variations of r_1 is a competition between these two effects. Note that the stabilisation effect will be weaker if the necessary FLB effects are not included in the equations.

In the limit of zero shear it is found that the Original Exfernal model (red curve) quickly gives unphysical growth rates if $r_1 < r_p$, which is expected since the equations are only valid in the region where q is constant and close to a rational surface. Moreover, as shear is increased (Figure 4.2b) the Original Exfernal model diverges even at $r_1 \geq r_p$. The Corrected Exfernal model (blue curve) remains close to the Reference model at small variations of r_1 even at modest shear, but as r_1 shifts to the left it slowly diverges from the Reference model (purple curve). In the Reference model the growth rate increases with r_1 moving towards zero, then saturates at around a normalised radius of $r/a \sim 0.4 - 0.6$. Remembering that in the interval $[0, r_1]$ the modes are taken to be independent and obey equation 4.4, saturation means that coupling and order $\mathcal{O}(\epsilon^4)$ effects can effectively be neglected in that interval.

Note that the Reference model is valid in the whole plasma, which means that the most accurate prediction of the growth rate must be obtained by setting $r_1 = 0$. This coincides with

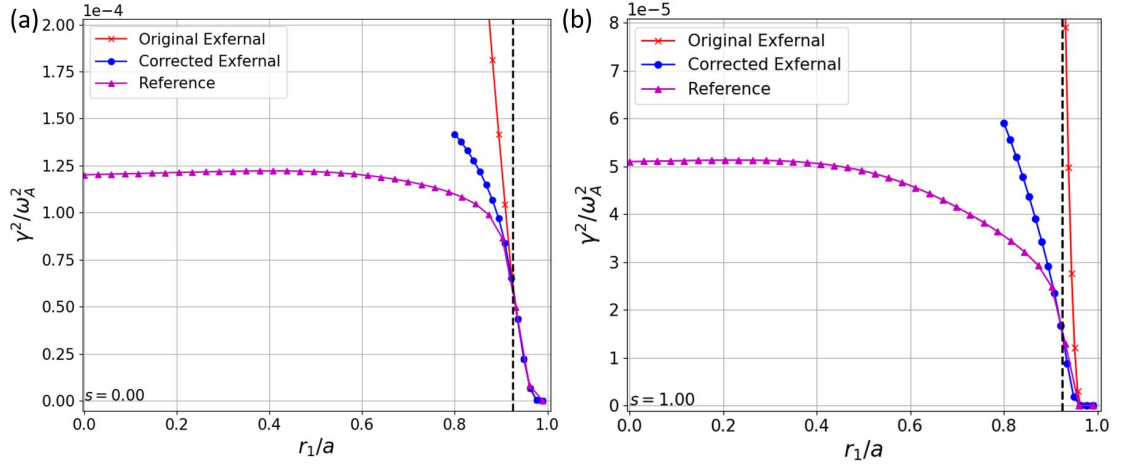


Figure 4.2: Growth rate as a function of the parameter r_1 at (a) $s = 0$ and (b) $s = 1$. The vertical dashed line indicates the value of r_p . The calculations adopt $\alpha = 3$, $m = 4$, $n = 1$, $q_* = 3.99$, $r_2 = a = 1$, $b = 1.3$, $a/R_0 = 1/10$, $d = 0.075$ and $r_p = a - d$. Black vertical dashed line indicates the value of r_p .

the maximisation of the growth rate, as decreasing r_1 increases the region over which coupling can occur, and coupling between the modes is destabilising. Nevertheless, to be consistent when comparing the different models we set $r_1 = r_p$ and $r_2 = a$, which corresponds to the pedestal region interval.

4.4.1 A comparative test: zero shear cases

Firstly, we study the impact of Δq corrections in the limit of zero shear by performing a parameter scan on the value of the safety factor plateau (q_*). As shown in figure 4.3 (a) instability is found for positive and negative Δq close to the rational surface, as previously demonstrated by numerous analytical and numerical studies [Bru+18b; Bru+18a; Bru+19a; Kle+19; Don+17; WG07]. Δq corrections at zero shear have only a weak impact in the growth rate, especially where the upper sideband external kink drive is weak, for $q_* < q_s$ where the main harmonic is non-resonant. For $q_* > q_s$ the upper sideband external kink drive is stronger, enhanced through toroidal coupling with the main mode infernal drive (whose resonance is inside the plasma), as reflected by the slight asymmetry in the growth rate parameter space towards positive Δq [Kle+18; ZKV13b]. This behaviour is confirmed through analysis of the plasma displacement radial profiles in figures 4.3 (c) and (d). For $\Delta q < 0$ the main mode is clearly dominant over the pedestal region. The opposite is true for $\Delta q > 0$, where the upper

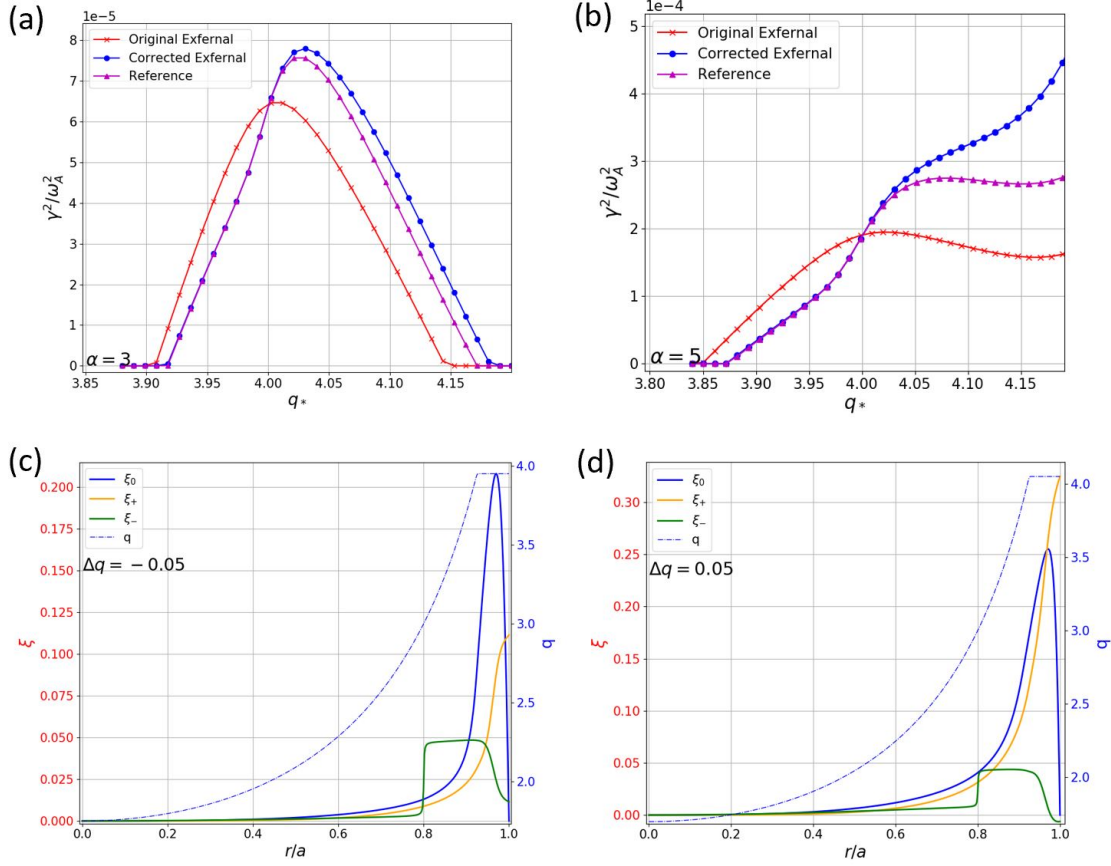


Figure 4.3: Growth rates as a function of q_* for (a) $\alpha = 3$ and (b) $\alpha = 5$. Radial component of the plasma displacement of the main mode (ξ_0) and sidebands (ξ_{\pm}) at (c) non-resonant case with $\Delta q = -0.05$ and (d) resonant case with $\Delta q = 0.05$. For illustration purposes we have set $r_1 = 0$ and used the *Reference* model in figures (c) and (d). Note that the main mode displacement remains localised within the pedestal region. The calculations adopt $m = 4$, $n = 1$, $b = 1.3$, $a/R_0 = 1/10$, pedestal width $d = 0.075$ and $r_p = a - d$.

sideband is as large as ξ_0 . In the latter case, the main mode becomes broader and expands into the high shear region through its interaction with the upper sideband. For high enough Δq the FLB contribution of the main mode eliminates the instability completely.

We now increase the infernal drive by increasing the pressure gradient in the pedestal (figure 4.3b). The coupling is now strong enough to maintain the instability even for reasonably high values of Δq . When finally Δq is sufficiently high to stabilise the infernal drive, the external kink drive dominates and maintains the instability through coupling with the main mode. It should be pointed out that even when $\Delta q > 0$ the instability exists due to the coupling with

the infernal drive, noting that an independent $(m + 1)/n$ external kink mode would be stable for the parameters used in these calculations. We finalise this discussion by reaffirming that Δq corrections have a weak effect in the exfernal modes at very low shear, which indicates that the Original Exfernal model provides a precise description of the instability where there is an extended region of very low magnetic shear.

4.4.2 The role of magnetic shear

We continue our analysis by performing a parameter scan in the magnetic shear. For this scan, stability is determined by a competition between the stabilising effect of shear and the destabilising effects of infernal and kink drives, where the kink drive is strongly influenced by the value of q_a . The computed growth rates are reported in figure 4.4 (a). The Original Exfernal mode fails to correctly assess the effect of edge shear due to a simplification of FLB stabilisation physics in the sideband equations. Moreover, the value of q_a (and so the external kink instability drive) increases with shear, which for the Original Exfernal model results in the mode not being stabilised by the FLB contribution of the main mode. A comparison with the results obtained using a flat safety factor confirms that the FLB stabilisation of the main mode is stronger when displacing a low-shear q-profile from the rational surface than when increasing magnetic shear.

Figure 4.4 (a) shows that the Corrected Exfernal model gives an excellent match to the Reference model, and thus recovers the role of magnetic shear on exfernal modes. We expect the FLB contribution of the sideband to have an important role on the stabilisation of the external kink drive. To investigate further, we neglect all Δq corrections in the equations that are not related with the effect of FLB stabilisation in the sidebands. This can be somewhat justified by noting that all but one of the safety factor corrections in the main mode equation 4.14 are proportional to Δq and not shear ($s \sim r \Delta q' / q_s$). For $q_* \sim q_s$ our model of the safety factor maintains a constant average $\Delta q \sim 0$ over the pedestal region upon variations of the magnetic shear, suggesting that terms proportional to Δq in the main mode equation 4.14 can be neglected. The resulting growth rates reproduce the main characteristic of the Reference model (green line in figure 4.4 (a), labelled as '+FLB'), showing that FLB corrections in the sidebands are indeed what stabilises the external kink drive, and therefore the exfernal model.

Even though the average Δq is constant over the pedestal region upon variations in the shear,

the Corrected Exernal model includes the effect of the local variation of Δq in the coupling terms. The resulting imbalance is destabilising, shifting the peak of the growth rates to $s \sim 0.2$. The effect is quickly overtaken by magnetic shear in the FLB contributions, which stabilises the mode at a limiting value of $s \sim 1.4$. The role of shear in exernal modes is quite intuitive by analysing the radial profiles of the plasma displacement in figures 4.4 (b) and (c). For relatively low shear ($s = 0.5$) the obtained eigenfunctions are quite similar to the case without shear, the weakening of the infernal drive being compensated by the increase of the external kink drive. Further increasing the shear reduces the infernal drive by localising the main mode around the rational surface, which in turn weakens the coupling with the sidebands and stabilises the mode.

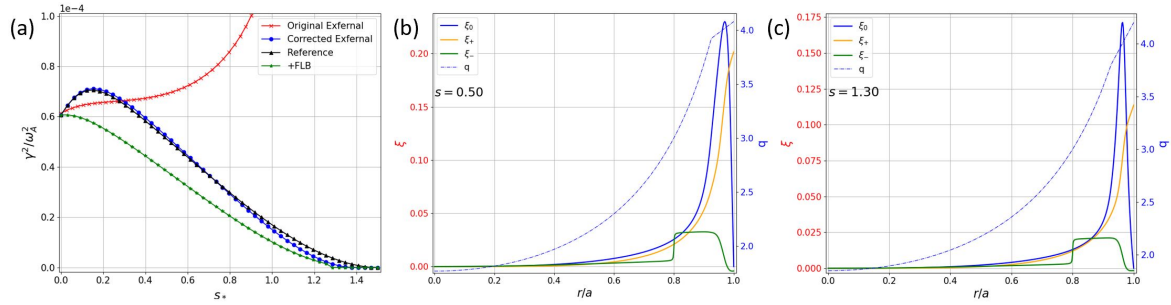


Figure 4.4: (a) Growth rates as a function of magnetic shear, where the line labelled as ‘+FLB’ corresponds to the Original Exernal model + Field Line Bending corrections to the safety factor expansion. Radial component of the plasma displacement of the main mode (ξ_0) and sidebands (ξ_{\pm}) at (b) $s = 0.5$ and (c) $s = 1.3$. For illustration purposes we have set $r_1 = 0$ and used the *Reference* model in figures (b) and (c). The calculations adopt $\alpha = 3$, $q_* = 4$, $m = 4$, $n = 1$, $b = 1.3$, $a/R_0 = 1/10$, pedestal width $d = 0.075$ and $r_p = a - d$.

4.4.3 Stability diagrams

Now that we have investigated the validity of the models and determined the important parameters in the equations, we proceed to calculate stability diagrams with physical relevance. To this end, we use the *Reference* model with $r_1 = 0$ and $r_2 = a$, as it is the most complete semi-analytical model. Indeed, this is the model that should compare best against the KINX and VMEC simulations shown later. We start by producing an ‘exernal’ $s - \alpha$ diagram, with s and α evaluated in the middle of the pedestal region, where α peaks. The resulting diagram is shown in figure 4.5a. It is found that exernal modes can support substantial shear without being stabilised, and that it increases linearly with pedestal pressure. We observe the same

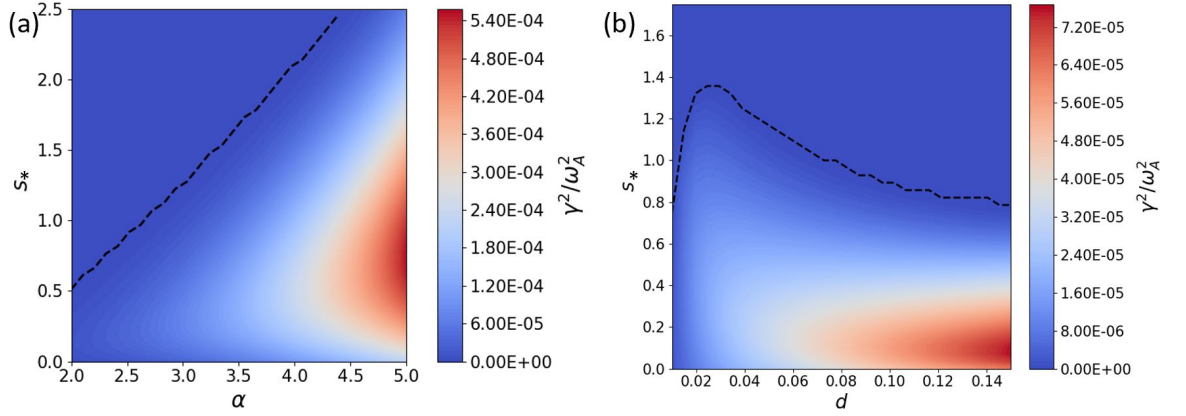


Figure 4.5: (a) $s - \alpha$ external stability diagram with $d = 0.05$ and (b) $s - d$ external stability diagram with $\alpha = 3$ at pedestal width $d = 0.06$. The dashed black line indicates in both cases the stability boundary, obtained when the numerical solution of the stability equations result in $\gamma^2 = 0$. The calculations adopt $m = 4$, $n = 1$, $b = 1.3$, $a/R_0 = 1/10$ and $r_p = a - d$.

behaviour as in figure 4.4, where the growth rate peaks at non-zero shear. The peak shifts to larger values of shear with increasing α due to the stronger coupling between the neighbouring harmonics.

Figure 4.6 shows the external unstable region in the more familiar infinite- n ballooning stability diagram, where the ballooning stability limit is a solution of equation [Wil+99]

$$\frac{d}{d\chi} \left\{ [1 + h^2] \frac{dy}{d\chi} \right\} + \alpha (\cos\chi + h \sin\chi + d_M) y = 0, \quad (4.20)$$

where χ is the ballooning angle, $h(\chi) = s\chi - \alpha \sin\chi$ and $d_M \approx \epsilon(q^{-2} - 1)$ is related to the Mercier coefficient. The external instability is located in the second region of ballooning stability, meaning that external and infinite- n ballooning modes are excited in different regions of the parameter space. This result agrees with previous ballooning analysis on VMEC simulations which found that QH-mode-like plasma profiles were stable against ballooning modes [Ham+21], and is consistent with the experimental observations where QH-mode is accessed at the peeling boundary of the peeling-ballooning stability diagram. Therefore, we speculate that very high- n ideal modes are not excited during QH-mode operation simply because the plasma is located on a stable region of the parameter space against such modes. However,

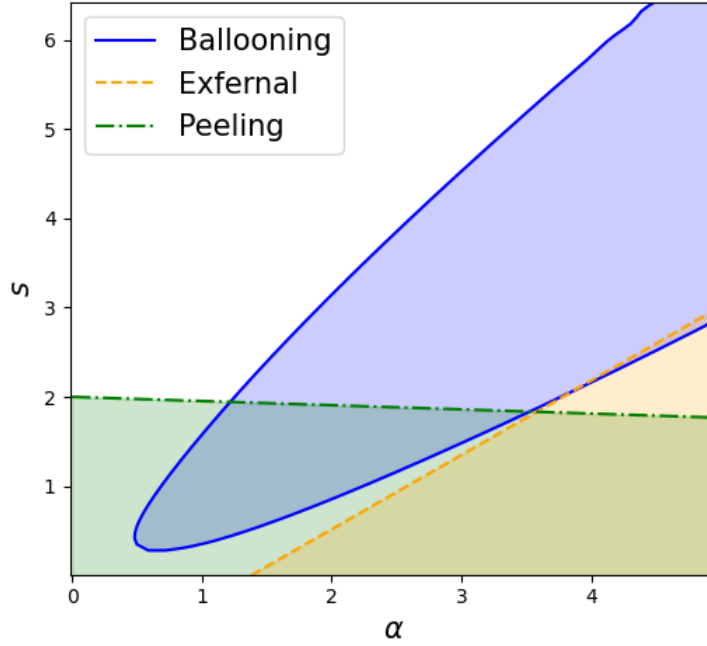


Figure 4.6: $s - \alpha$ stability diagram for external, peeling and ballooning modes

medium- n coupled peeling-ballooning modes might be unstable, and are assumed to be stabilised by sheared $\mathbf{E} \times \mathbf{B}$ flow [Bru+19a] as discussed in section § 3.1. Also plotted in figure 4.6 is the peeling stability boundary, obtained by expanding the peeling-ballooning equation (eq. 4 in reference [Wil+99]) around a single vacuum rational surface next to the plasma edge, resulting in the instability condition [Wil+99]

$$\alpha > -\frac{2(2-s)}{d_M}. \quad (4.21)$$

The peeling and external modes are superimposed on a large part of the stability diagram, though the mechanism for the excitation of each mode are very different as briefly discussed in section 3.1. An important difference between external and peeling modes is that peeling modes are only driven by edge current density and are stabilised by the presence of a plasma separatrix [SKK11; WG09], while external modes are current and pressure driven and the instability can be sustained in diverted plasmas, as will be shown in section § 4.6. Finally, we stress that peeling-ballooning and external $s - \alpha$ diagrams are different in nature. The

shear and pressure gradient for exfernal modes are evaluated over the pedestal region, while infinite- n ballooning is dependent on the local shear and α values at each flux surface, and for pure peeling modes these quantities are evaluated at the plasma edge. A comparison with the parameter space of coupled peeling-ballooning modes was not investigated in this work. However, figure 4.6 provides a notion of where in the parameter space the exfernal modes are located.

QH-modes have been experimentally observed with H-mode-like pressure pedestals [Bur+05], and most recently in the wide pedestal domain [Dii+17]. We now investigate the critical shear that can be achieved for a certain pedestal width. Reducing the size of the pedestal increases the localisation of the mode, which weakens the coupling and therefore has a stabilising effect. On the other hand reducing the pedestal width for a given pressure increases the pressure gradient, which has a destabilising effect. To vary the pedestal width in our model we perform a scan in the parameter d , setting $r_p = a - d$ while maintaining the pressure gradient such that $\alpha = 3$ at a pedestal width of $d = 0.06$. The stability diagram is shown in figure 4.5 (b). It is found that for a very narrow pedestal width the modes are less unstable and the critical shear is larger. Exfernal modes are more unstable for wide pedestals, but more easily stabilised by magnetic shear. This has an important implication because the current drive that weakens the shear in the pedestal region has its origin in the bootstrap current, which is proportional to the pressure gradient. A wide pedestal is associated with a lower bootstrap current, which results in higher magnetic shear over the region. On the contrary, a narrow pedestal is associated with a higher bootstrap current, which results in lower magnetic shear over the region.

4.5 Comparison with linear (KINX) and nonlinear (VMEC) codes

As discussed in Chapter 3, nonlinear saturated exfernal modes in the absence of strong equilibrium flows can be obtained by solving the 3D MHD equilibrium equation using the VMEC code. Boundary conditions are calculated from the interaction of the vacuum field with the plasma, where the vacuum field is computed through the Biot-Savart law from a set of JET-like filament coils carrying current. As it has been assumed throughout the thesis, we consider that such saturated modes correspond to the EHOs observed during QH-mode tokamak operation. For the 3D corrugation to develop, the equivalent axisymmetric equilibria must be linearly unstable. As done in section § 3.3.1, the KINX code is again used to assess the linear stability of 2D axisymmetric equilibria. The plasma profiles under consideration are shown in figure 4.7,

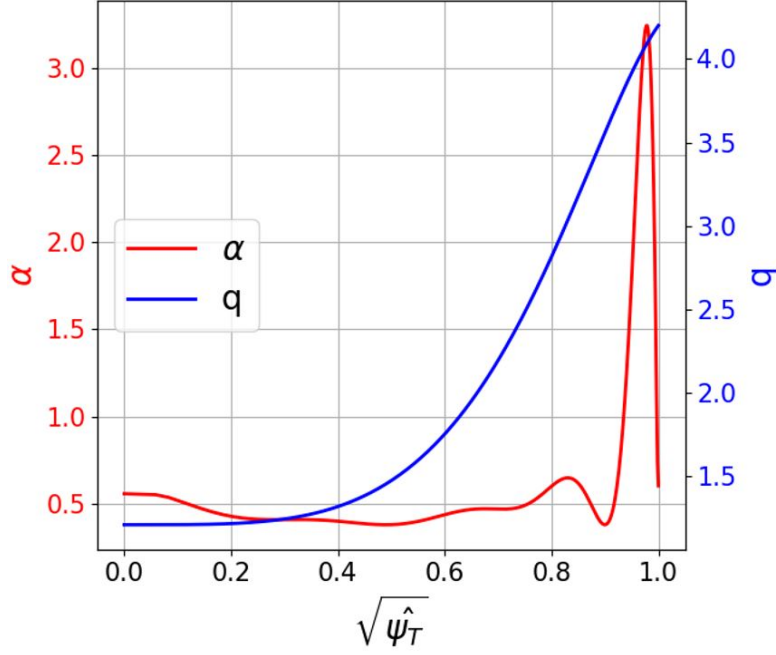


Figure 4.7: α and safety factor profiles used in VMEC simulations as a function of the squared root of the normalised toroidal flux.

where we note that the edge safety factor has finite magnetic shear and the pedestal width is roughly $d \approx 0.05$.

To isolate the effect of the infernal pressure-driven branch of the main mode, VMEC computations remove the current-driven branch of the main mode by setting $q_a > q_s$ [Kle+19]. For $q_* < q_s$ this is usually achieved by adding a spike to the safety factor at the edge, taking the value of q_a just above the rational surface of the main mode [Kle+19; ZKV13b]. It is argued that the spike also provides a more realistic transition between the low-shear and vacuum regions in diverted plasmas, which exhibit a sharp increase when approaching the separatrix [Kle+19]. The effect of such a spike on stability (including the spike going to infinity) will be discussed later in section 4.6.

Following the methodology described in section § 2.5.1 and exemplified in section § 3.3.1, we define the nonlinearly saturated radial displacement η as the normal distance between the flux surfaces of the 3D corrugated state and an equivalent neighbouring axisymmetric state, where the latter is obtained by removing all toroidal modes except $n = 0$ in the VMEC Fourier

expansion. The function $\eta(r, \theta, \phi)$ is mapped to a straight coordinate system and Fourier decomposed in toroidal and poloidal modes, giving a radial profile of the nonlinear perturbed amplitude contribution of each Fourier mode.

We perform two almost identical VMEC simulations, one with a flat safety factor at the edge (solid line in figure 4.8a, yielding $\gamma^2/\omega_A^2 = 0.0039$), and one with positive magnetic shear (dashed line in figure 4.8a, yielding $\gamma^2/\omega_A^2 = 0.0024$). The resulting Fourier decomposition of the radial nonlinear displacement is plotted in figure 4.8b for both cases, where the solid and dashed lines correspond to the equilibria with flat edge and sheared edge safety factor respectively. Axisymmetric equivalent VMEC equilibria were then used as the basis of linear MHD stability calculations using the KINX code [Deg+97], and the linear eigenfunctions for both cases are plotted in figure 4.8c. For consistency in the comparison between VMEC, KINX and our model, the KINX simulations were performed without the presence of the plasma separatrix. The linear growth rates and saturated amplitudes are quite similar for the two choices of q-profiles. Linear and nonlinear simulations show that the same mode is excited, confirming the notion that external modes can be excited even in the presence of modest edge magnetic shear. Notice again that the linear eigenfunctions and radial profiles of the nonlinear plasma displacement with finite edge shear exhibit the same characteristics as the ones found by our simplified large aspect ratio model.

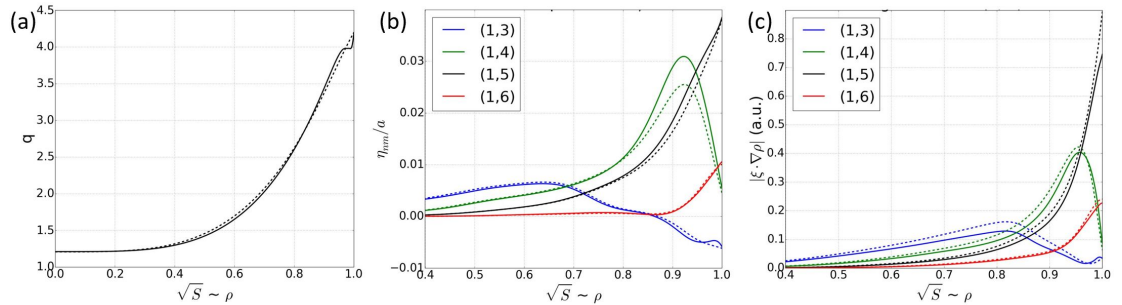


Figure 4.8: (a) Flat edge safety factor (solid line) and sheared safety factor (dashed line). (b) Fourier decomposition of the normalised nonlinear radial displacement calculated in VMEC. (c) Linear radial eigenfunctions calculated in KINX.

Finally, a series of simulations were performed for a broad scan of edge safety factor shapes. The average shear over the pedestal region was calculated and plotted in figure 4.9 against the KINX linear growth rate and VMEC nonlinear saturated amplitude of the $(m + 1)/n$ mode at the edge. Even though the plasma profiles and geometry is more realistic in the VMEC and

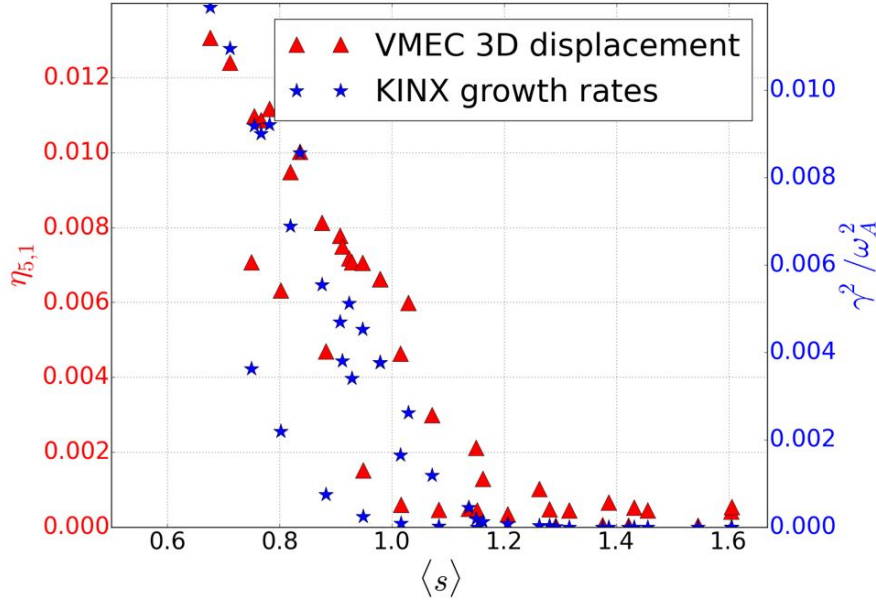


Figure 4.9: Amplitude of the $m + 1/n$ saturated mode calculated with VMEC (left axis) and linear growth rates (right axis) calculated with KINX. It is consistently found that the limiting shear is around unity.

KINX simulations, it is encouraging to find roughly the same limiting shear $s \sim 1.2$ as in our simplified analytical model for similar $\alpha \sim 3$ and $d \sim 0.05$.

4.6 Model of the plasma separatrix

QH-mode plasmas operate in diverted configuration, where the formation of an x-point in the edge makes the poloidal field vanish locally. The effect of such localisation is included in our model in the poloidal average of the safety factor¹, which is taken to go to infinity at the LCFS. This has an important implication on the upper sideband external kink drive, whose rational surface now lies inside the plasma [WG09; Huy05; SKK11].

It is clear that the external mode excitation mechanism is mostly determined by the coupling of infernal and external kink drives, with the external kink drive strongly depending on the value of q_a . The effect of q_a on edge modes has been previously studied in reference [ZKV17], where it was found that if q_a lies just above or just below a rational surface ($|q_a - m'/n'| < 1$,

¹The poloidal localisation of the divergence in the safety factor is not modelled in this work.

where m' correspond to an arbitrary (m, n) mode) the plasma becomes highly unstable and dominated by a peeling mode. Otherwise, the plasma is more stable and dominated by kink or infernal type modes. Our simplified analytical model considers three coupled poloidal harmonics. The peeling-like instability associated with the main mode (m, n) is removed by setting $\xi_{r0}^{(m)}(r_2) = 0$ at the boundary of the low shear region, as discussed in section § 4.3.3. We note that we may still reach the peeling-like instability of the $(m + 1, n)$ mode, although the growth rate should saturate before q_a is too close to $(m + 1)/n$ as q_a is increased towards infinity [ZKV17].

As a first approach to model the separatrix, the safety factor in the edge region is taken to be $q(r) = \frac{1-s_*(r/r_*)}{A[1-(r/a)^\lambda]+B}$, where $A = \frac{1-q_*B}{q_*[1-(r_*/a)^\lambda]}$, $B = \frac{1-s_*(1-a/r_*)}{q_a}$ and $\lambda \gg 1$. For comparison with section § 4.4, we use the Reference model with $r_1 = r_p$ and $r_2 = 0.99$, where r_2 is close to the location of sharp increase of the magnetic shear for $1 \ll \lambda = 500$. Poloidal coupling is avoided in the separatrix region due to the presence of large shear and low pressure gradient, so it is assumed that the modes obey equation 4.4. The boundary conditions at the plasma-vacuum interface are given by equation 4.19.

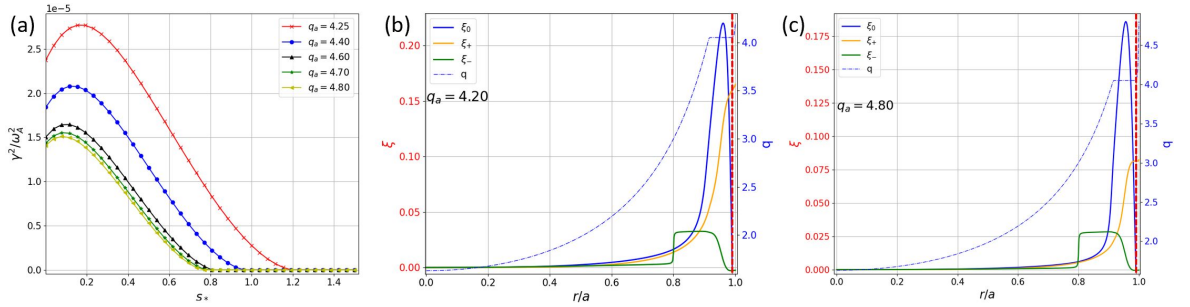


Figure 4.10: (a) Growth rate as a function of magnetic shear and q_a and radial component of the plasma displacement of the main mode (ξ_0) and sidebands (ξ_{\pm}) with (b) $q_a = 4.2$ and (c) $q_a = 4.8$. The calculations adopt $\alpha = 3$, $m = 4$, $n = 1$, $q_* = 4.$, $b = 1.3$, $a/R_0 = 1/10$, $d = 0.075$, $r_2 = 0.99$ and $r_p = a - d$. The separatrix region is indicated in figures (b) and (c) by the vertical red dashed line.

Figure 4.10 (a) shows the effect of q_a as a function of magnetic shear in the pedestal region. The external kink drive of the upper sideband gets reduced due to the increased magnetic shear over the separatrix region, with the growth rate saturating at $q_a \sim 4.70$. The effect of q_a on the radial components of the plasma displacement can be appreciated in figures 4.10 (b) and (c), where an increased value of q_a reduces the external kink drive of the upper sideband. Note that since $q_a < (m + 1)/n$, the external current-driven mode has not been completely

removed.

A logarithmic divergence of the safety factor is considered empirically realistic in tokamaks [Web09]. Therefore, to study the limit of $q_a \rightarrow \infty$ the separatrix is modelled as:

$$q(r) = \begin{cases} \frac{m-1}{\kappa[1-(r/r_-)^\mu] + n} & \text{if } r \leq r_p, \\ q_* [1 - s_* (1 - r/r_*)] & \text{if } r_p \leq r \leq r_x, \\ A \ln(a - r) & \text{if } r_x \leq r \leq a, \end{cases} \quad (4.22)$$

where r_x is the radius at which the safety factor starts diverging, $r_* = (r_p + r_x)/2$ and $A = \frac{q_* [1 - s_* (1 - r_x/r_*)]}{\ln(a - r_x)}$ guarantees continuity at r_x . The dispersion relation is obtained by solving the equations in the low-shear region, where the effect of the separatrix only enters in the form of boundary conditions at the interface with the separatrix region. For the lower sideband, the boundary condition at r_x is obtained by solving equation 4.4 with $m' = m - 1$ subject to the vacuum condition (equation 4.19) in the limit of $q \rightarrow \infty$. The upper sideband rational surface is now contained within the interval $[r_x, a]$, so the boundary condition is obtained by solving equation 4.4 with $m' = m + 1$ in the interval $[r_x, r_+]$, where r_+ is the radii of the upper rational surface at which a Neumann boundary condition is applied: $d\xi_{r1}^{(m+1)}/dr|_{r_+} = 0$. A second method to cast the boundary condition for the upper sideband is to solve equation 4.4 analytically in the interval $[r_x, a]$. The solution in the large shear limit can be written as sum of exponential integrals of logarithmic functions, but in the limit of very small inertia within the rational layer the solution reduces to a step function. Then, the boundary condition for the upper sideband in the low shear region could be approximated as a Neumann condition at r_2 : $d\xi_{r1}^{(m+1)}/dr|_{r_2} = 0$. It has been verified that both methods yield the same physics, with negligible difference in the growth rates or eigenfunctions.

We now investigate the effect of the safety factor corrections in the presence of a plasma separatrix by comparing the three different models analysed in section 4.4. For consistency in the comparison, we set $r_1 = r_p$ and $r_2 = r_x$. Figure 4.11 (a) shows the effect of the separatrix in the cases with flat safety factor (compare with figure 4.3 (a) with no separatrix). It is clear that the separatrix reduces the parameter space for excitation of the mode as well as the value of the growth rates. Now that the external kink drive has been drastically reduced, the instability drive

comes exclusively from the infernal contribution. Since the external kink drive on the Original Exfernal model is now constant for any value of Δq (as the equations are now independent of q_a) the growth rates are symmetric with respect to q_s independently of the pressure gradient. The Corrected Exfernal and Reference models continue to have a slight asymmetry towards positive Δq as a result of the higher order toroidal coupling contributions. Stronger coupling induced by an increase of the pressure gradient enhances the instability and expands the excitation parameter space (figure 4.11 (b)). Finally, an analysis of the eigenfunctions in figures 4.11 (c) and (d) shows that the main mode is clearly dominant independently of the sign of Δq , though for $\Delta q > 0$ the upper sideband is larger than for $\Delta q < 0$.

An interesting thing to note is that if the safety factor goes towards infinity at the edge (or in fact, if $q_a > (m + 1)/n$), then vacuum physics only enters the equations through the boundary condition of the lower sideband, whose effect at the plasma edge is weak. Figures 4.11 (c) and (d) show that the value of the lower sideband is almost zero at the edge, meaning that in principle a Dirichlet boundary condition could be approximated for the lower sideband, i. e. $\xi_{r1}^{(m-1)}(a) = 0$. As expected, applying such condition has negligible effects on the stability of external modes with separatrix, which means that these modes are formally internal (i.e. infernal) since no vacuum physics is needed to excite it. Nevertheless, the argument only applies when the safety factor has a very sharp increase at the edge which takes $q_a > (m + 1)/n$, in which case the plasma can be considered to be in a diverted configuration. For a limited configuration where $q_a < (m + 1)/n$, an ideal wall at the plasma interface would stabilise external modes [Bru+18a; Bru+18b]. This means that an unstable mode requires either a vacuum contribution from the upper sideband and/or the upper sideband rational surface being inside the plasma domain. This is because an ideal wall at the plasma edge completely stabilises the external kink drive, and therefore the external mode. On the other hand, within the approximations of our model, the separatrix isolates the unstable infernal drive from the wall stabilisation effect.

A case of the excitation of external modes in the presence of a separatrix has been previously reported in reference [Kle+19], where the KINX code was used to calculate the stability of QH-mode discharges in single-null diverted configuration. Even though our model of the separatrix is simplified, it reproduces all the reported characteristics in [Kle+19], namely: 1) The mode remains unstable, 2) the main mode is more localised in the pedestal than for the cases without separatrix, 3) the upper sideband has a sharp decay in the separatrix region

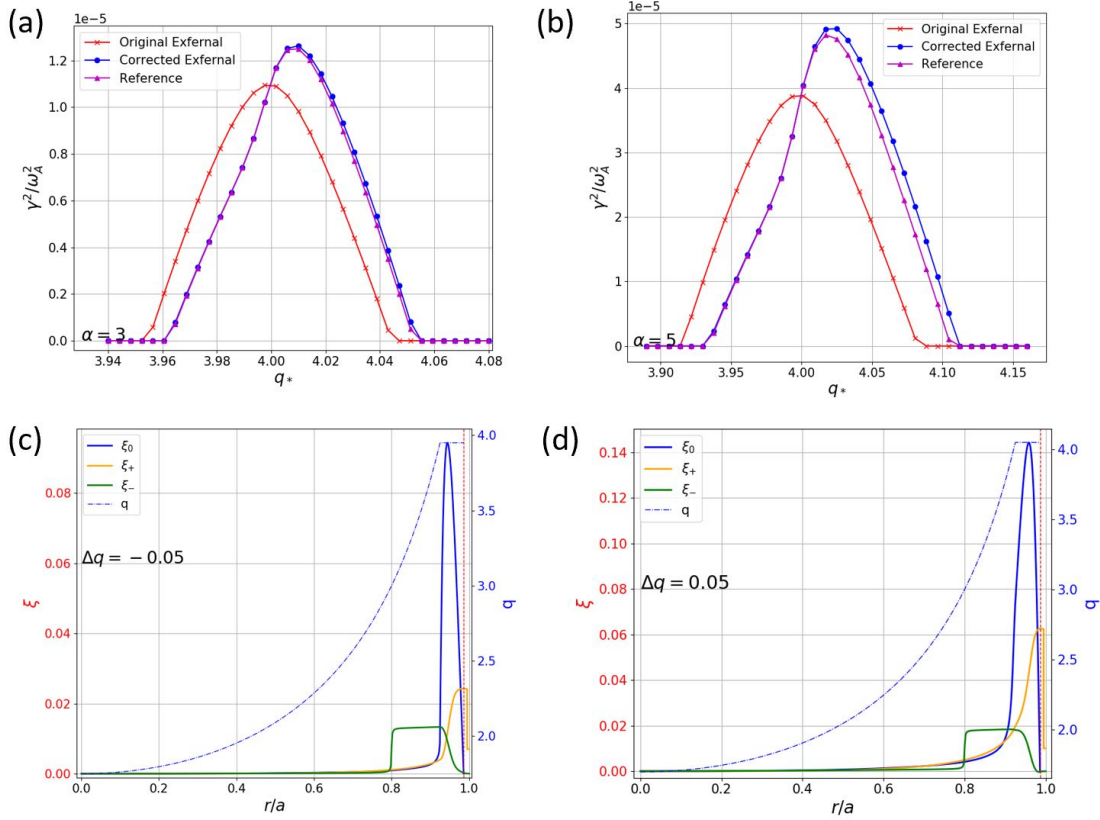


Figure 4.11: Growth rates as a function of q_* for (a) $\alpha = 3$ and (b) $\alpha = 5$ including a plasma separatrix. Radial component of the plasma displacement of the main mode (ξ_0) and sidebands (ξ_{\pm}) at (c) $\Delta q = -0.05$ and (d) $\Delta q = 0.05$ calculated with the Reference model and $r_1 = 0$. The vertical dashed line indicates the location of the separatrix at r_x , which has been removed only graphically for illustration purposes. The results take $m/n = 4$, $b = 1.3$, $a/R_0 = 1/10$, $d = 0.075$, $r_x = r_2 = 0.99$ and $r_p = a - d$.

(modelled by our step function solution), and 4) the upper sideband is slightly larger for $\Delta q > 0$. Note that the model of the separatrix presented on this thesis only includes the effect of the relevant sidebands rational surfaces being inside the plasma, as well as the effect of very high edge (off-pedestal) magnetic shear. The agreement with previous work could mean that that these effects are responsible for at least part of the observed physics. Nevertheless, a proper divergence on the safety factor or the 2D geometric effects related to the formation of the x-point are not modelled, which could both modify the stability conditions and stability limits of external modes.

Figure 4.12a shows that the overall effect of magnetic shear is stabilising. It is obtained once

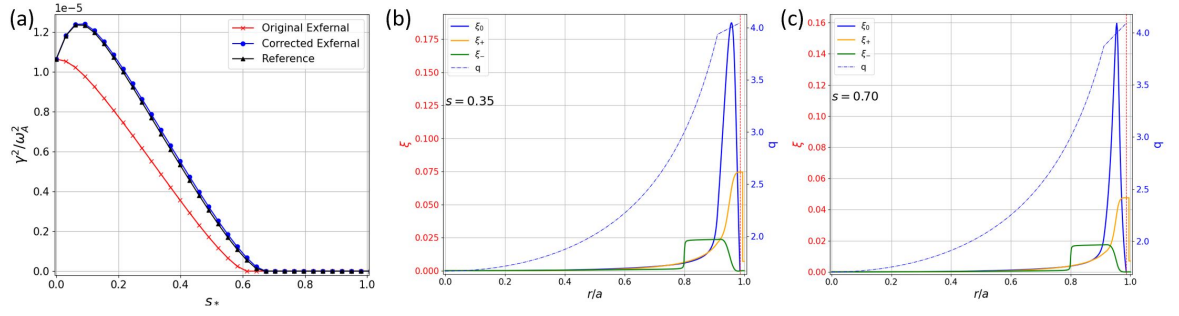


Figure 4.12: (a) Growth rates as a function of magnetic shear including a plasma separatrix. Radial component of the plasma displacement of the main mode (ξ_0) and sidebands (ξ_{\pm}) at (b) $s = 0.35$ and (c) $s = 0.7$ calculated with the Reference model and $r_1 = 0$. The vertical dashed line indicates the location of the separatrix at r_x , which has been removed only graphically for illustration purposes. The results take $\alpha = 3$, $q_* = 4$, $m/n = 4$, $b = 1.3$, $a/R_0 = 1/10$, $d = 0.075$, $r_x = r_2 = 0.99$ and $r_p = a - d$.

again that without the enhancement factor of the external kink drive the parameter space for exciting external modes is reduced, with a critical marginal stability shear of $s \sim 0.75$. Since the destabilising sideband contributions are significantly reduced by the separatrix, the FLB contribution of the main mode in the Original Externel model is enough to stabilise the mode. We can see that the Corrected Externel model has excellent agreement with the Reference. The role of shear is not affected by the presence of the separatrix, as reflected by the obtained eigenfunctions (figures 4.12 (b) and (c)): magnetic shear localises the main mode around the rational surface, weakening the infernal drive and the coupling with the sidebands.

One can note that the critical shear obtained with the 'spike' model of the safety factor saturates at $q_a < (m + 1)/n$, and coincides with the critical shear obtained with the logarithmic divergence. This suggests that the sharp increase of magnetic shear is enough to significantly reduce the instability drive of the current driven branch, as suggested by previous studies [SKK11; WG09]. One can conclude that a spike in the safety factor does provide a good model for the transition between the plasma and the vacuum region in ideal MHD calculations of external modes, so that more sophisticated separatrix modelling may not be needed.

4.6.1 Modification of the parameter space with a separatrix

We analyse the external $s - \alpha$ and pedestal width stability diagrams, now introducing a separatrix using our simplified model (figures 4.13 a) and b)). The calculations use the Reference

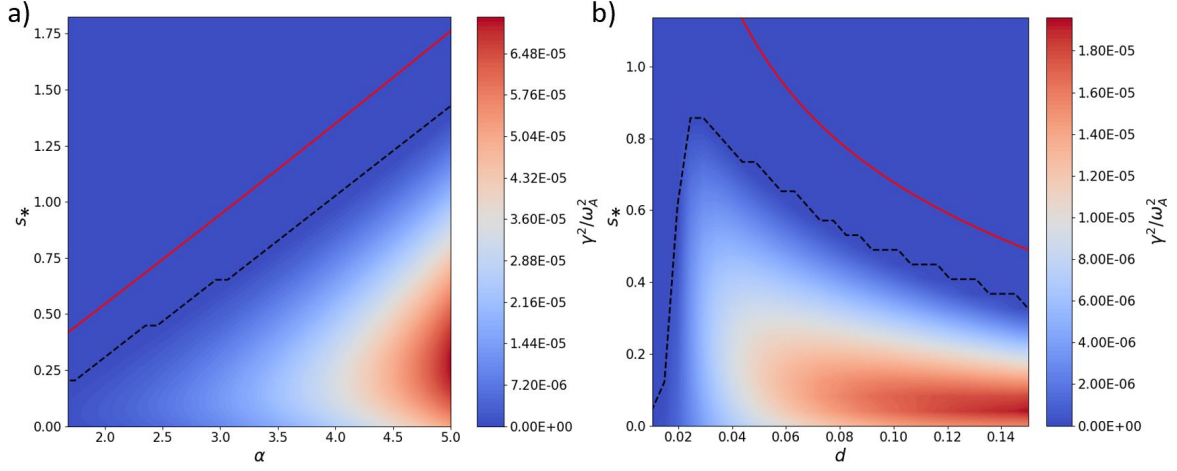


Figure 4.13: a) $s - \alpha$ external stability diagram with $d = 0.05$ and b) $s - d$ external stability diagram with $\alpha = 3$ at pedestal width $d = 0.06$. A model of the plasma separatrix is now included. The dashed black line indicates in both cases the stability boundary. The solid red line corresponds to the analytical estimation of the critical shear (equation 4.27) calculated in section 4.6.2 for a linear pressure dependence in the pedestal. The results take $m/n = 4$, $b = 1.3$, $a/R_0 = 1/10$, $r_x = r_2 = 0.99$ and $r_p = a - d$.

model, setting $r_1 = 0$ and $r_2 = r_x$. Since the separatrix has not killed the infernal drive of the mode, the stability diagrams show a similar behaviour as figure 4.5, but with the limiting shear and growth rates reduced due to the absence of the upper sideband external kink drive enhancement. Additional to the stability limit obtained numerically (dashed black line), the red solid line in figures 4.13 (a) and (b) show an analytical estimation of the marginal magnetic shear. The derivation is obtained with a simple model presented in the next subsection.

4.6.2 Analytical estimation of edge critical shear with a separatrix

For simplicity we consider the Original Exfernal model, which has been shown to describe the main effects of magnetic shear in a diverted plasma, and to give a good estimate of its critical value for instability in plasmas with separatrix. Recalling that the Original Exfernal model neglects corrections of order $\mathcal{O}(e^4, \Delta q^1)$, we can readily integrate equation 4.15 and substitute into equation 4.14 to obtain [Bru+18b; Bru+18a; GHH96]:

$$\frac{d}{dr} \left[r^3 Q^2 \frac{d}{dr} \xi_{r0}^{(m)} \right] - r(m^2 - 1) \left[Q^2 + r \frac{d}{dr} \tilde{\gamma}^2 \right] \xi_{r0}^{(m)} + \frac{r^2 \alpha}{R_0 q_s^2} \left(\frac{1}{q_s^2} - 1 \right) \xi_{r0}^{(m)} + \frac{\alpha}{2 q_s^2} \sum_{\pm} \frac{r^{1 \pm m}}{1 \pm m} L_{\pm} = 0, \quad (4.23)$$

where $Q^2 = (1/q - 1/q_s)^2 + \tilde{\gamma}^2$, $\tilde{\gamma}^2 = \gamma^2(1 + 2q_s^2)/(\omega_A^2 m^2)$ and L_{\pm} are the constants of integration that account for the coupling with the neighbouring sidebands. $L_{\pm} = \Lambda_{\pm} \int_{r_p}^{r_x} \alpha r^{1 \pm m} \xi_{r0}^{(m)} dr$, where Λ_{\pm} are defined in a similar way as in refs. [Bru+18a; Bru+18b; GHH96]

$$\Lambda_{\pm} = \frac{(1 \pm m)^2 [2 \pm m + \mathcal{B}_{\pm}(r_p)] [2 \pm m + \mathcal{B}_{\pm}(r_x)] r_x^{-2(1 \pm m)}}{(\pm m - \mathcal{B}_{\pm}(r_x)) [2 \pm m + \mathcal{B}_{\pm}(r_p)] - \left(\frac{r_p}{r_x} \right)^{2(1 \pm m)} (\pm m - \mathcal{B}_{\pm}(r_p)) (2 \pm m \mathcal{B}_{\pm}(r_x))}, \quad (4.24)$$

where $\mathcal{B}_{\pm}(r) = r \frac{d}{dr} \ln \left[\xi_{r0}^{(m \pm 1)}(r) \right]$. Let us define $h = d/(2r_*) \ll 1$ and assume that in the pedestal region the pressure and mass density profiles depend linearly on r so that α is constant. Thus, we approximate $\int_{r_p}^{r_x} \alpha r^{1 \pm m} \xi_{r0}^{(m)} dr \approx \alpha r_*^{1 \pm m} \int_{r_p}^{r_x} \xi_{r0}^{(m)} dr$. For the sake of convenience, we impose the normalisation $\int_{r_p}^{r_x} \xi_{r0}^{(m)} = 1$, which consequently formally yields $\xi_{r0}^{(m)}/a \sim h^{-1}$.

By introducing the variable $x = (r - r_*)/r_*$ and expanding around $x = 0$, the mass density and pressure are written as $\rho/\rho_p = P/P_p = (h - x)/(2h)$, where $\rho_p = \rho(r_p)$ and $P_p = P(r_p)$ are the values at the pedestal top. Taking $q(r_*) = q_s = m/n$ and expanding equation 4.23 around $x = 0$ reduces to

$$\frac{d}{dx} \left[f \frac{d}{dx} \xi_{r0}^{(m)} \right] + \frac{r \alpha}{R_0} \left(\frac{1}{q_s^2} - 1 \right) \xi_{r0}^{(m)} + \frac{\alpha}{2} \sum_{\pm} \frac{r_*^{\pm m}}{1 \pm m} L_{\pm} = 0 \quad (4.25)$$

where $f = s_*^2 x^2 + \gamma^2 \tau_A^2 \left(\frac{h-x}{2h} \right)$ with $s_* = r q' / q|_{r_*}$ and $\tau_A^2 = \frac{1}{(\omega_A(r_p) n)^2} (1 + 2q_s^2)$. Let us define the constant $U = \frac{\alpha}{2} \sum_{\pm} \frac{r_*^{\pm m} L_{\pm}}{1 \pm m}$. A rough estimate of the critical magnetic shear can be obtained by balancing the field line bending and coupling terms in the equation above, in the limit of $\gamma \rightarrow 0$ and under the assumption that the Mercier contribution is small (this will be proven later). Hence, assuming that $\frac{d}{dx} \sim \frac{1}{x} \sim \frac{1}{ah}$ and using the normalisation condition for $\xi_{r0}^{(m)}$, the critical

magnetic shear scales as $s_*^2 \sim ahU$. The solution to equation 4.25 can be written in terms of hypergeometric functions (see Ref. [Mik17]). Requiring that $\xi_{r0}^{(m)}$ vanishes at $x = \pm h$, imposing the normalisation condition for $\xi_{r0}^{(m)}$ in the solution and taking the limit of $\gamma \rightarrow 0$ yields the condition for marginal stability

$$1 = \frac{2hr_*U}{\mathcal{D}} \left(1 - \frac{1}{2} \frac{\Gamma\left(\frac{1}{4} + \frac{1}{4}\sqrt{1 + \frac{4\mathcal{D}}{s^2}}\right)}{\Gamma\left(\frac{5}{4} + \frac{1}{4}\sqrt{1 + \frac{4\mathcal{D}}{s^2}}\right)} \right), \quad (4.26)$$

where $\mathcal{D} = \frac{r_*\alpha}{R_0} \left(1 - \frac{1}{q_s^2}\right)$ is the Mercier contribution and Γ is the Gamma function. We note that the Mercier contribution is proportional to $\epsilon\alpha\xi_{r0}^{(m)}$, whereas the coupling contribution scales as α^2 . Assuming $\epsilon\xi_{r0}^{(m)}/a \sim \epsilon h^{-1} \sim 1$, it turns out that for sufficiently large pressure gradients the coupling contribution dominates over the weakly stabilising Mercier term, allowing us to expand equation 4.26 in the limit of $\mathcal{D} \ll 1$, finally giving

$$s_* = \sqrt{2hr_*U} - \frac{\mathcal{D}}{\sqrt{2hr_*U}}. \quad (4.27)$$

This expression has the very same dependencies on the rough scaling obtained previously, balancing field line bending and coupling contributions. Evaluating U requires expressions for the constants Λ_{\pm} . It is later shown that $U \approx \frac{7}{12r_*} m\alpha^2$, so that $s_* \approx \alpha \sqrt{\frac{7}{6}hm} - \frac{\mathcal{D}}{\alpha \sqrt{\frac{7}{6}hm}}$. Recalling that $\mathcal{D} \propto \alpha$, this expression immediately recovers the linear dependency of the critical shear on pedestal pressure obtained numerically by the Reference model (figure 4.13 (a)). Note that in the limit of $\alpha \rightarrow 0$, the only stabilising effect at zero shear comes from the Mercier term, meaning that without it, any pedestal pressure would excite an infernal instability for the case of $q_* = q_s$ and zero shear. This result was verified by removing the Mercier contribution in the Corrected Exernal model and solving the equations numerically.

Substituting the parameters used in the calculations above gives the marginal magnetic shear $s_* = 0.382\alpha - 0.233$ (solid red line in figure 4.13 (a)), whose dependence upon the parameter α is remarkably close to the one obtained by a linear fit of the numerical results shown in figure 4.13 (a) ($s_* = 0.368\alpha - 0.447$). Note that the numerical results in figure 4.13 (a) were obtained

with a \tanh -like pressure profile (α corresponding to the peak value within the pedestal), while the analytical estimation assumes a constant α . This results in an overestimation of the critical shear by equation 4.27. Solving the Original Exernal equations numerically using a linear pressure profile in the pedestal region gives a better match to our analytical estimation, as seen in figure 4.14.

Expressing α in terms of h allows a study into the critical shear as a function of pedestal width at constant pedestal pressure. Since $\alpha \sim 1/h$ and thus $\hat{s} \sim h^{-1/2}$, our simple analytical formula recovers as well the correct dependency of critical shear on pedestal width in figure 4.13 (b), except for small pedestal widths.

A final analytical estimation links the toroidal current density to the critical shear through the relation in cylindrical limit $J_{tor} = \frac{B_0}{rR_0} \frac{d}{dr} \left(\frac{r^2}{q} \right)$. Expanding this expression and plugging the value for the magnetic shear computed in equation 4.27, we obtain the following value of the required pedestal current density for the EHO excitation

$$J_{tor} \approx \frac{2B_0}{q_* R_0} \left(1 - \sqrt{\frac{hr_* U}{2}} + \frac{P}{2\sqrt{2hr_* U}} \right). \quad (4.28)$$

We stress that equation 4.28 is valid in a cylindrical limit and variations are expected for more accurate toroidal diverted geometry.

Analytical estimation of U

From previous computations performed with a simplified step-model for the current density and a sufficiently distant wall [Bru+18a; Bru+19a], we have $\mathcal{B}_+(r_p) \approx 3m + 2$, $\mathcal{B}_-(r_p) \approx m/6 - 1/4$ and $\mathcal{B}_+(r_x) \approx 2 - 3m$. The Neumann boundary condition for the upper sideband at the interface between the pedestal and separatrix regions means $\mathcal{B}_+(r_x) = 0$. It is worth pointing out that a more refined computation with a diffuse current profile does not give significantly different results [Bru+14a]. This specifies completely the coupling coefficient U through the constants L_{\pm} , so that

$$r_* U \approx \alpha^2 \left[\frac{(m+1)(m+2)}{2m+(2+m)Y} \left(\frac{r_*}{r_x} \right)^{2(1+m)} + \frac{(m-1)(m-2)}{m-2+3mZ} \left(\frac{r_*}{r_x} \right)^{2(1-m)} \right], \quad (4.29)$$

where $Y = (r_p/r_x)^{2(1+m)}$ and $Z = (r_p/r_x)^{2(1-m)}$. In the limit of m not too large and narrow pedestal width, we may approximate $r_* U \approx \frac{7}{12} m \alpha^2$. Figure 4.14 shows the analytical estimation obtained by inserting this expression into equation 4.27, and is compared with the numerical solution using the Original Exfernal and Corrected Exfernal models. In this case, a linear pressure profile in the pedestal region was adopted in the numerical calculations to have a better comparison with the analytical solution. The excellent match in the critical shear between the Original Exfernal model and the analytical estimation confirms that the approximations taken in the derivation of equation 4.27 are valid in these simplified cases. The Corrected exfernal model prediction of the critical shear is close to the analytical estimation for low α . As pressure gradient increases the destabilising order $\mathcal{O}(\epsilon^4, \Delta q/q_s)$ coupling corrections (which are not included in the analytical estimation) become stronger, separating the analytical estimation from the one of the Corrected Exfernal model.

4.7 Conclusions

This chapter presents the effect of finite edge shear on the excitation mechanism of exfernal modes has been investigated by deriving new differential equations describing infernal modes at the edge of a large aspect ratio tokamak plasma expansion. Such equations correspond to an extension of the original exfernal model, where we have included higher order $\Delta q/q_s$ terms in the safety factor expansion. The equations were solved numerically for equilibrium profiles containing key physical elements observed during QH-mode operation. The obtained solution was compared with the Original Exfernal model and with a Reference model, where the later was obtained by retaining the full safety factor in the leading order stability equations.

Except for the cases where a separatrix is present, we find that the parameter space for the excitation of exfernal modes depends mainly on the interplay between the edge infernal drive of the main mode and the external kink drive of the upper side band. The Original Exfernal model includes all the relevant physics to properly resolve the instability for the case of very low shear, but fails to predict the effect of edge magnetic shear due to the absence

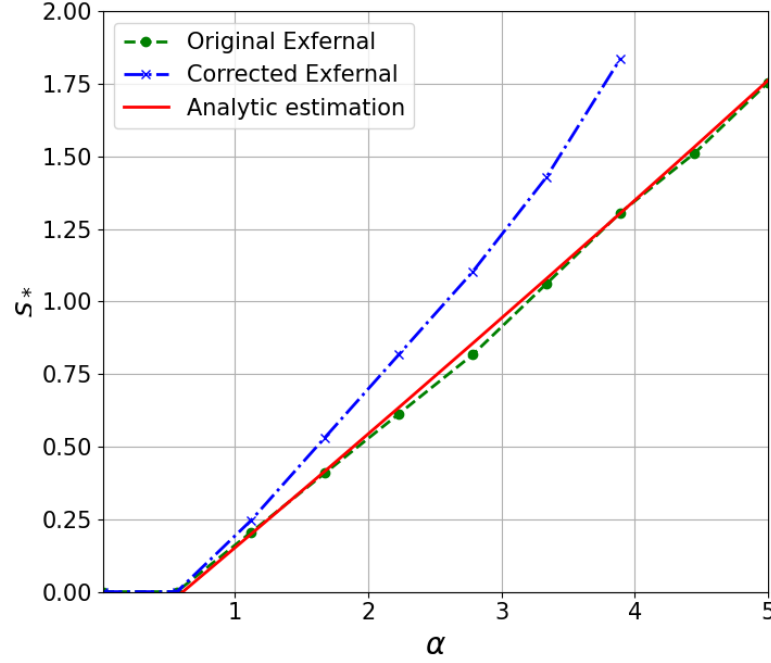


Figure 4.14: Comparison of the critical shear obtained the Original Exfernal model (blue line), Corrected Exfernal model (green line) and the analytical estimation (equation 4.27) using a linear pressure profile in the pedestal ($P/P_0 = (h - x)/(2h)$). Note that the dynamics of the instability is of an infernal mode since the connection to the vacuum is no longer necessary. The calculations adopt $m = 4$, $n = 1$, $b = 1.3$, $d = 0.06$, $a/R_0 = 1/10$, $r_p = a - d$, $r_x = 0.988$, $r_1 = r_x - d$ and $r_2 = r_x$.

of FLB cylindrical corrections in the sideband equations. Adding such corrections gives a good qualitative picture of the shear dependency of the instability, while higher order $\Delta q/q_s$ toroidal corrections have a weakly destabilising effect on the mode.

A comparison between our model and linear (KINX) and nonlinear (VMEC) codes was performed. It was found that external modes can be unstable in the presence of finite edge shear, and the critical shear for exciting such modes agrees well with the one found by our simplified large aspect ratio model. We can conclude that while external modes are stabilised by magnetic shear, but the excitation of the mode is nevertheless possible at modest edge magnetic shear in QH-mode-like pedestals. This relaxes the previous assumption of having a flat safety factor in the near vicinity of a rational surface at the edge.

The vacuum boundary conditions were later modified to include a plasma separatrix. Our simplified model finds that the presence of an x-point is stabilising by essentially nullifying the

external kink drive of the upper sideband. In this case the $\Delta q/q_s$ corrections in the sideband equations can be neglected, and the Original Exfernal model gives a good estimation of the growth rates and critical shear. Nevertheless, the excitation of the mode is robust and sustained by the infernal drive, though the growth rates and the instability parameter space are reduced. Even then, we find that the mode can support a magnetic shear of order unity at modest values of pressure gradient ($\alpha \sim 4$) and a typical pedestal width of $d \sim 0.06$. It is important to point out that a more accurate model of the separatrix might change this behaviour. For example, the infernal drive can be enhanced by the presence of kink-tearing modes, which have been found to be unstable in the presence of a separatrix [Huy05]. Lastly, in cases with and without separatrix, the Corrected Exfernal model presented in this chapter gives an excellent match to the reference case, meaning that the equations presented here should be sufficient to describe the stability of exfernal modes in the large aspect ratio approximation.

We stress again that our calculations neglect flows associated with the equilibrium electric field, arguing that it weakly affects low- n modes [Che+16], assuming also that its effect is independent of that of edge magnetic shear. In a more refined study the latter assumption might be relaxed. For example, as shown in reference [Che+17a], flow stabilisation of high- n modes is stronger for large edge current density (or equivalently low edge magnetic shear), which might impose a more severe constraint on the critical shear for marginal stability than the one calculated in this thesis.

EHOs are found to have a broad radial structure [Che+16] covering the whole pedestal. Even though the presence of magnetic shear localises the main mode around the rational surface, we have found that at moderate edge shear ($s \sim 0.5 - 1.$) the broad radial structure is sustained by coupling with the upper sideband kink drive. When the localisation of the mode is strong such as in high edge shear cases ($s \gtrsim 1.5$) or in the presence of a plasma separatrix, another mechanism is required to maintain the broadening of the main mode. In this respect, it has been found that $\mathbf{E} \times \mathbf{B}$ flow **shear** can cause radial expansion of the mode structure [Xu+17].

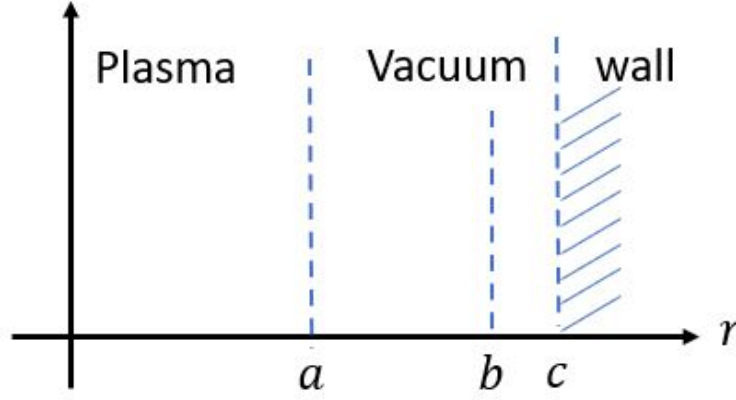
5 The effect of non-Axisymmetric Magnetic Perturbations on non-resonant external modes

Non-axisymmetric Magnetic Perturbation (MP) coils are typically used in tokamak plasmas to avoid the triggering of dangerous instabilities such as ELMs [Eva+04] and resistive wall modes (RWMs) [Oka+05]. With the installation of RMP systems in many of today's tokamaks (including ITER), MP coils can be used for other purposes, particularly, to widen the parameter space of weakly 3D tokamak configurations with optimised confinement properties. A good understanding of the plasma response to the MPs is required to robustly access such states. Modelling and simulations of MPs using linear and nonlinear techniques has been extensively studied in the past decades [LN88; LKN10; Yad+14; Co+15b; Kin+15; Ora+17; Fit18]. A good comparison between the most used numerical modelling approaches is presented in [Tur12; Tur+13]. Similar to the instability-driven 3D saturated states, as investigated in Chapters 3 and 4, the plasma response can be studied in a dynamic or in an equilibrium manner, and each of them can be developed using linear or nonlinear physics. In this chapter we explore the linear and non-linear equilibrium approaches, the linear one from the analytic point of view, and the nonlinear one using the VMEC free-boundary code. Both approaches presented here are based on solving the linear (or nonlinear) equilibrium ideal MHD equations in the presence of a non-axisymmetric magnetic component, so agreement in the limit of very small saturated amplitude is expected. Given the similarities of the linear eigenmode spectrum and the VMEC nonlinear radial saturated spectrum observed for some external instabilities (see [Kle+18; Kle+19] and Chapters 3 and 4), it is perhaps not surprising that agreement can found

even at moderate amplitude.

Three important physical effects are left out in the VMEC approach that could modify the plasma response to MPs: plasma resistivity, rotation and the presence of a resistive wall. In a typical discharge with resonant MPs, magnetic islands at the rational surfaces can interact with the resistive wall and slow down the plasma rotation, eventually leading to locked wall modes (if the island is large enough) and to the termination of the discharge. Previous studies comparing the equilibrium plasma response between linear MHD codes and the VMEC code concluded that the fundamental differences in the obtained results are mainly attributed to the insufficient resolution of the VMEC code to properly resolve the localised singular currents appearing at rational surfaces, which in turn would shield the plasma perturbation from going further into the plasma [Tur+13; Kin+15; Laz+16]. The work presented in this chapter is focused on saturated external modes whose physical drive does not rely on an exact resonance within the plasma, thus avoiding the limitations in the VMEC code. The goal of this chapter is twofold. Firstly, we show that VMEC is a useful tool to study the plasma response to non-axisymmetric external perturbations if the physics studied is independent of the induced current at rational surfaces. This is done by comparing a very simple analytical external kink model with the 3D saturated states calculated in VMEC. Secondly, and once the first goal is achieved, we study the modification of the parameter space on saturated external modes, which have been assumed in this thesis to be the Edge Harmonic Oscillations observed during QH-mode operation in tokamak plasmas. This corresponds to an important application since robust access to QH-mode in future machines could be aided by the application of MPs.

The chapter is structured as follows. Section § 5.1 presents the analytical and numerical models of the applied non-axisymmetric MPs. Section 5.2 applies both approaches to the case of saturated external kink modes, where a quantitative comparison is presented and shown to be in good agreement. Section 5.3 presents the application of MPs to the case of saturated external modes, where a comparison between the two approaches is presented and the expansion of the parameter space for saturated external modes is explored. Finally, section 5.4 presents a summary and conclusions of the work.


 Figure 5.1: Diagram of the plasma system with an antenna at $r = b$.

5.1 Models for the non-axisymmetric magnetic perturbations

5.1.1 The antenna time-invariant linear model

The analytical model under consideration is a subset of the one reported in reference [LN88], where an external non-axisymmetric magnetic perturbation is introduced through a surface current located in the vacuum region, as shown in figure 5.1. The coordinate system (r, θ, ϕ) is again used, where r labels flux surfaces, θ is the SFL poloidal angle and ϕ is the geometrical toroidal angle. The plasma region ($\in [0, a]$) is separated from an ideally conducting wall (located at $r = c$) by a vacuum region ($\in [a, c]$). At radius $r = b$ ($a < b < c$), an antenna with a current $I_A \propto e^{i(m\theta - n\phi)}$ provides a static helical perturbed magnetic field. The equation describing the perturbed vacuum magnetic flux for each independent poloidal mode is [LN88]

$$\nabla_{\perp}^2 \Psi_m(r, \theta, \phi) = \frac{\mu_0}{b} I_A \delta(r - b) e^{i(m\theta - n\phi)}. \quad (5.1)$$

Applying the tokamak ordering (§ 2.3.2), the solutions in the regions $a < r < b$ and $b < r < c$ are given respectively by

$$\begin{aligned}\Psi_m^{(1)}(r) &= A_m(r/b)^m + B_m(r/b)^{-m} \\ \Psi_m^{(2)}(r) &= C_m(r/c)^m + D_m(r/c)^{-m},\end{aligned}\tag{5.2}$$

where the constants are determined by the boundary conditions at the interfaces and current carrying layers, which read

$$\begin{aligned}\Psi^{(2)}(c) &= 0 \\ \Psi_m^{(1)}(a+\delta) &= \frac{B_0}{m} \frac{r}{R_0} k_{\parallel}(r) \xi_m(r) \Big|_{a-\delta} \\ \Psi_m^{(1)}(b-\delta) &= \Psi_m^{(2)}(b+\delta) \\ \left[\left[r \frac{d}{dr} \Psi_m \right] \right]_b &= \mu_0 I_A,\end{aligned}\tag{5.3}$$

where $k_{\parallel} = m/q - n$ is the dimensionless parallel wave number, B_0 and R_0 are the plasma magnetic field and major radius respectively evaluated at the magnetic axis, and $\xi_m(r)$ is the radial saturated plasma displacement with the same helicity as the antenna. The first condition corresponds to the vanishing of the perturbed normal magnetic field at the ideal conducting wall. The second and third conditions are derived invoking the continuity of the normal magnetic field at the plasma-vacuum interface and at the antenna respectively. The fourth condition is found by integrating equation 5.1 across the antenna, which is the equivalent jump condition of the tangential perturbed field $\delta B_m^{\theta} = -\Psi'_m$. The constants A_m, B_m, C_m and D_m are respectively given by

$$\begin{aligned}
 A_m &= -\frac{(b/a)^m [H_m I_\xi + 2\epsilon(a/c)^{2m} k_{\parallel a}]}{2m [1 - (a/c)^{2m}]} B_0 \xi_m(a) \\
 B_m &= \frac{(b/a)^{-m} [H_m I_\xi + 2\epsilon k_{\parallel a}]}{2m [1 - (a/c)^{2m}]} B_0 \xi_m(a) \\
 C_m &= \frac{(b/c)^m [(a/b)^{2m} - 1] I_\xi + 2\epsilon(a/c)^m k_{\parallel a}}{2 [(a/c)^{2m} - 1] m} B_0 \xi_m(a) \\
 D_m &= -\frac{(b/c)^m [(a/b)^{2m} - 1] I_\xi - 2\epsilon(a/c)^m k_{\parallel a}}{2 [(a/c)^{2m} - 1] m} B_0 \xi_m(a)
 \end{aligned} \tag{5.4}$$

where $\epsilon = a/R_0$, $I_\xi = \frac{I_A \mu_0}{B_0 \xi_m(a)}$ and $H_m = [1 - (b/c)^{2m}] (a/b)^m$. Note that the perturbed magnetic field is composed of two sources. The first one corresponds to the perturbed field generated by the saturated edge plasma corrugation ($\xi_m(a)$), and the second one corresponds to the non-axisymmetric field imposed externally. Therefore, the finite amplitude mode $\xi_m(a)$ which is in force balance with the applied non-axisymmetric field already contains the plasma response. In the limit of $\xi_m(a) \rightarrow 0$, the perturbed vacuum field corresponds to that of a helical winding current between two ideally conducting toroidal surfaces. Finally, we point out that the perturbed magnetic field from the antenna considers a single helical harmonic (m, n) . In reality, non-axisymmetric coils used in fusion experiments contain a spectrum of harmonics, and coupling between them and the plasma perturbation is possible. Nevertheless, previous work shows that a single helical harmonic in straight field line coordinates quite reasonably describes the plasma response [Kin+15]. That characteristic is also shown in this chapter for saturated external kink and external modes. Note that the validity of the linear model is limited to cases where the axisymmetric plasma in the absence of MPs is stable. This is because the absence of inertial forces in the linear model that would drive the plasma out of force balance, as discussed in section 5.2.

5.1.2 The VMEC nonlinear model

The calculation of external saturated states in the VMEC free boundary equilibrium code requires a description of the vacuum magnetic field. Such field is calculated through the Biot-Savart law from a series of one dimensional filaments carrying current using the MAKEGRID code from the STELLOPT package. Since VMEC is a 3D code, the filaments are not restricted to

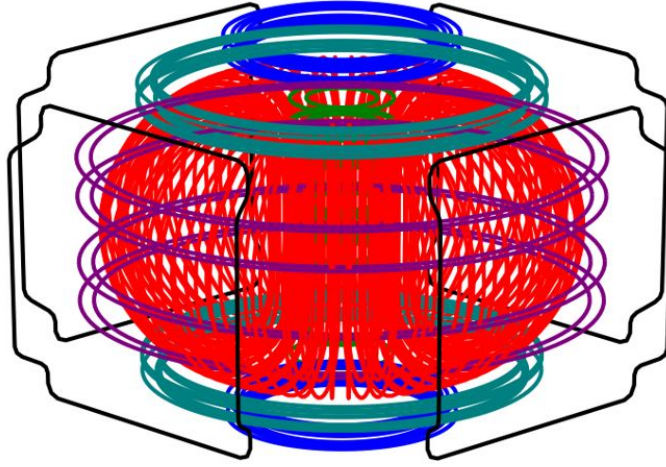


Figure 5.2: JET-like coil system, consisting on 32 toroidal coils (red), 6 poloidal coils (purple, green and blue) and 4 Error Field Correction Coils (black).

axisymmetry and MPs can easily be included by just adding a set of non-axisymmetric coils. The plasma equilibrium in VMEC is calculated self-consistently with the MPs, and therefore the plasma response is already included in the solution. A JET-like set of coils is used as illustrated in figure 5.2, consisting of 32 toroidal coils, 6 poloidal coils and 4 Error Field Correction Coils (EFCCs), where the later ones provide the non-axisymmetric perturbation. Toroidal and poloidal coils are made by 4 filaments carrying $1/4$ of the current, while the EFCCs are made by a single filament. In the JET tokamak, each EFCC contains 16 turns with a current capacity of 3 kA per turn [Bar+], resulting in a total of 48 kA per coil. Before calculating the saturated plasma states, it is useful to characterise the vacuum magnetic perturbations generated by the EFCCs. This section is also used to discuss two important numerical effects in VMEC related to 3D geometry that can influence the calculation of the equilibria and could lead to errors if not treated carefully. These effects are stellarator symmetry of the non-axisymmetric coils, and the inclusion (or exclusion) of the toroidal ripple.

While the VMEC code is able to calculate MHD equilibria without assuming any special symmetry, stellarator symmetry is chosen because the calculations are faster and have better convergence. In axisymmetric devices, stellarator symmetry is reduced to up-down symmetry, which is satisfied by the poloidal and toroidal coils in our set in figure 5.2 (refer to appendix A.1 for details). This coil set represents an up-down symmetric approximation of the real set of JET coils. If the EFCC coils are not correctly located with respect to the VMEC axis of symmetry,

5.1 Models for the non-axisymmetric magnetic perturbations

stellarator symmetry could be broken, so the geometry of the coils and the current applied to them require careful treatment. Figure 5.3a shows schematically the location of the EFCC coils in the tokamak system. Stellarator symmetry requires all scalar quantities, including current in the coils, to be mirrored about the $\phi = 0$ and $Z = 0$ planes. The current applied to coil number 1 (4) will be mirrored in coil number 2 (3), meaning that coils 1 and 2 (or 3 and 4) will flow in opposite directions, as shown in figure 5.3b. With such coil configuration it is possible to apply a dominant $n_{EFCC} = 1$ or $n_{EFCC} = 2$ vacuum magnetic perturbation without breaking stellarator symmetry by changing the current pattern in coils 1 and 4, as shown in figure 5.3b.

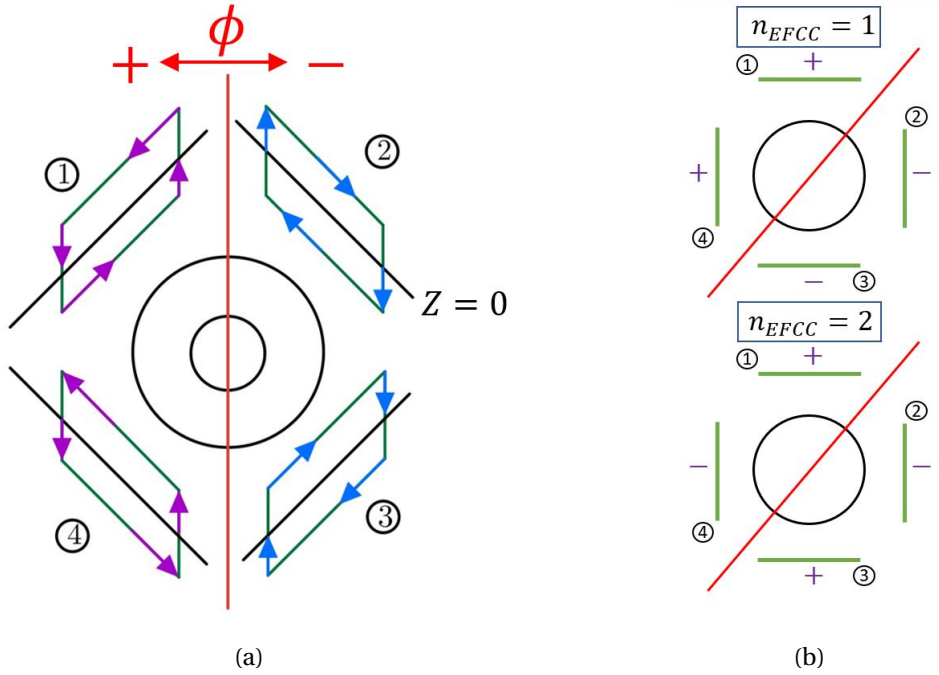


Figure 5.3: (a) Diagram of the EFCC of the JET-like set in VMEC. Stellarator symmetry means that the currents are mirrored with respect to the $\phi = 0$ plane (in red) and the $Z = 0$ plane (in black). Applied currents (in purple) in coils 1 and 4 are mirrored in coils 2 and 3 respectively (in blue). (b) Current patterns producing $n_{EFCC} = 1$ (top) or $n_{EFCC} = 2$ (bottom) dominant toroidal vacuum perturbations.

The perturbed toroidal spectrum is dominated by a $n_{EFCC} = 1$ or $n_{EFCC} = 2$ mode due to the EFCCs, but a second source of non-axisymmetric field exist because of the finite number of toroidal coils, denominated as ‘toroidal ripple’. In our JET-like coil set, the toroidal ripple has $n_{ripple} = 32$ dominant toroidal mode number. In the VMEC free-boundary code, the numerical grid considers a user-specified number of toroidal planes where the vacuum magnetic field

is to be calculated. To correctly resolve such toroidal ripple the sampling points must satisfy the Nyquist criterion, so at least 64 toroidal planes are necessary along with the inclusion of 65 toroidal modes in the VMEC Fourier expansion (equation A.2). Note that 65 toroidal modes in a VMEC equilibrium calculation corresponds to the toroidal spectrum $-32 < n_{VMEC} < 32$. The present study is not addressed to resolve the toroidal ripple nor the physics related with high- n modes. Moreover, simulations with a large number of toroidal modes generally do not converge well in VMEC and are extremely time consuming, so special care must be taken in deciding the appropriate number of toroidal planes used in the vacuum field calculation. For our JET-like set of coils, if the number of planes used is smaller than 64 (with the exception of 32,16,8,4,2), then the toroidal ripple will shift to an observable frequency due to aliasing. Figure 5.4 shows the toroidal spectrum of the radial perturbed magnetic field given by the toroidal field coils plus the EFCCs with 25, 32 and 80 planes in the VMEC numerical grid. It can be seen that using 25 coils shifts the toroidal ripple to $n_{ripple} = 32 - 25 = 7$, and that this mode is of the same order than the $n_{EFCC} = 1, 2$ produced by the EFCCs with 100kA at the LCFS. Contrary to the perturbation produced by the EFCCs, the toroidal ripple decays quite fast when going towards the magnetic axis, where the ripple is negligible compared to the EFCCs perturbed field (as seen in figure 5.4). It is noted that these modes exist on the vacuum field, but whether they will be captured by the VMEC equilibrium calculation will depend on the number of toroidal modes included in the VMEC Fourier expansion. For example, in a VMEC simulation with 30 toroidal planes, a ‘fictitious’ $n_{ripple} = 32 - 30 = 2$ vacuum perturbation will be included in the equilibrium calculation if $-2 < n_{VMEC} < 2$ toroidal modes are allowed in the VMEC Fourier expansion. Here relies the importance to carefully choose the number of toroidal planes in the calculation of the vacuum field, specially when studying the effect of externally applied MPs. The most sensible choice for our study is to completely eliminate the toroidal ripple, which is done by choosing 32 (or 16) toroidal planes in the VMEC numerical grid so that each plane coincides with a toroidal coil, giving the effect of an axisymmetric vacuum field coming from the toroidal field coils (as shown in figure 5.4).

The antenna model described in the previous section only considers a single helical mode (m, n) , while the EFCCs in our JET-like coil set have a wider toroidal and poloidal spectrum. To make a proper comparison with the analytical model, the poloidal *vacuum* spectrum in the VMEC simulations must be resolved in SFL coordinates. This is done by calculating the perturbed vacuum field from the EFCC coils alone using the MAKEGRID code. The cylindrical components of the obtained field $(\delta B^R, \delta B^Z, \delta B^\phi)$ are extracted at the location of the LCFS of

5.1 Models for the non-axisymmetric magnetic perturbations

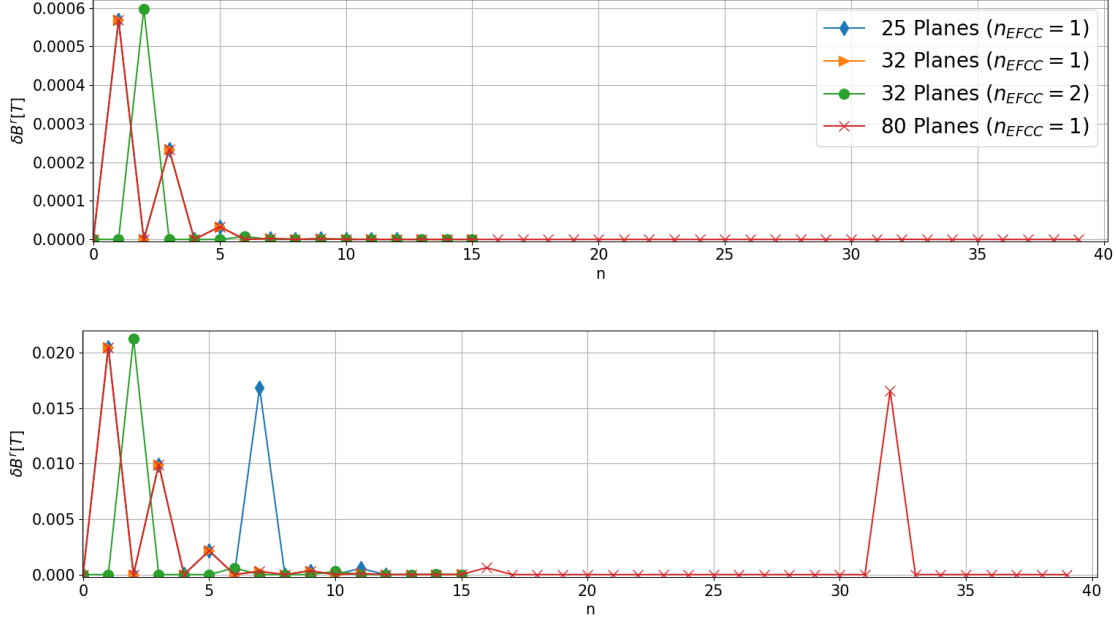


Figure 5.4: Toroidal Fourier decomposition of the vacuum magnetic field perturbation at the magnetic axis (up) and at the last closed flux surface (b) using different number of poloidal planes in the VMEC numerical grid. Note that the toroidal ripple shifts to an observable frequency if not enough planes are used. Also note that the toroidal ripple disappears if 32 planes are used. The current at the EFCCs was set to 100 kA for the calculation.

the neighbouring axisymmetric VMEC equilibria ($R(S=1, \theta_{SFL}), Z(S=1, \theta_{SFL})$), where θ_{SFL} is the SFL poloidal angle in VMEC. The components of the perturbed vacuum magnetic field in flux coordinates are calculated through the transformation

$$\begin{pmatrix} \delta B^s \\ \delta B^\theta \\ \delta B^\phi \end{pmatrix} = \begin{pmatrix} \partial_s R & \partial_\theta R & 0 \\ \partial_s Z & \partial_\theta Z & 0 \\ 0 & 0 & R \end{pmatrix}^{-1} \begin{pmatrix} \delta B^R \\ \delta B^Z \\ \delta B^\phi \end{pmatrix}, \quad (5.5)$$

so that the vacuum EFCC field in the normal direction to the plasma

$$\delta B_{EFCC}^r = \frac{R}{\mathcal{J}} \left[\frac{\partial Z}{\partial \theta} \delta B^R - \frac{\partial R}{\partial \theta} \delta B^Z \right] \frac{d}{dr} S \quad (5.6)$$

can be Fourier decomposed and compared to the analytical vacuum field from the antenna in the absence of a plasma

$$\delta B_{antenna}^r = -i \frac{H_m}{2a} \mu_0 I_A. \quad (5.7)$$

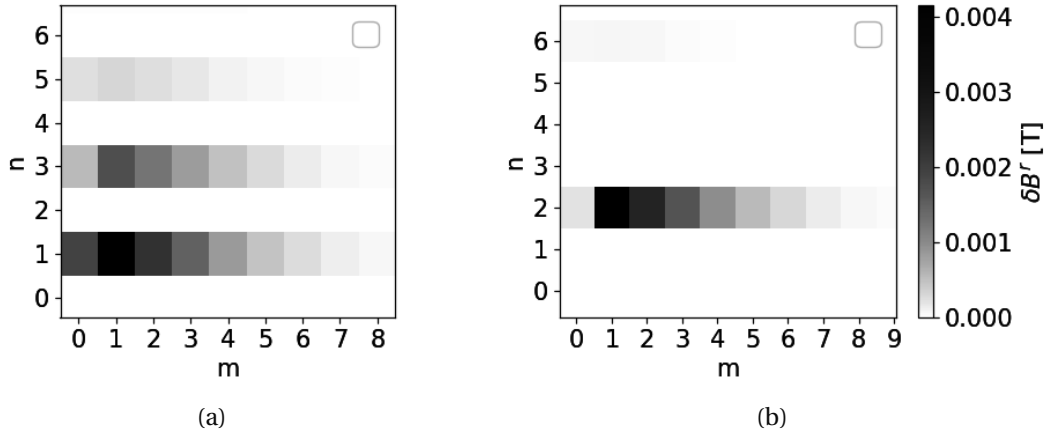


Figure 5.5: Poloidal and toroidal spectrum of the perturbed vacuum radial magnetic field δB_{EFCC}^r in SFL coordinates for (a) $n_{EFCC} = 1$ and (b) $n_{EFCC} = 2$ externally applied modes. Note that 32 toroidal planes in the VMEC numerical grid were used to eliminate the toroidal ripple.

In equations 5.5 and 5.6, R and Z describe the flux surfaces in the neighbouring axisymmetric VMEC equilibria, \mathcal{J} is the corresponding Jacobian and $S = \psi / \psi_{edge}$ is the radial VMEC flux function, which can be either the normalised toroidal or poloidal flux (see appendix A.1 for details). Figure 5.5 shows the spectrum of δB_{EFCC}^r in SFL coordinates at the LCFS for a $n_{EFCC} = 1$ and a $n_{EFCC} = 2$ mode applied by the EFCCs. As can be seen, the amplitude of the mode decays with increasing poloidal mode number, although the $m = 1$ mode is dominant in both cases. Even though the spectrum of the vacuum MP contains many harmonics, when comparing the VMEC results with analytic model it is assumed that only the vacuum component with the same helicity in SFL as the saturated edge mode has an effect in the final equilibrium state.

5.2 MP-induced saturated external kink modes

A non-resonant saturated external kink mode constitutes a good case of study for our analysis with the VMEC code and for the comparison with the analytical work because no singular ‘screening’ currents nor magnetic islands are formed in response to the MPs. It is also the simplest experimentally relevant external mode to analyse. It has been observed theoretically that marginally stable external kink modes grow and saturate in the presence of MPs [Boo01], and thus they might be related to the avoidance of ELMs in AUG and DIII-D discharges [Ora+17]. Finally, external kink modes are intrinsically connected with the external modes discussed in the previous chapters and in the following section of the present chapter.

5.2.1 Linear equilibrium equation for the analytic treatment of external kink modes with MP

The ideas on this chapter were partially discussed in section 2.5.1. Ideal MHD saturated instabilities typically exist in a plasma as a consequence of the nonlinear evolution of an unstable mode. Regardless of the dynamics that leads to saturation, the final plasma state is a solution of the ideal MHD 3D equilibrium equation. For certain types of modes, the equilibrium solutions can be found using the *linearised* ideal MHD equilibrium equation. To lowest order, a time invariant perturbation with mode number (m, n) satisfies Newcomb’s equation (2.56), introduced in section § 2.4.2 and repeated here once more for convenience,

$$\frac{d}{dr} \left[r^3 k_{\parallel}^2 \frac{d}{dr} \xi_m \right] - r(m^2 - 1) k_{\parallel}^2 \xi_m = 0, \quad (5.8)$$

where $\xi_m(r)$ inside the plasma is fully determined by adequate boundary conditions, given by equations 5.2 and 5.3. Integrating equation 5.8 across the plasma-vacuum interface gives

$$\left[k_{\parallel}^2 \frac{d}{dr} \xi_m \right]_a = 0, \quad (5.9)$$

where we note that ξ'_m is discontinuous across the boundary since $\delta B_m^{\theta} = \psi'_m \sim \xi'_m$ corresponds

to the jump of the tangential magnetic field. On the other hand, ξ_m is continuous across the boundary due to the continuity of the normal field ($\xi_m(a) \sim \delta B_m^r$), so we can divide the whole equation by the non-zero mode amplitude $\xi_m(a)$. On the vacuum side of $r = a$, we substitute $\xi_m = -i \frac{R_0}{B_0 k_{\parallel}} \delta B_m^r|_{a+\delta}$, giving the equilibrium condition

$$k_{\parallel}^2(a) \left(\frac{r}{a} [ln(\xi_m)]' \Big|_{a-\delta} - \left[ln \left(\frac{\delta B_m^r}{k_{\parallel}} \right) \right]' \Big|_{a+\delta} \right) = 0, \quad (5.10)$$

with two independent solutions

$$q(a) = m/n$$

$$\mathcal{B}_m = r \left[ln \left(\frac{\delta B_m^r}{k_{\parallel}} \right) \right]' \Big|_{a+\delta}. \quad (5.11)$$

where $\mathcal{B}_m = r [ln(\xi_m)]'|_{a-\delta}$ is typically calculated numerically from equation 5.8. The first solution is independent from the applied MP and corresponds to $k_{\parallel}(a) = 0$, giving a resonance at the plasma edge. For such a solution, the plasma response to a helical displacement will drive a singular current at the boundary to screen the magnetic perturbation, which as discussed in the introduction to this chapter, is not well represented in the VMEC code [Laz+16; Rei+15]. Moreover, the assumed boundary conditions neglect surface currents, so the physics included in the present model is incomplete¹. For these reasons, this work will not focus on the first equilibrium solution. The second equilibrium solution correspond to the parenthesis term in equation 5.10 equal to zero, where we note that δB_m^r contains both the perturbed field due to the saturated edge plasma corrugation and from the antenna. Substituting the solution to the perturbed vacuum field (5.2) gives an equation for the function I_{ξ}

$$H_m I_{\xi} = - \frac{\epsilon \left[m(m-1 + \mathcal{B}_m + (a/c)^{2m}(m+1 - \mathcal{B}_m)) - (a/c)^{2m}(m-1 - \mathcal{B}_m)nq_a - (m+1 + \mathcal{B}_m)nq_a \right]}{mq_a}, \quad (5.12)$$

¹A generalisation to include surface currents can be made without much difficulty by applying the boundary conditions described by Friedberg [Fre14], p. 356-358.

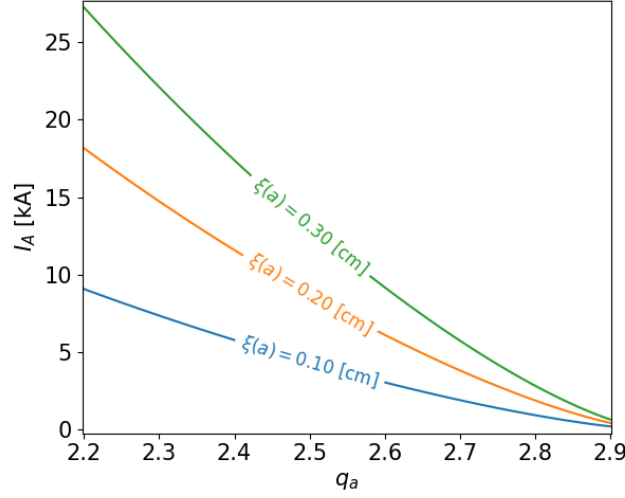


Figure 5.6: Necessary current in the antenna to obtain a saturated external kink mode of different amplitudes as a function of the edge safety factor q_a .

where the right hand side only depends on equilibrium parameters without the application of the MPs. Note that if $I_\xi = 0$, then equation 2.55 is exactly recovered. Equation 5.12 contains the solution to equations 5.1 and 5.8, and represents a plasma in equilibrium with a finite perturbation at the edge $\xi_m(a)$ when applying a current I_A to the antenna. One of the goals of this study is to verify this relation in the VMEC code, which will be achieved in section § 5.2.2. Though in this chapter we solve only for equilibrium states, it is useful to think of the problem in terms of the stability of the plasma in the absence of MPs. If the axisymmetric plasma is at marginal stability, then $I_A = 0$ is the only solution to equation 5.12 because the plasma is already in equilibrium to lowest order for an arbitrary perturbation amplitude. If the plasma is stable, then equation 5.12 will give the necessary current such that a saturated plasma perturbation with finite amplitude $\xi_m(a)$ remains in equilibrium with the perturbed field coming from the antenna. If the plasma is unstable, the linear analytical model predicts that the MPs would restore the plasma to force balance by creating a small amplitude external kink in equilibrium with the applied field perturbation. Note however that such scenario is not physical because the inertial forces that are in action when a finite growth rate is present are not captured by the linear equilibrium model [Tur12].

Let us consider a Wesson-like current density profile $j_\phi(r) = j_0[1 - (r/a)^2]^\nu$ [Wes78], which gives $q(r) = \frac{q_a(r/a)^2}{1 - [1 - (r/a)^2]^\nu}$ and $q_a/q_0 = 1 + \nu$. For such profile, equation 5.8 has to be solved

numerically in order to evaluate \mathcal{B}_m . By choosing $q_0 = 1.2$ an external kink with mode number ($m = 3, n = 1$) is unstable in the region $2.95 < q_a < 3$ in the absence of MPs. Figure 5.6 shows the evaluation of equation 5.12, where the necessary current to obtain a plasma equilibrium with saturated amplitude $\xi_m(a)$ is calculated as a function of the safety factor at the plasma boundary. It is found that a small amplitude saturated external kink mode can be induced with a modest current in the antenna over a region of the parameter space where an external kink is stable in the absence of MPs. Note that at marginal stability ($q_a \sim 2.95$) all curves converge to zero current, which is the only equilibrium solution for an arbitrary amplitude mode, consistent with the linear theory. The parameters used in the calculation are $a = 1.09m$, $b = 3.8m$, $c \rightarrow \infty$, $R_0 = 3.02m$ and $B_0 = 2.3T$, which roughly correspond to the JET-like plasma discussed in the next section.

5.2.2 Comparison with 3D states calculated with the VMEC code

Now that we have calculated the saturated amplitude of external kinks in the presence of an antenna producing a single helicity MP, we proceed to verify numerically that the physics included in our linear estimation can describe some of the main features of the saturated external kink modes. This is done by calculating the equilibrium states using the VMEC code under the application of MPs.

The calculation of 3D saturated states in VMEC follows the procedure outlined in section § 2.5.1, and exemplified in section § 3.3.1. In summary, a free boundary VMEC equilibria is calculated in 3D geometry along with its neighbouring axisymmetric state, where the later is obtained by restricting $n = 0$ toroidal modes in the VMEC Fourier expansion. Then, the nonlinear normal saturated plasma displacement is calculated by subtracting the 3D surface from the 2D surface at each location in the normal direction of the 2D surface. We point out that saturated external kink modes have already been successfully obtained using the VMEC code [Kle+18].

Following the analytical example outlined above, we use a Wesson-like current profile, with $q_0 = 1.2$ so that a cylindrical plasma would be external kink unstable in the interval $2.95 < q_a < 3$. The pressure profile is given by $P(s) = P_0(1 - s^2)$, where $P_0 = \beta_0 B_0^2 / (2\mu_0)$ with $\beta_0 = 0.02$ and $B_0 = 2.7T$. Here, $s = \sqrt{\psi_t / \psi_{t_{edge}}}$. Both the safety factor and pressure profiles are plotted in figure 5.7b. An almost circular cross section (weak triangularity and elongation) is used to improve the comparison with the analytical results. Figure 5.7a shows the LCFS at different

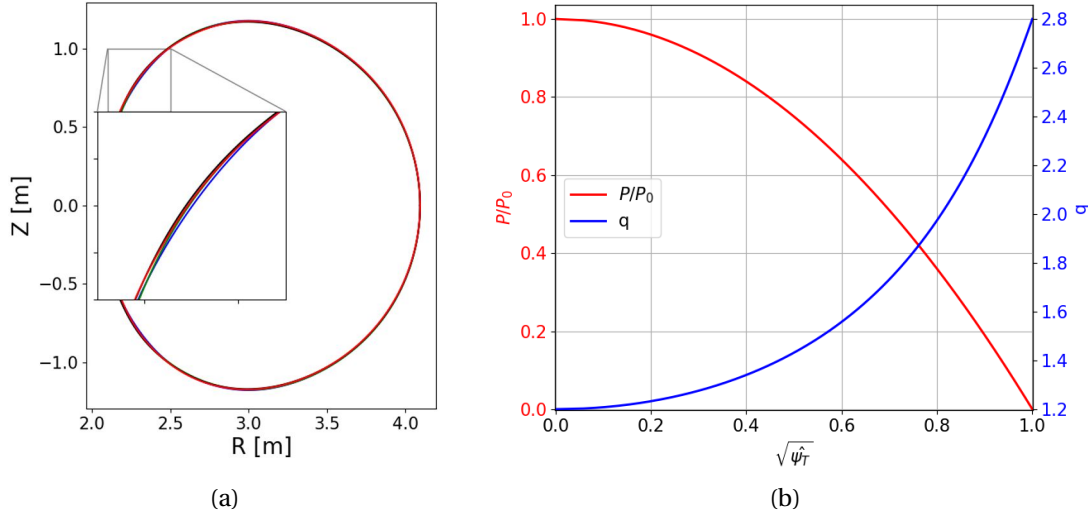


Figure 5.7: (a) Last closed flux surface of a VMEC equilibria with a Wesson-like current density profile at different toroidal angles. Note that there is a weak 3D perturbation visible by the mismatched surfaces. (b) Corresponding safety factor and pressure profiles.

toroidal angles for the case of $q_a = 2.8$, where we note that there is a weak 3D perturbation. The necessary currents in the coil set that are needed to produce this particular equilibrium are calculated using the VMEC fixed-boundary and FreeGS codes, as described in section § 3.3.1.

Figure 5.8a shows the saturated amplitude of the ($m = 3, n = 1$) nonlinear displacement as a function of q_a . A small saturated displacement exists between $2.7 < q_a < 3.1$ in the absence of MPs. This corresponds to a somewhat broader region than the range over which the analytical cylindrical model is unstable. Therefore, a comparison with the analytical model should consider $q_a < 2.7$. It can be seen that the amplitude of the saturated plasma displacement increases with the current applied to the EFCCs, and moreover, the parameter space where such equilibrium modes can be obtained is also expanded with the application of the non-axisymmetric MPs, consistent with our linear equilibrium theory (figure 5.6). We clarify that the saturated states calculated without MPs adopt a completely axisymmetric vacuum magnetic field, but an initial perturbation on the magnetic axis guess is necessary to steer VMEC towards a converged 3D state [Coo+10; Coo+11]. The Fourier decomposition of the nonlinear saturated displacement is plotted in figure 5.8b for $q_a = 2.8$ without the application of MPs, showing that the 3D state does indeed correspond to a saturated external kink. Note in particular that the coupling between poloidal modes is very weak, as the main ($m = 3, n = 1$) external kink strongly

dominates the spectrum. This makes our comparison with the analytical model more viable.

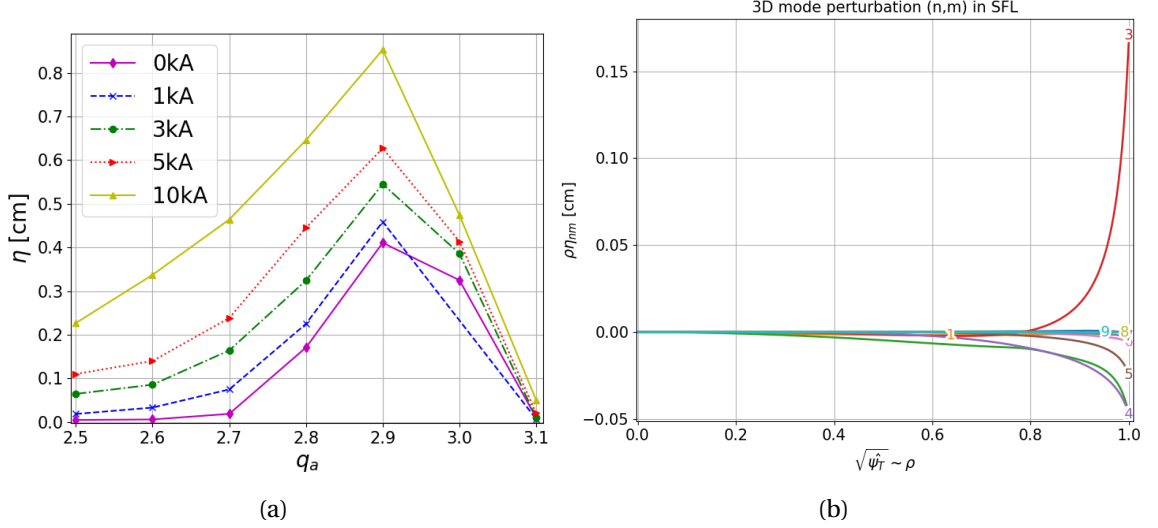


Figure 5.8: (a) ($m = 3, n = 1$) Fourier component of the nonlinear saturated plasma displacement calculated in VMEC at different applied currents as a function of the value of the edge safety factor q_a . (b) Poloidal spectrum of the nonlinear saturated plasma displacement with $n = 1$ for a Wesson-like current density profile, with $q_0 = 1.2$ and $q_a = 2.8$.

To make a quantitative comparison between the analytical model and the 3D saturated states obtained in VMEC, we plot the amplitude of the saturated ($m = 3, n = 1$) mode as a function of the vacuum radial perturbed magnetic field calculated through equation 5.7 for the linear equilibrium analytical model, and through equation 5.6 for the full nonlinear VMEC equilibria. As shown in figure 5.9, good agreement between the two approaches is obtained for cases where the axisymmetric equilibrium is stable in the absence of MPs. Three important implications can be derived from this result. The first one is that it seems that non-resonant saturated external perturbations can be accurately modelled with linear theory in the frame of ideal MHD provided that the mode is stable or only weakly unstable in the absence of MPs. The second one is that MPs could be used to expand the parameter space for the saturation of external instabilities. The third one is that since good agreement is found between the full nonlinear solution and the simplified one in cylindrical geometry, poloidal coupling of the plasma response with different harmonics of the MPs does not seem to be important, at least when the effect of the MPs is dominant. Finally, we point out that agreement between the analytical model and VMEC for cases where the equilibrium is external kink-unstable in the

absence of MPs was not obtained, which is in line with our previous prediction that the linear equilibrium model is inconsistent due to the absence of plasma inertia and the 3D nonlinear corrections associated with nonlinear saturation in the absence of the antenna. Instead, the MPs seem to enhance amplitude of the existent saturated external kink, as shown in figure 5.8a.

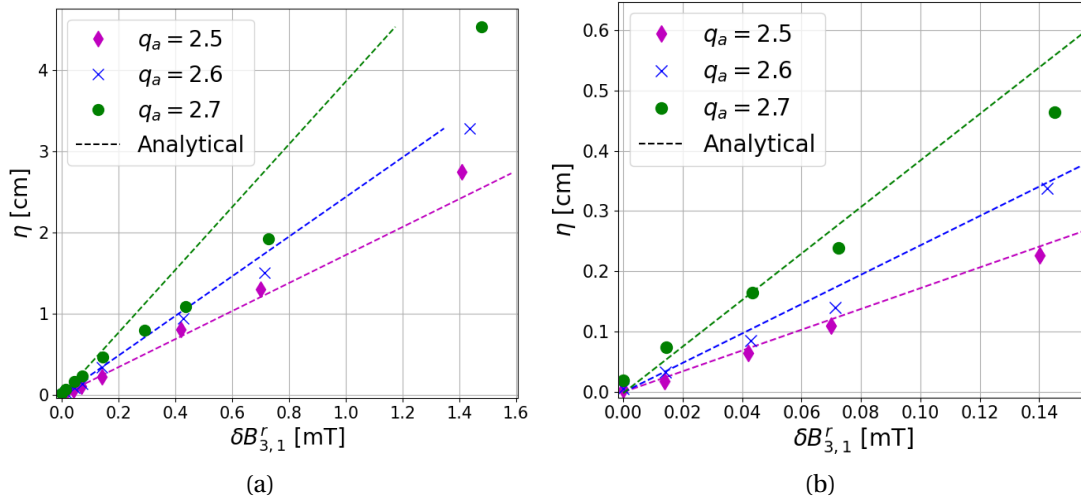


Figure 5.9: (a) Saturated amplitude of the external kink mode at the plasma edge as a function of the single helicity radial perturbed magnetic field. VMEC calculation (shown by the markers) is compared with the analytical estimation of our linear model (dashed lines) in equation 5.12. (b) Zoom over the region where the saturated amplitude is small, and thus where the analytical model is more valid.

5.3 MP-induced saturated external modes

As discussed at length during this thesis, an external mode couples an infernal instability drive located in the pedestal region with its upper sideband external kink drive. It has been shown in the previous section that saturated external kink modes can be induced by the use of externally applied MPs, so it is expected that MPs have a similar effect on external modes as well.

5.3.1 Linear equilibrium equation for external modes with MP

The analytical model of the plasma considers equilibrium profiles containing the key aspects observed during QH-mode, as described in section § 3.2, figure 3.3a. The safety factor monotonically increases in the region $r \in [0, r_p]$, where r_p is the radius of the pedestal top. Then the safety factor is flat in the region $r \in [r_p, a]$. For simplicity, only the case of zero magnetic shear is discussed, though a description of the equations with finite shear is given in appendix B.2. The antenna is again placed in the vacuum region, between the plasma boundary and the ideal wall. As discussed in section § 3.2, we separate the plasma into two regions, a high-shear and a low-shear region. The physics involving the external drive is on the low-shear region, located at the plasma pedestal. The equation describing an external time-invariant perturbation with mode number (m, n) is given by [HH88; GH96; Bru+18b]

$$\begin{aligned} \frac{d}{dr} \left[r^3 \left(\frac{1}{q} - \frac{1}{q_s} \right)^2 \frac{d}{dr} \xi_m \right] + \left[(1 - m^2) \left(\frac{1}{q} - \frac{1}{q_s} \right)^2 + \frac{\alpha}{q^2} \frac{r}{R_0} \left(\frac{1}{q^2} - 1 \right) \right] r \xi_m \\ + \frac{\alpha}{2q^2} \left[\frac{r^{1+m}}{1+m} L_+ + \frac{r^{1-m}}{1-m} L_- \right] = 0, \end{aligned} \quad (5.13)$$

where $q_s = m/n$ and the constants L_{\pm} appear after integration and substitution of the sideband equations

$$(r^{2\pm m} \xi_{m\pm 1})' = L_{\pm} r^{1\pm 2m} + \frac{1 \pm m}{2} r^{1\pm m} \alpha \xi_m. \quad (5.14)$$

Note that the saturated amplitude of the main mode and of the sidebands is in force balance with the applied external MP. The solution to equation 5.13 gives the linear equilibrium amplitude of the main mode in terms of the applied current in the antenna, which is embedded in the constants $L_{\pm} = L_{\pm}(I_A)$. It is therefore necessary to calculate the constants L_{\pm} in terms of the saturated amplitude of the main mode $\xi_m(r)$. Evaluation of equation 5.14 at $r = r_p$ and $r = r_a$ gives

$$\begin{aligned}\xi_{m\pm 1}(r_p) &= \frac{r_p^{\pm m} L_{\pm}}{2 \pm m + \mathcal{C}_{\pm}} \\ \xi_{m\pm 1}(a) &= \frac{a^{\pm m} L_{\pm}}{2 \pm m + \mathcal{B}_{\pm}},\end{aligned}\tag{5.15}$$

where $\mathcal{C}_{\pm} = r_p \xi'_{m\pm 1}(r_p) / \xi_{m\pm 1}(r_p)$ is calculated from the cylindrical solution of the sideband equations in the low-shear region: $r \in [0, r_p]$. Assuming Dirichlet boundary conditions for the main mode at $r = r_p$ and $r = a$ [Bru+18b; BGB21], the function $\mathcal{B}_{\pm} = a \xi'_{m\pm 1}(a) / \xi_{m\pm 1}(a)$ takes the same form as equation 5.11. Note that the vacuum MP is now assumed to be composed of two different harmonics corresponding to the upper and lower sideband helicities. The main harmonic is only affected by the MPs through coupling with the sidebands since the Dirichlet boundary condition at $r = a$ prohibits a direct effect from the vacuum perturbation. Integrating equation 5.14 in the interval $[r_p, a]$ gives

$$r^{2\pm m} \xi_{m\pm 1} \Big|_{r_p}^a = \frac{r^{2(1\pm m)} L_{\pm}}{2(1\pm m)} \Big|_{r_p}^a + \frac{1\pm m}{2} \int_{r_p}^a \alpha r^{1\pm m} \xi_m dr.\tag{5.16}$$

Finally, equations 5.11, 5.15 and 5.16 are solved for the constants L_{\pm}

$$L_{\pm} = \frac{a^{-2(1\pm m)} (1\pm m)^2 (2\pm m + \mathcal{C}_{\pm}) \left[(2\pm m + \mathcal{B}_{\pm}) \epsilon \mathcal{D}_{\pm} \pm 2a^{2\pm m} H_{\pm} \frac{I_A \mu_0}{B_0} \right]}{\epsilon \left[(2\pm m + \mathcal{C}_{\pm})(\pm m - \mathcal{B}_{\pm}) - (r_*/a)^{2(1\pm m)} (\pm m - \mathcal{C}_{\pm})(2\pm m + \mathcal{B}_{\pm}) \right]}\tag{5.17}$$

where $\mathcal{D}_{\pm} = \int_{r_p}^a \alpha r^{1\pm m} \xi_m dr$ and we have redefined

$$\begin{aligned}H_{\pm} &= \frac{[1 - (b/c)^{2(m\pm 1)}] (a/b)^{m\pm 1}}{[(m\pm 1)/q_a - n] [1 - (a/c)^{2(m\pm 1)}]} \\ \mathcal{B}_{\pm} &= \lim_{I_A \rightarrow 0} a \frac{\xi'_{m\pm 1}(a)}{\xi_{m\pm 1}(a)}.\end{aligned}\tag{5.18}$$

It is noted that in the limit of $I_A \rightarrow 0$, the definition of the constant L_{\pm} from previous papers

is recovered [HH88; GHH96; Bru+18b]. The amplitude of the antenna-driven, linearised equilibrium external mode is obtained by the solution of equation 5.13, which is an integro-differential equation for $\xi_m(r)$ in the region $r \in [r_p, a]$. Such an equation would typically be solved numerically. Nevertheless, a rough estimate of the linear equilibrium amplitude can be obtained by assuming a simplified pressure profile [Bru+18b]: $\alpha \propto P' = -P_p \delta(r - r_*)$ with $r_p < r_* < a$. We then have $\mathcal{D}_\pm = \hat{\beta}_* \epsilon_*^{-1} r_*^{2\pm m} \xi_m(r_*)$, with $\hat{\beta}_* = 2P_* q^2 / B_0^2$ and $\epsilon_* = r_* / R_0$. By writing the constants L_\pm and I_ξ as

$$I_\xi = \frac{I_A \mu_0}{B_0 \xi_m(r_*)} \quad (5.19)$$

$$L_\pm = (1 \pm m) r_*^{\mp m} \epsilon_*^{-1} \xi_m(r_*) (\Lambda_\pm \hat{\beta}_* + G_\pm H_\pm I_\xi),$$

where we note that the constants Λ_\pm are identical to those obtained in section 4.6.2 (equation 4.24), equation 5.13 can be integrated across r_* to give

$$I_\xi = -\frac{2\epsilon_*^2}{(H_+ G_+ + H_- G_-) \hat{\beta}_*} \left(\frac{1}{2\epsilon_*^2} \hat{\beta}_*^2 (\Lambda_+ + \Lambda_-) + \left[\frac{r \xi'_m}{\xi_m} \right]_{r_*} \frac{\Delta q^2}{q_s^2} + \left(\frac{1}{q^2} - 1 \right) \hat{\beta}_* \right). \quad (5.20)$$

It is pointed out that in the limit of $I_A \rightarrow 0$, equation 5.20 satisfies the marginal stability equation for external modes [Bru+18b]. In the open intervals $[r_p, r_*)$ and $(r_*, a]$, the equation for ξ_m 5.13 reduces to Newcomb's equation (5.8) with $k_\parallel = \text{constant}$, and the solution takes a very simple form (equation 5.8 in [Bru+18b]), leading to

$$\left[\frac{r \xi'_m}{\xi_m} \right]_{r_*} = \frac{2m [(r_*/r_p)^{2m} - (r_*/a)^{2m}]}{[(r_*/r_p)^{2m} - 1] [(r_*/a)^{2m} - 1]} \sim -\frac{2(a + r_p)}{a - r_p}. \quad (5.21)$$

To evaluate equation 5.20 it is necessary to solve Newcomb's equation in the high-shear region to calculate the constants \mathcal{C}_\pm . For that purpose, the following shape of the safety factor profile is used

$$q(r) = \begin{cases} \frac{q_0(\kappa+n)}{\kappa[1-(r/r_-)^\mu]+n} & \text{if } r \in [0, r_p], \\ q_p & \text{if } r_p \leq r \leq a \end{cases} \quad (5.22)$$

where m, n are the poloidal and toroidal mode numbers of the main infernal mode, r_- roughly defines the radius of the lower sideband rational surface, q_0 is the safety factor at the magnetic axis, μ defines how peaked is the profile, and the constant κ guarantees the continuity of the profile at $r = r_p$.

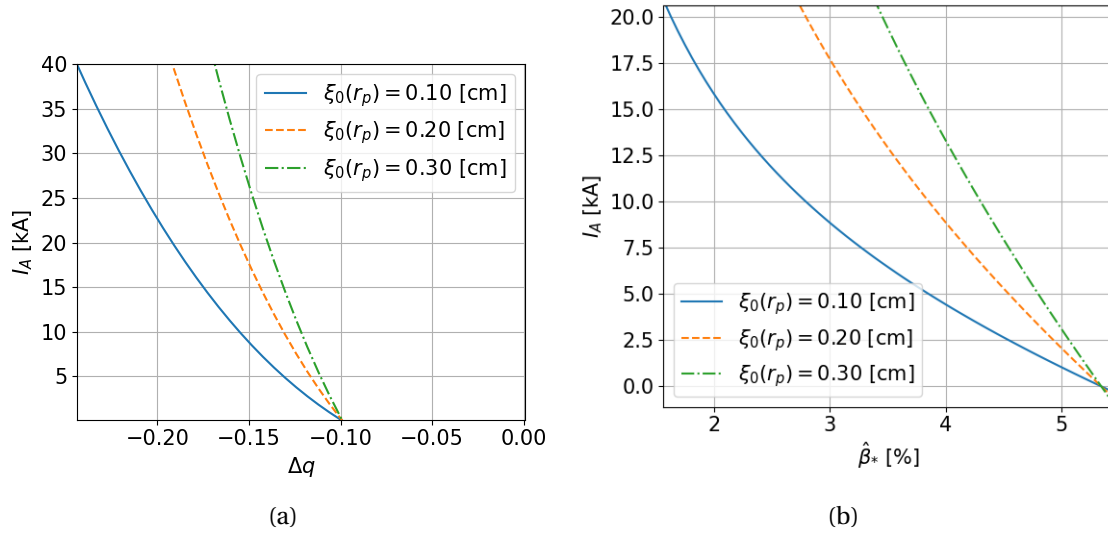


Figure 5.10: Necessary current in the antenna to obtain a saturated external mode of different amplitudes as a function of (a) the distance to the rational surface in the pedestal (Δq) and (b) the value of $\hat{\beta}_*$. Figure (a) considers $\hat{\beta}_* = 0.045$, and figure (b) considers $\Delta q = -0.12$.

Figure 5.10 shows the antenna current as a function of the value of Δq and $\hat{\beta}_*$, corresponding to the evaluation of equation 5.20 for different values of the linearised equilibrium amplitude. It is pointed out that all curves converge to zero at $\Delta q \sim -0.1$ in figure 5.10a, and at $\hat{\beta}_* = 5.2\%$ in figure 5.10b. These points in the parameter space correspond to the marginally stable points in the absence of MPs. The parameters used in this calculations were $a = 1.14$ m, $b = 2.40$ m, $c = \infty$, $\epsilon_* = 0.40$, $r_p/a = 0.95$, $r_-/a = 0.85$, $B_0 = 2.5$ T, $\mu = 0.6$ and $q_0 = 1.2$, which roughly correspond to the JET-like QH-mode plasma calculated in the next section.

5.3.2 Comparison with 3D states calculated with the VMEC code

Once more, we follow the procedure outlined in section § 2.5.1 to calculate the 3D saturated states in VMEC. For the comparison in this section, a more realistic QH-mode-like equilibria is investigated, which is plotted in figure 5.11. Note that the safety factor is the same as in the analytical model given by equation 5.22, with the exception of the spike at the edge that takes the value of q_a above the $(m = 4, n = 1)$ rational surface. The effect of such a spike on the stability of the plasma was discussed in section § 4.6, and the particular consequences of the spike on the interaction with external MPs will be discussed below. Figure 5.11a shows the LCFS of the 3D saturated equilibria at different toroidal angles in the absence of MPs, revealing a strong 3D distortion of the plasma edge. Such 3D distortion corresponds to a saturated external mode, which is speculated to be the EHOs observed during QH-mode operation. The large amplitude of the saturated mode found by VMEC is similar to what is was found in previous studies of QH-mode operation in JET-like plasmas [Kle+18; BGB21].

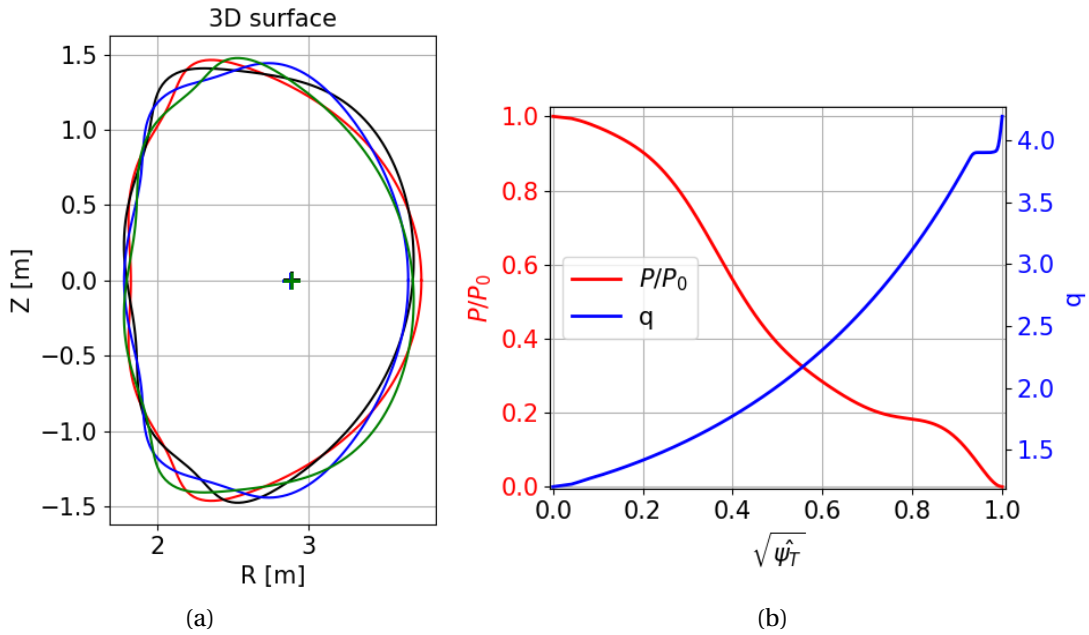


Figure 5.11: (a) LCFS at equally spaced toroidal angles in QH-mode equilibrium with $q_p = 3.98$ and without the application of MPs. (b) Pressure and safety factor profiles in VMEC.

A quantitative comparison between the analytical equilibrium model and the VMEC results is more challenging for this more advanced case because of a number of reasons. Firstly, due to all the simplifications in the derivation of equation 5.20 (step-like pressure profile,

flat safety factor, etc.). Secondly, the vacuum perturbed magnetic field affecting each of the sideband harmonics scales differently in both approaches, i.e. $\frac{\delta B_{EFCC}^r(m-1,n)}{\delta B_{EFCC}^r(m+1,n)} \neq \frac{\delta B_{antenna}^r(m-1,n)}{\delta B_{antenna}^r(m+1,n)}$. This is because in the analytical model the vacuum perturbed magnetic field scales with the poloidal mode number m as given by equation 5.7, while in VMEC it follows the EFCC poloidal geometry (figure 5.5). Nevertheless, examination of the linear eigenfunctions of marginal cases without the application of MPs show that the lower sideband vacuum connection is also weak. Therefore, we can neglect the effect of MPs on the lower sideband and only consider the $(m+1, n)$ Fourier component of the vacuum radial perturbed field in both approaches. Thirdly, the value of the safety factor at the boundary is different in both approaches since the analytical model does not require a spike at the plasma edge. Note that the coupling between the upper sideband external kink drive with the MPs is highly sensitive to the value of q_a . While some of these difficulties could be avoided by numerically solving the integro-differential equation 5.13, a direct evaluation of our analytical estimation (5.20) gives a rough approximation of the saturated amplitude.

In order to compare the two approaches we need to analyse an equilibrium that is linearly stable in the absence of MPs. We choose $q_p = 3.88$, which corresponds to a point with vanishing nonlinear amplitude of the plasma displacement in the absence of MPs (see figure 5.13a). The comparison is shown in figure 5.12. The saturated amplitude in VMEC has a linear dependency on the $(m=5, n=1)$ component of the vacuum radial perturbed field, similar to the analytical model. Moreover, the calculated saturated amplitude of the plasma displacement in both approaches is of the same order of magnitude. The difference in the slope between the two approaches could be due to the reasons mentioned above. We point out that the vacuum radial perturbed field in the nonlinear numerical approach is only the one corresponding to the upper sideband helicity ($m=5, n=1$). In the linear analytical approach, the current I_A in equation 5.20 is substituted by δB_{m+1}^r using equation 5.7. Then it is assumed that $G_+/G_- \ll 1$ (which for our case is $\sim 10^{-2}$) to isolate δB_{m+1}^r from the amplitude of the mode $\xi_m(r_*)$.

5.3.3 Beyond linear modelling: The extended parameter space of saturated external modes

One of the main goals of this work is to verify that EHOs (or saturated external modes) can be induced over a wider parameter space with the assistance of externally applied magnetic perturbations. In the previous section it was shown using analytical and numerical approaches

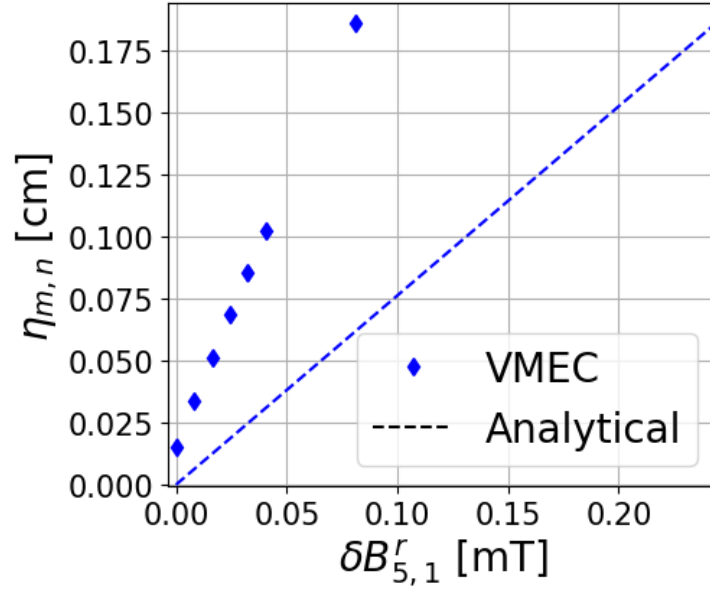


Figure 5.12: Saturated amplitude of the main infernal mode ($m = 4, n = 1$) at the pedestal calculated in VMEC and in the analytical model as a function of the ($m = 5, n = 1$) Fourier component of the vacuum radial perturbed magnetic field. The value of the safety factor plateau is $q_p = 3.88$, where the mode is stable and very close to marginal stability in the absence of MPs.

that MPs can indeed be used for such purposes. Now we go beyond the validity of the linear model and analyse the effect of MPs also in cases where the plasma is external-unstable in the absence of MPs. Figure 5.13a shows the saturated amplitude of the main infernal ($m = 4, n = 1$) mode at the pedestal as a function of the value of the safety factor plateau q_p and magnetic shear s over the pedestal region. A significant expansion of the parameter space is observed for both parameter scans. Since the amplitude of the saturated modes is not small anymore, the validity of the linear model is limited even for the cases where the external modes were induced only by the MPs (i.e. cases that are external-stable in the absence of MPs). Still, it is possible to check that the same external mode is excited with and without MPs at different regions of the parameter space by analysing two equilibria with similar amplitude with and without MPs. Figure 5.13b shows the poloidal Fourier spectrum of the nonlinear saturated plasma displacement for $q_p = 3.98$ at 0 kA, and for 3.90 at 100 kA. As can be seen, the exact same mode is observed, confirming that the parameter space of static external modes is expanded by the application of MPs.

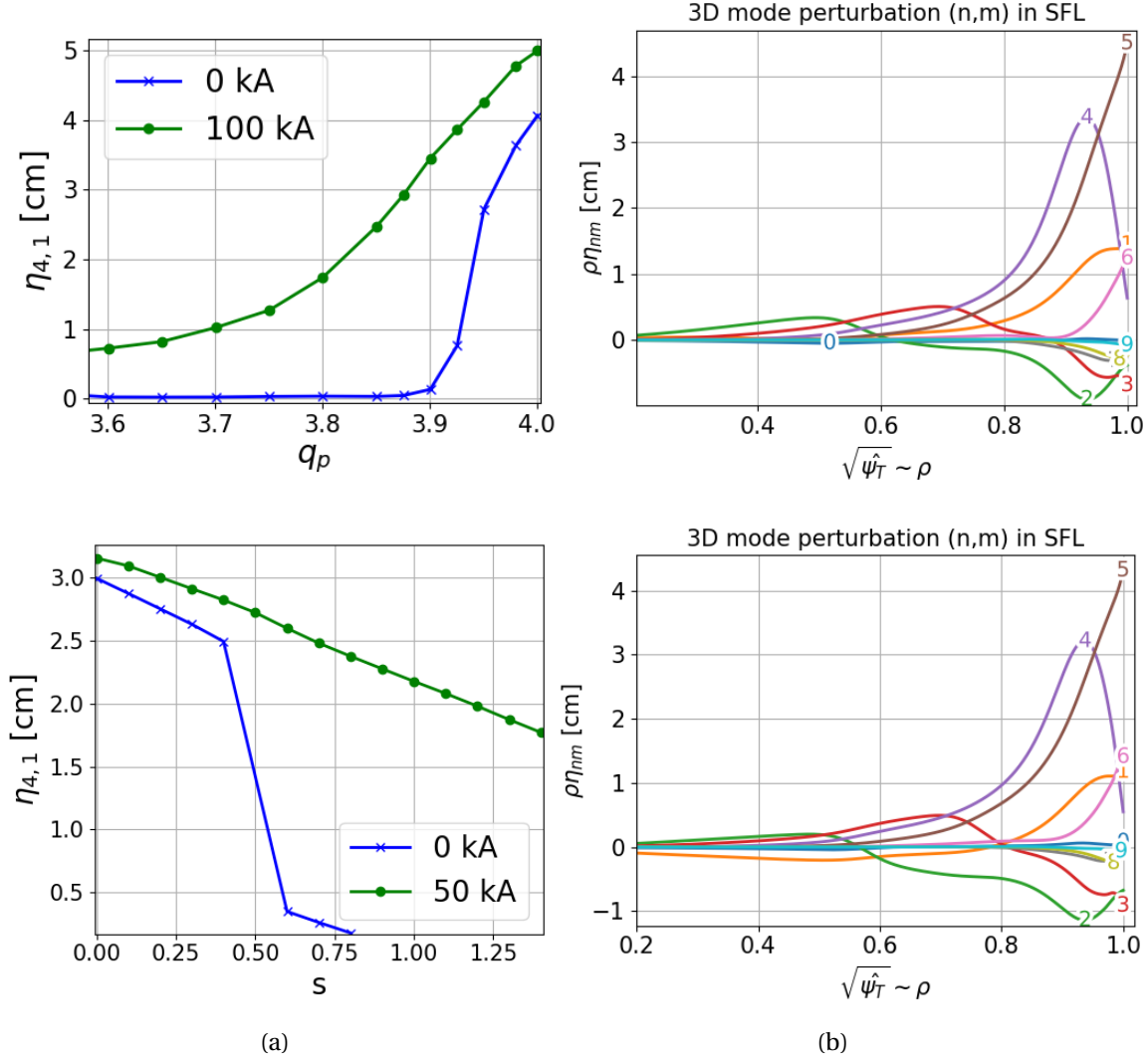


Figure 5.13: (a) Peak of the $(m = 4, n = 1)$ Fourier component of the nonlinear plasma displacement evaluated at the pedestal as a function of the value of the safety factor plateau (up) and (b) of the magnetic shear (bottom). (b) Poloidal Fourier spectrum (with $n = 1$) of the nonlinear plasma displacement with flat safety factor and $q_p = 3.98$ and 0 kA (up), and with $q_p = 3.90$ and 100 kA (bottom).

5.4 Summary and conclusions

In this chapter we have presented two approaches to model non-axisymmetric magnetic perturbations in tokamak plasmas. The first one invokes the analytical model developed in [LN88], which corresponds to an antenna located in the vacuum region in between the plasma surface

and an ideal wall. The current in the antenna produces a perturbed helical magnetic field, which modifies the boundary conditions of the linearised ideal MHD equilibrium equations. The second method uses a set of non-axisymmetric coils, where the vacuum magnetic field is evaluated numerically through Biot-Savart law. The vacuum field is then used to calculate a nonlinear equilibrium state in the VMEC free boundary code. We point out that in both approaches the obtained plasma displacement is in force balance with the applied MPs, so the plasma response is automatically included in the solution. To make a quantitative comparison of the applied MP, in the nonlinear VMEC approach the radial perturbed vacuum field is Fourier decomposed in SFL coordinates using the geometry of the axisymmetric equilibria. Then, the amplitude of the helical component of interest is compared with the radial vacuum field of the antenna calculated in the absence of a plasma.

On a first instance, both approaches to model the MPs were applied to the case of a saturated external kink. It was found that such saturated modes can be induced by the application of MPs, and the saturated amplitude of the plasma displacement is in quantitative agreement in both approaches for parameters for which the plasma is linearly stable in the absence of MPs. This means that, within the approximations of the ideal MHD model, there is a good understanding of the mechanism that describes the effect of the applied perturbed field on non-resonant external modes. On a second instance we also model equilibrium states with MPs for the case of saturated external modes. For this complex case, the quantitative agreement was limited, but the order of magnitude of the saturated plasma displacement, as well as the linear dependency of the amplitude on the applied MP was observed in both approaches.

Finally, the VMEC code was used to estimate the increase of the parameter space of saturated EHOs with the application of MPs. An extensive parameter scan was performed with respect to the value of the safety factor at the plateau and the magnetic shear in the pedestal. In both cases it was found that a significant increase in the parameter space can be achieved by the application of MPs. By analysing the Fourier spectrum of the saturated amplitude in equilibria with and without the application of MPs at different locations of the parameter space, it was concluded that the same mode can be excited with the help of MPs.

6 General conclusions and outlook

This thesis has investigated the parameter space for the excitation and saturation of Edge Harmonic Oscillations (EHOs). This has been done under the frame of the ideal MHD model using both linear and nonlinear approaches, aided with both analytical and numerical tools. Two main theories on the origin of EHOs exist in the literature, either the EHOs correspond to kink/peeling modes driven unstable by plasma flows, or they correspond to external modes driven unstable by the coupling of large pressure gradient in a region with weak FLB stabilisation. This thesis mainly focused on the second theory. Throughout the chapters of the thesis it has been found that linearly unstable and nonlinearly saturated external modes can be consistently obtained in plasmas containing the key elements observed during QH-mode operation. In Chapter 3 it was found using linear KINX stability calculations and nonlinear VMEC equilibrium calculations that such saturated modes can be obtained within the QH-mode baseline scenario on the DEMO1 tokamak design. Guiding centre orbit calculations using the VENUS-LEVIS code found that the 3D magnetic structure created by the EHOs in DEMO weakly increase ($< 0.1\%$) the fast ion first orbit losses, but alters the pattern in which the particles are deposited into the PFC. An immediate extension of this work is to characterise the parameter space of the saturation of external modes in DEMO in order to eventually obtain larger amplitude edge corrugations, which could drive larger fast ion losses. Concerning the study of fast ion confinement, additional loss mechanisms other than first orbit losses could be considered in the VENUS-LEVIS simulations.

Later in Chapter 3 it was found that saturated external kink modes obtained in VMEC equilibrium calculations can successfully be recovered by initial value nonlinear JOREK simulations.

This provides a cross-validation between the ‘equilibrium’ and ‘dynamic’ approaches for the calculation of saturated external modes. However, for the saturated pressure-driven external modes, VMEC and JOEREK simulations obtained a different dominant toroidal harmonic of the initially unstable external mode. Nevertheless, the physical drive of the saturated instability was apparently the same for both codes. The reason for the disagreement is not fully resolved, but is speculated to be due to the different physics models at and near the plasma-vacuum interface adopted by the two codes. While VMEC enforces closed magnetic flux surfaces that are free to move, with ideal boundary conditions at the plasma-vacuum interface, in JOEREK the vacuum region is defined by a sharp increase in plasma resistivity. Such a difference does not seem to have an important effect on the current-driven external kink case over ideal time scales. Future work would look into resolving this issue in order to make the comparison between the codes more accurate. Alternatively, a different set of nonlinear codes that use the same plasma-vacuum boundary conditions could be used for the comparison between the ‘equilibrium’ and the ‘dynamic’ approaches.

Since QH-mode plasmas are observed experimentally without a complete flattening in the safety factor profile, Chapter 4 explored the parameter space for the excitation of linear external modes with respect to edge magnetic shear. This was done by solving a newly derived set of external mode equations that include higher order corrections in $\Delta q/q_s$, where $q_s = m/n$, $q(r) = q_s + \Delta q(r)$ and $\Delta q(r)/q_s \ll 1$. As a result, an ‘ $s - \alpha$ ’ external instability diagram was produced. It was found that external modes are located in the second region of stability of infinite- n ballooning modes, although it was concluded the external-unstable region of the parameter space could be also shared with unstable medium- n peeling-ballooning modes. Such modes are expected to be stabilised by equilibrium poloidal and diamagnetic sheared flow in experiments (and more refined models), as described in reference [Bru+19a]. Upon analysis of the obtained parameter space, it was found that the edge magnetic shear can be of order unity and still excite an instability of external kind. This result was recovered in linear stability calculations using the KINX code, and in nonlinear equilibrium calculations using the VMEC code. Later, a simple model of the plasma separatrix (with the safety factor having logarithmic divergence at the plasma boundary) was implemented and solved. Since the upper sideband rational surface lies inside the plasma for this case, the connection with the vacuum region is no longer needed for the mode to be unstable, which is now formally an internal (infernal) mode. It was concluded that either a vacuum region *or* a separatrix are needed for the mode to be unstable. Absence of the two effects results on the mode being stable. An

obvious extension of the work is the inclusion of flows associated with the equilibrium radial electric field (E_r), the inclusion of plasma resistivity and plasma shaping. This is because flow stabilisation of high- n modes is stronger for low edge magnetic shear [Che+17a], which might impose a more severe constraint on the critical edge magnetic shear than the one calculated in this work. Coupling of the infernal drive with a resistive external kink drive coming from the upper sideband in cases with a plasma separatrix can enhance the instability and therefore increase the parameter space of external modes in diverted configurations. A more detailed model of the plasma separatrix, including a proper *local* divergence of the safety factor as well as the shaping effects leading to the formation of the x-point is also needed. Finally, it has been experimentally observed that the parameter space of QH-mode access is wider for strongly shaped plasmas [Bur+05]. Therefore, the role of plasma shaping in the excitation of external modes should be explored.

Finally, Chapter 5 studied the interaction between non-resonant external instabilities and non-axisymmetric magnetic perturbations (MPs). This was undertaken using two approaches: first, using an analytical linear model of an antenna which produces a static helical perturbation, and second, through nonlinear calculations using the VMEC code. For the two cases of study (external kink and external modes) it was found both in the analytical model and in VMEC simulations that MPs can extend the parameter space where saturated external instabilities can be found. A comparison between the two approaches was performed, finding quantitative agreement for the external kink case, but only qualitative agreement for the external mode case. It was concluded that the differences found in the external case might be originated on the many approximations taken in the derivation of the analytical model. Future work would improve such approximations in order to obtain a better analytical estimation of the saturated amplitude of external modes in the presence of MPs. We point out that agreement was only obtained in cases where the mode was stable in the absence of MPs. This is because the linear perturbed equilibrium model does not capture the effect of inertia that would be present if there is a finite growth rate, meaning that the obtained linear ‘saturated states’ are not in force balance if the mode is unstable in the absence of the antenna. A further outlook of this work is the implementation of the linear analytical model in VENUS-MHDpy in the form of an inhomogeneous forcing function added to the eigenvalue problem, as explained in [Tur12; Tur+13].

The findings presented in this thesis have advanced the present understanding into the excita-

General conclusions and outlook

tion and saturation mechanism of external modes, which could be helpful for the development of QH-mode scenarios in current and future tokamaks. Other important plasma parameters are still open for exploration to fully discover the parameter space of external modes, such as equilibrium flows, plasma resistivity, plasma shaping, and further physics beyond-MHD.

A Numerical tools

A.1 The VMEC code

The **Variational Moments Equilibrium Code** (VMEC) [HW83; HRM86] finds a static ideal MHD equilibria in 3D by minimising the total plasma energy (magnetic + fluid + vacuum) through the functional

$$W = \int_P \left(\frac{|\mathbf{B}|^2}{2\mu_0} + \frac{P}{\Gamma-1} \right) dx^3 - \int_V \frac{|\mathbf{B}_V|^2}{2\mu_0} dx^3. \quad (\text{A.1})$$

The minimisation procedure is performed through a variational principle of the energy functional using a steepest-descent iteration method, where the states of minimal energy correspond to MHD equilibrium solutions [KK58]. Particularly, the minimisation is constrained by the assumption of nested magnetic flux surfaces, which is consistent with ideal MHD theory. The minimisation stops when the static force balance equation (2.21) is satisfied in every direction up to a user-defined level of accuracy. The VMEC code has recently been updated to include the effect of toroidal equilibrium flow [Coo+14].

Equilibrium calculations can be performed assuming either fixed or free boundary. Note that for fixed boundary, the second integral on equation A.1 vanishes. In free boundary simulations a vacuum field must be provided externally, and the energy of the plasma is minimised together with the energy of the vacuum field. Normally, the vacuum magnetic field is calculated from

a set of current-carrying filaments through the Biot-Savaart law. The code MAKEGRID from the STELLOPT package performs such calculation on a rectangular (R, Z) at a fixed number of toroidal planes, where R and Z are the cylindrical coordinate variables.

The energy integral is discretised using a double Fourier decomposition in the poloidal and toroidal directions, while the integration in the radial direction is performed using a discrete mesh of the radial variable. The coordinate system used by the VMEC code is similar to the one described in section 2.2, with the radial variable defined as either the poloidal or toroidal flux normalised to its value at the plasma edge ($s = \psi / \psi(s = 1)$). The physical quantities are connected to the 3D space through the mapping of orthogonal cylindrical coordinates (R, ϕ, Z) into flux coordinates (s, θ, ϕ) . It is worth noticing that in VMEC the covariant basis vector \hat{e}_ϕ in both coordinate systems points counter-clockwise when looking the torus from the top (figure 1 in [HW83]), meaning that the cylindrical set is right handed but the flux coordinate set is left-handed. The mapping is given by

$$\begin{aligned} R(s, \theta, \phi) &= \sum_{mn} [R_c^{mn}(s) \cos(m\theta - n\phi) + R_s^{mn}(s) \sin(m\theta - n\phi)] \\ Z(s, \theta, \phi) &= \sum_{mn} [Z_c^{mn}(s) \cos(m\theta - n\phi) + Z_s^{mn}(s) \sin(m\theta - n\phi)] \\ \lambda(s, \theta, \phi) &= \sum_{mn} [\lambda_c^{mn}(s) \cos(m\theta - n\phi) + \lambda_s^{mn}(s) \sin(m\theta - n\phi)], \end{aligned} \tag{A.2}$$

where λ is the function that makes the field lines straight, as discussed in section 2.2. This is of particular importance because the flux coordinate system used in the VMEC code is not a SFL system, but can be easily transformed by the change of variable

$$\theta_{SFL} = \theta + \lambda(s, \theta, \phi). \tag{A.3}$$

The magnetic field is given in the same form as in equation 2.14, so it can be fully expressed in terms of the Fourier expansion in equation A.2 and the poloidal and toroidal magnetic fluxes. VMEC requires as an input the flux functions $p(s)$ and $\langle J^\phi \rangle(s)$ (or $\iota(s)$), where $p(s)$ is the plasma pressure, $\langle J^\phi \rangle(s)$ is the surface average of the toroidal current and $\iota(s) = 1/q(s)$

is the rotational transform. Boundary conditions are also required, i.e. a description of the plasma boundary and the total enclosed toroidal flux, where the later is used to calculate the toroidal magnetic field strength in fixed boundary simulations. In free boundary simulations, the description of the boundary is taken as the first guess, and the enclosed toroidal flux is used to calculate the area of the poloidal cross section. Through the minimisation of the energy, the volume of the magnetic surfaces is varied until the desired equilibrium is reached. VMEC then outputs the full equilibrium decomposed in Fourier components in the same form as expressed in equation A.2.

A.1.1 Stellarator symmetry

The number of acquirable states that can be obtained by VMEC can be reduced by exploiting what is called *stellarator symmetry* [DH98]. General 3D plasma configurations posses such symmetry if the scalar functions describing the equilibrium in cylindrical coordinates fulfils the relation $f(R, -\phi, -Z) = \pm f(R, \phi, Z)$, i.e. quantities are mirrored with respect to the planes $Z = 0$ and $\phi = 0$. Vector field components also need to fulfil $\mathbf{V}(V_R, V_\phi, V_Z) = \mathbf{V}(-V_R, V_\phi, V_Z)$. In flux coordinates, this symmetry reads $f(s, -\theta, -\phi) = \pm f(s, \theta, \phi)$, and the coordinate map results in $R(s, -\theta, -\phi) = R(s, \theta, \phi)$ and $Z(s, -\theta, -\phi) = -Z(s, \theta, \phi)$. Considering this parity and equation A.2, VMEC's mapping of the coordinates assuming stellarator symmetry reduces to

$$\begin{aligned} R(s, \theta, \phi) &= \sum_{mn} R_c^{mn}(s) \cos(m\theta - n\phi) \\ Z(s, \theta, \phi) &= \sum_{mn} Z_s^{mn}(s) \sin(m\theta - n\phi) \\ \lambda(s, \theta, \phi) &= \sum_{mn} \lambda_s^{mn}(s) \sin(m\theta - n\phi). \end{aligned} \tag{A.4}$$

This greatly simplifies VMEC calculations and increases the convergence of the algorithm. If a coil set producing the equilibrium vacuum field has stellarator symmetry, then the magnetic field will also have stellarator symmetry [DH98]. This is of particular importance when using 3D coils on inherently 2D plasma configurations, such as the application of resonant magnetic perturbations discussed in Chapter 5. As it turns out, most stellarators are designed to have stellarator symmetry, and in tokamaks stellarator symmetry reduces to up-down symmetry. In reality, both types of design will not have this kind of symmetry exactly due to the toroidal

ripple. Most notably, tokamaks that operate with a single null divertor (only one x-point, like JET or ITER) break stellarator symmetry.

A.2 The FreeGS code

The FreeGS code [Dud] is a python library that solves the static (non-rotating) Grad-Shafranov equation in free boundary using a nonlinear Picard iteration method. The code was particularly useful for this thesis because given a certain set of coils, FreeGS uses a feedback control routine to calculate the required current in the coils that would produce the desired equilibrium. The calculation of the currents is constrained by either the location of the x-points, the value of the poloidal flux at a certain locations, or both. Note that depending of how many constraints and coils are specified, there might be more unknowns than degrees of freedom, or conversely, more degrees of freedom than unknowns. This results on an ill-posed problem, as there might be infinite solutions, or no solution at all. The FreeGS code fixes this issue by using the Tikhonov regularisation method to produce a unique solution, but still unrealistically large currents can be obtained. To avoid this, a good strategy is to set one the coil currents equal to a realistic value, then the rest of the coil currents will be calculated ‘normalised’ to that value.

Apart from the description of the coil set, the plasma profiles dp/ds and FdF/ds are needed as an input, where $s = \psi_p(s)/\psi_p(1)$ is the normalised poloidal flux. These profiles are constructed by providing the value of the pressure at the magnetic axis ($P(0)$) and the total toroidal current (I_p). This sets the toroidal current density to

$$J_\phi = L \left[\beta_0 R + \frac{1 - \beta_0}{R} \right] (1 - s^{\alpha_m})^{\alpha_n} \quad (\text{A.5})$$

where L is a proportionality constant, $\beta_0 = 2\mu_0 P(0)/B_0^2$, α_m and α_n are parameters that can be set by the user, and R is the normalised major radius. The value of L and β_0 are obtained from the following integrals

$$\begin{aligned}
P(0) &= -L\beta_0 R \int (1 - s^{\alpha_m})^{\alpha_n} d\psi_p \\
I_p &= L \int \left[\beta_0 R + \frac{1 - \beta_0}{R} \right] (1 - s^{\alpha_m})^{\alpha_n} dR dZ.
\end{aligned} \tag{A.6}$$

Alternatively, the shape of the profiles can be arbitrarily specified as function of s , but the convergence of the numerical method can be affected by the complexity of the functions.

A.3 The KINX stability code

The KINX code [Deg+97] solves the ideal MHD linear stability problem in axisymmetric plasmas surrounded by a vacuum region and delimited by a metallic wall. The formulation of the stability problem is based on the weak form of the ideal MHD perturbed equations, corresponding to the sum of the perturbed potential and kinetic energies (equation 2.43). A flux coordinate system is used, where an hybrid finite element scheme is used to discretise the MHD operator in both radial and poloidal directions to avoid spectral pollution [Gru+81b; Gru+81a]. The numerical equilibrium required in KINX is computed by the CAXE code, which has the advantage of calculating MHD equilibria on a grid adapted to magnetic surfaces which can include a separatrix with an x-point. In this thesis, the equilibria is first calculated in CHEASE [LBS96], then later interfaced to KINX through the CAXE code. A stability calculation in KINX gives the growth rates and eigenvectors, which correspond to the different projections of the plasma displacement ξ , given by

$$\xi = \xi^\psi \frac{\nabla G \times \mathbf{B}}{B^2} + \xi^G \frac{\mathbf{B} \times \nabla \psi}{B^2} + \xi^B \frac{\mathbf{B}}{B}, \tag{A.7}$$

where the magnetic field is represented in Clebsch form as $\mathbf{B} = \nabla \psi \times \nabla G$ and ψ is the poloidal flux.

B Mathematical derivations

B.1 Equilibrium toroidal flow

It is considered that the plasma field velocity only flows in the toroidal direction, which is somewhat justified because the poloidal flow is strongly damped due to neoclassical effects [CBT87] (i.e. $u^\theta \ll u^\phi$). Moreover, the lowest order plasma flow must lie on flux surfaces in order for the plasma to be confined (i.e. $\mathbf{u} \cdot \nabla s = 0$). Therefore, the equilibrium flow can be expressed as

$$\mathbf{u} = R^2 \Omega(s) \nabla \phi \tag{B.1}$$

where the toroidal angular frequency $u^\phi = \Omega(s)$ is a flux function. This restriction requires further assumptions on the geometry of the system. Substituting ideal Ohm's law (2.5) into equilibrium Faraday's law (2.6) and taking the toroidal contravariant component gives

$$\begin{aligned} 0 &= [\nabla \times (\mathbf{u} \times \mathbf{B})] \cdot \nabla \phi \\ &= \nabla \cdot [\nabla \phi \times (\mathbf{B} \times \mathbf{u})] \\ &= (\mathbf{B} \cdot \nabla) u^\phi - B^\phi \nabla \cdot \mathbf{u} - (\mathbf{u} \cdot \nabla) B^\phi, \end{aligned} \tag{B.2}$$

Mathematical derivations

where in the last equality equation 2.8 has been used. Note that Ω will only be a flux function if ρ , B^ϕ and Ω are independent of the toroidal variable ϕ , which is the case of axisymmetry (see section §2.3.1). Then it follows from the mass conservation equation (2.2) that the equilibrium toroidal flow is incompressible: $\nabla \cdot \mathbf{u} = 0$. Also due to axisymmetry the last term on equation B.2 vanishes: $(\mathbf{u} \cdot \nabla) B^\phi = \Omega \partial_\phi B^\phi = 0$. The equation finally gives $\mathbf{B} \cdot \nabla \Omega = \partial_\theta \Omega = 0$, implying that Ω is a flux function. It is now straightforward to obtain

$$(\mathbf{u} \cdot \nabla) \mathbf{u} = -\frac{1}{2} \Omega^2(s) \nabla R^2, \quad (\text{B.3})$$

which means that the force derived from toroidal rotation is only centripetal. An expression for the pressure is derived from the parallel equilibrium equation

$$\begin{aligned} \rho \mathbf{B} \cdot [(\mathbf{u} \cdot \nabla) \mathbf{u}] &= -\mathbf{B} \cdot \nabla P \\ \mathbf{B} \cdot \nabla \left(\frac{m_i}{4T(s)} \Omega^2(s) R^2 \right) &= \mathbf{B} \cdot \nabla (\ln(P)) \end{aligned} \quad (\text{B.4})$$

where the plasma density ρ has been substituted using equation 2.1 and it has been assumed that $(\mathbf{B} \cdot \nabla) T = 0$ due to the fast thermal transport along the field lines. Equation B.4 can be integrated along the field lines to give

$$P(s, R) = \hat{P}(s) e^{U(s)(R^2 - R_0^2)} \quad (\text{B.5})$$

with $U(s) = \frac{m_i}{4T} \Omega^2$ and $\hat{P}(s)$ is the pressure without the effect of rotation. Comparing this result with equation 2.22, it is clear that pressure is no longer constant in plasmas with toroidal rotation: the centrifugal force pushes the plasma radially outwards producing a mismatch between the pressure surfaces and flux surfaces.

The variation of the energy functional (equation A.1) needs to be consistent with the MHD equilibrium equation with flow (2.18), which is the case if $\Omega'(s) \simeq 0$ in regions with significant 3D distortion [Coo+14]. This formulation is not valid for general 3D geometry, but the

approximation holds well enough for small 3D perturbations and is exact in axisymmetry.

B.2 Corrected sideband equations with shear

As found in Chapter 4, the physics of edge magnetic shear is well captured by the inclusion of the first order $\mathcal{O}(\Delta q/q_s)$ corrections in the sideband equations related to field line bending stabilisation. To ease the notation from Chapter 4, we rename $\xi_{r0}^{(m)} \rightarrow \xi_0$ and $\xi_{r1}^{(m\pm 1)} \rightarrow \xi_{\pm}$. The equations for the sidebands are then

$$\begin{aligned} \frac{d}{dr} \left[r^{-(1\pm 2m)} \frac{d}{dr} (r^{2\pm m} \xi_{\pm}) \right] &= \frac{1\pm m}{2} \frac{d}{dr} (r^{\mp m} \alpha \xi_0) \\ &+ 2(1\pm m) \left[\frac{d}{dr} \left[\frac{\Delta q}{q_s} r^{-(1\pm 2m)} \frac{d}{dr} (r^{2\pm m} \xi_{\pm}) \right] - (2\pm m) r^{\mp m} \frac{\Delta q'}{q_s} \xi_{\pm} \right] \end{aligned} \quad (\text{B.6})$$

Integrate the equation from r_1 to r

$$\begin{aligned} r^{-(1\pm 2m)} \frac{d}{dr} (r^{2\pm m} \xi_{\pm}) &= \frac{1\pm m}{2} r^{\mp m} \alpha \xi_0 \\ &+ 2(1\pm m) \left[\frac{\Delta q}{q_s} r^{-(1\pm 2m)} \frac{d}{dr} (r^{2\pm m} \xi_{\pm}) - (2\pm m) \int_{r_1}^r r^{\mp m} \frac{\Delta q'}{q_s} \xi_{\pm} dr \right] + C_0^{\pm} + C_1^{\pm} \end{aligned} \quad (\text{B.7})$$

Note that taking a definite integral sets the constants of integration C_0^{\pm} and C_1^{\pm} to be:

$$C_0^{\pm} = r_1^{\mp m} \xi_{\pm}(r_1) (2\pm m + \mathcal{B}^{\pm}(r_1)) \quad (\text{B.8})$$

$$C_1^{\pm} = -2(1\pm m) \frac{\Delta q(r_1)}{q_s} C_0^{\pm} \quad (\text{B.9})$$

where $\mathcal{B}^{\pm}(r) = r \xi'_{\pm}(r) / \xi_{\pm}(r)$. The order $(\Delta q/q_s)^0$ is

$$r^{-(1\pm 2m)} \frac{d}{dr} (r^{2\pm m} \xi_{\pm}) = \frac{1\pm m}{2} r^{\mp m} \alpha \xi_0 + C_0^{\pm} \quad (\text{B.10})$$

when integrating from r_1 to r we get

$$\xi_{\pm} = \frac{1\pm m}{2} r^{2\pm m} \hat{\xi}_{\pm}^0 + C_0^{\pm} \frac{r^{\pm m}}{2(1\pm m)} + D_0^{\pm} r^{-(2\pm m)} \quad (\text{B.11})$$

with $\hat{\xi}_{\pm}^0 = \int_{r_1}^r r^{1\pm m} \alpha \xi_0 dr$. We note once again that since this is a definite integral, the constant D_0^{\pm} is determined, and equal to $D_0^{\pm} = r_1^{2\pm m} \xi_{\pm}(r_1) - C_0^{\pm} \frac{r_1^{2(1\pm m)}}{2(1\pm m)}$. We use equation B.8 to get:

$$D_0^{\pm} = C_0^{\pm} r_1^{2(1\pm m)} \frac{\pm m - \mathcal{B}^{\pm}(r_1)}{2(1\pm m)(2\pm m + \mathcal{B}^{\pm}(r_1))} \quad (\text{B.12})$$

We substitute equations B.10 and B.11 into the order $\mathcal{O}(\Delta q/q_s)$ terms of equation B.7 (right hand side) to get:

$$\begin{aligned} r^{-(1\pm m)} \frac{d}{dr} (r^{2\pm m} \xi_{\pm}) &= \frac{1\pm m}{2} \alpha \xi_0 \left[1 + 2(1\pm m) \frac{\Delta q}{q_s} \right] - r^{\pm m} (1\pm m)^2 (2\pm m) \int_{r_1}^r r^{-2(1\pm m)} \frac{\Delta q'}{q_s} \hat{\xi}_{\pm}^0 dr \\ &+ C_0^{\pm} r^{\pm m} \left[1 \pm m \frac{\Delta q - \Delta q(r_1)}{q_s} - r_1^{2(1\pm m)} \frac{(2\pm m)(\pm m - \mathcal{B}^{\pm}(r_1))}{2\pm m + \mathcal{B}^{\pm}(r_1)} \int_{r_1}^r r^{-2(1\pm m)} \frac{\Delta q'}{q_s} dr \right] = 0 \end{aligned} \quad (\text{B.13})$$

Equation B.13 is to be substituted into the main mode equation (3.2).

B.2.1 Calculation of the constants of integration

First, we evaluate equation B.13 at r_2 to obtain

$$\begin{aligned} \xi_{\pm}(r_2) (2 \pm m + \mathcal{B}^{\pm}(r_2)) = & -r_2^{\pm m} (1 \pm m)^2 (2 \pm m) \int_{r_1}^{r_2} r^{-2(1 \pm m)} \frac{\Delta q'}{q_s} \hat{\xi}_{\pm}^0 dr \\ & + C_0^{\pm} r_2^{\pm m} \left[1 \pm m \frac{\Delta q(r_2) - \Delta q(r_1)}{q_s} - r_1^{2(1 \pm m)} \frac{(2 \pm m)(\pm m - \mathcal{B}^{\pm}(r_1))}{2 \pm m + \mathcal{B}^{\pm}(r_1)} \int_{r_1}^{r_2} r^{-2(1 \pm m)} \frac{\Delta q'}{q_s} dr \right] \end{aligned} \quad (\text{B.14})$$

Also note that evaluation equation B.13 at r_1 gives identically zero. Finally, integrate equation B.13 from r_1 to r_2 to give

$$\begin{aligned} r_2^{2 \pm m} \xi_{\pm}(r_2) - r_1^{2 \pm m} \xi_{\pm}(r_1) = & \frac{1 \pm m}{2} \int_{r_1}^{r_2} r^{1 \pm m} \alpha \xi_0 \left(1 + 2(1 \pm m) \frac{\Delta q}{q_s} \right) dr \\ & - (1 \pm m)^2 (2 \pm m) \int_{r_1}^{r_2} r^{1 \pm 2m} \left[\int_{r_1}^r r^{-2(1 \pm m)} \frac{\Delta q'}{q_s} \hat{\xi}_{\pm}^0 dr \right] dr \\ & + C_0^{\pm} \int_{r_1}^{r_2} r^{1 \pm 2m} \left[1 \pm m \frac{\Delta q - \Delta q(r_1)}{q_s} - r_1^{2(1 \pm m)} \frac{(2 \pm m)(\pm m - \mathcal{B}^{\pm}(r_1))}{2 \pm m + \mathcal{B}^{\pm}(r_1)} \int_{r_1}^r r^{-2(1 \pm m)} \frac{\Delta q'}{q_s} dr \right] dr \end{aligned} \quad (\text{B.15})$$

Equations B.8, B.14 and B.15 are used to determine uniquely C_0^{\pm} , $\xi_{\pm}(r_1)$ and $\xi_{\pm}(r_2)$. We have then

$$C_0^{\pm} = \frac{\mathcal{T}_1^{\pm} + \mathcal{T}_2^{\pm} + \mathcal{T}_3^{\pm}}{\mathcal{T}_4^{\pm} + \mathcal{T}_5^{\pm} + \mathcal{T}_6^{\pm} + \mathcal{T}_7^{\pm}} \quad (\text{B.16})$$

where we have defined the following terms

$$\begin{aligned}
\mathcal{T}_1^\pm &= 2q_s [2 \pm m + \mathcal{B}^\pm(r_1)] [2 \pm m + \mathcal{B}^\pm(r_2)] (1 \pm m)^3 (2 \pm m) \int_{r_1}^{r_2} r^{1 \pm 2m} \left[\int_{r_1}^r r^{-2(1 \pm m)} \frac{\Delta q'}{q_s} \xi_\pm^0 dr \right] dr \\
\mathcal{T}_2^\pm &= -q_s [2 \pm m + \mathcal{B}^\pm(r_1)] [2 \pm m + \mathcal{B}^\pm(r_2)] (1 \pm m)^2 \int_{r_1}^{r_2} r^{1 \pm m} \alpha \xi_0 \left[1 + 2(1 \pm m) \frac{\Delta q}{q_s} \right] dr \\
\mathcal{T}_3^\pm &= -2q_s [2 \pm m + \mathcal{B}^\pm(r_1)] (1 \pm m)^3 (2 \pm m) r_2^{2(1 \pm m)} \int_{r_1}^{r_2} r^{-2(1 \pm m)} \frac{\Delta q'}{q_s} \xi_\pm^0 dr \\
\mathcal{T}_4^\pm &= -2q_s m [2 \pm m + \mathcal{B}^\pm(r_1)] [2 \pm m + \mathcal{B}^\pm(r_2)] (1 \pm m) \int_{r_1}^{r_2} r^{1 \pm 2m} \frac{\Delta q - \Delta q(r_1)}{q_s} dr \\
\mathcal{T}_5^\pm &= -2q_s [\pm m - \mathcal{B}^\pm(r_1)] [2 \pm m + \mathcal{B}^\pm(r_2)] (1 \pm m) (2 \pm m) r_1^{2(1 \pm m)} \int_{r_1}^{r_2} r^{1 \pm 2m} \left[\int_{r_1}^r r^{-2(1 \pm m)} \frac{\Delta q'}{q_s} dr \right] dr \\
\mathcal{T}_6^\pm &= 2q_s [\pm m - \mathcal{B}^\pm(r_1)] (1 \pm m) (2 \pm m) r_1^{2(1 \pm m)} r_2^{2(1 \pm m)} \int_{r_1}^{r_2} r^{-2(1 \pm m)} \frac{\Delta q'}{q_s} dr \\
\mathcal{T}_7^\pm &= q_s \left([\pm m - \mathcal{B}^\pm(r_1)] [2 \pm m + \mathcal{B}^\pm(r_2)] r_1^{2(1 \pm m)} - [\pm m - \mathcal{B}^\pm(r_2)] [2 \pm m + \mathcal{B}^\pm(r_1)] r_2^{2(1 \pm m)} \right) \\
&\quad \mp 2m [2 \pm m + \mathcal{B}^\pm(r_1)] (1 \pm m) (\Delta q(r_2) - \Delta q(r_1)) r_2^{2(1 \pm m)}
\end{aligned} \tag{B.17}$$

Note that the zero order $\mathcal{O}((\Delta q/q_s)^0)$ (which makes $\mathcal{T}_1^\pm = \mathcal{T}_3^\pm = \mathcal{T}_4^\pm = \mathcal{T}_5^\pm = \mathcal{T}_6^\pm = 0$) recovers the results from previous papers [GHH96; HH88].

B.3 Reference model in Chapter 4

The *Reference model* is obtained in large aspect ratio tokamak following the tokamak ordering (§ 2.3.2), keeping terms up to order $\mathcal{O}(\epsilon^4)$ and without any assumptions on the order of the magnetic shear or safety factor. This model serves as a benchmark of the expansion of the safety factor performed for equations 4.14 - 4.17. The equation for the main mode is

$$\begin{aligned}
 & \frac{1}{r} \frac{d}{dr} \left[r^3 \left(\frac{1}{q} - \frac{n}{m} \right)^2 \frac{d}{dr} \xi_{r0}^{(m)} \right] - (m^2 - 1) \xi_{r0}^{(m)} \left(\frac{1}{q} - \frac{n}{m} \right)^2 \\
 & \frac{1}{4m^4 q^6 R_0^2} \left\{ n^2 \left((2m^2 R_0 \left(- (R_0 \alpha^2 + 4r\alpha + 2\Delta) m^2 - (7m^2 + 5) R_0 (\Delta')^2 + 2\Delta + 2((m^2 + 2)r + (2m^2 + 1)\alpha R_0) \Delta' \right) \right. \right. \\
 & - 3(5m^4 - 3m^2 + 4n^2) r^2) \xi_{mr0}(r) + r \left((2R_0 (6\Delta + (4r + R_0 (2\alpha - 3\Delta')) \Delta') m^2 + 5(3m^2 - 4n^2) r^2) \xi'_{mr0}(r) \right. \\
 & + r \left(2R_0 \left(R_0 (\Delta')^2 + 2\Delta \right) m^2 + (3m^2 - 4n^2) r^2 \right) \xi''_{mr0}(r) \left. \right) q^6 + 2mn \left((15m^4 + 7m^2 + 4n^2) r^2 \right. \\
 & + 2mR_0 \left(R_0 (m(7m^2 + 17) + 2(2m^2 + 1)nrq') (\Delta')^2 - m(2r(m^2 + 2nrq'm + 5) \right. \\
 & + R_0 (\alpha(4m^2 + 2nrq'm + 9) - r\alpha') \Delta' + 2m(m^2 - 1)\Delta + \alpha(m(4m^2 + 3)r + (m^3 + m)\alpha R_0) \left. \right) \xi_{mr0}(r) \\
 & - r \left((5(3m^2 - 4n^2) r^2 + 2mR_0 (6m\Delta + \Delta' (4mr + R_0 (2m\alpha - (3m + 2nrq') \Delta')) \right) \xi'_{mr0}(r) \\
 & + r \left(2R_0 \left(R_0 (\Delta')^2 + 2\Delta \right) m^2 + (3m^2 - 4n^2) r^2 \right) \xi''_{mr0}(r) \left. \right) q^5 + m \left(r \left((4R_0 (\Delta (3m + 2nrq') + 2mr\Delta') m^2 \right. \right. \\
 & + 2R_0^2 \Delta' (2m\alpha - 3(m + 2nrq') \Delta') m^2 + (3m^2 - 4n^2) r^2 (5m + 2nrq') \left. \right) \xi'_{mr0}(r) + mr \left(2R_0 \left(R_0 (\Delta')^2 + 2\Delta \right) m^2 \right. \\
 & + (3m^2 - 4n^2) r^2 \left. \right) \xi''_{mr0}(r) \left. \right) - m \left((15m^4 + 23m^2 + 6nrq'm - 36n^2) r^2 + 2R_0 (n^2 \alpha' r^2 + (4m^4 + 8m^2 + n^2) \alpha r \right. \\
 & + 2m(m(m^2 - 1)\Delta - r(m(m^2 + 8) + 2(4m^2 + 3)nrq') \Delta') \left. \right) + 2mR_0^2 (m(m^2 + 3)\alpha^2 - 2(2m(m^2 + 4) \\
 & + (4m^2 + 5)nrq') \Delta' \alpha + \Delta' (2mr\alpha' + \Delta' (m(7m^2 + 29) + 2nr(q'(8m^2 + 2nrq'm + 19) - 2rq'')) \left. \right) \left. \right) \xi_{mr0}(r) \left. \right) q^4 \\
 & - 2m^2 r \left((2m\Delta' (q' (2m(m^2 + 3)\alpha - (m(4m^2 + 17) + 4(m^2 + 1)nrq') \Delta') + 2mr\Delta' q'') R_0^2 \right. \\
 & + 2(2m^2 (2m^2 + 3)rq'\Delta' - n(3m\alpha + nrq'\alpha + mr\alpha')) R_0 + r(32mn + r(2n^2 rq'' - 3(m^2 - 6n^2)q')) \left. \right) \xi_{mr0}(r) \\
 & + rq' \left((3m^2 - 4n^2) r^2 - 2m^2 R_0 \left(R_0 (\Delta')^2 - 2\Delta \right) \right) \xi'_{mr0}(r) \left. \right) q^3 - 2m^2 r \left(4m^2 (m^2 + 2) r R_0^2 (q')^2 (\Delta')^2 \right. \\
 & + mR_0 (3\alpha(m + 2nrq') + mr\alpha') - 2r(8m^2 + nr(3nr(q')^2 + 22mq' + 2mrq'')) \left. \right) \xi_{mr0}(r) q^2 - 4m^3 r^2 (mq'' r^2 \\
 & + q' (r(13m + 8nrq') - 2m\alpha R_0) \left. \right) \xi_{mr0}(r) q + 20m^4 r^4 (q')^2 \xi_{mr0}(r) \left. \right\} \\
 & + \frac{1}{2(m-1)mq^4 R_0} \left\{ n^2 \left((2(m-2)(m-1)r + R_0 (\alpha - (m-1)r\alpha' + 2(m-2)m\Delta')) \xi_{(m-1)r1}(r) + r \left((R_0 ((3-2m)\alpha \right. \right. \right. \\
 & + 2(2m-1)\Delta') - 4(m-1)r) \xi'_{(m-1)r1}(r) + 2rR_0 \Delta' \xi''_{(m-1)r1}(r) \left. \right) q^4 - 2n \left(((m-1)r(2m^2 - 5m + nrq' + 2) \right. \\
 & + R_0 (\alpha(m + (m-1)nrq') - (m-1)mr\alpha' + \Delta' ((m-1)nq'' r^2 + (2m-1)((m-2)m - nrq')) \left. \right) \xi_{(m-1)r1}(r) \\
 & - r \left((2(m-1)(2m-1)r + R_0 ((2(m-2)m + 1)\alpha + ((3-2m)nrq' - (1-2m)^2) \Delta')) \xi'_{(m-1)r1}(r) \right. \\
 & + (1-2m)rR_0 \Delta' \xi''_{(m-1)r1}(r) \left. \right) q^3 + ((2(m-1)r((m-2)(m-1)m + nrq') + R_0 (- (m-1)r\alpha' m^2 \\
 & + 2(m-1)\alpha(nrq' + 1)m + 2\Delta' ((m-2)(m-1)m^2 + nr(q'(-2m^2 + m - (m-1)nrq') + 2(m-1)mrq'')) \left. \right) \left. \right) \xi_{(m-1)r1}(r) \\
 & + r \left(((1-m)m(4(m-1)r + (2m-3)\alpha R_0) + 2R_0 ((m-1)m(2m-1) + (4m^2 - 6m + 1)nrq') \Delta') \xi'_{(m-1)r1}(r) \right.
 \end{aligned}$$

$$\begin{aligned}
& + 2(m-1)mrR_0\Delta'\xi''_{(m-1)r1}(r))q^2 + 2(m-1)mr^2((m-1)q' - mR_0\Delta'q'')\xi_{(m-1)r1}(r) + (1-2m)R_0q'\Delta'\xi'_{(m-1)r1}(r))q \\
& + 2(m-1)m^2r^2R_0(q')^2\Delta'\xi_{(m-1)r1}(r)\Big\} \\
& + \frac{1}{2m(m+1)q^4R_0}\Big\{n^2((2(m+1)(m+2)r + R_0(\alpha + (m+1)r\alpha' + 2m(m+2)\Delta'))\xi_{(m+1)r1}(r) + r((4(m+1)r \\
& + R_0((2m+3)\alpha - 2(2m+1)\Delta'))\xi'_{(m+1)r1}(r) + 2rR_0\Delta'\xi''_{(m+1)r1}(r))q^4 + 2n((-m-1)r((m+2)(2m+1) - nrq') \\
& - R_0(\alpha(m - (m+1)nrq') + m(m+1)r\alpha' + \Delta'((2m+1)(m(m+2) + nrq') - (m+1)nr^2q''))\xi_{(m+1)r1}(r) \\
& - r((2(m+1)(2m+1)r + R_0((2m(m+2) + 1)\alpha - ((2m+1)^2 + (2m+3)nrq')\Delta'))\xi'_{(m+1)r1}(r) \\
& + (2m+1)rR_0\Delta'\xi''_{(m+1)r1}(r))q^3 + ((2(m+1)r(m(m+1)(m+2) + nrq') + R_0((m+1)r\alpha'm^2 \\
& - 2(m+1)\alpha(nrq' - 1)m + 2\Delta'((m+1)(m+2)m^2 + nr(q'(m(2m+1) + (m+1)nrq') - 2m(m+1)r q''))\xi_{(m+1)r1}(r) \\
& + r((4mr(m+1)^2 + R_0(m(m+1)(2m+3)\alpha - 2(m(m+1)(2m+1) + (4m^2 + 6m+1)nrq')\Delta'))\xi'_{(m+1)r1}(r) \\
& + 2m(m+1)rR_0\Delta'\xi''_{(m+1)r1}(r))q^2 - 2m(m+1)r^2((m+1)q' - mR_0\Delta'q'')\xi_{(m+1)r1}(r) \\
& + (-2m-1)R_0q'\Delta'\xi'_{(m+1)r1}(r))q - 2m^2(m+1)r^2R_0(q')^2\Delta'\xi_{(m+1)r1}(r)\Big\} = 0.
\end{aligned}$$

The equation for the upper sideband is

$$\begin{aligned}
& \frac{1}{r}\frac{d}{dr}\left[r^3\left(\frac{1}{q} - \frac{n}{m+1}\right)^2\frac{d}{dr}\xi_{(m+1)r1}(r)\right] - m(m+2)\left(\frac{1}{q} - \frac{n}{m+1}\right)^2\xi_{(m+1)r1}(r) \\
& \frac{1}{2m(m+1)q^4R_0}\Big\{n^2q^4(\xi_{mr0}(r)(R_0(\alpha + 2(m^2-1)\Delta' - mr\alpha') + 2(m-1)mr) + r(\xi'_{mr0}(r)(R_0(\alpha(1-2m) \\
& + 2(2m+1)\Delta') - 4mr) + 2rR_0\Delta'\xi''_{mr0}(r)) - 2nq^3(\xi_{mr0}(r)(R_0(\Delta'((2m+1)(m^2 - nrq' - 1) + mn r^2q'')) \\
& + \alpha(mnrq' + m+1) - m(m+1)r\alpha') + mr((m-1)(2m+1) + nrq')) + r(\xi'_{mr0}(r)(R_0(\alpha - 2\alpha m^2 \\
& + \Delta'((2m-1)nrq' + (2m+1)^2)) - 2m(2m+1)r) + (2m+1)rR_0\Delta'\xi''_{mr0}(r)) \\
& + q^2(\xi_{mr0}(r)(R_0(2\Delta'(nr(2m(m+1)r q'' - q'(2m^2 + mn r q' + 3m+1)) + (m-1)m(m+1)^2) \\
& + 2\alpha m(m+1)(nrq' + 1) - m(m+1)^2r\alpha') + 2mr(m^3 - m + nrq')) + r(\xi'_{mr0}(r)(2R_0\Delta'((4m^2 + 2m-1)nrq' \\
& + m(m+1)(2m+1)) - m(m+1)(4mr + \alpha(2m-1)R_0)) + 2m(m+1)rR_0\Delta'\xi''_{mr0}(r)) \\
& + 2m(m+1)qr^2(\xi_{mr0}(r)(mq' - (m+1)R_0\Delta'q'') + (-2m-1)R_0\Delta'q'\xi'_{mr0}(r)) + 2m(m+1)^2r^2R_0\Delta'(q')^2\xi_{mr0}(r)\Big\} = 0,
\end{aligned}$$

and for the lower sideband

$$\begin{aligned}
 & \frac{1}{r} \frac{d}{dr} \left[r^3 \left(\frac{1}{q} - \frac{n}{m-1} \right)^2 \frac{d}{dr} \xi_{(m-1)r1}(r) \right] - (m-2)m \left(\frac{1}{q} - \frac{n}{m-1} \right)^2 \xi_{(m-1)r1}(r) \\
 & \frac{1}{2(m-1)m q^4 R_0} \left\{ n^2 q^4 (\xi_{mr0}(r) (R_0(\alpha + 2(m^2 - 1)\Delta' + mr\alpha') + 2m(m+1)r) + r(\xi'_{mr0}(r)(4mr + R_0(\alpha(2m+1) \right. \\
 & + 2(1-2m)\Delta')) + 2rR_0\Delta'\xi''_{mr0}(r))) + 2nq^3 (\xi_{mr0}(r) (R_0(\Delta'((1-2m)(m^2 + nrq' - 1) + mn r^2 q'') + \alpha(mnrq' - m + 1) \\
 & - (m-1)mr\alpha') + mr(-2m^2 - m + nrq' + 1)) + r(\xi'_{mr0}(r) (R_0(\alpha - 2\alpha m^2 + \Delta'((2m+1)nrq' + (1-2m)^2)) \\
 & + 2(1-2m)mr) + (1-2m)rR_0\Delta'\xi''_{mr0}(r))) + q^2 (\xi_{mr0}(r) (R_0(2\Delta'(nr(q'(2m^2 + mn r q' - 3m + 1) - 2(m-1)mrq'') \\
 & + m(m+1)(m-1)^2) - 2\alpha m(m-1)(nrq' - 1) + m(m-1)^2 r\alpha') + 2mr(m^3 - m + nrq')) \\
 & + r(\xi'_{mr0}(r) ((m-1)m(4mr + \alpha(2m+1)R_0) - 2R_0\Delta'((4m^2 - 2m - 1)nrq' + (m-1)m(2m-1))) \\
 & + 2(m-1)mrR_0\Delta'\xi''_{mr0}(r))) - 2(m-1)mqr^2 (\xi_{mr0}(r) (mq' - (m-1)R_0\Delta'q'') + (1-2m)R_0\Delta'q'\xi'_{mr0}(r)) \\
 & \left. - 2(m-1)^2 mr^2 R_0\Delta'(q')^2 \xi_{mr0}(r) \right\} = 0.
 \end{aligned}$$

Writing the safety factor as $q(r) = q_s + \Delta q(r)$, with $\Delta q(r)/q_s \ll 1$, we can expand the equations above with respect to the small variable $\Delta q(r)/q_s$. Keeping only terms of order $\mathcal{O}((\Delta q/q_s)^0)$ in the expansion recovers the *Original exfernal* model. Keeping terms of order $\mathcal{O}((\Delta q/q_s)^1)$ recovers the *Corrected exfernal* model.

C VENUS-MHDpy code

C.1 Motivation and numerical method

Following the ‘beta’ version of the VENUS-MHD code written in Fortran by S. Lanthaler [Lan20], VENUS-MHDpy is a Python adaptation of the code created to address the known problems of the original version. Among those problems stand out the normalisation of the physical quantities, implementation of vacuum boundary conditions, and portability of the code outside of the Swiss Plasma Centre. Since the VENUS-MHDpy code is to be upgraded to include kinetic effects, one of the goals was to optimise simplicity and modularity without sacrificing efficiency¹. VENUS-MHDpy runs in Python3, the basic version uses only standard Python libraries (numpy, scipy and matplotlib), does not need to be compiled and can be installed locally as a Python library.

The VENUS-MHDpy code is a suit of Python modules designed to discretise second order differential operators using a Fourier-finite element method in 3 dimensions. The differential operator is applied to a vector of numerical variables as $\mathcal{A}\mathbf{X}$, where $\mathcal{A} = \mathcal{A}(s, \theta)$ is a $N \times N$ matrix of differential operators and $\mathbf{X} = (X^1, X^2, \dots, X^N)$ is a N -dimension vector. Each component (X^i) of the vector depends on the variables (s, θ, ϕ) as

$$X^i(s, \theta, \phi) = \sum_{m=m_-}^{m_+} X_m^i(s) e^{i(m\theta + n\phi)}, \quad (\text{C.1})$$

¹The code is in fact ~ 5 times faster than the Fortran equivalent in single core tests.

where n and m are integer numbers. The Fourier decomposition of the vector components is suitable to describe a toroidal system, with s a measure of the inner radii of the torus (which is often normalised), θ a measure of the angle in the poloidal direction, and ϕ the toroidal angle. It is assumed that the vector \mathbf{X} can be described by a single toroidal mode number n . The vector \mathbf{X} is then composed by $N \times M_{tot}$ variables which depend only on s , with $M_{tot} = m_+ - m_-$. The application of the VENUS-MHDpy code to the MHD stability problem requires the discretisation of the problem

$$\sum_{\sigma=0}^{N_t} \mathcal{A}_{(\sigma)} \frac{\partial^\sigma}{\partial t^\sigma} \mathbf{X}(s, \theta, \phi, t) = 0 \quad (\text{C.2})$$

where the differential operators $\mathcal{A}_{(\sigma)}$ depend on the MHD model that is to be used. For example, the ideal MHD model considers $\mathbf{X} = (\xi^r, \xi^\theta, \xi^\phi)$, $\mathcal{A}_2 = \rho \mathbf{I}$ and $\mathcal{A}_0 = \delta \mathbf{F}(\boldsymbol{\xi})$ as given by equation 2.39. Once the operators are discretised, the VENUS-MHDpy code can in principle evolve an initial plasma state using an explicit (or implicit, depending of the MHD model) time integration method. Up to now, a normal mode time dependency on time is assumed: $\mathbf{X}(s, \theta, \phi, t) = \tilde{\mathbf{X}}(s, \theta, \phi) e^{\lambda t}$, so that equation C.2 can be written as a general eigenvalue problem. The discretisation of each of these operators is undertaken using a finite element method for the variable s . First, each of the operators applied to the vector \mathbf{X} are written in weak form as

$$\mathcal{A}(\mathbf{Y}, \mathbf{X}) = \int \mathbf{Y}^* \cdot \mathcal{A} \mathbf{X} dV, \quad (\text{C.3})$$

where $\mathbf{Y} = (Y^1, Y^2, \dots, Y^N)$ is a test function that exists in the same space as the vector \mathbf{X} and has the same form as equation C.1, and dV is the volume of the computational domain. The discretisation of the radial variable s is performed following the Galerkin method by decomposing the functions $X_m^i(s)$ into finite elements as

$$X_m^i(s) = \sum_{k=1}^{N_s} X_{(m,k)}^i \Lambda_k^{(v)}(s), \quad (\text{C.4})$$

where $\Lambda_k^{(\nu)}$ is the k^{th} B-spline of order ν . In VENUS-MHDpy, the finite elements can be defined by the user to arbitrary order (ν) for each of the vector components X^i . This mixed representation is implemented to avoid a numerical problem called ‘spectral pollution’ [Gru+81b]. Such phenomena occurs in the ideal MHD model if for example the divergence of the perturbed field does not exactly vanish numerically ($\nabla \cdot \delta \mathbf{B} \neq 0$), which can happen if there is a mismatch in the polynomial representation of the relevant numerical variables. The mixed Fourier-finite element discretisation method implemented in VENUS-MHDpy is also adopted by the Erato [Gru+81b], MISHKA [Mik98], CASTOR [Ker+98; Str+05], and MINERVA [Aib+09] MHD stability codes. Substituting equations C.1 and C.4 into equation C.3 gives the explicit integral form of the discretised matrix $\mathcal{A}(\mathbf{Y}, \mathbf{X})$

$$\mathcal{A}(\mathbf{Y}, \mathbf{X}) = 2\pi \sum_{i,j}^N \sum_{m_X, m_Y = m_-}^{m_+} \sum_{k,l}^{N_s} \mathcal{A}_{(i,j,m_X,m_Y,k,l)} Y_{(m_Y,k)}^i X_{(m_X,l)}^j \quad (\text{C.5})$$

with

$$\mathcal{A}_{(i,j,m_X,m_Y,k,l)} = \sum_{p,q=0}^1 \int \frac{d^p}{ds^p} \Lambda_k^{(\nu_i)}(s) \frac{d^q}{ds^q} \Lambda_l^{(\nu_j)}(s) \left[\int A_{(i,j,p,q)}(s, \theta, m_X, m_Y) e^{i(m_X - m_Y)\theta} d\theta \right] ds, \quad (\text{C.6})$$

where the coefficients $A_{(i,j,p,q)}(s, \theta, m_X, m_Y)$ depend on the model under consideration. Because of the Fourier decomposition of the numerical variables and test functions, the derivatives with respect to θ and ϕ can be replaced by $\partial_\theta X^i \rightarrow i m_X$, $\partial_\theta (Y^i)^* \rightarrow -i m_Y$, $\partial_\phi X^i \rightarrow i n$ and $\partial_\phi (Y^i)^* \rightarrow -i n$. Note that the integral in ϕ was performed in advance since there is no dependence on the toroidal angle ($X(Y)^* \sim e^{in\phi} e^{-in\phi}$), giving the factor 2π .

The VENUS-MHDpy code is a flexible tool to discretise different MHD stability models including various physical effects. Continuing the work presented in [Lan20], the implementation of the models uses Mathematica to perform extensive algebraic manipulations to obtain the coefficients $A_{(i,j,p,q)}(s, \theta, m_X, m_Y)$, which are automatically converted into Python code. Up to now, the static and stationary ideal MHD models are implemented in the VENUS-MHDpy code as linear general eigenvalue problems, which are solved by the function `eigs` from the `scipy`

sparse linear algebra library.

C.2 Numerical implementation: A finite element implementation for vector languages

Building such a large matrix requires the use of at least 6 loops performing different integrals over the indexes i, j, m_X, m_Y, k and l as described by equation C.5. Since Python is a high-level programming language, such procedure would be extremely inefficient. Instead, VENUS-MHDpy computes the integrals by blocks of (i, j) pairs, which are the only 2 loops that are not vectorised within the code². The discretisation loops roughly resemble the following structure:

```

1      for i,j in range(IJpair):
2
3          Mpol = FFT_Mpol(i,j)
4          Bsplines = BsplineGauss(i,j)
5          Mrad = InterpGauss(Mpol)
6
7          for d in Diagonals:
8              Matrix[d] = Mrad*Bsplines

```

For each (i, j) pair, the integral with respect to the poloidal angle θ is performed numerically using a single Fast Fourier Transform (FFT), then the (m_X, m_Y) Fourier components are used to build the local $M_{tot} \times M_{tot}$ matrix block (function `FFT_Mpol(i, j)`). Such procedure has been extremely optimised by using the `fftn` function built within the `scipy` python library, which performs a FFT at each radial location in a vectorised manner. The integrals with respect to the radial variable s are performed using the Gaussian quadrature rule. The loop over the radial variable (k, l) is replaced by a loop over the matrix diagonal arrays, where the number of arrays depends on the B-spline order of the (i, j) pair of numerical variables (For example, if $v_i = v_j = 1$, then only 3 diagonal arrays are present in the matrix: Lower off-diagonal, diagonal and upper off-diagonal arrays). The B-splines (k, l) are calculated only at the Gaussian nodes that give a no-null contribution to the integrals for each diagonal array, which also depends on the order of the B-splines considered (function `BsplineGauss(i, j)`). The Fourier components of the poloidal integral are interpolated at the same Gaussian nodes and build into a matrix (function `InterpGauss(Mpol)`). Such interpolation is performed taking

²These loops can be easily parallelised since each (i, j) block is independent.

advantage of vectorised operations. The full matrix for each (i, j) pair is finally calculated by multiplying the B-spline array times the poloidal integral matrix and summing over the appropriate Gaussian nodes. Such matrix operations are carried out in an optimised way by taking advantage of the vector operations in the numpy Python library, and can be GPU parallelised with relative ease using the cupy Python library.

C.3 Normalisation in VENUS-MHDpy

The MHD models implemented into the VENUS-MHDpy code calculate the stability of an axisymmetric equilibrium plasma. Such equilibrium is currently obtained numerically using the VMEC fixed boundary code in axisymmetric configuration. An interface between VMEC and VENUS-MHDpy was created in order to normalise the relevant physical quantities and to map the equilibrium into a right-handed straight field line coordinate system. The normalisation adopted by VENUS-MHDpy is

$$\begin{aligned}
 \nabla &= \frac{\hat{\nabla}}{R_0}, & \mathbf{B} &= \hat{\mathbf{B}}B_0, & f &= B_0 R_0^2 \hat{f}, & \hat{\rho} &= \frac{\rho}{\rho_0} = \frac{P}{P_0} \frac{T_0}{T} \\
 F &= B_0 R_0 \hat{F}, & \delta \mathbf{A} &= R_0 B_0 \delta \hat{\mathbf{A}}, & P &= \frac{B_0^2 \hat{P}}{\mu_0}, & \omega &= \omega_A \hat{\omega} \\
 \mathbf{u} &= u_A \hat{\mathbf{u}}, & \omega_A &= \frac{B_0}{R_0 \sqrt{\mu_0 \rho_0}}, & u_A &= R_0 \omega_A = \frac{B_0}{\sqrt{\mu_0 \rho_0}}, & \hat{T} &= \frac{T}{u_A} = \frac{\mu_0 P_0}{2 B_0^2} \left(\frac{T}{T_0} \right) \\
 \hat{\Omega} &= \frac{\Omega}{\omega_A} = \frac{M_0}{2} \sqrt{\frac{\mu_0 P_0}{B_0^2}} \left(\frac{\Omega}{\Omega_0} \right), & \hat{U} &= R_0^2 U = \frac{M_0^2}{2} \left(\frac{\Omega}{\Omega_0} \right)^2 \frac{T_0}{T}, & M_0^2 &= \frac{\Omega_0^2 R_0^2}{2 T_0}
 \end{aligned} \tag{C.7}$$

where the normalised quantities have a hat ($\hat{}$). In equation C.7, R_0 , B_0 , T_0 , Ω_0 , P_0 , ρ_0 , M_0 , u_a and ω_A are the major radius, magnetic field, temperature, toroidal rotation frequency, pressure, density, Mach number, Alfven speed and Alfven frequency evaluated at the magnetic axis in SI units. The quantities F and f define the magnetic field as $\mathbf{B} = f \nabla \phi \times \nabla s + F \nabla \phi$, and the quantity $U(s)$ is defined in section B.1. Note that in VMEC with flow [Coo+14], the rotation frequency Ω and temperature T are only given as normalised profiles with respect to its value on axis.

C.4 Benchmark and convergence test

In order to test the convergence of the VENUS-MHDpy code, we implemented the Laplacian Disk differential equation $\nabla^2 X = \lambda X$, where $\nabla^2 X = \partial_s^2 X + \partial_s X/s + \partial_\theta^2 X/s^2$. Analytical solution to this problem is given by the Bessel functions. Application of the boundary conditions $X(s=0) < |\infty|$ and $X(s=1) = 0$ gives the solution to the eigenvalues, which are roots of the Bessel functions of the first kind. We obtain a convergence order of 2ν (figure C.1a), where ν is the order of the B-spline used for the discretisation.

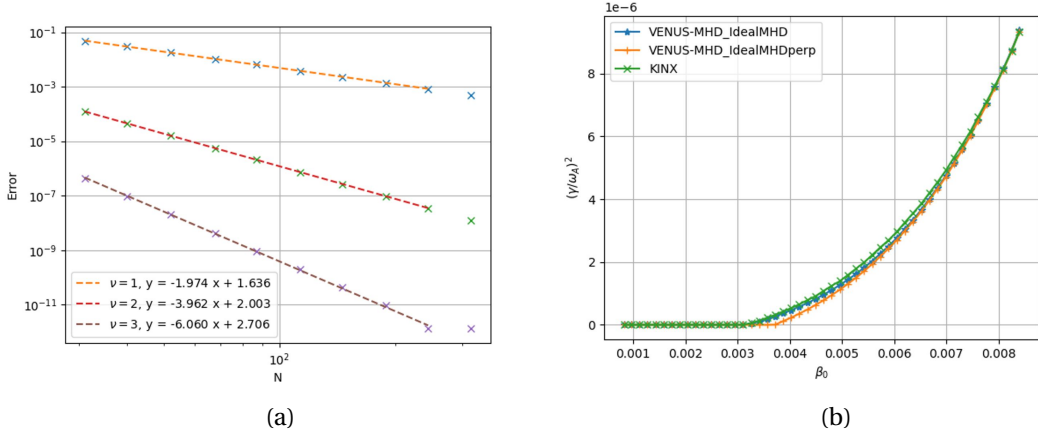


Figure C.1: (a) Convergence of the VENUS-MHDpy code for the Laplace disk eigenvalue problem. The error in the calculation of the eigenvalues converges with an order of 2ν , with ν the B-spline order used in the discretisation. (b) Benchmark of the VENUS-MHDpy code against the KINX code for the case of an internal kink mode.

The VENUS-MHDpy code was benchmarked against the KINX [Deg+97] ideal MHD stability code. An internal ($m=1, n=1$) kink mode parameter scan, varying the value of the $\beta_0 = \frac{2\mu_0 P_0}{B_0^2}$ was selected for the test. Two static ideal MHD models implemented in the VENUS-MHDpy code were used, the full ideal MHD model and the perpendicular ideal MHD model. As it is well known from theory, the growth rates in the perpendicular MHD model are scaled by a known factor $\gamma_\perp = \sqrt{1+2q^2}\gamma$ close to marginal stability. Therefore, the perpendicular growth rates were multiplied by the enhancement factor $\sqrt{3}$. The result of the benchmark is reported in figure C.1b, showing good agreement between the two codes.

C.5 Future prospects

The goal of the VENUS-MHDpy code is to have a general and flexible tool to compare different physics models under the same numerical environment. Analytical models can also be implemented with relative ease using specialised `Mathematica` scripts, so the code could be used to benchmark analytical approximations including different physical effects. Soon, the code will be upgraded to include vacuum boundary conditions and plasma resistivity with strong flows.

A major upgrade to the code is the inclusion of kinetic effects (tentatively called VENUS-KMHD), which is being undertaken by the following generation of students at the Swiss Plasma Centre. To necessary velocity space dimensions related to the calculation of the perturbed distribution function moments are added to the code as components in the vector \mathbf{X} . For example, for the ideal MHD perpendicular model, the vector has the following form

$$\mathbf{X} = (\xi^s, \xi^\perp, \delta f(v_{\perp 0}, v_{\parallel 0}), \delta f(v_{\perp 0}, v_{\parallel 1}), \dots, \delta f(v_{\perp 0}, v_{\parallel N_{\parallel}}), \delta f(v_{\perp 1}, v_{\parallel 0}), \dots, \delta f(v_{\perp N_{\perp}}, v_{\parallel 0}), \dots, \delta f(v_{\perp N_{\perp}}, v_{\parallel N_{\parallel}})), \quad (\text{C.8})$$

where N_{\parallel} and N_{\perp} give the grid size of the velocity space variables, and each component depends on the spatial coordinates (s, θ, ϕ) as given in equation C.1. This representation uses the same structure as VENUS-MHDpy with fluid models, but increases the number of variables from $N \sim 10$ (in the most complex fluid models) to $N \sim 10^3$. The implementation required some parallelisation on the building matrix blocks of the code, which has been successfully implemented and tested. A following scaling-up of the code will be the use of the SLEPc4py Python library to solve the eigenvalue problem, which includes tools of massive parallelisation.

D Acronyms

MHD: Magnetohydrodynamics
SFL: Straight Field Line
FLB: Field Line Bending
MP: Magnetic Perturbations
RMP: Resonant Magnetic Perturbations
EFCCs: Error Field Correction Coils
VMEC: Variational Moments Equilibrium Code
ELM: Edge Localised Modes
PFC: Plasma Facing Components
H-mode: High-confinement mode
QH-mode: Quiescent High-confinement mode
TB: Transport Barrier
EHOs: Edge Harmonic Oscillations
LCFS: Last Closed Flux Surface
NBI: Neutral Beam Injection
ECE: Electron Cyclotron Emission
BES: Beam Emission Spectroscopy
ITER: International Thermonuclear Experimental Reactor
JET: Joint European Torus
JT60: Japan Torus 60
ASDEX-U: Axially Symmetric Divertor Experiment - Upgrade
MAST: Mega Ampere Spherical Tokamak

Acknowledgements

First, to my thesis supervisor Prof. Jonathan Graves. Thank you for giving me the opportunity to work in such an exciting project. For always treating me with the respect and professionalism of a colleague, but with the pedagogic approach of a true mentor. Thank you for the work environment you have set along your students, which allows us to work and develop our own ideas. Thanks for always having an open door for long discussions and for the brilliant insights you provided me during them. You were the central piece in which I polished the ideas and results developed during this thesis. I am truly grateful to have worked under your supervision, and I hope we collaborate again in the future.

To the jury members Dr. Sergei Mendevev, Dr. Chris Ham and Dr. Jennifer Schober for reading the thesis and for providing me with very insightful feedback. Your comments and questions increased the quality of the manuscript.

The work presented in this thesis was only possible thanks to the people who set the theoretical and numerical bases described in the thesis, to which I am thankful. To Dr. Anthony Cooper for your innovative work on the 3D equilibrium approach to MHD perturbed states. I am sorry to have bother you during retirement but thank you for sparing some time to answer my questions about the VMEC code. To Dr. Daniele Brunetti and Prof. Jonathan Graves, for developing the theoretical basis of the excitation of external modes. Thank you Daniele for your availability and your numerous ideas, many of which resulted in essential parts of the papers published during the making of this thesis. You have a passion for the true and elegant solutions which I only hope I share. Hopefully we can collaborate again. A special thanks

Acknowledgements

goes to Dr. Andreas Kleiner, who worked on this topic before me and came up with innovative solutions to categorise the 3D saturated states. Thanks for sharing those secrets with me at the very beginning of my journey. To Rohan Ramasmy for the many online discussions about JOREK and nonlinear physics, which greatly expanded my horizons of numerical knowledge. I hope to one day meet you in person. To Fabien, I am very grateful for the many discussions about the development of the VENUS-MHDpy code. This final part of the PhD journey was one of the ones I enjoyed the most. On this respect, I would also like to thank Samuel Lanthaler for his constant help on the development of the code. Thank you for your disposition and availability, and I hope we cross our paths again in the future.

To Eduardo Neto, my office mate during most of my time at SPC. Thank you for helping me with both physics and numerical issues, particularly on the compilation of the VMEC code. Thanks for all the discussions about physics and life. You have an immovable spirit for what you believe is the right thing, and you have my admiration for that. I wish I had been more persistent on being a better friend to you. Thank you for putting up with me during almost 4 years. To Arsene, for your unconditional friendship and support during my years here. The fire in your soul is contagious, and I hope I can live to that one day. To Pedro, for very warmly welcoming me to SPC, to the sausages and to Swiss life. Thank you for all the experiences we shared here and there. To Andre and Mike, for your friendship and for pushing me to explore this beautiful country in new ways.

To the MHD group: Mike, Antoine, Margot, Fabien, Andreas, Eduardo, Cristian, Joaquim, Joachim, and of course Jon. Thank you for listening incessantly to my work during the meetings and for your help during the times I got stuck on my research. I am profoundly grateful to all of the SPC community (services, administration staff, researchers, post-docs and my fellow PhD students). This laboratory is like no other, and I consider myself extremely lucky to have belonged to such a warm and supportive community of scientists. To Arsene, Mike, Baptiste, Eduardo, Samuel, Andreas, Simon, Mirko, Andre, Antoine(s), Hamish, Pedro, Antonio, Fabien, Claudia, Margot, Lorenzo(s), Mohan and all the many other PhD students at SPC. Thank you for having taken this journey together, and for the many experiences we shared.

To my friends outside of SPC: Gina, Rapha, Ana, Immi, Yael, Marco, Francisco, Fer, Joel, Cristina, Vale and Avril. You are family to us, and have truly made us feel like we have a home in Switzerland. Thank you all for the help and support you gave us, which improved every aspect of our lives. Even though we might leave Switzerland, a part of our heart stays here with

you, and be sure we will come back for it.

To my family in Mexico. Papá y mamá, ustedes son los verdaderos arquitectos de la persona que soy ahora. Muchas gracias por siempre estimular mis capacidades y motivarme a seguir mis sueños. Gracias a ustedes soy una persona increíblemente privilegiada en todos los sentidos, lo cual me ha traído hasta aquí. Muchas gracias a mis hermanos Ricardo, Daniela y Alejandra por su apoyo incondicional durante estos 4 años. Ustedes han sido mis compañeros de vida y mi trayectoria hasta aquí no hubiera sido posible sin ustedes.

Finally, to my wife Karen. Primero que nada te agradezco profundamente que me hayas seguido hasta Suiza a cumplir mis sueños, aún cuando significaba sacrificar algunos de los tuyos. Muchas gracias por estar conmigo en las buenas, las malas y las peores. Estos 4 años y medio han estado llenos de alegría y entusiasmo gracias a tí. Gracias por escucharme pacientemente hablar de física, de mis problemas en el trabajo, o de cualquier cosa que pesara en mi cabeza. Gracias por motivarme y creer en mí cuando me sentía derrotado. Si tuve algún éxito aquí, sea cual sea, es compartido contigo.

Bibliography

- [AAM15] R. Albanese, R. Ambrosino, and M. Mattei. “CREATE-NL+: A robust control-oriented free boundary dynamic plasma equilibrium solver”. In: *Fusion Engineering and Design* 96-97 (Oct. 2015), pp. 664–667. ISSN: 0920-3796. DOI: 10.1016/J.FUSENGDES.2015.06.162.
- [Aib+09] N. Aiba et al. “MINERVA: Ideal MHD stability code for toroidally rotating tokamak plasmas”. In: *Computer Physics Communications* 180.8 (Aug. 2009), pp. 1282–1304. ISSN: 00104655. DOI: 10.1016/j.cpc.2009.02.008.
- [Aib+21] N. Aiba et al. “Stabilization of kink/peeling modes by coupled rotation and ion diamagnetic drift effects in quiescent H-mode plasmas in DIII-D and JT-60U”. In: *Nuclear Fusion* 61.12 (Nov. 2021), p. 126044. ISSN: 0029-5515. DOI: 10.1088/1741-4326/AC318E. URL: <https://iopscience.iop.org/article/10.1088/1741-4326/ac318e%20https://iopscience.iop.org/article/10.1088/1741-4326/ac318e/meta>.
- [Amb19] R Ambrosino. *PMI-5.2.4-T015-2001 Report on Equilibrium Development: Final Report 2019*. Tech. rep. 2019.
- [Bar+] I Barlow et al. *The Error Field Correction Coils on the JET Machine*. Tech. rep. EURATOM/UKAEA.
- [Ber+58] I. B. Bernstein et al. “An energy principle for hydromagnetic stability problems”. In: *Proceedings of the Royal Society of London. Series A. Mathematical and Physical Sciences* 244.1236 (Feb. 1958), pp. 17–40. ISSN: 0080-4630. DOI: 10.1098/rspa.1958.0023. URL: <https://royalsocietypublishing.org/>.
- [BGB21] Guillermo Bustos Ramirez, Jonathan P Graves, and Daniele Brunetti. “Edge Harmonic Oscillations in plasmas with a separatrix and the effect of edge magnetic

- shear". In: *Plasma Physics and Controlled Fusion* 63.12 (Oct. 2021), p. 124004. ISSN: 0741-3335. DOI: 10.1088/1361-6587/ac2d77. URL: <https://iopscience.iop.org/article/10.1088/1361-6587/ac2d77%20https://iopscience.iop.org/article/10.1088/1361-6587/ac2d77/meta>.
- [Boo01] Allen H Boozer. "Error Field Amplification and Rotation Damping in Tokamak Plasmas". In: (2001). DOI: 10.1103/PhysRevLett.86.5059.
- [Bru+14a] D. Brunetti et al. "Fast growing resistive two fluid instabilities in hybrid-like tokamak configuration". In: *Plasma Physics and Controlled Fusion* 56.7 (July 2014), p. 075025. ISSN: 13616587. DOI: 10.1088/0741-3335/56/7/075025. URL: <http://stacks.iop.org/0741-3335/56/i=7/a=075025?key=crossref.bcd0e4d03bcb0eb507ff704da70fee5a>.
- [Bru+14b] D. Brunetti et al. "Ideal saturated MHD helical structures in axisymmetric hybrid plasmas". In: *Nuclear Fusion* 54.6 (June 2014), p. 064017. ISSN: 17414326. DOI: 10.1088/0029-5515/54/6/064017. URL: <http://stacks.iop.org/0029-5515/54/i=6/a=064017?key=crossref.fbd8c7c991c607649e2e22c24f36e038>.
- [Bru+18a] D. Brunetti et al. "Analytic stability criteria for edge MHD oscillations in high performance ELM free tokamak regimes". In: *Nuclear Fusion* 58.1 (Jan. 2018), p. 014002. ISSN: 17414326. DOI: 10.1088/1741-4326/aa9456. URL: <http://stacks.iop.org/0029-5515/58/i=1/a=014002?key=crossref.32c26fac145698f95b778144a2a37619>.
- [Bru+18b] Daniele Brunetti et al. "Analytic study on low-n external ideal infernal modes in tokamaks with large edge pressure gradients". In: *Journal of Plasma Physics* 84.2 (Apr. 2018), pp. 1–22. ISSN: 14697807. DOI: 10.1017/S002237781800020X. URL: https://www.cambridge.org/core/product/identifier/S002237781800020X/type/journal_article.
- [Bru+19a] D. Brunetti et al. "Excitation Mechanism of Low- n Edge Harmonic Oscillations in Edge Localized Mode-Free, High Performance, Tokamak Plasmas". In: *Physical Review Letters* 122.15 (Apr. 2019), p. 155003. ISSN: 10797114. DOI: 10.1103/PhysRevLett.122.155003. URL: <https://link.aps.org/doi/10.1103/PhysRevLett.122.155003>.
- [Bru+19b] D. Brunetti et al. "Helical equilibrium magnetohydrodynamic flow effects on the stability properties of low-n ideal external-infernal modes in weak shear tokamak configurations". In: *Plasma Physics and Controlled Fusion* 61.6 (June 2019),

- p. 064003. ISSN: 13616587. DOI: 10.1088/1361-6587/ab0f0b. URL: <http://stacks.iop.org/0741-3335/61/i=6/a=064003?key=crossref.0be718106b044cf441d340287bdd551d>.
- [Bru+22] D Brunetti et al. “Understanding JET-C quiescent phases with edge harmonic magnetohydrodynamic activity and comparison with behaviour under ITER-like wall conditioning”. In: *Plasma Physics and Controlled Fusion* 64.4 (Apr. 2022), p. 044005. ISSN: 0741-3335. DOI: 10.1088/1361-6587/ac4d3a. URL: <https://iopscience.iop.org/article/10.1088/1361-6587/ac4d3a>.
- [BSG20] Guillermo Bustos-Ramirez, Cristian Sommariva, and Jonathan Graves. *PMI-5.2.5-T013-D001: Study of fast ion confinement in QH-mode in DEMO1. Final Report 2020*. Tech. rep. 2020.
- [Bur+01] K. H. Burrell et al. “Quiescent double barrier high-confinement mode plasmas in the DIII-D tokamak”. In: *Physics of Plasmas* 8.5 II (May 2001), pp. 2153–2162. ISSN: 1070664X. DOI: 10.1063/1.1355981. URL: <http://aip.scitation.org/doi/10.1063/1.1355981>.
- [Bur+04] K H Burrell et al. “Edge radial electric field structure in quiescent H-mode plasmas in the DIII-D tokamak”. In: *Plasma Physics and Controlled Fusion*. Vol. 46. 5 SUPPL. A. IOP Publishing, May 2004, A165–A178. DOI: 10.1088/0741-3335/46/5A/018. URL: <http://stacks.iop.org/0741-3335/46/i=5A/a=018?key=crossref.ccb8c3ef4d1da355ba0686401a69eedd>.
- [Bur+05] K. H. Burrell et al. “Advances in understanding quiescent H-mode plasmas in DIII-D”. In: *Physics of Plasmas*. Vol. 12. 5. American Institute of Physics, May 2005, pp. 1–10. DOI: 10.1063/1.1894745. URL: <http://aip.scitation.org/doi/10.1063/1.1894745>.
- [Bur+16] K. H. Burrell et al. “Discovery of stationary operation of quiescent H-mode plasmas with net-zero neutral beam injection torque and high energy confinement on DIII-D”. In: *Physics of Plasmas* 23.5 (May 2016), p. 056103. DOI: 10.1063/1.4943521. URL: <http://aip.scitation.org/doi/10.1063/1.4943521>.
- [Bus+75] M. N. Bussac et al. “Internal Kink Modes in Toroidal Plasmas with Circular Cross Sections”. In: *Physical Review Letters* 35.24 (1975), pp. 1638–1641. ISSN: 00319007. DOI: 10.1103/PhysRevLett.35.1638.

Bibliography

- [CBT87] Peter J. Catto, Ira B. Bernstein, and Massimo Tessarotto. “Ion transport in toroidally rotating tokamak plasmas”. In: *Physics of Fluids* 30.9 (Sept. 1987), pp. 2784–2795. ISSN: 0031-9171. DOI: 10.1063/1.866045.
- [CF10] Antoine J. Cerfon and Jeffrey P. Freidberg. ““one size fits all” analytic solutions to the Grad-Shafranov equation”. In: *Physics of Plasmas* 17.3 (Mar. 2010), p. 032502. ISSN: 1070664X. DOI: 10.1063/1.3328818. URL: <http://aip.scitation.org/doi/10.1063/1.3328818>.
- [Cfe+20] The Cfetr Physics Team et al. “Low-n global ideal MHD instabilities in the CFETR baseline scenario”. In: *Plasma Physics and Controlled Fusion* 62.8 (Aug. 2020), p. 13. ISSN: 13616587. DOI: 10.1088/1361-6587/ab97f0. URL: <https://doi.org/10.1088/1361-6587/ab97f0>.
- [Che+16] Xi Chen et al. “Rotational shear effects on edge harmonic oscillations in DIII-D quiescent H-mode discharges”. In: *Nuclear Fusion* 56.7 (July 2016), p. 076011. ISSN: 17414326. DOI: 10.1088/0029-5515/56/7/076011. URL: <http://stacks.iop.org/0029-5515/56/i=7/a=076011?key=crossref.b38c477dbdeef420ce6562a3a7487720>.
- [Che+17a] J. G. Chen et al. “Impact of $E \times B$ shear flow on low-n MHD instabilities”. In: *Physics of Plasmas* 24.5 (May 2017), p. 050704. ISSN: 1070-664X. DOI: 10.1063/1.4984257. URL: <http://aip.scitation.org/doi/10.1063/1.4984257>.
- [Che+17b] Xi Chen et al. “Bifurcation of quiescent H-mode to a wide pedestal regime in DIII-D and advances in the understanding of edge harmonic oscillations”. In: *Nuclear Fusion* 57.8 (June 2017), p. 086008. ISSN: 17414326. DOI: 10.1088/1741-4326/aa7531. URL: <https://doi.org/10.1088/1741-4326/aa7531>.
- [CHT78] J. W. Connor, R. J. Hastie, and J. B. Taylor. “Shear, periodicity, and plasma ballooning modes”. In: *Physical Review Letters* 40.6 (Feb. 1978), pp. 396–399. ISSN: 00319007. DOI: 10.1103/PhysRevLett.40.396. URL: <https://link.aps.org/doi/10.1103/PhysRevLett.40.396>.
- [Cle22] Daniel Clery. “OUT OF GAS”. In: *Science* (2022). URL: <https://www.science.org/content/article/fusion-power-may-run-fuel-even-gets-started>.
- [Coo+10] W. A. Cooper et al. “Tokamak magnetohydrodynamic equilibrium states with axisymmetric boundary and a 3D helical core”. In: *Physical Review Letters* 105.3 (July 2010), p. 035003. ISSN: 00319007. DOI: 10.1103/PHYSREVLETT.105.035003/

- FIGURES/7/MEDIUM. URL: <https://journals.aps.org/prl/abstract/10.1103/PhysRevLett.105.035003>.
- [Coo+11] W. A. Cooper et al. “Helical core tokamak MHD equilibrium states”. In: *Plasma Physics and Controlled Fusion* 53.12 (Nov. 2011), p. 124005. ISSN: 0741-3335. DOI: 10.1088/0741-3335/53/12/124005. URL: <https://iopscience.iop.org/article/10.1088/0741-3335/53/12/124005%20https://iopscience.iop.org/article/10.1088/0741-3335/53/12/124005/meta>.
- [Coo+14] W. A. Cooper et al. “An approximate single fluid 3-dimensional magnetohydrodynamic equilibrium model with toroidal flow”. In: *Plasma Physics and Controlled Fusion* 56.9 (Sept. 2014), p. 94004. ISSN: 13616587. DOI: 10.1088/0741-3335/56/9/094004.
- [Coo+15a] W. A. Cooper et al. “A 3-D MHD equilibrium description of nonlinearly saturated ideal external kink/peeling structures in tokamaks”. In: *Journal of Plasma Physics* 81.6 (Dec. 2015), p. 515810605. ISSN: 14697807. DOI: 10.1017/S0022377815001221. URL: http://www.journals.cambridge.org/abstract_S0022377815001221.
- [Coo+15b] W. A. Cooper et al. “Free boundary equilibrium in 3D tokamaks with toroidal rotation”. In: *Nuclear Fusion* 55.6 (June 2015), p. 063032. ISSN: 17414326. DOI: 10.1088/0029-5515/55/6/063032. URL: <http://stacks.iop.org/0029-5515/55/i=6/a=063032?key=crossref.0837a6662a218209478ddf3a9ec54c92>.
- [Coo+16] W. A. Cooper et al. “Saturated ideal kink/peeling formations described as three-dimensional magnetohydrodynamic tokamak equilibrium states”. In: *Physics of Plasmas* 23.4 (Apr. 2016), p. 040701. ISSN: 10897674. DOI: 10.1063/1.4945743. URL: <http://aip.scitation.org/doi/10.1063/1.4945743>.
- [Deg+97] L. Degtyarev et al. “The KINX ideal MHD stability code for axisymmetric plasmas with separatrix”. In: *Computer Physics Communications* 103.1 (June 1997), pp. 10–27. ISSN: 00104655. DOI: 10.1016/S0010-4655(97)00037-4.
- [DH98] R.L. Dewar and S.R. Hudson. “Stellarator symmetry”. In: *Physica D: Nonlinear Phenomena* 112.1-2 (Jan. 1998), pp. 275–280. ISSN: 0167-2789. DOI: 10.1016/S0167-2789(97)00216-9. URL: <https://www.sciencedirect.com/science/article/pii/S0167278997002169>.
- [Dha+91] William D. D’haeseleer et al. *Flux Coordinates and Magnetic Field Structure: A Guide to a Fundamental Tool of Plasma Theory*. 1st ed. Springer, 1991.

Bibliography

- [Dii+17] The Diii-D Team et al. “Stationary QH-mode plasmas with high and wide pedestal at low rotation on DIII-D”. In: *Nuclear Fusion* 57.2 (Feb. 2017), p. 022007. ISSN: 17414326. DOI: 10.1088/0029-5515/57/2/022007. URL: <http://stacks.iop.org/0029-5515/57/i=2/a=022007?key=crossref.186310b65bf05bdbe03d94264cf551bc>.
- [Don+17] G. Q. Dong et al. “Stability of ideal and non-ideal edge localized infernal mode”. In: *Physics of Plasmas* 24.11 (Nov. 2017), p. 112510. ISSN: 1070-664X. DOI: 10.1063/1.4990595. URL: <http://aip.scitation.org/doi/10.1063/1.4990595>.
- [Don+19] G. Q. Dong et al. “Non-linear interplay between edge localized infernal mode and plasma flow”. In: *Nuclear Fusion* 59.6 (June 2019), p. 066011. ISSN: 17414326. DOI: 10.1088/1741-4326/ab130b. URL: <http://stacks.iop.org/0029-5515/59/i=6/a=066011?key=crossref.c129ad2eab9db68bda0bacc36336897>.
- [Dud] Ben Dudson. *FreeGS*. URL: <https://github.com/bendudson/freeds>.
- [Eva+04] T. E. Evans et al. “Suppression of large edge-localized modes in high-confinement DIII-D plasmas with a stochastic magnetic boundary”. In: *Physical Review Letters* 92.23 (June 2004), p. 235003. ISSN: 00319007. DOI: 10.1103/PHYSREVLETT.92.235003/FIGURES/5/MEDIUM. URL: <https://journals.aps.org/prl/abstract/10.1103/PhysRevLett.92.235003>.
- [FFH92] A.R Field, G Fussmann, and J.V Hofmann. “Measurement of the radial electric field in the ASDEX tokamak”. In: *Nuclear Fusion* 32.7 (July 1992), pp. 1191–1208. ISSN: 0029-5515. DOI: 10.1088/0029-5515/32/7/I09.
- [Fit18] Richard Fitzpatrick. “Two-fluid nonlinear theory of response of tokamak plasma to resonant magnetic perturbation”. In: *Phys. Plasmas* 25 (2018), p. 112505. DOI: 10.1063/1.5053804. URL: <https://doi.org/10.1063/1.5053804>.
- [För81] U. Förstner. “Metal Concentrations in River, Lake, and Ocean Waters”. In: *Metal Pollution in the Aquatic Environment*. Berlin, Heidelberg: Springer Berlin Heidelberg, 1981, pp. 71–109. DOI: 10.1007/978-3-642-69385-4_{\ }3.
- [FR60] E. Frieman and Manuel Rotenberg. “On Hydromagnetic Stability of Stationary Equilibria”. In: *Reviews of Modern Physics* 32.4 (Oct. 1960), pp. 898–902. ISSN: 0034-6861. DOI: 10.1103/RevModPhys.32.898. URL: <https://link.aps.org/doi/10.1103/RevModPhys.32.898>.
- [Fre14] Jeffrey P. Freidberg. *Ideal MHD*. Vol. 1. Cambridge University Press, 2014.

- [Fri53] Irving Friedman. “Deuterium content of natural waters and other substances”. In: *Geochimica et Cosmochimica Acta* 4.1-2 (Aug. 1953), pp. 89–103. ISSN: 0016-7037. DOI: 10.1016/0016-7037(53)90066-0.
- [Gar+11] A. M. Garofalo et al. “Advances towards QH-mode viability for ELM-stable operation in ITER”. In: *Nuclear Fusion* 51.8 (Aug. 2011), p. 083018. ISSN: 00295515. DOI: 10.1088/0029-5515/51/8/083018. URL: <http://stacks.iop.org/0029-5515/51/i=8/a=083018?key=crossref.f4ab00f6659dbbd61164b6989b5c9fcb>.
- [Gar+15] A. M. Garofalo et al. “The quiescent H-mode regime for high performance edge localized mode-stable operation in future burning plasmas”. In: *Physics of Plasmas* 22.5 (May 2015), p. 056116. ISSN: 10897674. DOI: 10.1063/1.4921406. URL: <http://scitation.aip.org/content/aip/journal/pop/22/5/10.1063/1.4921406>.
- [GC81] J. M. Greene and M. S. Chance. “The second region of stability against ballooning modes”. In: *Nuclear Fusion* 21.4 (Apr. 1981), pp. 453–464. ISSN: 0029-5515. DOI: 10.1088/0029-5515/21/4/002. URL: <http://stacks.iop.org/0029-5515/21/i=4/a=002?key=crossref.0afd53bc0cb380f1124ac75d107b2a43%20http://adsabs.harvard.edu/abs/1981NucFu..21..453G>.
- [GCW22] J. P. Graves, M. Coste-Sarguet, and C. Wahlberg. “Pressure driven long wavelength MHD instabilities in an axisymmetric toroidal resistive plasma”. In: *Plasma Physics and Controlled Fusion* 64.1 (Dec. 2022), p. 014001. ISSN: 13616587. DOI: 10.1088/1361-6587/ac3496. URL: <https://iopscience.iop.org/article/10.1088/1361-6587/ac3496%20https://iopscience.iop.org/article/10.1088/1361-6587/ac3496/meta>.
- [GHH00] J. P. Graves, R. J. Hastie, and K. I. Hopcraft. “The effects of sheared toroidal plasma rotation on the internal kink mode in the banana regime”. In: *Plasma Physics and Controlled Fusion* 42.10 (Oct. 2000), p. 1049. ISSN: 0741-3335. DOI: 10.1088/0741-3335/42/10/304. URL: <https://iopscience.iop.org/article/10.1088/0741-3335/42/10/304%20https://iopscience.iop.org/article/10.1088/0741-3335/42/10/304/meta>.
- [GHH96] C. G. Gimblett, R. J. Hastie, and T. C. Hender. “An analytic study of the magnetohydrodynamic stability of inverse shear profiles”. In: *Physics of Plasmas* 3.9 (1996), pp. 3369–3374. ISSN: 1070664X. DOI: 10.1063/1.871612.

Bibliography

- [Gib22] Elizabeth Gibney. “Nuclear-fusion reactor smashes energy record”. In: *Nature* 602.7897 (Feb. 2022), p. 371. ISSN: 14764687. DOI: 10.1038/D41586-022-00391-1.
- [GJW71] John M. Greene, John L. Johnson, and Katherine E. Weimer. “Tokamak Equilibrium”. In: *Physics of Fluids* 14.3 (1971), p. 671. ISSN: 00319171. DOI: 10.1063/1.1693488. URL: http://pof.aip.org/resource/1/pfldas/v14/i3/p671_s1%5Cnhttp://link.aip.org/link/PFLDAS/v14/i3/p671/s1&Agg=doi.
- [Gla60] Lovberg Ralph Harvey Glasstone Samuel. *Controlled Thermonuclear Reactions: An Introduction to Theory and Experiment*. Van Nostrand, 1960, p. 523.
- [Glu20] Rachel Gluck. *Middle school student achieved nuclear fusion in his family playroom*. Oct. 2020. URL: <https://www.guinnessworldrecords.com/news/2020/10/middle-school-student-achieved-nuclear-fusion-in-his-family-playroom-631163#:~:text=Hours%20before%20his%2013th%20birthday,family%20home%20in%20Memphis%2C%20Tennessee.&text=This%20could%20only%20mean%20one,person%20to%20achieve%20nuclear%20fusion..>
- [Gor15] M. J. Gorley. “Critical Assessment 12: Prospects for reduced activation steel for fusion plant”. In: *Materials Science and Technology* 31.8 (June 2015), pp. 975–980. ISSN: 0267-0836. DOI: 10.1179/1743284714Y.0000000732.
- [GP04] Hans Goedbloed and Stefaan Poedts. *Principles of magnetohydrodynamics: with applications to laboratory and astrophysical plasmas*. Vol. 1. Cambridge University Press, 2004.
- [GR58] H Grad and H Rubin. “Hydromagnetic Equilibria and Force-Free Fields”. In: *Journal of Nuclear Energy* 7 (1958), pp. 284–285.
- [Gra+19] J. P. Graves et al. “Reduced models for parallel magnetic field fluctuations and their impact on pressure gradient driven MHD instabilities in axisymmetric toroidal plasmas”. In: *Plasma Physics and Controlled Fusion* 61.10 (Aug. 2019), p. 104003. ISSN: 13616587. DOI: 10.1088/1361-6587/ab368b. URL: <https://doi.org/10.1088/1361-6587/ab368b>.
- [Gru+81a] R Gruber et al. *HERA AND OTHER EXTENSIONS OF ERATO*. Tech. rep. 1981, pp. 363–376.
- [Gru+81b] R. Gruber et al. “Erato stability code”. In: *Computer Physics Communications* 21.3 (1981), pp. 323–371. ISSN: 00104655. DOI: 10.1016/0010-4655(81)90013-8.

- [Ham+21] C. J. Ham et al. “Towards understanding reactor relevant tokamak pedestals”. In: *Nuclear Fusion* 61.9 (Sept. 2021), p. 096013. ISSN: 17414326. DOI: 10.1088/1741-4326/ac12e9. URL: <https://doi.org/10.1088/1741-4326/ac12e9>.
- [HC07] G. T A Huysmans and O. Czarny. “MHD stability in X-point geometry: Simulation of ELMs”. In: *Nuclear Fusion*. Vol. 47. 7. IOP Publishing, July 2007, pp. 659–666. DOI: 10.1088/0029-5515/47/7/016. URL: <https://iopscience.iop.org/article/10.1088/0029-5515/47/7/016%20https://iopscience.iop.org/article/10.1088/0029-5515/47/7/016/meta>.
- [HH88] R. J. Hastie and T. C. Hender. “Toroidal internal kink stability in tokamaks with ultra flat q profiles”. In: *Nuclear Fusion* 28.4 (1988), p. 585. ISSN: 0029-5515. DOI: 10.1088/0029-5515/28/4/005.
- [Hoe+21] M. Hoelzl et al. “The JOEKE non-linear extended MHD code and applications to large-scale instabilities and their control in magnetically confined fusion plasmas”. In: *Nuclear Fusion* 61.6 (May 2021), p. 065001. ISSN: 0029-5515. DOI: 10.1088/1741-4326/ABF99F. URL: <https://iopscience.iop.org/article/10.1088/1741-4326/abf99f%20https://iopscience.iop.org/article/10.1088/1741-4326/abf99f/meta>.
- [Höl+12] M Hölzl et al. “Coupling JOEKE and STARWALL Codes for Non-linear Resistive-wall Simulations”. In: *Journal of Physics: Conference Series* 401 (Dec. 2012), p. 012010. ISSN: 1742-6588. DOI: 10.1088/1742-6596/401/1/012010.
- [HRM86] S. P. Hirshman, W. I. van RIJ, and P. Merkel. “Three-dimensional free boundary calculations using a spectral Green’s function method”. In: *Computer Physics Communications* 43.1 (Dec. 1986), pp. 143–155. ISSN: 00104655. DOI: 10.1016/0010-4655(86)90058-5.
- [Hud+12] S. R. Hudson et al. “Computation of multi-region relaxed magnetohydrodynamic equilibria”. In: *Physics of Plasmas* 19.11 (Nov. 2012), p. 112502. DOI: 10.1063/1.4765691. URL: <https://aip.scitation.org/doi/abs/10.1063/1.4765691>.
- [Huy05] G. T.A. Huysmans. “External kink (peeling) modes in x-point geometry”. In: *Plasma Physics and Controlled Fusion* 47.12 (Dec. 2005), pp. 2107–2121. ISSN: 07413335. DOI: 10.1088/0741-3335/47/12/003. URL: <http://stacks.iop.org/0741-3335/47/i=12/a=003?key=crossref.140058eed36c4d50874760eac5ffd024>.

Bibliography

- [HW83] S. P. Hirshman and J. C. Whitson. “Steepest-descent moment method for three-dimensional magnetohydrodynamic equilibria”. In: *Physics of Fluids* 26.12 (June 1983), pp. 3553–3568. ISSN: 10706631. DOI: 10.1063/1.864116.
- [JN22] Eduardo José and Lascas Neto. “Heavy impurity transport in the presence of 3D MHD ideal perturbations”. PhD thesis. 2022.
- [Ker+98] W. Kerner et al. “CASTOR: Normal-Mode Analysis of Resistive MHD Plasmas”. In: *Journal of Computational Physics* 142.2 (May 1998), pp. 271–303. ISSN: 00219991. DOI: 10.1006/jcph.1998.5910.
- [KH13] Pushker A. Kharecha and James E. Hansen. “Prevented mortality and greenhouse gas emissions from historical and projected nuclear power”. In: *Environmental science & technology* 47.9 (May 2013), pp. 4889–4895. ISSN: 1520-5851. DOI: 10.1021/ES3051197. URL: <https://pubmed.ncbi.nlm.nih.gov/23495839/>.
- [Kin+15] J. D. King et al. “Experimental tests of linear and nonlinear three-dimensional equilibrium models in DIII-D”. In: *Physics of Plasmas* 22.7 (July 2015), p. 072501. ISSN: 10897674. DOI: 10.1063/1.4923017. URL: <http://aip.scitation.org/doi/10.1063/1.4923017>.
- [KK58] M. D. Kruskal and R. M. Kulsrud. “Equilibrium of a Magnetically Confined Plasma in a Toroid”. In: *Physics of Fluids* 1.4 (Nov. 1958), p. 265. ISSN: 00319171. DOI: 10.1063/1.1705884. URL: <https://aip.scitation.org/doi/10.1063/1.1705884>.
- [Kle+18] A. Kleiner et al. “Free boundary 3D ideal MHD equilibrium calculations for nonlinearly saturated current driven external kink modes in tokamaks”. In: *Nuclear Fusion* 58.7 (July 2018), p. 074001. ISSN: 17414326. DOI: 10.1088/1741-4326/aac607. URL: <http://stacks.iop.org/0029-5515/58/i=7/a=074001?key=crossref.a36ff8e6e101991c9bdd70a61b5a59f7>.
- [Kle+19] A. Kleiner et al. “Current and pressure gradient triggering and nonlinear saturation of low- n edge harmonic oscillations in tokamaks”. In: *Plasma Physics and Controlled Fusion* 61.8 (Aug. 2019), p. 084005. ISSN: 0741-3335. DOI: 10.1088/1361-6587/ab2444. URL: <https://iopscience.iop.org/article/10.1088/1361-6587/ab2444>.
- [Kre+13] I. Krebs et al. “Nonlinear excitation of low- n harmonics in reduced magnetohydrodynamic simulations of edge-localized modes”. In: *Physics of Plasmas* 20.8

- (Aug. 2013), p. 082506. ISSN: 1070-664X. DOI: 10.1063/1.4817953. URL: <https://aip.scitation.org/doi/abs/10.1063/1.4817953>.
- [Lan20] Samuel Lanthaler. “Kinetic-MHD stability of virtually collisionless plasmas”. In: (2020), p. 177. DOI: 10.5075/epfl-thesis-10142. URL: <http://infoscience.epfl.ch/record/276595>.
- [Las+21] E Lascas Neto et al. “Heavy impurity transport in tokamaks subject to plasma rotation, NTV and the influence of saturated ideal MHD perturbations”. In: *Plasma Physics and Controlled Fusion* 64.1 (Nov. 2021), p. 014002. ISSN: 0741-3335. DOI: 10.1088/1361-6587/AC3964. URL: <https://iopscience.iop.org/article/10.1088/1361-6587/ac3964> %20https://iopscience.iop.org/article/10.1088/1361-6587/ac3964/meta.
- [Law57] J D Lawson. “Some Criteria for a Power Producing Thermonuclear Reactor”. In: *Proceedings of the Physical Society. Section B* 70.1 (Jan. 1957), pp. 6–10. ISSN: 0370-1301. DOI: 10.1088/0370-1301/70/1/303.
- [Laz+16] Samuel A. Lazerson et al. “Verification of the ideal magnetohydrodynamic response at rational surfaces in the VMEC code”. In: *Physics of Plasmas* 23.1 (Jan. 2016), p. 012507. ISSN: 1070-664X. DOI: 10.1063/1.4939881. URL: <https://aip.scitation.org/doi/abs/10.1063/1.4939881>.
- [LBS96] H. Lütjens, A. Bondeson, and O. Sauter. “The CHEASE code for toroidal MHD equilibria”. In: *Computer Physics Communications* 97.3 (1996), pp. 219–260. ISSN: 00104655. DOI: 10.1016/0010-4655(96)00046-X.
- [Leh+97] Rich Lehoucq et al. *ARPACK: Solution of Large Scale Eigenvalue Problems with Implicitly Restarted Arnoldi Methods*. 1997. URL: <https://www.caam.rice.edu/software/ARPACK/>.
- [Liu+15] F. Liu et al. “Nonlinear MHD simulations of Quiescent H-mode plasmas in DIII-D”. In: *Nuclear Fusion* 55.11 (Sept. 2015), p. 113002. ISSN: 17414326. DOI: 10.1088/0029-5515/55/11/113002. URL: <http://stacks.iop.org/0029-5515/55/i=11/a=113002?key=crossref.6b1609fe1e964e9ae0bbcfb17b2bb026>.
- [Liu+18] F Liu et al. “Nonlinear MHD simulations of QH-mode DIII-D plasmas and implications for ITER high Q scenarios”. In: *Plasma Physics and Controlled Fusion* 60.1 (Jan. 2018), p. 014039. ISSN: 13616587. DOI: 10.1088/1361-6587/aa934f.

Bibliography

- URL: <http://stacks.iop.org/0741-3335/60/i=1/a=014039?key=crossref.c2c4bd95370e0e4d1f18b1b9112801a2>.
- [Liu+20] Chong Liu et al. “Lithium Extraction from Seawater through Pulsed Electrochemical Intercalation”. In: *Joule* 4.7 (July 2020), pp. 1459–1469. ISSN: 25424351. DOI: 10.1016/j.joule.2020.05.017.
- [LKN10] Yueqiang Liu, A. Kirk, and E. Nardon. “Full toroidal plasma response to externally applied nonaxisymmetric magnetic fields”. In: *Physics of Plasmas* 17.12 (Dec. 2010), p. 122502. ISSN: 1070664X. DOI: 10.1063/1.3526677. URL: <http://aip.scitation.org/doi/10.1063/1.3526677>.
- [LL10] Hinrich Lütjens and Jean François Luciani. “XTOR-2F: A fully implicit Newton-Krylov solver applied to nonlinear 3D extended MHD in tokamaks”. In: *Journal of Computational Physics* 229.21 (Oct. 2010), pp. 8130–8143. ISSN: 00219991. DOI: 10.1016/j.jcp.2010.07.013. URL: <https://www.sciencedirect.com/science/article/pii/S0021999110003967>.
- [LLK16] N. J. Lopes Cardozo, A. G.G. Lange, and G. J. Kramer. “Fusion: Expensive and Taking Forever?” In: *Journal of Fusion Energy* 35.1 (Feb. 2016), pp. 94–101. ISSN: 01640313. DOI: 10.1007/S10894-015-0012-7/TABLES/1. URL: <https://link.springer.com/article/10.1007/s10894-015-0012-7>.
- [LN88] E. Lazzaro and M. F. F. Nave. “Feedback control of rotating resistive modes”. In: *Physics of Fluids* 31.6 (Sept. 1988), p. 1623. ISSN: 00319171. DOI: 10.1063/1.867004. URL: <https://aip.scitation.org/doi/10.1063/1.867004>.
- [LNL19] Jiangang Li, Mingjiu Ni, and Yu Lu. “The frontier and perspective for tokamak development”. In: *National Science Review* 6.3 (May 2019), pp. 382–383. ISSN: 2095-5138. DOI: 10.1093/nsr/nwz029.
- [Mana] Many Authors. *Death rates per unit of electricity production*. URL: <https://ourworldindata.org/grapher/death-rates-from-energy-production-per-twh>.
- [Manb] Many Authors. *Spherical Tokamak for Energy Production*. URL: <https://step.ukaea.uk/>.
- [Man22] Many Authors. *Mitigation of Climate Change Climate Change 2022*. Tech. rep. 2022. URL: <https://www.ipcc.ch/site/assets/uploads/2018/05/uncertainty-guidance-note.pdf>.

- [Mar+09] A. Marinoni et al. “The effect of plasma triangularity on turbulent transport: modeling TCV experiments by linear and non-linear gyrokinetic simulations”. In: *Plasma Physics and Controlled Fusion* 51.5 (May 2009), p. 055016. ISSN: 0741-3335. DOI: 10.1088/0741-3335/51/5/055016.
- [Mik17] A. B. Mikhailovskii. *Instabilities in a confined plasma*. 2017. DOI: 10.1201/9780203750728.
- [Mik98] A. B. Mikhailovskii. “Generalized MHD for numerical stability analysis of high-performance plasmas in tokamaks”. In: *Plasma Physics and Controlled Fusion* 40.11 (Nov. 1998), pp. 1907–1920. ISSN: 07413335. DOI: 10.1088/0741-3335/40/11/007. URL: <https://iopscience.iop.org/article/10.1088/0741-3335/40/11/007%20https://iopscience.iop.org/article/10.1088/0741-3335/40/11/007/meta>.
- [MP80] E. K. Maschke and H. Perrin. “Exact solutions of the stationary MHD equations for a rotating toroidal plasma”. In: *Plasma Physics* 22.6 (June 1980), pp. 579–594. ISSN: 00321028. DOI: 10.1088/0032-1028/22/6/007.
- [MPT87] J. Manickam, N. Pomphrey, and A. M.M. Todd. “Ideal mhd stability properties of pressure driven modes in low shear tokamaks”. In: *Nuclear Fusion* 27.9 (Sept. 1987), pp. 1461–1472. ISSN: 17414326. DOI: 10.1088/0029-5515/27/9/009. URL: <http://stacks.iop.org/0029-5515/27/i=9/a=009?key=crossref.fc14153420e14d14b0e674be7546604c>.
- [New60] William A. Newcomb. “Hydromagnetic stability of a diffuse linear pinch”. In: *Annals of Physics* 10.2 (June 1960), pp. 232–267. ISSN: 1096035X. DOI: 10.1016/0003-4916(60)90023-3.
- [Ödb+98] A. Ödholm et al. “Sawteeth-induced impurity transport in tokamak plasmas”. In: *Physics of Plasmas* 3.3 (June 1998), p. 956. ISSN: 1070-664X. DOI: 10.1063/1.871800. URL: <https://aip.scitation.org/doi/abs/10.1063/1.871800>.
- [Oka+05] M. Okabayashi et al. “Control of the resistive wall mode with internal coils in the DIII-D tokamak”. In: *Nuclear Fusion* 45.12 (Nov. 2005), p. 1715. ISSN: 0029-5515. DOI: 10.1088/0029-5515/45/12/028. URL: <https://iopscience.iop.org/article/10.1088/0029-5515/45/12/028%20https://iopscience.iop.org/article/10.1088/0029-5515/45/12/028/meta>.
- [Ora+17] F. Orain et al. “Non-linear modeling of the plasma response to RMPs in ASDEX Upgrade”. In: *Nuclear Fusion* 57.2 (Feb. 2017), p. 022013. ISSN: 0029-5515. DOI:

- 10.1088/0029-5515/57/2/022013. URL: <http://stacks.iop.org/0029-5515/57/i=2/a=022013?key=crossref.2fa669a0584be70076f9c0a7c26b41a9>.
- [Oya+06] N. Oyama et al. “Pedestal conditions for small ELM regimes in tokamaks”. In: *Plasma Physics and Controlled Fusion* 48.5A (Apr. 2006), A171. ISSN: 0741-3335. DOI: 10.1088/0741-3335/48/5A/S16. URL: <https://iopscience.iop.org/article/10.1088/0741-3335/48/5A/S16%20https://iopscience.iop.org/article/10.1088/0741-3335/48/5A/S16/meta>.
- [Pan+20] A. Y. Pankin et al. “Towards validated MHD modeling of edge harmonic oscillation in DIII-D QH-mode discharges”. In: *Nuclear Fusion* 60.9 (Sept. 2020), p. 092004. ISSN: 17414326. DOI: 10.1088/1741-4326/ab9afe. URL: <https://doi.org/10.1088/1741-4326/ab9afe>.
- [Pee00] A G Peeters. “The bootstrap current and its consequences”. In: *Plasma Physics and Controlled Fusion* 42.12B (Dec. 2000), B231–B242. ISSN: 0741-3335. DOI: 10.1088/0741-3335/42/12B/318.
- [Pfe+14] D. Pfefferlé et al. “VENUS-LEVIS and its spline-Fourier interpolation of 3D toroidal magnetic field representation for guiding-centre and full-orbit simulations of charged energetic particles”. In: *Computer Physics Communications* 185.12 (Dec. 2014), pp. 3127–3140. ISSN: 00104655. DOI: 10.1016/j.cpc.2014.08.007.
- [Por+] L Porte et al. “THE ROUTE TO HIGH PERFORMANCE, DEMO RELEVANT, NEGATIVE TRIANGULARITY TOKAMAK OPERATION ON TCV”. In: (). URL: <https://nucleus.iaea.org/sites/fusionportal/Shared%20Documents/FEC%202020/fec2020-preprints/preprint0982.pdf>.
- [Püt+13] T Pütterich et al. “Observations on the W-transport in the core plasma of JET and ASDEX Upgrade”. In: *Plasma Physics and Controlled Fusion* 55.12 (Dec. 2013), p. 124036. ISSN: 0741-3335. DOI: 10.1088/0741-3335/55/12/124036.
- [Ram+22] R. Ramasamy et al. “Modeling of saturated external MHD instabilities in tokamaks: A comparison of 3D free boundary equilibria and nonlinear stability calculations”. In: *Physics of Plasmas* 29.7 (July 2022), p. 072303. ISSN: 1070-664X. DOI: 10.1063/5.0090008. URL: <https://aip.scitation.org/doi/10.1063/5.0090008>.
- [Rei+15] A Reiman et al. “Tokamak plasma high field side response to an $n = 3$ magnetic perturbation: a comparison of 3D equilibrium solutions from seven different codes”. In: (2015). DOI: 10.1088/0029-5515/55/6/063026.

- [Sha58] V D Shafranov. “On Magnetohydrodynamical Equilibrium Configurations”. In: *J. Exptl. Theoret. Phys. (U.S.S.R.)* 6 (1958), pp. 710–722.
- [SKK11] S. Saarelma, O. J. Kwon, and A. Kirk. “X-point effect on edge stability”. In: *Plasma Physics and Controlled Fusion* 53.2 (Feb. 2011), p. 025011. ISSN: 07413335. DOI: 10.1088/0741-3335/53/2/025011. URL: <https://iopscience.iop.org/article/10.1088/0741-3335/53/2/025011>
<https://iopscience.iop.org/article/10.1088/0741-3335/53/2/025011/meta>.
- [Sny+07] P. B. Snyder et al. “Stability and dynamics of the edge pedestal in the low collisionality regime: Physics mechanisms for steady-state ELM-free operation”. In: *Nuclear Fusion* 47.8 (Aug. 2007), pp. 961–968. ISSN: 00295515. DOI: 10.1088/0029-5515/47/8/030. URL: <http://stacks.iop.org/0029-5515/47/i=8/a=030?key=crossref.e315015157354730c97ccf03803b56de>.
- [Sol+10] E R Solano et al. “Observation of Confined Current Ribbon in JET Plasmas”. In: *Physical Review Letters* (2010). DOI: 10.1103/PhysRevLett.104.185003.
- [Sol68] L S Solov’ev. “The theory of Hydromagnetic Stability of Toroidal Plasma Configurations”. In: *Soviet Physics JETP* 26.2 (1968).
- [Str+05] E. Strumberger et al. “Numerical MHD stability studies: Toroidal rotation, viscosity, resistive walls and current holes”. In: *Nuclear Fusion* 45.9 (2005), pp. 1156–1167. ISSN: 00295515. DOI: 10.1088/0029-5515/45/9/016.
- [Sut+04] W Suttrop et al. “Study of quiescent H-mode plasmas in ASDEX Upgrade”. In: *Plasma Physics and Controlled Fusion* 46.5A (Apr. 2004), A151. ISSN: 0741-3335. DOI: 10.1088/0741-3335/46/5A/016. URL: <https://iopscience.iop.org/article/10.1088/0741-3335/46/5A/016>
<https://iopscience.iop.org/article/10.1088/0741-3335/46/5A/016/meta>.
- [Sut+05] W. Suttrop et al. “Studies of the ‘Quiescent H-mode’ regime in ASDEX Upgrade and JET”. In: *Nuclear Fusion* 45.7 (July 2005), p. 721. ISSN: 0029-5515. DOI: 10.1088/0029-5515/45/7/021. URL: <https://iopscience.iop.org/article/10.1088/0029-5515/45/7/021>
<https://iopscience.iop.org/article/10.1088/0029-5515/45/7/021/meta>.
- [Tur+13] A. D. Turnbull et al. “Comparisons of linear and nonlinear plasma response models for non-axisymmetric perturbations”. In: *Physics of Plasmas* 20.5 (May

Bibliography

- 2013), p. 056114. ISSN: 1070664X. DOI: 10.1063/1.4805087. URL: <http://aip.scitation.org/doi/10.1063/1.4805087>.
- [Tur12] A. D. Turnbull. "Plasma response models for non-axisymmetric perturbations". In: *Nuclear Fusion* 52.5 (May 2012), p. 054016. ISSN: 00295515. DOI: 10.1088/0029-5515/52/5/054016. URL: <http://stacks.iop.org/0029-5515/52/i=5/a=054016?key=crossref.d91cc08977247d51feb1596d19da3d6f>.
- [US 22] U.S. Geological Survey. *Mineral Commodity Summaries 2022 - Lithium*. Tech. rep. U.S. Geological Survey, 2022. URL: <https://pubs.usgs.gov/periodicals/mcs2022/mcs2022-lithium.pdf>.
- [Vie18] E. Viezzer. "Access and sustainment of naturally ELM-free and small-ELM regimes". In: *Nuclear Fusion* 58.11 (Sept. 2018), p. 115002. ISSN: 0029-5515. DOI: 10.1088/1741-4326/AAC222. URL: <https://iopscience.iop.org/article/10.1088/1741-4326/aac222%20https://iopscience.iop.org/article/10.1088/1741-4326/aac222/meta>.
- [Wag07] F Wagner. "A quarter-century of H-mode studies". In: *Plasma Physics and Controlled Fusion*. Vol. 49. 12 B. 2007, p. 1. DOI: 10.1088/0741-3335/49/12B/S01. URL: <https://iopscience.iop.org/article/10.1088/0741-3335/49/12B/S01/pdf>.
- [WCG09] C. Wahlberg, I. T. Chapman, and J. P. Graves. "Importance of centrifugal effects for the internal kink mode stability in toroidally rotating tokamak plasmas". In: *Physics of Plasmas* 16.11 (Nov. 2009), p. 112512. ISSN: 1070664X. DOI: 10.1063/1.3263683. URL: <http://aip.scitation.org/doi/10.1063/1.3263683>.
- [Web09] A. J. Webster. "Magnetohydrodynamic stability at a separatrix. II. Determination by new conformal map technique". In: *Physics of Plasmas* 16.8 (Aug. 2009), p. 082503. ISSN: 1070664X. DOI: 10.1063/1.3194271. URL: <http://aip.scitation.org/doi/10.1063/1.3194271>.
- [Wen+13] R. P. Wenninger et al. "Non-linear magnetic perturbations during edge-localized modes in TCV dominated by low n mode components". In: *Nuclear Fusion* 53.11 (Nov. 2013), p. 8. ISSN: 00295515. DOI: 10.1088/0029-5515/53/11/113004. URL: <https://iopscience.iop.org/article/10.1088/0029-5515/53/11/113004%20https://iopscience.iop.org/article/10.1088/0029-5515/53/11/113004/meta>.

- [Wes78] J. A. Wesson. *Hydromagnetic stability of tokamaks*. Jan. 1978. DOI: 10.1088/0029-5515/18/1/010. URL: <http://stacks.iop.org/0029-5515/18/i=1/a=010?key=crossref.1914854c29ae679c6024bde39db67378>.
- [WG07] C. Wahlberg and J. P. Graves. “Stability analysis of internal ideal modes in low-shear tokamaks”. In: *Physics of Plasmas* 14.11 (Nov. 2007), p. 110703. ISSN: 1070664X. DOI: 10.1063/1.2811929. URL: <http://aip.scitation.org/doi/10.1063/1.2811929>.
- [WG09] A. J. Webster and C. G. Gimblett. “Magnetohydrodynamic stability of a toroidal plasma’s separatrix”. In: *Physical Review Letters* 102.3 (Jan. 2009), p. 035003. ISSN: 00319007. DOI: 10.1103/PhysRevLett.102.035003. URL: <https://link.aps.org/doi/10.1103/PhysRevLett.102.035003>.
- [WH66] A A Ware and F A Haas. “Stability of a Circular Toroidal Plasma under Average Magnetic Well Conditions”. In: *Citation: The Physics of Fluids* 9 (1966), p. 956. DOI: 10.1063/1.1761797. URL: <https://doi.org/10.1063/1.1761797>.
- [WH88] F. L. Waelbroeck and R. D. Hazeltine. “Stability of low-shear tokamaks”. In: *Physics of Fluids* 31.5 (June 1988), p. 1217. ISSN: 00319171. DOI: 10.1063/1.866750. URL: <https://aip.scitation.org/doi/10.1063/1.866750>.
- [Why+10] D G Whyte et al. “I-Mode: An H-Mode Energy Confinement Regime with L-Mode Particle Transport in Alcator C-Mod. I-mode: An H-mode Energy Confinement Regime with L-mode Particle Transport in Alcator C-Mod”. In: (2010).
- [Wil+06] H. R. Wilson et al. “Magneto-hydrodynamic stability of the H-mode transport barrier as a model for edge localized modes: an overview”. In: *Plasma Physics and Controlled Fusion* 48.5A (Apr. 2006), A71. ISSN: 0741-3335. DOI: 10.1088/0741-3335/48/5A/S06. URL: <https://iopscience.iop.org/article/10.1088/0741-3335/48/5A/S06%20https://iopscience.iop.org/article/10.1088/0741-3335/48/5A/S06/meta>.
- [Wil+99] H. R. Wilson et al. “Ideal magnetohydrodynamic stability of the tokamak high-confinement-mode edge region”. In: *Physics of Plasmas* 6.5 I (May 1999), pp. 1925–1934. ISSN: 1070664X. DOI: 10.1063/1.873492. URL: <http://aip.scitation.org/doi/10.1063/1.873492>.
- [Xu+17] G. S. Xu et al. “ $E \times B$ flow shear drive of the linear low- n modes of EHO in the QH-mode regime”. In: *Nuclear Fusion* 57.8 (Aug. 2017), p. 086047. ISSN: 17414326.

Bibliography

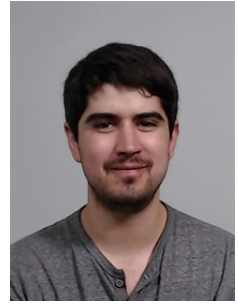
- DOI: 10.1088/1741-4326/aa7975. URL: <http://stacks.iop.org/0029-5515/57/i=8/a=086047?key=crossref.c436ae5e5e60ffceec64590b9e4cef26>.
- [Yad+14] D Yadykin et al. “Effect of the external helical fields on the plasma boundary shape in JET”. In: *Nuclear Fusion* 54.1 (Jan. 2014), p. 013016. ISSN: 00295515. DOI: 10.1088/0029-5515/54/1/013016. URL: <http://stacks.iop.org/0029-5515/54/i=1/a=013016?key=crossref.ebe080198716fdc31753ce654cb3feb7>.
- [ZHS12] P Zhu, C C Hegna, and C R Sovinec. “Stabilizing effects of edge current density on pedestal instabilities”. In: *Phys. Plasmas* 19 (2012), p. 32503. DOI: 10.1063/1.3692089. URL: <https://doi.org/10.1063/1.3692089>.
- [ZKV13a] L. J. Zheng, M. T. Kotschenreuther, and P. Valanju. “Behavior of $n = 1$ magnetohydrodynamic modes of infernal type at high-mode pedestal with plasma rotation”. In: *Physics of Plasmas* 20.1 (Jan. 2013), p. 012501. ISSN: 1070664X. DOI: 10.1063/1.4773898. URL: <http://aip.scitation.org/doi/10.1063/1.4773898>.
- [ZKV13b] L. J. Zheng, M. T. Kotschenreuther, and P. Valanju. “Low- n magnetohydrodynamic edge instabilities in quiescent H-mode plasmas with a safety-factor plateau”. In: *Nuclear Fusion* 53.6 (May 2013), p. 063009. ISSN: 00295515. DOI: 10.1088/0029-5515/53/6/063009. URL: <https://iopscience.iop.org/article/10.1088/0029-5515/53/6/063009/meta>.
- [ZKV17] L. J. Zheng, M. T. Kotschenreuther, and P. Valanju. “The sensitivity of tokamak magnetohydrodynamics stability on the edge equilibrium”. In: *Physics of Plasmas* 24.10 (Oct. 2017), p. 102503. ISSN: 10897674. DOI: 10.1063/1.4986036. URL: <http://aip.scitation.org/doi/10.1063/1.4986036>.

Guillermo Bustos-Ramirez

Date of birth: April 10, 1993

Nationality: Mexican

✉ guillermo.bustosramirez@epfl.ch
✉ guillermobustosramirez@hotmail.com



Education

- 2018 – 2022 **Ph.D candidate**
Swiss Plasma Center (SPC)- EPFL, Lausanne, Switzerland.
Thesis title: *Linear and nonlinear stability of tokamak plasmas with weak magnetic shear*.
Advisor: Dr. Jonathan Graves
- 2016 – 2017 **M.Sc. in Fusion energy** (Awarded Distinction)
University of York, York, UK.
Thesis title: *Eruptive plasmas: Explosive instabilities in tokamaks*.
Advisors: Dr. Christopher Ham and Prof. Howard Wilson.
- 2011 – 2015 **B.Sc. in Physics** (Awarded laureate recognition)
División de Ciencias e Ingenierías de la Universidad de Guanajuato, Guanajuato, México.
9.4/10, equivalent to a 1st class degree according to UK NARICK for the National College for Teaching and Leadership (NCTL).

Publications






Journal Articles

- 1 **Bustos-Ramirez, G.**, Graves, J. P., & Brunetti, D. (n.d.). Effect of non axisymmetric magnetic perturbation on non-resonant external modes. *To be submitted to Plasma Physics and Controlled Fusion*.
- 2 Ramasamy, R., **Bustos-Ramirez, G.**, Hoelzl, M., Graves, J., López, G. S., Lackner, K., & Günter, S. (2022). Modeling of saturated external MHD instabilities in tokamaks: A comparison of 3D free boundary equilibria and nonlinear stability calculations. *Physics of Plasmas*, 29(7), 072303.
doi:10.1063/5.0090008
- 3 Brunetti, D., Ham, C. J., Graves, J. P., Lazzaro, E., Nowak, S., **G Bustos-Ramirez**, ... Viezzer, E. (2022). Understanding JET-c quiescent phases with edge harmonic magnetohydrodynamic activity and comparison with behaviour under ITER-like wall conditioning. *Plasma Physics and Controlled Fusion*, 64(4), 044005. doi:10.1088/1361-6587/ac4d3a
- 4 **Bustos-Ramirez, G**, Graves, J. P., & Brunetti, D. (2021). Edge Harmonic Oscillations in plasmas with a separatrix and the effect of edge magnetic shear. *Plasma Physics and Controlled Fusion*, 63(12), 124004.
doi:10.1088/1361-6587/ac2d77
- 5 Esparza, D., **Bustos-Ramirez, G.**, Carriles, R., López-Luke, T., Zarazúa, I., Martínez-Benítez, A., ... De la Rosa, E. (2017). Studying the role of CdS on the TiO₂ surface passivation to improve CdSeTe quantum dots sensitized solar cell. *Journal of Alloys and Compounds*, 728, 183.
doi:10.1016/j.jallcom.2017.08.221

Conference contributions

- Advanced modelling and existence conditions of Edge Harmonic Oscillations. **Invited talk** at the JOINT VARENNA - LAUSANNE INTERNATIONAL WORKSHOP, September 12 - 16, 2022
- The operating space of Edge Harmonic oscillations in static plasmas. **Invited talk** at 10th International workshop on "Stochasticity in Fusion Plasmas (SFP)-3D physics in stellarators and tokamaks", Jul. 12 - 15, 2021.
- Refined Modelling of Edge Harmonic Oscillation. **Poster presentation** at the JOINT VARENNA - LAUSANNE INTERNATIONAL WORKSHOP, October 12 - 16, 2020.
- Modelling of non-linear Edge Harmonic Oscillations and the effect of non-axisymmetric magnetic coils. **Poster presentation** at 46th European Physical Society Conference on Plasma Physics (EPS 2019), July 8 to 12, 2019.
- Eruptive instabilities in plasmas. **Poster presentation** at Fusion Frontiers and Interfaces Workshop 2017, York, UK.
- From Zero to the device in quantum dots sensitized solar cells. **Poster presentation** at the LVIII National Physics Meeting, Yucatán, México 2015.
- 3D object segmentation oriented to the recognition and cell count. **Contributed talk** at the VI summer science congress, Guanajuato, México 2013.

Academic experience

- | | |
|-------------|---|
| 2018 – 2022 |  Swiss Plasma Center (SPC) EPFL, Switzerland.
<i>Doctoral Thesis.</i> Equilibrium and stability calculations of 2D and 3D plasma configurations in toroidal devices focused on advanced tokamak scenarios. Development of linear MHD stability solver in High performance Python. |
| 2016 |  Culham Centre for Fusion Energy, UK.
<i>MSc Thesis.</i> Investigation of the eruption of flux tubes in magnetically confined plasmas using non-linear ballooning theory and application of flux tube saturation in realistic tokamak geometries. |
| 2015 – 2016 |  Centro de Investigaciones en Óptica (Research Center in Optics), México.
<i>BSc Thesis.</i> Synthesis and characterisation of CdSeTe/CdSe Core/Shell quantum dots and application in photocurrent generation. Investigation of the properties of CdSeTe and CdSe nanocrystal interfaces. |
| 2014 |  University of Notre Dame, US.
<i>Research Experience for Undergraduates.</i> Study and simulation of stopping and extraction of radioactive ion from a gas chamber produced by the TWINSOL system. |
| 2013 |  Universidad Autónoma de Aguascalientes, México.
<i>Summer project.</i> Software development oriented to the recognition and cell count on medical microscopy images of the bone marrow of rats. |

Skills

Language skills	📖 Spanish (native), English (fluent), French (intermediate)
Coding skills	📖 High performance Python, C++, Fortran, MPI, Matlab, Mathematica.
Plasma physics software	📖 VMEC, KINX, CHEASE, FreeGS, VENUS-MHDpy.

Other

Teaching experience

Teaching assistanship

- Computational Physics I, 2nd year physics, EPFL. (Autumn semester)
- Computational Physics II, 2nd year physics, EPFL. (Spring semester)

Student supervision of semester projects

- Tom Emerit, EPFL 2022, Effect of equilibrium plasma flows on the stability of internal and external modes: A benchmark of the VENUS-MHDpy code.
- Tom Emerit, EPFL 2021, Analytical derivation of the effect of shaping in Edge Harmonic Oscillations.
- Veronica Orlandi, EPFL 2020, Effect of Shaping in the Excitation of Edge Harmonic Oscillations.

Awards and Achievements

- Excellence in Teaching Assistance price, awarded by the Phycis school of EPFL.
- Scholarship holder from CONACyT (National Commission for Science and Technology of Mexico) to complete M.Sc. in Fusion Energy at the University of York, UK.
- Scholarship holder from the Division of Nuclear Physics of the Mexican Physical Society and National Science Foundation to perform *Research Experience for Undergraduates*, at University of Notre Dame, US.

Science communication

- Experimental observation of cosmic rays using the integrated camera on smartphones. Science communicator at the levels of middle and high school (2015-2016).
- Active collaborator in the program *Academia de Niños y Jóvenes en la Ciencia* (2012-2013).

Other interests

Guitar, chess, basketball, science fiction, fantasy, nature.